Enhanced dynamic performance testing method for line-concentrating solar thermal collectors

Von der Fakultät für Maschinenbau
der Technischen Universität Carolo-Wilhelmina zu Braunschweig

zur Erlangung der Würde

einer Doktor-Ingenieurin (Dr.-Ing.)

genehmigte Dissertation

von: Annie Zirkel-Hofer

aus: Fürth

eingereicht am: 09. August 2017
mündliche Prüfung am: 30. Januar 2018

Gutachter: Prof. Dr.-Ing. Stephan Scholl
Prof. Dr. Werner Platzer
Prof. Dr.-Ing. Ulrike Krewer

2018

'I want a copy of permit number A38'

—Asterix in 'The Twelve Tasks of Asterix' by René Goscinny and Albert Uderzo, 1976—

Abstract

This thesis presents an enhanced dynamic performance evaluation method for line-concentrating solar thermal collectors. Due to its dispatchability and large storage capacity, concentrating solar power is considered of high relevance in the future renewable energy mix for both, electricity generation and industrial process heat supply. To fully exploit this potential and legitimize investments within this sector, a reliable and meaningful performance testing is essential. Dynamic testing is especially useful for outdoor testing, particularly on-site, lacking of laboratory facilities and therefore requiring in situ measurements. Those complex test conditions prevail for systems of larger dimensions such as line-concentrating collectors. A flexible, dynamic performance evaluation method allows for a significant reduction of testing time, effort, and consequently costs. Steady-state operating requirements do not have to be fulfilled as demanded in the currently valid and widely accepted testing standard ISO 9806:2013.

For this reason, the present thesis comprehensively addresses diverse aspects of dynamic in situ performance testing. Among smaller features, the elaborated approach includes a quality assessment of the evaluation results in terms of confidence computations. This is commonly not available for thermal collector testing so far. Besides, the thesis comprises an elaborate guideline for the proper selection of measurement instrumentation as well as a detailed proposal of an appropriate testing strategy for line-concentrating collectors. Applying both aspects as recommended, the quality of evaluation results may be significantly increased. For the first time, the enhanced approach of this thesis additionally enables the dynamic evaluation of collectors operating with steam as a heat transfer fluid. Moreover, the newly advanced testing approach is thoroughly validated with measurement data. The thesis includes a comprehensive application of the proposed procedure to diverse test collectors, ranging from small-scale medium-temperature linear Fresnel collectors to large-scale high-temperature parabolic troughs, including different heat transfer fluids and receiver designs. The exemplary evaluations of this variety of test collectors succeed well. They thereby demonstrate the general capabilities and practicability, as well as a broad validity of the developed alternative testing method. It therefore proves to be a powerful and beneficial extension of the current testing standard to more complex test situations. Flexible and simultaneously reliable certification procedures are considered crucial for the further establishment of solar thermal technologies and their global acceptance.

Kurzfassung

Die vorliegende Arbeit stellt eine erweiterte dynamische Auswertungsmethodik für die Leistungsmessung von linienkonzentrierenden Solarthermiekollektoren vor. Die konzentrierende Solarthermie ist aufgrund ihrer großen Speicherfähigkeit und Regelbarkeit von großer, weltweiter Bedeutung für eine zukünftige, regenerative Energieversorgung, insbesondere in den Bereichen der Stromerzeugung sowie der industriellen Prozesswärme. Um dieses Potential vollständig zu erschließen und Investitionen in diesem Bereich zu legitimieren, ist ein verlässliches und aussagekräftiges Testen der Leistungsfähigkeit solcher Systeme essenziell. Dynamische Testmethoden sind dabei speziell für Außentests vor Ort sehr hilfreich, da für diese Testbedingungen keine Laboranlagen zur Verfügung stehen und daher in-situ Messungen erforderlich sind. Besonders in großen Systemen, wie sie bei linienkonzentrierenden Kollektoren üblich sind, herrschen diese komplexen Testbedingungen vor. Eine flexible, dynamische Auswertungsmethode erlaubt es, die Testzeiten und entsprechend die Kosten der Tests deutlich zu reduzieren. Stationäre Betriebsbedingungen sind dabei nicht erforderlich, im Gegensatz zu den Anforderungen der momentan gültigen und weit akzeptierten Testmethode der Norm ISO 9806:2013.

Aus diesem Grund werden in vorliegender Arbeit verschiedene Aspekte einer dynamischen in-situ Auswertungsmethode vorgestellt. Neben kleineren Bestandteilen beinhaltet das erweiterte Auswertungsverfahren eine Qualitätsbewertung der Testergebnisse in Form von Konfidenzintervallen. Diese Berechnungen sind für gewöhnlich bei thermischen Testmethoden bisher nicht verfügbar. Darüber hinaus beinhaltet die Arbeit einen ausführlichen Leitfaden zur Auswahl geeigneter Messtechnik und eine detailliert ausgearbeitete Versuchsplanung. Die Umsetzung der daraus resultierenden Empfehlungen kann die Qualität der Auswertungsergebnisse deutlich verbessern. Der Auswertungsansatz erlaubt es zudem zum ersten Mal direkt-verdampfende Kollektoren unter dynamischen Bedingungen zu testen. Die erweiterte Testmethode ist umfassend mit Messdaten validiert. Die Arbeit beinhaltet daher eine breite und umfangreiche Anwendung der erarbeiteten Auswertungsmethode auf diverse Testkollektoren. Diese reichen von kleineren linearen Fresnel-Kollektoren im Mitteltemperaturbereich bis zu großen Hochtemperatur-Parabolrinnen, die unterschiedlichste Wärmeträgermedien und Receiverdesigns aufweisen. Die exemplarischen Auswertungen dieser Vielzahl an Testkollektoren gelingen erfolgreich. Damit bestätigen sie die allgemeingültige Funktionsweise und Anwendbarkeit der erarbeiteten alternativen Testmethode. Das neue Testverfahren stellt somit eine leistungsstarke und äußerst wertvolle Erweiterung der aktuellen Testnorm auf komplexe Testbedingungen dar. Ein flexibles und gleichzeitig verlässliches Zertifizierungsverfahren wird als unabdingbar erachtet für die zukünftige Etablierung der Solarthermie-Technologie und deren globaler Akzeptanz.

Acknowledgments

This comprehensive approach of dynamic performance testing certainly did not result from a vacuum, but many people have contributed and supported me on the rocky road to an elaborate testing procedure.

Every test campaign and data evaluation causes considerable cost of material and personnel, especially when they are not state of the art yet. For this reason, I thank the DBU (DEUTSCHE BUNDESSTIFTUNG UMWELT) for the financial and social support in the context of its PhD scholarship program. Moreover, several national and international research projects partly funded the development of this alternative testing procedure or provided access to test facilities. Major contributions were obtained by the BMWI (DEUTSCHES BUNDESMINISTRERIUM FÜR WIRTSCHAFT UND ENERGIE) within the projects *StaMeP* (16UM0095) and *ZeKon-InSitu* (0325560), as well as by the EUROPEAN UNION 7TH FRAMEWORK PROGRAMME (FP7/2007-2013) within the projects *FRESH-NRG* (308792), *SFERA-II* (312643), and *STAGE-STE* (609837). In this regard, I would like to additionally thank each of the six collector manufacturers and test facilities individually for giving me access to their sites and eventually approving the use of their measurement data within this thesis. Performance testing is a highly confidential and sensitive topic for industrial companies, especially in a non-standardized framework. I highly appreciate the companies for entrusting me their performance data and the responsibility of an adequate use and reporting of the test results. Every—even perfect—methodology is useless without its practical application and proof.

In the context of my PhD work, I would like to thank Prof. STEPHAN SCHOLL for accepting me as an external PhD candidate within his university institute. His scientific guidance and feedback concerning relevant aspects are highly appreciated.

I thank WERNER PLATZER for initially giving me the opportunity to work at Fraunhofer ISE on the topic of concentrating solar thermal. Since then, he has continuously guided me, giving valuable input concerning the general scope and conditions of suitable testing procedures.

Particularly, ANNA HEIMSATH did a great job in mentoring my PhD research on daily basis. Throughout the last years, she gave me consistent guidance and regular revision of my work. Profound discussions and detailed input concerning specific requirements highly contributed to the comprehensive approach of the present procedure.

KORBINIAN KRAMER gave me valuable insights into the world of certification and accreditation procedures in order to set the basis for a new procedure being able to cope with present standards. Moreover, he persistently provided me the view and requirements from the low-temperature solar thermal world, ensuring a wide application of the elaborated approach.

Concerning practical testing, SVEN FAHR gave me worthwhile input on relevant issues and challenges of collector testing. His profound hands-on experience and corresponding joint discussions were of essential support in order to assure the practicability of the dynamic testing procedure.

DANIEL BÜCHNER, EDWIN HERNÁNDEZ, JORIS NETTELSTROH, and TARIQ ZAHW completed their Master or Bachelor theses under my guidance, helping to further develop specific aspects of the global testing procedure. Especially, the work of STEPHEN PERRY as a scientific student assistant continuously improved the procedure and its implementation by his sound mathematical/statistical and programming skills.

Lots of colleagues and staff made my work at Fraunhofer ISE during the last years nicer and easier—with relaxing lunch brakes, simulation support, administrative discussions, motivating words, acquisition meetings, persuasion to Club Mate, standardization talks, conference preparations, 'party evening beers' and many other special and fruitful moments. I thank all of them: GREGOR BERN, RAYMOND BRANKE, TOM FLURI, PEDRO HORTA, PETER JAKOB, SIMON LUDE, PETER NITZ, KAROLINA ORDÓÑEZ MORENO, MARCO PERGHER, SHAHAB ROHANI, DE WET VAN ROOYEN, PETER SCHÖTTL, THOMAS SCHMIDT, BERNHARD SEUBERT, ALEXANDER VOGEL, VERENA ZIPF, and THEDA ZOSCHKE.

Furthermore, I would like to thank all my friends and Frisbee teammates for tolerating my absence, especially at the end of my PhD time, and still being there by my side.

The most continuing and reliable part within the last years represented my family. My parents, IRENA and HARALD, always encouraged me to do what I actually like, which finally lead to where I am now. My brother and sister-in-law, WANJA and VIOLA, gave me objective insights into common—and maybe not so common—issues of a PhD. Without their experienced assistance, continuous understanding, and support, this thesis would not be the way it is now. My cutie NILS is the best dispersion ever, his amusement especially motivating in the last months of really long office days. My family-in-law as well, always had my back throughout the entire time and encouraged me in harder times.

Most importantly I thank my better half FELIX for who he is. He had the most challenging part to cover and completed this tough period with distinction. He provided excellent mental and physical support, his patience and persistence, his sensitivity and ongoing motivation, and eventually his infinite backup are overwhelming—and I didn't even ask for it. There are no words that describe his brilliant part and my gratitude for this! Du bist einfach der Beste :*! Tausend Dank!

Freiburg im Breisgau, February 2017

Contents

List of Figures

List of Tables

Acronyms

AENOR	Asociación Española de Normalización y Certificación
BS	Bootstrapping
CEN	European Committee for Standardization
CENELEC	European Committee for Electrotechnical Standardization
CFD	Computational Fluid Dynamics
CI	Confidence Interval
ColSim	System Simulation Program for Thermal Systems and Controllers
COP21	United Nations Framework Convention on Climate Change, 21st Conference of the Parties
CPC	Compound Parabolic Concentrator
CSP	Concentrating Solar Power
DLR	Deutsches Zentrum für Luft- und Raumfahrt
DisPAT	Dynamic in situ Performance and Acceptance Testing
DISS	Direct Solar Steam
DNI	Direct Normal Irradiance
DSG	Direct Steam Generation
DT	Dynamic Testing
EPFM	Extended Plug-Flow Model
EU	European Union
HTF	Heat Transfer Fluid
IAM	Incidence Angle Modifier
iid	identically and independently distributed
IEC TC	International Electrotechnical Commission Technical Committee
ISE	Institute for Solar Energy Systems
LFC	Linear Fresnel Collector
MLR	Multiple Linear Regression
MURD	Mean Unsigned Relative Deviation
PFM	Plug-Flow Model
PSA	Plataforma Solar de Almería in Spain
PTC	Parabolic Trough Collector
PV	Photovoltaic
QDT	Quasi-Dynamic Testing

RMS	Root Mean Square
RMSE	Root Mean Square Error
RSS	Random Sub-Sampling
SD	Steam Drum
SFERA	Solar Facilities for the European Research Area
SIMPLE	Semi-Implicit Method for Pressure-Linked Equations
SIMPLER	Semi-Implicit Method for Pressure-Linked Equations—Revised
SST	Steady-State Testing
STAGE-STE	Scientific and Technological Alliance for Guaranteeing the European excellence in concentrating Solar Themal Energy
TDMA	Tri-Diagonal Matrix Algorithm
TRM	Thermal Resistance Model
VDI	Association of German Engineers

Symbols and Indices

Symbol	Description	Unit
a_i	diverse coefficients (e.g., IAM equation / SIMPLER)	
A	area	m^2
A_{Ap}	aperture area	m^2
A_{eff}	effective aperture area	m^2
α	percentile	–
b	bootstrapping block length	–
b_i	diverse coefficients (e.g., IAM equation / SIMPLER)	
C	covariance matrix	
c_p	specific heat capacity	$^{kJ}/_{kgK}$
c_i	diverse coefficients (e.g., heat loss equation QDT method / SIMPLER)	
CI	confidence interval	
d_i	diverse coefficients (e.g., SIMPLER)	
δ	collector tilt angle	$^\circ$
Δ	difference	
E	total energy	kJ
e_i	i-th normalized bootstrap residual	–
E_{in}	inner energy	kJ
E_{kin}	kinetic energy	kJ
E_{pot}	potential energy	kJ
ε	error (different definitions according to Equation (7.1) to Equation (7.7))	
η	thermal collector efficiency	–
$\eta_{0,b}$	conversion factor	–
η_{opt}	optical efficiency	–
$\eta_{opt,0}$	optical efficiency at normal incidence	–
f	focal length	m
F'	collector efficiency factor	–
f_{end}	end loss factor	–
f_{meas}	measured objective function	
f_{sim}	simulated objective function	
f_{soil}	soiling factor	–
f_{focus}	focus factor	–
g	gravitational acceleration	$^{m}/_{s^2}$

Symbol	Description	Unit
G_b	beam irradiance	W/m^2
G_{bn}	beam normal irradiance	W/m^2
G_{bT}	beam irradiance on tracked surface	W/m^2
G_d	diffuse irradiance	W/m^2
γ_c	collector azimuth angle	$°$
γ_s	solar azimuth angle	$°$
h	specific enthalpy	kJ/kg
$\dot{H}_{out}$	outlet flow enthalpy	kW
h_{eff}	effective height of collector	m
h_{rec}	receiver height	m
HL_{100}	heat loss at fluid reference temperature difference $T_{HTF} - T_{amb} = 100\,K$	W/m
J	Jacobian matrix	
K_b	IAM for beam/direct irradiance	–
K_d	IAM for diffuse irradiance	–
K_L	longitudinal IAM	–
K_T	transversal IAM	–
l	length	m
λ	specific thermal conductivity	W/mK
m	mass	kg
$\dot{m}$	mass flow rate	kg/s
$MURD_M$	mean unsigned relative difference to the mean value	–
n	number of diverse variables (e.g., data points, measurands, angle bins, measurement days)	–
N	number of nodes	–
p	number of parameters	–
p	pressure	bar
$\hat{p}$	pressure correction in SIMPLER procedure	bar
p^*	guessed pressure in SIMPLER procedure	bar
ϕ	discretization variable	
$\dot{q}$	specific power	kW/m^2
$\dot{Q}$	(usable, flow-bound) collector power output	kW
$\dot{Q}_{abs}$	collector power at absorber surface	kW
$\dot{Q}_{gains}$	collector power gains	kW
$\dot{Q}_{HL}$	collector power heat loss	kW
$\dot{Q}_{inert}$	unsteady, inert ratio of the collector power gains	kW
R	number of bootstrapping replicates	–
r_i	i-th bootstrap residual	
ρ	density	kg/m^3
$S(\theta)$	objective function depending on parameter vector θ	–
S_ϕ	source term in SIMPLER equations	
$S_{\phi,ci}$	constant part of source term in SIMPLER equations	
$S_{\phi,pi}$	proportional part of source term in SIMPLER equations	
σ	standard deviation	
t	time coordinate	s

Symbol	Description	Unit
T	temperature	°C / K
τ	sheer stress	Pa
θ/θ_i	incidence angle	°
θ	parameter vector	
$\widehat{\theta}$	best-fit parameter vector	
$\widehat{\theta}^*$	bootstrapping best-fit parameter distribution	
θ_L	longitudinal incidence angle	°
θ_{LS}	longitudinal solar incidence angle, angle between solar vector and transversal plane	°
θ_T	transversal incidence angle	°
θ_z	solar zenith angle	°
u	standard uncertainty	
u_c	combined standard uncertainty	
U_c	expanded and combined standard uncertainty	
u_i	heat loss coefficients DT method	
v	velocity	$^{m}/_{s}$
v^*	guessed velocity in SIMPLER procedure	$^{m}/_{s}$
$\widehat{v}$	velocity correction in SIMPLER procedure	$^{m}/_{s}$
$\tilde{v}$	pseudo-velocity in SIMPLER procedure	$^{m}/_{s}$
V	Volume	m^3
v_s	solar vector	
v_s^*	local solar vector	
w_{Ap}	aperture width	m
w_c	collector width	m
x	space coordinate	m
X	measurement data matrix	
X_i	measurand (random variable)	
$\dot{x}$	steam quality	–
y	objective variable	
y	estimate of measurand Y, result of a measurement	
Y	calculated measurand (random variable)	
y^*	bootstrap replicate of objective variable	
$\widehat{y}$	simulated objective variable of best-fit parameters $\widehat{\theta}$	

Index	Meaning
abs	absorber
amb	ambient
$\bar{y}$	bar over variable, mean of variable y
c	collector
DSG	direct steam generation
e	spatial index according to Figure 4.1
E	spatial index according to Figure 4.1
evap	evaporation
FW	feed water flow
HTF	heat transfer fluid
i	diverse index variable
ident	identified value
in	inlet
j	diverse index variable
L	longitudinal
m	mean
mean	mean
meas	measured
n	node index variable
n	number of diverse variables (e.g., data points, measurands, angle bins, measurement days)
N	number of nodes
node	node
out	outlet
p	spatial index according to Figure 4.1
P	spatial index according to Figure 4.1
rec	recirculation flow
rel	relative
sat	saturation
SD	steam drum
sim	simulated
steam	steam flow
sum	sum of flows
sys	system
t	time index variable
T	transversal
true	true reference value
w	spatial index according to Figure 4.1
W	spatial index according to Figure 4.1
water	water flow
0	time index variable for time step before

Chapter 1

Introduction

1.1 Motivation

Scarcity of fossil resources, energy security, and climate change are forcing communities, states, and companies worldwide to pursue alternatives to the conventional power generation. At the latest with the Paris Agreement of the UN Climate Conference (COP21) in 2015, limiting global warming and mitigating climate change has become internationally aware and compulsory. To meet the current EU and national targets, renewable energy resources—mainly solar, wind, biomass, hydro, and geothermal energy—will play an important role in the world's future energy mix. However, technologies like Photovoltaic (PV) or wind energy are subject to strong fluctuations due to weather and daytime. As they additionally have a low energy storage potential, they are currently not suited to provide base load power. One key benefit of Concentrating Solar Power (CSP) represents its dispatchability due to large storage capacities of thermal energy in comparison to electric energy. Thereby, CSP is able to provide energy at clouded time periods or at night. [Teske and Leung, 2016]

The CSP technology is based on the principle of focusing incoming solar radiation on a specific absorber. Figure 1.1 shows the different technologies currently available. A distinction is made between point-focusing and line-focusing systems: solar towers as well as parabolic dish systems concentrate the available solar radiation onto a focal point, whereas Parabolic Trough Collectors (PTCs) or Linear Fresnel Collectors (LFCs) focus the sun light onto a receiver tube in form of a focal line. Depending on the implementation and type of construction, the systems may provide different levels of working temperatures. According to the temperature level and other characteristics, different heat transfer media are used: pressurized water, thermal oil, and currently molten salt are the commonly used fluids. Higher efficiencies may be reached with the direct evaporation of water—so-called Direct Steam Generation (DSG)—in the receiver, because the produced steam may directly be fed to the steam network or turbine and therefore no additional heat exchanger is required. [Lovegrove and Stein, 2012, pp. 3–7,17]

Concentrating collectors can be designed in two different scales. Large-scale collectors are implemented in larger solar fields for electricity generation, whereas small-scale collectors are used for industrial process heat integration. Apart from their scalability, also their modularity makes line-concentrating collectors particularly suited for the integration into industrial processes. By a flexible connection of the collector modules in parallel or series, the generated power or heat of the system may be easily adapted to the required

Figure 1.1: Overview of different CSP systems. Upper left: linear Fresnel collector (© DLR/Novatec), upper right: solar tower (© NARED/Abengoa), lower left: parabolic trough (© Schott AG), lower right: parabolic dish (© DLR).

demand. Heat generation in general represents 56 % of the final energy consumption in Germany. For industrial process heat, 21 % of the final energy consumption are required [Lauterbach et al., 2012]. Worldwide even 24 % of the final energy consumption are used for the heat generation in industrial processes [Horta et al., 2017]. For the reduction of CO_2 emissions, the energy statistics show the important role worldwide of renewable heat supply in general and small-scale CSP in particular, as these systems are able to provide the required working temperatures between 100–400 °C.

One important requirement for all CSP systems is a high direct solar irradiation over a long period of time within the year. Therefore, CSP facilities are only meaningful to be installed in sunny regions with semi-arid climate characterized by few clouds and clear sky. Figure 1.2 depicts the yearly sum of available direct solar irradiation worldwide. Regions marked in yellow show a high potential for CSP with a large offer of solar radiation—such as southern Spain, California, the Sahara region, Chile, South Africa, and Australia. Even though the CSP technology has expanded rapidly in the last ten years converting it from a newly introduced to a reliable energy generation solution, the installed capacity worldwide only amounts to around 4.9 GW (as of December 2015). Nevertheless, the potential of CSP is estimated far greater. In a moderate development scenario, the solar thermal power capacity is estimated to reach around 20 GW in 2020 [Teske and Leung, 2016].

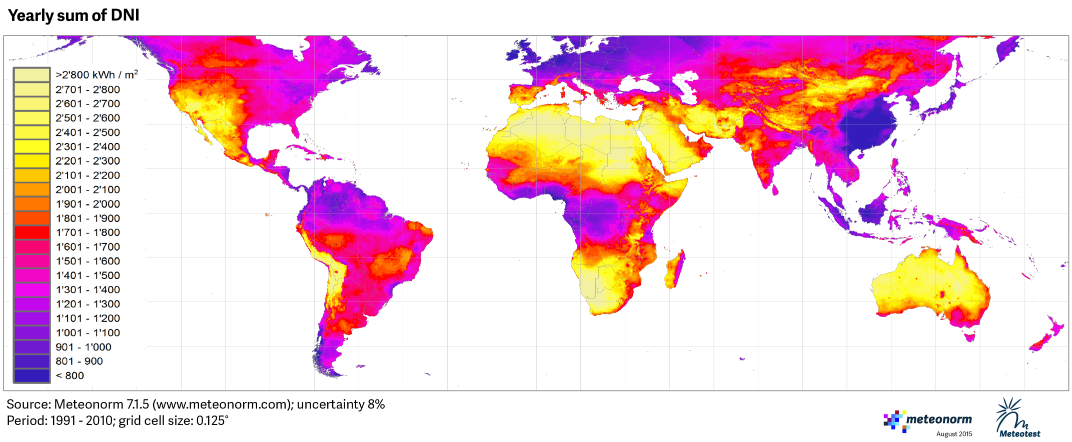

Figure 1.2: Worldwide available yearly sum of Direct Normal Irradiance. High potential regions are marked in yellow with DNI values > 2200 kWh/m^2 (© Meteonorm).

To fully exploit this potential, to establish and to increase the market penetration of this emerging technology, as well as to legitimize investments within this sector, a reliable and significant performance evaluation is essential. A dependable performance test sets the basis for a further development of the collector technology, as design and material improvements directly translate to increased efficiency or lower production costs. Moreover, reliable performance evaluation provides indicators for meaningful comparisons between collectors, which plays an important role for diverse aspects of standardization and certification. A quality label (such as the Solar Keymark [CEN and CENELEC, 2006]) creates transparency and comparability of the involved technologies, increases trust, and raises fair competition, resulting in a grown ambition to innovation.

Parabolic Trough Collectors (PTCs) as line-focusing systems currently represent the most common of the CSP technologies, being commercially installed since the early 1980s. Nevertheless, they still present a less established technology compared to low-temperature solar thermal collectors. Only since 2013, the currently valid and widely accepted testing standard ISO 9806 [ISO 9806, 2013, 2017] [1] also includes concentrating solar collectors within its scope of application. However, its content was not specifically adapted to concentrating technologies and therefore the testing standard is not fully applicable to concentrating collectors in general.

Concentrating collectors exceed the dimensions of standard low-temperature collectors by far. Accordingly, laboratory testing is hardly feasible for these types of collectors, requiring outdoor testing instead. In outdoor test facilities, steady-state measurement conditions as demanded in the indoor labs are very time consuming to fulfill, because ambient conditions like ambient temperature and solar irradiance cannot be controlled. Therefore, an alternative testing method based on a quasi-dynamic testing approach has been included in the testing standard ISO 9806:2013. It allows for dynamically varying

[1] Note that during the preparation until the submission of the present thesis, the international testing standard ISO 9806 in its version of 2013 was valid. Up to the final date of publication, a new version of the international standard ISO 9806:2017 was published—with its European EN and German DIN versions still pending. The work of the present thesis is therefore based on the testing standard ISO 9806:3013. Major parts of this version correspond to the updated version ISO 9806:2017 with slight adaptations and extensions, which do not significantly affect the general procedures referenced within the present thesis.

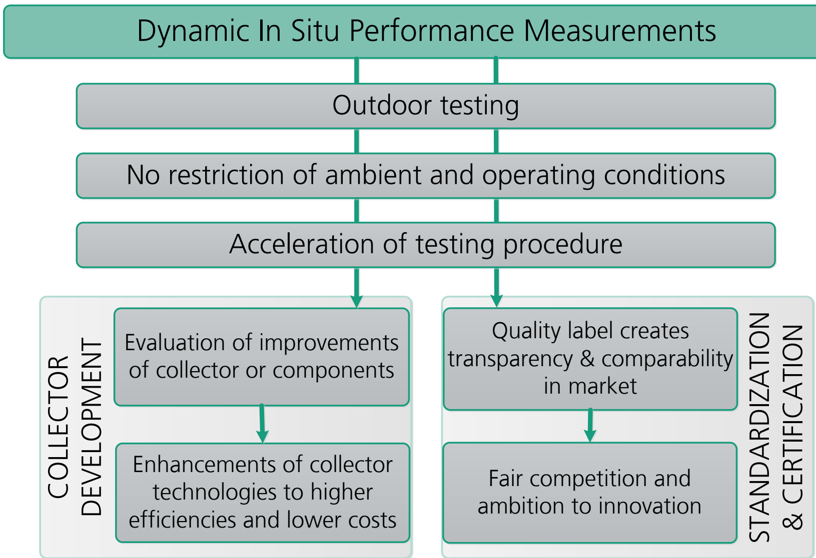

Figure 1.3: Aim and potential of dynamic in situ performance evaluation. The illustration focuses on development and standardization aspects of concentrating solar thermal collectors.

ambient conditions, but requires the inlet temperature and mass flow rate to be in steady state (yielding the naming of 'quasi-dynamic'). Nonetheless, these outdoor measurements are very cost-expensive, since they require large heating and cooling capacities to fulfill the steady-state operating requirements. Moreover, concentrating solar collectors are preferably and more appropriately tested within larger systems (as they are installed for their actual purpose), in modules, collector loops, or complete solar fields. These facilities are mostly put up at the production site of the manufacturer or at the final installation site of the end user. On-site performance testing requires an adapted recording and evaluation of in situ measurement data, which mostly demands a more flexible evaluation of dynamic measurement data under unsteady ambient and operating conditions. Figure 1.3 summarizes the aim and potential of performance evaluations based on dynamic in situ measurements.

Against this background the need for a fully dynamic performance evaluation procedure for concentrating solar thermal collectors becomes evident. This thesis addresses this particular aspect of enhanced dynamic in situ performance testing of line-concentrating collectors. Among smaller features, the elaborated approach includes a quality assessment of the evaluation results, which is commonly not available for thermal collector testing so far. Besides, the thesis comprises a comprehensive guideline for the proper selection of measurement instrumentation as well as a detailed proposal of an appropriate testing strategy for line-concentrating collectors. Applying both aspects as recommended, the quality of evaluation results may be significantly increased. For the first time, the enhanced approach of this thesis additionally enables the dynamic evaluation of collectors operating with steam as a heat transfer fluid.

The basis of the methodology can be applied to point-focusing systems as well, but the below introduced performance evaluation procedure focuses on line-concentrating systems in general. As the recent technology of linear Fresnel collectors (LFCs) is less investigated than the one of parabolic troughs, several characteristics and particularities of LFC testing are specifically discussed within certain chapters of this thesis.

■ 1.2 General Structure of This Thesis

To introduce the new performance evaluation method (referred to as the Dynamic Testing (DT) method within this thesis), the corresponding theoretical background is set in Chapter 2. As a basis for the specific enhancements required for the dynamic performance evaluation procedure, the state of the art and theory of dynamic collector testing with focus on concentrating solar thermal collectors is presented. Moreover, the chapter includes a summarized description of the used experimental facilities. The test facilities operating with solar collectors of different type, heat transfer fluid, and size provide a variety of measurement data for the validation of the proposed testing procedure. In this way, particular and individual elements of the procedure are validated on the one hand. On the other hand, the diversity of available measurement data ensures a comprehensive validation of the complete developed testing and evaluation procedure as a whole.

With the background set, Chapter 3 to Chapter 7 address diverse aspects and elements of the newly developed performance evaluation procedure. Detailed adaptations and enhancements of the dynamic testing method are derived, ranging from the general implementation structure, over direct steam generation, to the statistical assessment of the test results and including recommendations of appropriate measurement instrumentation as well as testing strategies. Note that the main theory of the general concept for dynamic performance testing is introduced in Chapter 2, whereas the specific methodology of the different elaborated elements are outlined within the corresponding chapters. This approach is pursued to assure a simple traceability of the structure, logic, and line of reasoning of the developed dynamic performance evaluation procedure.

The core of the proposed evaluation procedure is based on fitting measurement data of the test collector to simulation results, as schematically illustrated in Figure 1.4. Therefore, all developed elements of the enhanced dynamic testing method are related to specific parts of this fitting procedure. In Figure 1.4, the structure and sequence of the developed elements are sketched referring to the different chapters of the present thesis where the particular elements are discussed.

The general adaptation of the dynamic testing method concerning the specific evaluation structure, optimization procedure, and simulation model is derived in Chapter 3. The initial main premise for the further development of the dynamic testing method consisted in comparing and thereby validating it to the current state of the art in form of the normative Quasi-Dynamic Testing (QDT) method. As this method is not directly applicable for LFCs, an extension of it and its validation is introduced in Section 3.1.

One aspect of a comprehensive testing method lies in featuring a procedure applicable to collectors operating with different Heat Transfer Fluids (HTFs) such as pressurized water, thermal oil, and direct steam. Chapter 4 is dedicated to the adaptation of the evaluation method to DSG.

Dependable and meaningful reporting of test results requires specifications concerning confidence levels and uncertainty bands of the determined parameters. Therefore, one important element represents the statistical assessment of the evaluation quality. Its methodology and capabilities are described in Chapter 5.

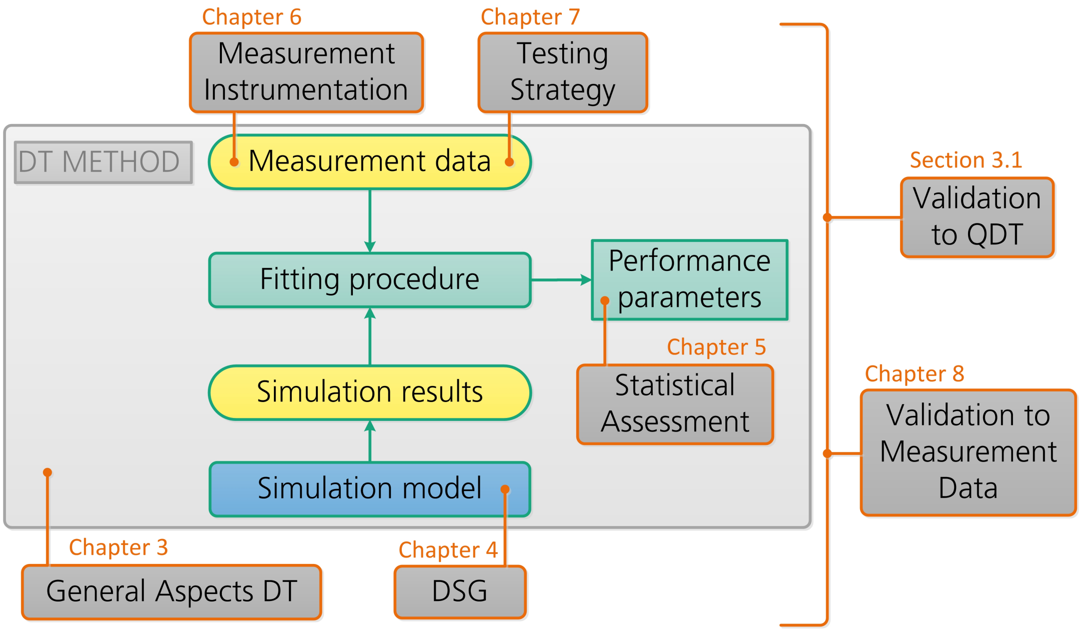

Figure 1.4: Investigated and developed elements of the dynamic performance evaluation method. Structure and sequence of the developed elements are sketched with respect to their relation to the DT method.

Measurement data constitute one key element of the testing method. To record significant and reliable measurement data, Chapter 6 comprises a guideline on the selection of proper measurement instrumentation depending on its uncertainties.

Moreover, the information content of the measurement data influences the quality of evaluation results and consequently determines the representativeness of the test results. For this reason, Chapter 7 presents the derivation and conclusion of a detailed testing strategy.

Finally, Chapter 8 includes the validation of the enhanced evaluation procedure to measurement data. It provides a comprehensive and general application of the newly advanced testing procedure to diverse test collectors ranging from small-scale medium-temperature linear Fresnel collectors to large-scale high-temperature parabolic troughs, including different heat transfer fluids and receiver designs. Thereby, the enhanced dynamic evaluation method is validated as a whole, proving its capabilities and practicability in terms of meaningful and reliable performance testing.

In the closing Chapter 9, overall results are summarized and concluded, allowing for the proposal of a comprehensive, consistent, and representative dynamic performance evaluation procedure.

Chapter 2

General Concept and Experimental Facilities

2.1 Literature Overview on Collector Testing Procedures

A detailed literature screening was compiled and already published in Hofer et al. [2016]. Wide parts of the following section correspond to this publication, with some paragraphs summarized, modified, or extended. The literature overview showed a multiplicity of different publications in the field of solar-thermal collector testing procedures. For this reason, the screened publications with their respective testing procedures were divided into two aspects: their testing methodology on the one hand and their application on the other, allowing a more structured and traceable comparison of the different testing methods. In Figure 2.1, the detailed literature review is summed up according to the introduced categories. The methodologies are grouped into Steady-State Testing (SST), Quasi-Dynamic Testing (QDT) and Dynamic Testing (DT), whereas the application of the published testing procedures is classified into non-tracking (stationary) collectors, tracking concentrating collectors, and large solar fields of tracking concentrating collectors.

The upper part of Figure 2.1, highlighted in light blue, shows that the majority of publications in the field of collector testing deals with non-tracking collectors. In this area, numerous testing and evaluation procedures have been published. For clarity reasons, publications of steady-state testing for non-tracking collectors have not been listed, as they are plenty and of less interest concerning testing procedures for concentrating collectors. Especially the quasi-dynamic testing procedure was investigated, adapted, and applied in several publications for different technologies, mainly based on the work done by the research group of Perers (e.g., see Perers [1993, 1997]). Moreover, the QDT method represents one of the proposed testing methods within the current testing standard ISO 9806 [2013]. As a counterpart to the QDT procedure, the dynamic testing method was firstly introduced by Muschaweck and Spirkl [1993], containing a more sophisticated collector simulation tool with the benefit of less restrictions in measurement data. The QDT method is based on a linear collector equation and quite strict boundary conditions, which allows the use of Multiple Linear Regression (MLR). In contrast, the DT method is based on different kinds of specific (dynamic) collector simulation models, allowing the evaluation of less restricted measurement data in terms of varying inlet temperatures, mass flow rates, and solar irradiance. Consequently, the use of dynamic

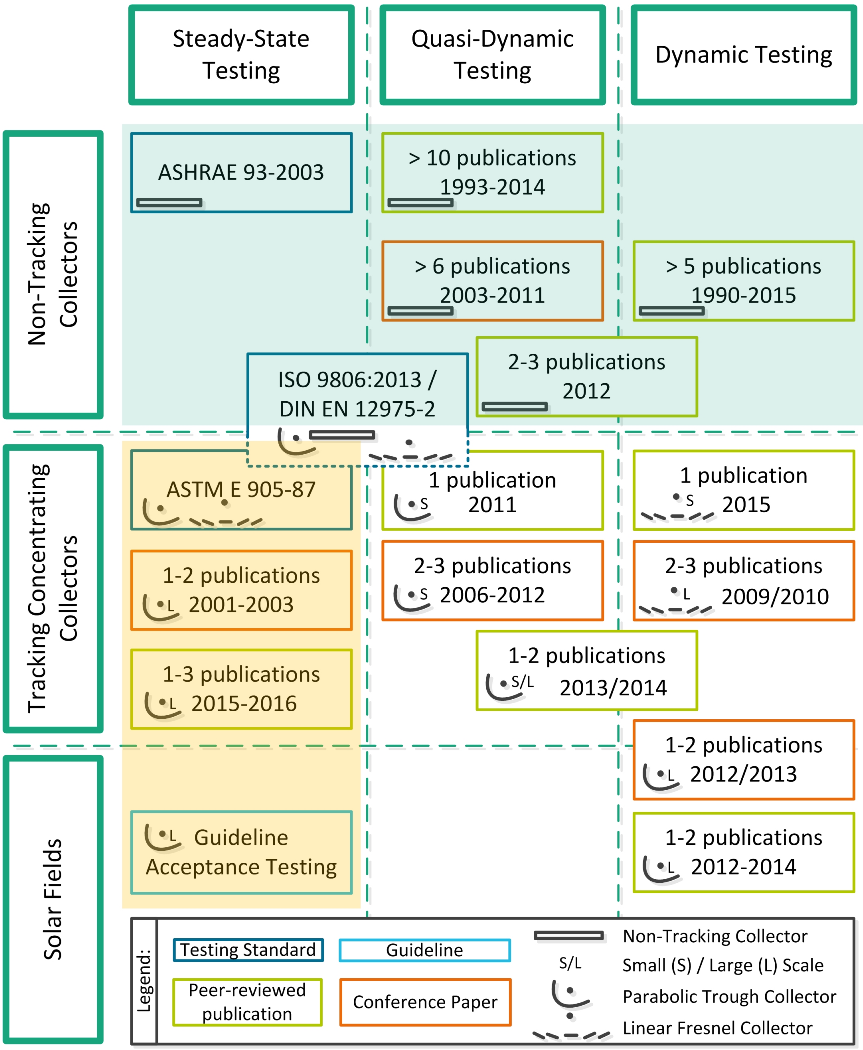

Figure 2.1: Summary of published testing and evaluation procedures with focus on concentrating solar collectors. Overview on state of the art of testing procedures in literature, differentiating between the type of testing method (steady-state, quasi-dynamic and dynamic) and its application (to non-tracking collectors, tracking concentrating collectors and solar fields). [adapted from Hofer et al., 2016]

models requires a combination with more complex optimization algorithms, consisting, for example, of a non-linear least-squares minimization approach or others. A comparison of both mathematical approaches by Fischer et al. [2003] showed that they are equivalent in their results, least-squares minimization only being more flexible in its application. An approach in-between QDT and DT is presented by Kong et al. [2012b]. It uses the MLR of the quasi-dynamic procedure with an enhanced linear collector equation, allowing for more dynamic measurements data. However, this approach is still reliant on some degree of steady-state data [see Kong et al., 2012a,b; Xu et al., 2012]. Additionally, numerous (quasi-) dynamic testing methods have been presented, differing in their specific physical, mathematical, or data collecting approaches. A detailed overview and comparison of (quasi-) dynamic testing methods in the field of non-tracking collectors can be found in Kong et al. [2012a] and Nayak and Amer [2000].

In the area of tracking concentrating collectors, the American testing standard ASTM E 905 – 87 [2007] is based on steady-state testing. Even a guideline for the acceptance testing of parabolic trough solar fields is based on steady-state measurements [Kearney, 2011]. Another approach of steady-state testing was applied for measuring the performance of large parabolic trough collectors [Valenzuela et al., 2014]. It is currently considered as a first reference approach for the proposal of a national standard in the Spanish National Committee AENOR[1] [see Sallaberry et al., 2016] and will be an input for discussion in the International Committee IEC TC[2] 117 (Solar thermal electric plants). Nevertheless, these testing procedures are either very time consuming or (if not the latter) mostly not comprehensively characterizing the collector or field performance, because they are limited to particular conditions (high solar irradiance, normal incidence at solar noon etc.).

In Figure 2.1, the testing standard ISO 9806:2013 is marked with dotted lines in the area of tracking concentrating collectors, as it is not fully applicable to all concentrating collectors without modifications. Publications in this field show that the QDT method is successfully applied particularly for small-scale parabolic trough collectors (marked with an S), because restrictions to measurement conditions can still be met [see Fischer et al., 2006; Janotte et al., 2009]. On this account, for a global characterization of large-scale collectors (marked with an L), either parabolic trough or linear Fresnel, mainly the dynamic testing method is applied, as with higher working temperatures, energy loads to be cooled to meet steady inlet conditions cannot be fulfilled easily. In particular, for the characterization of linear Fresnel collectors due to their special optical characteristics in terms of a two-dimensional Incidence Angle Modifier (IAM), new approaches by dynamic parameter identification [Platzer et al., 2009; Hofer et al., 2015a] or modifications to the QDT methods are inevitable (compare with Hofer et al. [2015a] and Section 3.1). This approach is pursued and developed within the present thesis. Xu et al. [2013, 2014] enhanced the QDT method for parabolic trough collectors, based on the work of Kong et al. [2012b], to be able to evaluate dynamic measurement data for these larger systems. However, the determined parameters of this new method do not correspond to any physical meaning, precluding a specific characterization of optical and thermal collector performance. This implies that the different identified parameters do not have a meaning on their own. Consequently, this approach is rather useful to evaluate the general energy output and system efficiency over a wider time span instead of balancing instantaneous collector power outputs.

Apart from the steady-state guideline for the acceptance testing of solar fields, there are few publications presenting a more sophisticated characterization and acceptance testing of parabolic trough solar fields based on dynamic testing procedures [see Janotte, 2012; Janotte et al., 2012, 2014]. Quasi-dynamic testing is rarely applied to large collectors or solar fields, which might be an indication that the QDT method with its restriction in measurement data is not entirely suited for the performance evaluation of larger systems.

With the existence of testing standards for non-tracking collectors (in Figure 2.1 highlighted area in light blue) and for steady-state testing procedures (in Figure 2.1 high-

[1]Asociación Española de Normalización y Certificación
[2]International Electrotechnical Commission Technical Committee

Table 2.1: Survey results concerning different currently used evaluation procedures and their specific application. The survey differentiates between testing method, collector and system under test, and heat transfer fluid used. [adapted from Hofer et al., 2016]

Category	Type	Share
Testing method	SST	8 %
	QDT	67 %
	DT	25 %
Evaluated collector type	parabolic trough	83 %
	linear Fresnel	25 %
	non-tracking collectors	33 %
System under test	solar collector	83 %
	solar field	33 %
Heat transfer fluid used	thermal oil	67 %
	pressurized water	50 %
	molten salt	8 %
	direct steam (SST)	16 %
	direct steam (DT)	0 %

lighted area in light orange), standardization in the area of dynamic testing procedures for tracking concentrating solar collector and fields is still lacking, while research and its publication is existing but scarce. To get a more comprehensive overview on current testing approaches, a survey on (not necessarily published) currently implemented dynamic testing and evaluation procedures was conducted within the European project STAGE-STE[3] (for more information see Hofer et al. [2016]). According to the list of participants, the survey was particularly concentrated on research institutions and relevant industries focused on tracking/concentrating solar thermal collectors and fields, as the literature review showed a gap of publications in this area (see right bottom part of Figure 2.1). Within the ten participants, the characteristics of 12 different testing/evaluation procedures were analyzed. Table 2.1 summarizes the general aspects of the different evaluation procedures.

The results show that around 67 % of the evaluation procedures are based on a quasi-dynamic testing approach. 25 % are based on dynamic testing procedures and 8 % are only able to evaluate in steady-state measurement conditions. They furthermore show that the majority (83 %) of the evaluation procedures are used for the characterization of parabolic trough collectors, whereas only 25 % are used for linear Fresnel collectors and 33 % for non-tracking medium temperature collectors[4]. 83 % of the evaluation methods are designed for solar collector evaluation, only 25 % can be applied to solar fields. Concerning the used heat transfer fluid for the characterization of the systems, mainly thermal oil (67 %) and pressurized water (50 %) are used, whereas only 8 % of the evaluation methods are performed with molten salt. A performance evaluation with direct steam based on a dynamic measurement approach does currently not exist within the partners of the survey. 16 % indicate that performance evaluation based on steady-state measurements can be performed. The figures show that the most commonly used evaluation method is designed for parabolic trough collectors operating with thermal oil or pressurized water. A reason why the evaluation methods can rarely be applied to other

[3]Scientific and Technological Alliance for Guaranteeing the European excellence in concentrating Solar Themal Energy

[4]The percentages do not add up to 100 % as there are several methods that can be used for several collector types.

collector types and heat transfer fluids may have to do with their lower prevalence on the one hand. The complexity and peculiarities linked to these systems under test may be of significant influence on the other hand, requiring more elaborate and sophisticated evaluation procedures.

All in all, both analyses—literature review and survey—showed the same tendency: the quasi-dynamic evaluation procedure according to the testing standard ISO 9806:2013 is mainly used in the context of tracking concentrating collectors for the performance assessment of parabolic trough collectors operating with thermal oil or pressurized water. These common solar systems can be evaluated with minor adaptation to the testing standard. Nevertheless, evaluation procedures focusing on in situ measurements in solar fields or collectors are scarce and complex. The same applies for an evaluation of linear Fresnel collectors or other systems operating with non-common heat transfer media like molten salt and direct steam. Since those are still presenting testing-wise challenging systems under real test conditions, a more sophisticated evaluation procedure such as the dynamic testing method is likely to be better suited. In terms of testing standardization, the DT method may present a considerable alternative to overcome the limitations of the normative QDT procedure and assure a reliable and comparable in situ performance assessment of large concentrating solar systems. The high relevance and potential of the DT method for the performance evaluation of concentrating collector represents the foundation and starting point of the present thesis. Its objective is the development of a comprehensive, viable, and therefore representative testing procedure, especially with respect to linear Fresnel systems, larger solar fields, and systems operating with direct steam.

■ 2.2 Basic Concept of Testing Procedures

The main approach pursued in collector testing consists in balancing inputs and outputs of the system under test, that is, the measuring of internal (process) and external (ambient) properties and thereof derive the performance of the system. For the system under test, the boundaries have to be clearly defined. They may consist of a single collector, module, row, or entire solar field. The defined boundaries of the system determine the location of the measurands of input and output quantities and eventually influence the derived overall performance. Different models exist to deduce the system performance by means of a thermal characterization. The primary methods used within the present thesis are the QDT and the DT method.

The basic concept of thermal characterization lies in the derivation of empirical, summarized performance correlations from thermal-hydraulic measurement data. This means that the derived (also called identified) performance parameters represent aggregated values, including numerous (known, as well as several not specifically known) effects in one parameter value. It therefore represents the contrary approach to physical modeling, where it is attempted to describe and reproduce detailed physical effects by means of sophisticated or simplified physical relations. For this reason, many product properties concerning geometry and material (such as, e.g., optical and thermal behavior) need to be included. Because they are deduced from specific measurements, the included properties show some degree of uncertainty. In many cases, particular component data is even not directly measurable and has to be estimated. The physical modeling approach is particularly suited for the product development, allowing detailed studies on specific effects as well as providing essential and valuable information for plausibility checks. Apart from these plausibility checks, physical modeling, however, is not meaningful to apply for testing purposes. In collector tests, the overall product characteristics (such as efficiency, durability, expediency, and so forth) are examined. The products are therefore treated as a black box, where specific details are not considered of particular interest but rather the overall performance.

■ 2.2.1 Quasi-Dynamic Testing QDT

The quasi-dynamic testing method represents one of the proposed testing procedures anchored in the current testing standard for solar thermal collectors ISO 9806 [2013]. It uses a quasi-dynamic (i.e., a semi-steady, which is not fully dynamic nor fully steady-state) approach by describing the thermal-hydraulic collector behavior by means of a one-node collector equation with the following simplified form for concentrating collectors [ISO 9806, 2013, p. 62, adapted to the nomenclature of the present thesis]

$$\begin{aligned}\frac{\dot{Q}}{A_{Ap}} = \frac{\dot{m} \cdot c_p \cdot (T_{out} - T_{in})}{A_{Ap}} &= \eta_{0,b} \cdot K_b(\vec{v}_s^{\,*}) \cdot G_{bT} + \eta_{0,b} \cdot K_d \cdot G_d - \\ &- c_1 \cdot (T_m - T_{amb}) - c_2 \cdot (T_m - T_{amb})^2 - c_5 \cdot \frac{dT_m}{dt},\end{aligned} \tag{2.1}$$

where the collector power output $\dot{Q}$—depending on the mass flow rate $\dot{m}$, specific heat capacity c_p and temperature difference $(T_{out} - T_{in})$—is defined as a function of optical performance parameters (as $\eta_{0,b}$, $K_b(\vec{v}_s^{\,*})$ and K_d) and aggregated thermal performance parameters (as c_1, c_2 and c_5). The specific meaning of all parameters are explained thoroughly in Appendix A. For an exemplary sketch of the balanced system and its measurement points, refer to Figure B.1.

Equation (2.1) shows that the QDT method uses the steady-state equation $\dot{Q} = \dot{m}c_p\Delta T$, including a dynamic capacity term c_5 to satisfy the potential dynamics of a variation in solar irradiance G_{bT} and hence mean fluid temperatures T_m. Nevertheless, this approach is only valid if inlet mass flow rates and inlet temperatures of the collector remain constant (±1 K in temperature and ±2% in mass flow rate). [ISO 9806, 2013, p. 56]

The one-node collector equation can be resolved via MLR, allowing a direct identification of the performance parameters of the collector under test (see Figure 2.2(a)). The QDT method originates from the work of Perers [1993], was put into practice in numerous collector testing and investigations [e.g., Nayak and Amer, 2000; Fischer et al., 2004; Rojas et al., 2008; Osório and Carvalho, 2014] and has been adapted continuously [Perers, 1997, 2011]. It therefore represents a widely accepted testing method, thoroughly checked for practicability and reliable validity.

However, the MLR requires a linear relation between the collector performance parameters to be determined. These conditions cannot always be met, in particular in the case of LFCs due to their special optical characteristics in terms of a two-dimensional incidence angle modifier K_b[5]. Moreover, in outdoor or in situ measurements—which are particularly relevant for larger systems as line-concentrating solar collectors—constant inlet temperatures and mass flow rates are very time-consuming or cost-intensive to fulfill, if feasible at all. To overcome these restrictions in the evaluation procedure and measurement data as well as to increase the applicability of a testing method for concentrating collectors, the DT method presents a potentially valuable alternative.

[5] Remedy is found by an iterative procedure introduced in Section 3.1.

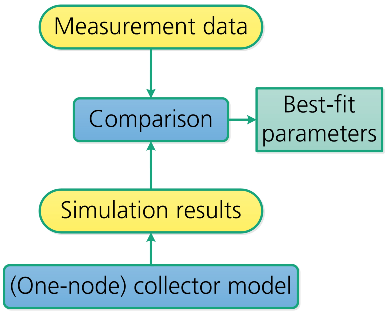

(a) MLR

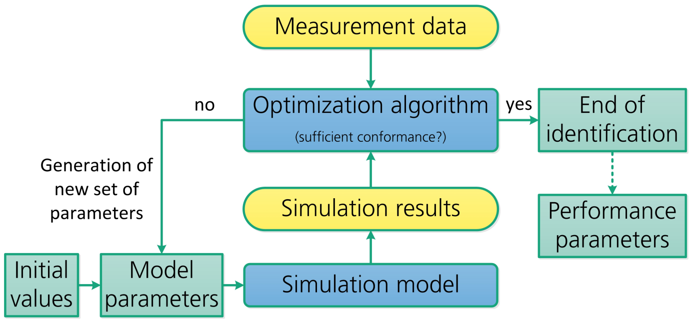

(b) Iterative optimization

Figure 2.2: Different approaches of parameter identification. The MLR (a) allows a direct deduction of the best-fit parameters, whereas the optimization approach (b) requires an iterative procedure.

■ 2.2.2 Dynamic Testing DT

The main benefit of the DT method[6] represents its higher flexibility in measurement data, because inlet conditions do not have to be kept constant. In contrast to the QDT, the dynamic testing method does not use a semi-steady one-node equation but a dynamic multi-node model instead. Accordingly, the rather simple mathematical MLR approach is not applicable, which would allow a direct deduction of the best-fit parameters from measurement data (see Figure 2.2(a)). Alternatively, an iterative parameter identification method based on an optimization procedure as sketched in Figure 2.2(b) builds the core of the DT method.

General Procedure

In the dynamic parameter identification method, measurement data is compared to simulation data, which are obtained by means of a collector simulation model. This simulation model reproduces the dynamics of the collector performance accurately, depending on so-called model parameters (i.e., the performance parameter of the collector, which are introduced in detail in Appendix A). The key element of this procedure represents the optimization algorithm. According to the deviations between measurement and simulation, it generates new sets of model parameters until measurement and simulation coincide best and convergence is reached. The model parameters leading to the convergence are the actual performance parameters of the collector deduced from thermal measurement test data. These parameters are also commonly referred to as ‘identified parameters’ or ‘identification results’.

This basic approach of the dynamic testing method for concentrating collectors was introduced by Platzer et al. [2009]. As a first instance, it only addressed the evaluation of optical parameters of an LFC, determining the heat loss parameters separately. Ray tracing[7] values were merely used as supporting points, but not required for the evaluation.

[6]Note that within the present thesis the wording of the dynamic testing method is considered equivalent to the wording of a dynamic performance evaluation method.

[7]Physical modeling by tracing the path of sun beams, reproducing effects like reflection, absorption, transmission, scattering, and so forth.

However, the procedure was structured in a way that only single measurement days could be evaluated. The combination of the individual results of the separate days made it difficult to report consistent final results.

This work built the starting point for enabling a comprehensive testing and evaluation procedure with the initial requirement of processing all available measurement days collectively in order to determine both optical and thermal performance parameters simultaneously in one global evaluation approach. Thereby, a flexible and comprehensive use of all measurement data and its coherent information is ensured. Furthermore, several specific elements were enabled, which will be particularly discussed in the following chapters.

Specific Implementation

Concerning the specific implementation of the dynamic parameter identification procedure, three different software/programming packages are utilized. For the collector simulation model, the in-house software of Fraunhofer ISE[8], ColSim[9] is used [Wittwer, 1999]. It consists of a multi-node, plug-flow model, based on simplified Navier-Stokes equations, capable of reproducing highly dynamic scenarios with little computational effort but still acceptable accuracy [Wittwer et al., 2001]. The detailed physical model and numerical approach is derived in Appendix C.1. By importing the collector input measurement data (like inlet mass flow, temperature, irradiance, ambient temperature, etc.), ColSim calculates the outlet temperature of the collector. The difference between simulated and measured collector outlet temperature currently represents the objective function of the optimization procedure. More details on the use and adaptation of this objective function are given in Section 3.2.1 and Section 4.3.

For the optimization procedure, the software package Dakota[10] is implemented [Adams et al., 2016]. The Dakota toolkit consists of a freeware developed by Sandia National Laboratories featuring flexible implementation options with extensible interfaces between simulation models and iterative analysis methods. Global and local, as well as gradient-based and gradient-free optimization algorithms are available and easily accessible (for more information see Section 3.2.2).

The linking of the simulation model with the optimization software is accomplished by several self-developed data processing scripts, implemented in the programming language Python and mainly using the packages and libraries of Pandas[11], NumPy[12] and Matplotlib[13]. Pre-processing is required to edit and transfer measurement data into a standardized format with consistent units. Moreover, post-processing scripts are carried out to assess the identification quality of the test results, create confidence intervals and error bars, as well as plotting and summarizing final results. This structure was successively developed in parts within the work of Büchner [2014] and Nettelstroth [2015]. More information on the detailed implementation structure of the parameter identification procedure are given in Büchner and Hofer [2015] and Nettelstroth and Hofer [2016].

[8] Fraunhofer Institute for Solar Energy Systems

[9] System Simulation Program for Thermal Systems and Controllers

[10] A Multilevel Parallel Object-Oriented Framework for Design Optimization, Parameter Estimation, Uncertainty Quantification, and Sensitivity Analysis

[11] `http://pandas.pydata.org`

[12] `http://www.numpy.org`

[13] `http://matplotlib.org`

In this way, the dynamic testing method is capable of using measurement data without specific restrictions in the inlet conditions with varying temperatures, mass flow rates, and solar irradiance. This allows for an evaluation of dynamic start-up and cool-down periods of the collector, providing valuable additional information of the collector performance. Certainly, this flexibility comes at the cost of higher computational complexity of the method. Nevertheless, this effort might be worth it with regard to the high potential of decreasing testing time and effort for concentrating solar collectors. For this reason, the dynamic testing method is enhanced in order to create a reliable, meaningful, and viable performance evaluation method. The capabilities of the DT method with respect to diverse aspects of collector testing and its applicability are proven within the present thesis, enabling a valuable and comprehensive testing procedure for line-concentrating collectors in particular as well as solar thermal collectors in general.

■ 2.2.3 Collector Performance Parameters

The specific characteristics of the performance parameters to be identified within a thermal collector testing procedure depend on the system under test. The procedure of this thesis focuses on line-concentrating solar thermal collectors comprising Parabolic Trough Collectors (PTCs) and Linear Fresnel Collectors (LFCs). Corresponding performance parameters are commonly divided into optical and thermal properties of the collector. Comprehensive explanations, detailed descriptions, and proper definitions concerning the basics of the systems under test and its specific parameters are elaborately given in Appendix A. In the context of line-concentrating collectors, the performance parameters mainly consist of:

- the optical efficiency at normal incidence $\eta_{opt,0}$, describing the collector efficiency at a sun position normal to the aperture area,
- the Incidence Angle Modifier (IAM), characterizing the angular behavior of the collector efficiency depending on the solar incidence,
- as well as the heat loss coefficients u_0/u_1, defining the thermal heat loss of the receiver.

Be aware that in the area of CSP, standardized definitions of those parameters are not yet existent, which are generally valid, widely accepted, and uniformly used. They are, however, focus of ongoing standardization effort within this community. Especially concerning an appropriate and universally valid definition of the IAM, diverse concepts exist. Particular caution has to be applied on the specific incidence angles that are used for the IAM calculation. Furthermore, it has to be checked if particular effects, such as cosine loss or end loss, are in- or excluded in the IAM. For specific details refer to Section A.2.3.

Within the present thesis, the IAM for PTCs is defined depending on the incidence angle with the variable $K(\theta_i)$. For LFCs, the two-dimensional IAM is split into a transversal part $K_T(\theta_T)$ and longitudinal factor $K_L(\theta_{LS})$. The corresponding angle definitions are elaborately explained in Section A.2.3 and schematically depicted in Figure A.3. The definitions within this thesis are designed in order to adequately cope with the complexity and diversity of the entire spectrum of solar thermal collectors and avoid inconsistencies. In case of doubt concerning correct and universal definitions, detailed explanations and exemplary illustrations are given in Appendix A.

■ 2.3 Evaluated Test Collectors and Their Facilities

Within the work on the further development of the dynamic testing procedure, access was granted to different facilities of line-concentrating solar collectors. Measurement data of these facilities were used to validate particular aspects and specific elements as well as the complete elaborated performance evaluation procedure as a whole. The corresponding test facilities are referred to by the below introduced nomenclature. The naming considers the type of collector (LFC and PTC) and the heat transfer fluid used (water (w), direct steam (s) and thermal oil (o)). Furthermore, the test facilities show additional differences relating to categories like receiver design (evacuated vs. non-evacuated receiver), scale (small-scale process heat and large-scale solar field collectors), absorber tube (single vs. multiple tube), operating conditions, and others. The main characteristics of the test facilities are summarized in Table 2.2. Not all data of all test collectors are fully available to public, because some information is sensitive and underlies confidentiality restrictions. However, for the purpose of the measurement data within the present thesis—as to a validation of the developed performance evaluation method—no absolute values are of particular interest. The aim is rather to compare different evaluations (e.g., including and not including developed enhancements) in order to show the added value and practicability of the developed aspects for the testing method. In the following, a short characterization of the investigated collector test facilities is presented. Schematic sketches of the evaluated test facilities can be found in Figure B.1 of Appendix B. Note that hereafter the different facilities are standardly referred to as 'test collectors', even though some facilities are more appropriately characterized as collector modules, field loops, or solar fields. For the current purpose, a further differentiation is not considered relevant and therefore neglected. The characterization of the particular systems is based on balancing the specific inlet and outlet properties of the test collectors distinctly excluding potential losses of the piping before and after the system.

Test Collector `LFC_w1`

Measurement data of this LFC test collector operating with pressurized water were recorded by an in situ measurement campaign at the site of an industry costumer, where the gained solar heat is lead into an industrial process. High precision and accuracy measurement equipment was selected and installed by Fraunhofer ISE, assuring a high quality of the recorded test data. The collector was cleaned regularly. Restrictions in operating conditions limited test data to a small range and low level of fluid temperatures smaller than 165 °C. The test campaign at `LFC_w1` therefore supplied valuable measurement data for a general validation of the testing and evaluation procedure, especially for an optical characterization due to a wide range of solar incidence situations. However, small temperature levels coupled with the generally low absorber heat loss of an evacuated tube inhibit a thermal heat loss determination. For an exemplary illustration of the test facility, refer to Figure B.1(a).

Test Collector `LFC_w2`

Test data of this LFC represent the main measurement data basis of the present thesis. It serves as a comprehensive reference test campaign. In this way, a large amount of measurement data is available. Furthermore, it facilitates the most reliable data, as direct

Table 2.2: Main characteristics of the investigated collector test facilities. Measurement data of several test facilities with diverse differences in categories like collector type, receiver design, geometries, heat transfer fluid, as well as operating conditions are used to validate the proposed performance evaluation procedure.

Test collector	LFC_w1	LFC_w2	LFC_w3	LFC_s1	PTC_s1	PTC_o1
Collector type	LFC	LFC	LFC	LFC	PTC	PTC
Receiver	evacuated	evacuated	non-evacuated	non-evacuated	evacuated	evacuated
Geometry						
Length / m	25	12	20	54	400	600
Width* / m	7.5	8	14	19	5.76	5.76
Height$^{\diamond}$ / m	4	4	8.1	8.1	1.7	1.7
A_{Ap} / m^2	131	75	230	720	2212	3318
Fluid	water	water	water	DSG	DSG	thermal oil
Latitude	49 °	48 °	-26 °	43 °	37 °	39 °
Orientation$^{\odot}$	17 ° W	20 ° W	0 ° N–S	0.55 ° W	0 ° N–S	0 ° N–S
Cleaning	regularly	regularly	measured reflectance	measured reflectance	measured reflectance	measured reflectance
Nr. test days	23	73	27	5	9	4
$U_c(\dot{Q})^{\triangleleft}$ / kW	0.70	0.53	2.98	11.12	22.37	29.21
$U_{c,rel}(\dot{Q})^{\triangleleft}$	1.39 %	1.65 %	4.54 %	4.10 %	1.84 %	3.94 %
Ref. $u(sensor)^{\triangleleft}$	Table B.2.1	Table B.2.2	Table B.2.3	Table B.2.4	Table B.2.5	Table B.2.6
Operating Conditions						
T_{in} / °C	35–150	10–210	12–190	145–265	180–290	245–280
T_{out} / °C	45–165	10–225	12–195	150–270	140–310	255–370
$\dot{m}_{in}$ / kg s^{-1}	0.9–1.0	0.5–0.9	2.5–3.1	1.3–2.0	1.0–1.7	3.4–4.2
p / bar	12	25–30	37–42	5–55	12–105	10–14
θ_T / θ_{LS}	wide variation	wide variation	wide variation	little variation	medium variation	little variation

* corresponds to collector width in case of LFC and aperture width in case of PTC
$^{\diamond}$ corresponds to height of receiver above primary mirrors in case of LFC and focal lengths in case of PTC
$^{\odot}$ zero due south, clockwise positive, i.e., 17 ° W = 17 ° from South to West
$^{\triangleleft}$ For details on the calculation of the overall, combined uncertainty of the collector power output $U_c(\dot{Q})$ and details concerning sensor uncertainty $u(sensor)$, additionally see Chapter 6 and Appendix E.

supervision of the tests was realized. On-site measurements were recorded and operated by skilled and trained personal of Fraunhofer ISE. Fully traceable operating conditions could be assured, since malfunctioning and anomalies of the system were dependably reported. Maintenance of the sensors and collector was continuously ensured. Regular cleaning as well as soiling measurements guarantee well-defined collector conditions, reducing the potential of error sources. A large spectrum of solar incidence situations as well as a wide range and high level of fluid temperatures could be realized. An exemplary schematic of the test collector is given in Figure B.1(a).

Test Collector `LFC_w3`

This test collector consists of an LFC prototype installed at a test facility of a research department of a company. It features a special non-evacuated, multi-tube receiver. Therefore, measurement data of this collector provided valuable information to demonstrate the capability of the developed testing procedure with respect to different receiver types, inducing different magnitudes of heat loss. Collector and facility were not in perfect condition with several broken receiver glass enclosures and broken mirror segments. They merely result in a higher heat loss and lower optical efficiencies. Because absolute performance values are not of interest, these aspects are not considered relevant for the general validation and demonstration of practicability of the testing procedure. By this test campaign, access to a wide range of temperature levels and solar incidence situations was provided. The collector was not cleaned, but soiling determined on the basis of reflectance measurements. Figure B.1(a) exemplarily illustrates the evaluated test facility.

Test Collector `LFC_s1`

`LFC_s1` represents a prototype test facility at a research department of a company. It consists of a large-scale LFC equipped with a non-evacuated receiver operated with direct steam in recirculation mode with steam drum. Only few measurement data were available of this collector. It features higher sensor uncertainty, as installed instrumentation is not designed for testing but rather for control purposes. Due to the limited number of measurement days, only small variation of solar incidence was provided, inhibiting a determination of IAM characteristics. Steady-state data as well as dynamic time periods were available allowing a comparison and validation of the dynamic data evaluation to results obtained from steady data. As merely a small temperature range was realized, no explicit determination of heat loss parameters under steady-state is feasible. However, the evaluation of the optical efficiency is feasible for both and shows the functional capability of the adaptation of the evaluation procedure to DSG. In addition, heat loss can be identified on the basis of dynamic data. As the system is well-characterized, measurement data may adequately be used to validate the extended evaluation procedure to dynamic compressible fluid flow. For a schematic of the test facility, see Figure B.1(c).

Test Collector `PTC_s1`

Access was granted within the SFERA-II project[14] to the DISS[15] facility of the Plataforma Solar de Almería in Spain (PSA). The DISS facility is part of a large test facility and research center on concentrating solar power. It consists of a PTC loop with evacuated absorber tubes operated with direct steam in different operating modes. The steam loop has been in operation for more than 15 years and 10.000 operating hours with lots of different test and measurement campaigns perusing different objectives. For more details on the test loop, see Zarza et al. [2004]; Valenzuela et al. [2005]; Lobón et al. [2014a]. Numerous studies and investigations using measurement data of the facility were published (see, e.g., Bonilla et al. [2012]; Biencinto et al. [2016]; Xu and Wiesner [2015]; Elsafi [2015]). The measurement data of the DISS loop used within the present thesis consisted of archive measurement data in recirculation mode of the years 2000–2002. For the validation, data of the evaporation part of the loop (consisting of a 400 m collector row) and the steam drum were taken. A large amount of different data is available, with steady as well as specific dynamic process conditions, such as steps in mass flow rate, Direct Normal Irradiance (DNI) dynamics, rise of inlet temperature, and so forth. Therefore, measurement data provided a valuable basis for the validation of the extended DSG simulation model and the adapted evaluation procedure to DSG collectors. A schematic of the test loop is given in Figure B.1(d).

[14] Solar Facilities for the European Research Area, for more information see http://sfera2.sollab.eu.
[15] Direct Solar Steam

Test Collector PTC_o1

Measurement data of the PTC_o1 collector were recorded by in situ testing at a PTC solar field loop operated with thermal oil in a commercial PTC power plant. As a consequence, merely a small number of data were recorded with standard instrumentation for control purposes. Nevertheless, the data provided a valuable basis to check the capability of the evaluation procedure with respect to different kind of heat transfer fluids, system boundaries, and scales. Figure B.1(b) schematically illustrates the evaluated solar field loop.

Chapter 3

Specific Aspects of the Dynamic Testing Procedure

3.1 Comparison to the Current Testing Standard

In Section 2.2.2, the overall concept of the newly implemented alternative DT method was already introduced. To make sure that its general approach is universally valid as well as equally capable and reliable as the normative QDT method of the testing standard ISO 9806 [2013], both basic methods were compared to each other as a first step. Thereby, is was initially ensured that it is reasonable and justified to use and particularly to further develop the alternative DT method. This comparison is therefore considered a first basic validation of the general dynamic evaluation procedure. Detailed results of this first validation were already published in Hofer et al. [2015a]. The comparison verified the general capability and suitability of the new procedure. The following section is based on this publication in a summarized and slightly adapted way.

3.1.1 Extension of the QDT Method for LFC

In Section 2.2.1, the general form of the one-node collector Equation (2.1) for concentrating-collectors of the QDT method was presented. For LFCs, optical and thermal specifics, as comprehensibly explained in Appendix A, have to be included as follows:

Incidence Angle Modifier

The two-dimensional IAM of linear Fresnel collectors coupled with the staggered shape of the transversal IAM curve imply the determination of discrete values for every angle step along both optical axes of the collector. Therefore, $K_b(\vec{v}_s^{\,*}) = K_T(\theta_T) \cdot K_L(\theta_{LS})$ needs to be included in the collector equation.

Conversion Factor

Since good heat conversion is assumed for concentrating collectors, the conversion factor is set equal to the optical efficiency at normal incidence with $\eta_{b,0} = \eta_{opt,0}$.

Diffuse Irradiance

For concentrating collectors, diffuse irradiance is supposed to be of minor contribution. The influence of diffuse irradiance was analyzed within Hofer et al. [2015a], where the same data basis of collector `LFC_w1` was evaluated with and without including diffuse irradiance. Results revealed a mean absolute difference of the optical efficiency over the entire identified angle space of approximately 0.34 %-pts. With regard to common uncertainty bounds of thermal collector tests (as elaborately derived in Chapter 6), this difference is considered insignificant. For a graphical illustration of the detailed deviations, see Hofer et al. [2015a, pp. 90–91]. As a consequence, the results support the presumption of neglecting diffuse irradiation in performance evaluations for concentrating collectors with a concentration ratio[1] larger than 80. For this reason, $K_d = 0$ is considered in the following.

Including the mentioned specifics of LFCs, the one-node equation takes the form:

$$\frac{\dot{Q}}{A_{Ap}} = \eta_{opt,0} \cdot K_T(\theta_T) \cdot K_L(\theta_{LS}) \cdot G_{bn} - c_1 \cdot \Delta T - c_2 \cdot \Delta T^2 - c_5 \cdot \frac{dT_m}{dt}, \tag{3.1}$$

For the stepwise identification of IAM values, an already presented extended MLR approach was applied as elaborated in Perers [1997]. Due to the two-dimensional factorization of the IAM, however, the standard and extended MLR method cannot be used directly. The non-iterative fast-matrix approach of the MLR can only be applied to a linear parameter function with several summands. For a product of parameters to be identified, such as the case for the optical efficiency of LFCs, the MLR is not suited. Consequently, the MLR was expanded with an iterative procedure in order to be able to determine the IAM values for a defined set of discrete angles along both optical axes. Figure 3.1 depicts a sketch of the developed iteration process.

Starting points for the evaluation can be K_T- and K_L-values obtained by ray tracing simulations. They even can be calculated from simple geometric approximations (such as the cosine function), since it could be proven that evaluation results do not depend on the starting values. These values are then adapted in a stepwise identification procedure by an iterative approach. In each step, one IAM factor is kept constant (e.g., $K_L(\theta_{LS})$ marked in orange in Figure 3.1) while the corresponding $K_T(\theta_T)$-factor (among the thermal parameters according to Equation (3.1), which are marked in green) is adjusted in the identification procedure. After this step, the newly identified $K_T(\theta_T)$-values are held constant and $K_L(\theta_{LS})$-values identified, which are fixed in the subsequent identification. Equally, the evaluation procedure could begin with identifying the $K_L(\theta_{LS})$ first and keeping $K_T(\theta_T)$-values constant. The initial fixation does not influence the final evaluation results. Because each IAM factor tends towards unity for small angles, the optical efficiency at normal incidence can be identified using the data points with such small angles. It can thus be adapted in every iteration step. This iterative procedure is performed until changes in all identified parameter values between subsequent iterations become insignificant (i.e., $< 0.05 - 0.1\,\%$).

■ 3.1.2 Comparison of QDT and DT Results

For the comparison of both methods, measurement data of the test collector `LFC_w1` were evaluated. The temperature range of the underlying measurement data were not particularly wide and high (between 80–150 °C). For a relatively small temperature range,

[1] aperture area to the projected absorber area

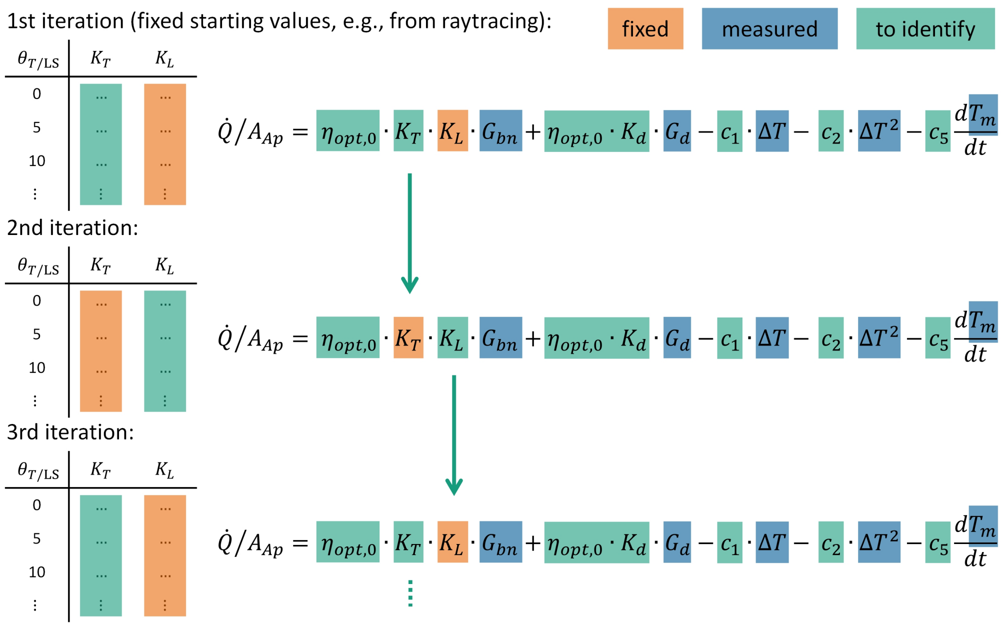

Figure 3.1: Sketch of the iterative MLR procedure. Adapted approach of the QDT method for the determination of transversal and longitudinal IAM of linear Fresnel collectors. [adapted from Hofer et al., 2015a]

the heat loss of a collector can also be described by a linear dependency on the temperature. Since the optical efficiency also represents a linear factor of the collector power output, a strong correlation between optical and thermal parameters cannot be ruled out. Further explanations and approaches to reduce correlation between optical and thermal parameters are presented in Chapter 7. Moreover, heat loss proved to be only about 1% of the solar gains of the collector, leading to dominating optical parameters and a low significance of the heat losses at small fluid temperatures. To make sure to be able to compare both methods on the very same reproducible basis and to avoid a potential error in the conclusions for the comparison of the two methods, heat loss coefficients were not determined in the subsequent parameter identifications. They were set constant to characteristic values of an evacuated glass envelope receiver ($u_0 = 0.0399\, W/m{\cdot}K$ and $u_1 = 0.0011\, W/m{\cdot}K^2$), which were obtained by simplified heat loss simulations with a Thermal Resistance Model (TRM) as roughly introduced in Section 3.3.

To be able to comprehensively compare the two different evaluation methods, three parameter identifications were performed. The first was based on the QDT method as previously introduced with a data set of about 20 days and an evaluation time step of five minutes. The inlet temperature had to be maintained constant and only the outlet temperature could vary due to varying irradiance. Thus, a relatively large measurement data set of around 20 days was needed to collect enough data fitting these requirements. The second evaluation was based on the DT procedure, but considers the same dataset as the QDT evaluation. A third identification was purely based on a DT procedure with the evaluation of four exemplary and representative dynamic days. Moreover, they included high dynamics, even with an extreme temperature rise not representing typical operating conditions of a common collector test. Nevertheless, the identification results for all three

Table 3.1: Short summary of characteristics of the QDT and DT method. Differences and similarities concerning different properties for both testing and evaluation procedures. [Hofer et al., 2015a]

Variable	QDT	DT
Inlet temperature	± 1 K	variable
Mass flow	± 1 %	variable
Inlet and outlet pressure	not relevant, only p-level for c_p	considered
Direct normal irradiance	variable	variable
Consideration diffuse irradiance	yes	no
Time step measurement data	5 s	5 s
Simulation model	one-node model	multi-node model
Optimization procedure	MLR	least-squares/genetic
Time step evaluation	5 minutes	5–20 seconds
Figure of merit minimization error	$\dot{Q}$	T_{out}
Capacity term	c_5 included	included in plug-flow model
Heat loss calculation with reference to	T_m	T_{HTF}
Reference heat loss coefficients	aperture area collector	receiver length
End loss included in IAM	yes	both options available

cases show a Root Mean Square (RMS) difference for the optical efficiency at normal incidence $\eta_{opt,0}$ of 0.9 %-pts. A comparison with results reached in a round-robin test [Weißmüller et al., 2012], in which approximately ±2 %-pts. of difference were obtained, indicates an essential equivalence between the testing methods.

Furthermore, the absolute mean deviation of the optical efficiency η_{opt} over the entire identified angle space between the QDT and the DT method of the very same data base was about 0.89 %-pts. The mean absolute deviation between the QDT and the DT method based on merely four measurement days resulted in a slightly higher value of 0.98 %-pts. Although the two compared evaluation approaches are using completely different measurement data on the one hand and different collector models on the other, good agreement in the identified optical performance parameters could be reached. For a graphical illustration and detailed results, see Hofer et al. [2015a, pp. 91–93]. A brief summary of the basic characteristics and differences of both methods is given in Table 3.1. All in all, the good conformance of results within this first verification built a crucial starting point for the further development of an alternative dynamic testing and evaluation method. The results particularly demonstrate the general capability and applicability of the new method with higher flexibility than currently existing methods.

■ 3.2 Optimization Procedure

The optimization procedure of the DT method is designed to minimize the deviation between simulation and measurement data of the tested collector to be able to derive the desired performance parameters. In this way, the objective function of the optimization algorithm is defined by the RMS of the deviation in terms of

$$RMS = \sqrt{\frac{1}{n}\sum_{i=1}^{n}(y_{meas,i} - y_{sim,i})^2}. \tag{3.2}$$

Accordingly, y_i represents the variable of the objective function of time step or data point i to be compared, which may differ between different evaluation approaches.

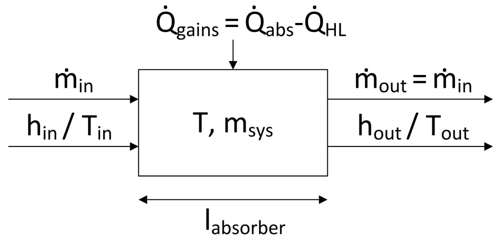

Figure 3.2: Exemplary simplified energy balance over absorber tube. Incoming and outgoing fluid flow as well as incoming solar gains are influencing the state of the absorber tube.

■ 3.2.1 Variable of the Objective Function

As already introduced in the previous chapter, for the QDT evaluation the objective variable of the thermal power $\dot{Q}$ is used, whereas in the DT method the temperature variable T_{out} is taken. Perers [2011] recommends an optimization to the variable $\dot{Q}$, but does not explain nor derive this recommendation. To understand the differences and similarities of both approaches, a simple energy balance is drawn to the absorber tube of a collector (as sketched in Figure 3.2) operating with incompressible media, which is defined by

$$\dot{Q}_{gains} = \dot{m} \cdot c_p \cdot (T_{out} - T_{in}) + \frac{T^{t+1} - T^t}{\Delta t} \cdot m_{sys} \cdot c_{p,sys}, \tag{3.3}$$

where the incoming solar gains $\dot{Q}_{gains}$ (consisting of the solar power reaching the absorber $\dot{Q}_{abs}$ and the fluid heat loss $\dot{Q}_{HL}$) are transferred to the fluid flowing through the absorber. According to Patankar [1980], the fluid state is defined (in a simplified version) by a 'convective' part represented by the spacial discretization dQ/dx. The second term refers to the 'unsteady' part of the energy balance which is defined as the temporal discretization dQ/dt. It represents the intrinsic energy change, that is, the power transferred to the capacity of the system. It thereby consists of the power linked to the inertia of the system. Usually, for incompressible media, the relation $\dot{Q} = mc_p\Delta T$ is applied, assuming steady-state conditions and the unsteady part to equal zero. To avoid misunderstanding of the different power definitions, the convective part is referred to in the following with the single variable $\dot{Q}$. It represents the usable mass flow bound power output of the collector. In short, it will be referred to the collector power output. The unsteady term of the energy balance will be defined by the variable $\dot{Q}_{inert}$.

Applying this concept to the one-node equation of the QDT procedure yields for incompressible HTFs:

$$\dot{Q} = \overbrace{\dot{m} \cdot c_p \cdot (T_{out} - T_{in})}^{\dot{Q}_{meas}} = \overbrace{\overbrace{\underbrace{\eta_{opt} \cdot G_{bT} \cdot A_{Ap}}_{\dot{Q}_{abs}} - \underbrace{c_1 \cdot \Delta T - c_2 \cdot \Delta T^2}_{\dot{Q}_{HL}}}^{\dot{Q}_{gains}} - \overbrace{c_5 \cdot \frac{dT_m}{dt}}^{\dot{Q}_{inert}}}^{\dot{Q}_{sim}}. \tag{3.4}$$

In the QDT approach, the measured and simulated collector power output are compared, including a simplified term for the inertia of $\dot{Q}_{inert}$. If no dynamics in inlet temperature and mass flow rate occur, this simplification is justified. However, with dynamics in these

Table 3.2: Differences in identification results for the objective variable $\dot{Q}$ vs. T. Relative deviation of identified $\eta_{opt,0}$ and mean relative deviation of longitudinal and transversal IAM for the QDT and DT evaluations of Section 3.1.

Data base	$\Delta(\eta_{opt,0})$	Mean $\Delta(K_T)$	Mean $\Delta(K_L)$
QDT	0.41 %	0.39 %	0.13 %
DT	0.05 %	0.08 %	0.05 %

variables the simple term may not reproduce the dynamic behavior accurately enough. For this reason, the dynamic part is simulated by ColSim within the DT method, considering not only a one-node equation but a discretization of the absorber tube. Thereby, the collector outlet temperature T_{out} is simulated and compared to the measured one. Certainly, the optimization approach could also be applied to the collector power output $\dot{Q}$ with

$$\begin{aligned}\dot{Q}_{meas} &= \dot{m} \cdot c_p(T_{out,meas} - T_{in,meas}),\\ \dot{Q}_{sim} &= \dot{m} \cdot c_p(T_{out,sim} - T_{in,meas}).\end{aligned} \tag{3.5}$$

Because the term considering the inlet temperature and mass flow rate is the same for measurement and simulation, this part is canceled out in the calculation of the objective function (since $\dot{Q}_{meas}$ is subtracted from $\dot{Q}_{sim}$). The only difference in both approaches is the mean fluid capacity depending on the measured or simulated fluid temperature. Consequently, equal results arise when considering the temperature or the power output of the collector as an objective variable. However, this approach makes use of a steady balance of the collector power output by defining $\dot{Q} = mc_p\Delta T$, even though dynamic conditions prevail in the DT method. For changes in inlet temperature and mass flow rate, Equation (3.5) does not represent the actual collector power output but merely the steady part. To avoid misinterpretations, the collector outlet temperature is chosen as an objective variable for incompressible fluids.

As an example, the QDT and DT evaluation of Section 3.1 are performed with both objective variables. The relative deviations of the identified parameters based on T and $\dot{Q}$ as an objective variable are given in Table 3.2. For the IAM, the mean relative deviation over all identified angle bins is listed. The QDT shows slightly higher differences of the identified performance parameters. Nevertheless, the largest deviation of 0.41 % in $\eta_{opt,0}$ still indicates a marginal influence of the objective variable. For the evaluation based on dynamic data, the difference is even smaller with the largest value being 0.08 % of identified transversal IAM. Altogether, the results justify the use of the outlet temperature as a objective variable for the dynamic optimization procedure.

Note that this derivation is considering incompressible fluid flow with constant mass flow rate between inlet and outlet. For other systems, particularly DSG collectors, these assumptions are not valid. An adoption of the objective variable is therefore required. A detailed derivation, explanation, and adaptation of the procedure to this context is addressed in Chapter 4.

3.2.2 Optimization Algorithm

Available Optimization Algorithms

The previously introduced objective variable of the function to be minimized can be evaluated by means of different optimization algorithms. In general, local versus global optimization procedures are differentiated. For a detailed overview and introduction to different optimization approaches, refer to Rao [2009]. Local optimization algorithms are better suited for unimodal optimization problems, that is, when the objective function contains only one determined minimum. Global approaches are particularly efficient for multimodal optimization problems. In those cases, the objective function is more complex containing several local minima, which might be leading to erroneous results with a local optimization approach.

Local methods are mostly gradient-based. Thereby, the search direction depends on the (local) gradient direction of the objective function. Commonly, the gradient is approximated by a Taylor polynomial of first or second order. First order approaches—as, for example, the Cauchy algorithm [see Rao, 2009, pp. 339–341]—show fast convergence if the optimum is far away from the current value. To the contrary, second order approaches provide fast convergence if the current value is near to its optimum (such as the Newton procedure [Rao, 2009, pp. 345–347]). Trust regions methods [Ulbrich, 2012, pp. 77–80] combine both first and second order procedures (such as, e.g., the Marquardt algorithm [Rao, 2009, pp. 348–349]). They are particularly suited for least-square optimization problems such as the present optimization case of the dynamic evaluation procedure. For this reason, this represents the standardly used optimization algorithm also referred to as the least-squares algorithm. Furthermore, the Newton algorithm as a first order approach is implemented for the use within the parameter identification procedure. Besides, the global optimization algorithm of a genetic algorithm is enabled to warrant a proper identification of more complex multimodal optimization problems [see Rao, 2009, pp. 694–702].

Selection of Proper Optimization Approach

The suitability of an algorithm strongly depends on the particular optimization problem. Therefore, no universally valid recommendation concerning an appropriate optimization procedure is feasible. Experience with the optimization procedure of the dynamic parameter identification has shown that in general the implemented local approaches of Newton and least-squares algorithm succeed well. In addition, they reveal to be more efficient in terms of the number of required iterations until convergence. A gradient step size of larger than 0.02 performed well within the present collector evaluations. A smaller gradient step size may provide identification results very near to the initial starting values and should therefore be avoided or its suitability specifically checked.

However, local procedures as the Newton or least-squares method do not properly work for global optimization problems with several local minima and one global optimum. This may be the case in more complex test situations such as the evaluation of DSG collectors. Mostly, those optimization problems entail a higher RMS value of the objective function coupled with an identification of more than one parameter. An indication for a failure of local methods represents the dependency of the identified results on the starting values, even for large gradient step sizes. That being the case, the use of a global procedure, such as the implemented genetic algorithm, is advised. Similarly, no generally valid settings of this algorithm can be recommended. They mostly represent a compromise between convergence (i.e., small number of iterations) and exploration of the parameter space (i.e., capability of finding the global optimum). For the evaluations within the present thesis, mostly a population size of 15–30 was applied. Mutation rates ranged between 0.005–0.05 with crossover rates of 0.8–0.95. Nevertheless, the use of a genetic algorithm requires caution and double-checking of identified results for plausibility. Note that the use of a genetic algorithm generally requires a higher number of iterations. For this reason, it is not advised to be used for simple optimization problems where the local procedures succeed reliably.

■ 3.3 Heat Loss Equation

■ 3.3.1 Ambient Parameters

To make sure to properly describe and eventually characterize the heat loss in performance tests, a broad heat loss study for linear Fresnel collectors was performed. The analysis was based on a simulation model developed at Fraunhofer ISE—the so-called Thermal Resistance Model (TRM)—addressing heat transfer characteristics of LFCs. The energy balance of an LFC receiver is influenced by the existence of an additional secondary reflector in contrast to standardly investigated parabolic troughs. The TRM is considered an extension of the heat transfer model proposed by Forristall [2003], which is designed for PTC. The model solves a net of energy balances and heat transfer equations under steady-state condition. Details of the specific implementation approach of the TRM can be found in Heimsath et al. [2014b].

In Zahw [2014], the TRM was applied to a global heat loss sensitivity analysis, revealing influencing and particularly non-influencing factors concerning material properties, ambient parameters, and operating conditions for three LFC receiver configurations. The studied receiver cases represent configurations installed in reality: an evacuated absorber tube with secondary mirror, an absorber tube with non-evacuated glass envelope and secondary mirror, as well as an absorber tube with glass plate cover. An exemplary illustration of the three cases is given in Figure A.2 of Appendix A. The global sensitivity analysis revealed an influence of the ambient temperature and wind velocity on the overall heat loss, while other studied parameters showed to be negligible. Both factors are generally considered in the testing standard ISO 9806 [2013]. Moreover, it revealed a noticeable effect of the amount of absorbed radiation of the secondary reflector, which in turn is characterized by the incoming DNI. For this reason, a parameter study was elaborated for these three ambient conditions on the heat loss for the three introduced receiver designs. The results were published within Hofer et al. [2015b]. Because the incoming DNI to the secondary reflector depends on the aperture area of the collector, the study differentiated between small-scale and large-scale collectors. Details on the set characteristics of both cases are given in Table 3.3. For the detailed results, refer to this publication. The available test collectors within the present thesis either feature a receiver with evacuated absorber tube or an absorber tube receiver with glass plate cover. Accordingly, only those two configurations are particularly analyzed in the following. All in all, the results in Hofer et al. [2015b] revealed a small influence of DNI, wind, and am-

Table 3.3: Implemented characteristics of LFC reference cases. Exemplary small- and large-scale LFC reference collector for the performed heat loss study. [extracted from Hofer et al., 2015b]

Variable	Unit	Small-scale	Large-scale
Aperture width	m	6.4	12.8
Absorber temperature	°C	100–250	250–550
Fluid	–	pressurized water	molten salt

bient temperature on the heat loss of an evacuated envelope receiver. For the glass plate receiver configuration, a more significant effect of all three parameters is discernible.

However, the study was performed for one fixed absorber temperature, which is expected to have a prevailing impact on the overall heat loss. Besides, in collector performance tests, the heat loss is not measured directly, but derived from measurements of the overall collector power output. In this way, a good and meaningful identification of heat loss depends on its share to the measured collector power output. Thus, an additional analysis was performed studying the influence of the previous effects on both, heat loss and collector power output. It consisted of a multi-parameter study by means of Latin-hypercube sampling with a variation of absorber temperature, ambient temperature, solar irradiance, and wind velocity. Thereby, a representative sampling of arising heat loss and power output is generated. For this sample, Table 3.4 lists the mean share of heat loss related to the power output for the two reference cases/scales with different receiver configurations. To exemplary evaluate the effect of ambient conditions, a change from 1 to 4 m/s in wind speed was chosen, respectively a change from 800 to 500 W/m^2 in DNI, and from 15 to 35 °C for the ambient temperature. All three cases represent realistic but rather large variations of ambient parameters. In Table 3.5, the mean shares of the resulting change in heat loss related to the power output are given. They reveal that even with a large variation of ambient parameters under steady-state, the share to the power output is smaller than 0.6 % in the largest case for the non-evacuated receiver configuration with glass plate. All other cases comprise even smaller ratios. As the accuracy and precision of measuring the collector power output is limited—for details concerning the influence and derivation of the measurement uncertainty see Chapter 6—differences of smaller than 0.6 % are not considered to be reliably identified as a separate factor. The ambient temperature may be included in the heat loss equation without introducing an individual term by fitting the heat loss to the temperature difference $(T_{HTF} - T_{amb})$. It is therefore included in the heat loss equation, even though its contribution is of subordinate importance. Based on these findings, wind speed and irradiance, however, are not recommended to be included in the heat loss equation for the studied collector and receiver cases. Concerning the heat loss of a PTC receiver without secondary mirror, analog

Table 3.4: Mean share of the heat loss related to the collector power output. Results are based on the multi-parameter heat loss study for an exemplary small- and large-scale LFC with evacuated absorber tube envelope or non-evacuated receiver with glass plate cover.

Reference case	Evacuated envelope	Non-evacuated glass plate
Small-scale	0.8 %	3.4 %
Large-scale	4.3 %	10.3 %

Table 3.5: Mean share of the heat loss difference to the collector power output due to changes in ambient conditions. Arising difference in heat loss relative to the mean collector power output $\Delta\dot{Q}_{HL}/\dot{Q}$ are listed according to significant changes in irradiance, wind speed, and ambient temperature.

Change in	Evacuated envelope		Non-evacuated glass plate	
	Small-scale	Large-scale	Small-scale	Large-scale
DNI	0.02 %	0.07 %	0.41 %	0.05 %
Wind speed	0.05 %	0.18 %	0.33 %	0.60 %
Ambient temperature	0.05 %	0.05 %	0.42 %	0.23 %

results are expected. The mentioned characteristics of a secondary mirror only slightly influence the change in heat loss due to ambient conditions and its share to the collector power output. This is particularly valid for the case of an evacuated tube, which is mainly installed for parabolic troughs. As a result, no adaptation of the empirical heat loss equation for LFCs nor PTCs is required.

■ 3.3.2 Polynomial Order

With regard to the polynomial order of the heat loss equation in thermal testing, commonly the potency of two of the fluid temperature is taken [ISO 9806, 2013]. For concentrating collectors in particular, the potency of four is currently under discussion[2]. Thus, the heat loss sample of the previous multi-parameter study is fit to an equation with linear and quadratic temperature factor (i.e., $u_0 \cdot \Delta T + u_1 \cdot \Delta T^2$) as well as to an equation with linear and quartic temperature (i.e., $u_0 \cdot \Delta T + u_1 \cdot \Delta T^4$). With both fits based on the same data basis and the original fluid temperature, the heat loss is subsequently calculated. The mean difference of both calculated heat losses is evaluated and its share to the collector power output summarized in Table 3.6. With the highest mean deviation approximately being 0.34 % of the collector power output, the difference between both fits is not identifiable in a collector test by measuring the collector power output. The results therefore indicate that a fourth polynomial order of the heat loss equation is not substantially improving the heat loss performance characterization of concentrating solar collectors. Based on these results, the commonly used potency of two is selected for the further description and identification of heat loss parameters within the following chapters.

Table 3.6: Mean share of heat loss difference to the collector power output due to the polynomial order of the heat loss equation. The mean difference of second to forth order polynomial fit in heat loss relative to the collector power output $\Delta\dot{Q}_{HL}/\dot{Q}$ is given.

Collector	Evacuated envelope	Non-evacuated glass plate
Small-scale	0.04 %	0.20 %
Large-scale	0.22 %	0.34 %

[2]The discussion originates from the common reporting of heat loss equations for concentrating collector receiver tubes deduced from separate component testing of the absorber tube. Note that these equations imply the use of the potency of four of the outer surface temperature instead of fluid temperatures.

Chapter 4

Expansion to Direct Steam Generating Collectors

In the case of collectors operating with DSG, water is used as a HTF which is directly evaporated in the collector. In this way, evaporation of the heat transfer fluid takes place inside the absorber tube. In most cases, the produced steam is then fed into a steam drum or separator in order to obtain totally saturated steam. Subsequently, the steam is led into a process steam network of a production line in industry or to a steam turbine generating electricity. This concept provides the advantage that no additional heat exchanger is required, since the conventional two-circuit system is reduced to a single-circuit system working with the same heat transfer fluid. This provokes lower investments and higher efficiencies of the system [Eck et al., 2003], because on the one hand the power block efficiency increases due to higher pressure and temperature of the steam (as no exergy is lost within the heat exchanger). On the other hand, pumping power can be reduced, leading to an overall increased cost-effectiveness of this concept [Hirsch et al., 2014]. Moreover, with the use of demineralized water, the environmental risk of this option can be significantly reduced, as leakage of the thermal oil can be ruled out [Fernández-García et al., 2010]. Nevertheless, the concept of DSG is technologically more challenging due to higher operating pressures and the presence of a two-phase flow inside the absorber tube. The differences in the thermodynamic properties of water and steam, as well as higher temperature gradients result in a more complex simulation and control of the system [Fernández-García et al., 2010]. Stability of the complete facility as well as start-up and cool-down periods are significantly more sophisticated than in the conventional concept of using one-phase flow as a heat transfer fluid [Hirsch et al., 2014].

Direct steam generation can be operated in different modes. In recirculation mode, the two-phase outlet flow of the solar collector is separated in a subsequent steam drum. The remaining liquid part of the steam drum is usually recirculated to the inlet of the solar system. According to Eck et al. [2003], the recirculation mode is at present the best suited option to run direct steam generating systems, because it enables a robust, stable, and therefore more efficient operation [Hirsch et al., 2014]. By now, the recirculation mode is the only commercially installed and viable option for direct steam generation in concentrating solar systems (see Krüger et al. [2012] and Feldhoff et al. [2014]). Due to its simple operation, it is additionally more suited for the integration into industrial processes. Thus, for the development of a testing and evaluation method for DSG collectors within this thesis, the focus is put on this operation mode.

One objective of the present thesis is the characterization and testing of direct steam generating collectors. Therefore, the currently proposed testing and evaluation procedure has to be adapted. Due to the presence of a two-phase flow, a compressible fluid is used as a heat transfer medium, which may result in differences between the inlet and outlet mass flow rate. For incompressible media, density changes and therefore changes in the outlet mass flow rate are not relevant to consider. Hence, it is sufficient to only measure the mass flow once in the fluid circuit, which is not the case for DSG. Additionally, as the outlet temperature of the collector remains constant during evaporation, this variable is not characteristic for the DSG collector performance. Instead of outlet temperatures, the steam quality or enthalpy of the collector outlet should be evaluated. Until now, the steam quality of a stream cannot be measured directly. All these aspects require an adaptation of the measurement concept for direct steam generating systems. A change in the measurement concept consequently requires a modification of the evaluation procedure as well. Apart from different inlet and outlet measurands, the objective function of the parameter identification procedure has to be adjusted. These aspects of the general evaluation procedure will be addressed in Section 4.3. To correctly evaluate the performance of DSG collectors, the currently used simulation model in ColSim needs to be extended to accuratly reproduce the dynamics of a system operating with compressible fluids. Within Section 4.1, the numerical approach currently implemented in ColSim, the approaches used in relevant literature, and the proposed extension of the simulation model are presented. In Section 4.2, the results of the different simulation approaches are compared, summarized, and validated to DSG measurement data.

■ 4.1 Adaptation of the Simulation Model

The unsteady water and steam flow along a heated absorber tube can be described by the three conservation equations of energy, mass, and momentum, which are the natural laws governing fluid flow and energy transport. The non-simplified three-dimensional conservation equations (also called Navier-Stokes equations) are capable of describing fluid flow with high precision, hence being able to reliably model and simulate real flow phenomena. Nevertheless, analytical solutions are only available for a limited number of simplest applications and geometries. In most cases, the solutions have to be computed numerically [Lecheler, 2011, p. 1]. However, numerical computations of such solutions are very time-consuming for many technical applications [Lecheler, 2011, p. 29]. Consequently, the conservation equations have to be simplified to achieve a good compromise between physical accuracy and computational speed. The entire derivation of the non-simplified three-dimensional conservation equations can be found in Lecheler [2011, pp. 8–21]. [Hernández, 2015a]

■ 4.1.1 Currently Used Plug-Flow Model PFM

The mathematical model and numerical approach currently implemented in ColSim—the so-called Plug-Flow Model (PFM)—uses a simplified version of the energy conservation equation in order to calculate the specific enthalpy of the fluid from one state (plug) to another in spatial and temporal direction. For the derivation of the differential equations, three basic conceptual simplifications can be assumed within the context of DSG simulations for line-concentrating collectors [see Lippke, 1994, p. 21]. First, the fluid flow along the absorber tube can be considered one-dimensional, because the length of the absorber tube exceeds by far all other relevant dimensions. Second, the fluid flow is in thermodynamic equilibrium, meaning that liquid water and steam have the same temperature. And third, the slip ratio between water and steam is neglected, resulting in the consideration of a homogeneous two-phase flow.

The introduced assumptions lead to the following general, one-dimensional, homogeneous energy equation

$$\begin{aligned}\frac{d}{dt}(E) &= \frac{\partial}{\partial t}(E) + \frac{\partial}{\partial x}(vE) \\ &= \rho v g \sin(\delta) - \frac{\partial}{\partial x}(vp) - \frac{\partial}{\partial x}(\tau v) - \dot{q} - \frac{\partial}{\partial x}(\lambda \frac{\partial T}{\partial x}),\end{aligned} \tag{4.1}$$

with the variables

$E = E_{in} + E_{kin} + E_{pot}$	= the total energy with v being the velocity of the fluid,
$\rho v g \sin(\delta)$	= gravitational force with collector tilt δ,
$\frac{\partial}{\partial x}(vp)$	= work due to pressure change,
$\frac{\partial}{\partial x}(\tau v)$	= work by friction force,
$\dot{q}$	= local radiative heat exchange,
$\frac{\partial}{\partial x}(\lambda \frac{\partial T}{\partial x})$	= heat conduction.

It represents the starting equation for the derivation of the PFM equation. Several other assumptions and simplification are furthermore included concerning negligible and summarized effects, leading to the final non-discretized plug-flow equation

$$A\rho \frac{\partial h}{\partial t} + \dot{m} \frac{\partial h}{\partial x} = -A \cdot \dot{q}, \tag{4.2}$$

For the specific and detailed derivation of the PFM equation, see Section C.1. All included assumptions and simplifications are additionally summarized in Table 4.1.

In ColSim, the solution of Equation (4.2) is discretized with equidistant temporal (Δt) and spacial (Δx) mesh size. Backward differencing in time and upwind differencing in spatial direction is applied. The source term $-A \cdot \dot{q}$ corresponds to the solar gains, that is, $-A \cdot \dot{q} = Q_{gains,n}/\Delta x \cdot \Delta t$, with $Q_{gains,n} = Q_{abs,n} - Q_{HL,n}$ of each absorber node n. This leads to the final discretization equation used in ColSim's PFM [analog to Wittwer, 1999]

$$m_{node}(h_n^t - h_n^{t-1}) = -\dot{m}^t(h_n^t - h_{n-1}^t)\Delta t + Q_{gains,n}. \tag{4.3}$$

This concept and numerical approach implies that the mass balance is fulfilled so that the mass inside the absorber is kept constant (as m_{node} in Equation (4.3)), and the mass flow rate across the absorber is set equal to the mass flow rate at entrance and exit ($\dot{m}$ in Equation (4.3)). This equals to an unsteady mass balance. The pressure field calculation along the absorber is kept simple by estimating it with a linear interpolation between inlet and outlet pressure of the absorber tube [Hernández, 2015a]. In this way, a stable—because implicit—discretization approach is available, allowing large simulation time steps and therefore small computation time, since only a simplified energy balance has to be solved.

The numerical approach of the PFM with its assumptions and simplifications is very suitable to reproduce incompressible fluid flow correctly. For an accurate simulation of

Table 4.1: Overview of assumptions included in the PFM. Summarized simplifications implemented in the current PFM concept. For detailed explanations, refer to Section C.1.

Number	Assumption	Included in
1	one-dimensional energy balance	general energy equation
2	thermodynamic equilibrium between water and steam	general energy equation
3	no slip between water and steam	general energy equation
4	no heat conduction along absorber	specific PFM implementation
5	friction work is lead to the fluid in terms of heat	specific PFM implementation
6	gravitational work is neglected	specific PFM implementation
7	kinematic and potential energy are neglected	specific PFM implementation
8	no volume change work	specific PFM implementation
9	steady mass balance	general PFM concept
10	linear interpolation of pressure	general PFM concept

two-phase flow as in direct steam generating systems, this approach is not entirely suited. The steady mass balance is valid for direct steam generation under steady-state conditions, but fails to correctly reproduce dynamics of the system (which is the focus of the present thesis). With an increasing evaporation of water (i.e., increasing steam quality), the density of the fluid, therefore velocities and hence outlet mass flow rates are subject to significant changes. Against this background, the need emerges of an extension of the current PFM to DSG collectors under dynamic operating conditions. The mathematical and numerical assumptions of the future model have to be chosen wisely to be able to correctly reproduce the dynamics of compressible fluids under the condition of manageable computational effort. Current literature on DSG simulation approaches gives an orientation on required, acceptable, and viable simplifications while simulating DSG.

■ 4.1.2 Existing DSG Models in Literature

In current literature on DSG, various mathematical/physical models and their numerical solutions are presented. They can be distinguished predominantly by the way the two-phase flow is considered in the conservation equations [Feldhoff et al., 2015]. Very complex models—mainly adapted from the nuclear industry—resolve six conservation equation: mass, energy, and momentum for the two phases of water and steam. This allows a detailed study of local heat transfer, flow phenomena, and flow patterns (see Moya et al. [2011]; Serrano-Aguilera and Valenzuela [2016]). Similarly, three-dimensional Computational Fluid Dynamics (CFD) simulations (as presented in Lobón et al. [2014a] and Lobón et al. [2014b]) allow a detailed local study of the thermal-mechanical behavior of the absorber tube with direct steam. Nevertheless, these simulations allocate a lot of memory space and have large simulation times. This is why they are better suited for local studies in shorter time periods, for example, to identify critical process conditions [Biencinto et al., 2016].

The conservation equations can be significantly simplified if homogeneous fluid flow is assumed [Feldhoff et al., 2015]. In this way, steam and water are considered in thermodynamic equilibrium (i.e., water and steam have the same temperature level), with the same velocities (i.e., slip is neglected) and equally distributed within the cross section [Lippke, 1994, p. 21]. Fluid flow through a long absorber tube—like in the case of DSG in line-concentrating collectors—can be treated as one-dimensional, because the length is significantly larger than the diameter of the tube [Lippke, 1994; Hirsch et al., 2005]. These basic assumptions and simplifications have been considered in various publications (see Walter [2001]; Hirsch et al. [2005]; Hirsch [2005]; Lippke [1994]).

Biencinto et al. [2016] use a quasi-dynamic simulation approach implemented in TRNSYS, taking into account the effect of thermal inertia to realistically model transients of the system. Differences in the outlet mass flow rate due to condensation and evaporation are considered. Pressure loss to account for the momentum equation is calculated separately by a hydraulic model. Similarly, Hirsch et al. [2005] solves a steady momentum equation separately to a transient mass and energy balance. The reason for this is that the propagation of changes in mass and energy are much slower than the propagation of changes in pressure, justifying a separate, quasi-steady consideration of the momentum equation. This approach—the separation of the pressure calculation (i.e., momentum conservation equation) from the mass and energy balance—is the basic concept of the first extension of the simulation model to DSG within the present thesis, in the following referred to as Extended Plug-Flow Model (EPFM).

Bonilla et al. [2012] use a finite volume method with a staggered grid for the discretization of all three unsteady mass, energy, as well as momentum conservation equations. Likewise, Walter [2001] presents a detailed derivation and explanation of the mathematical model and numerical approach used within his publication. Although, within this publication, evaporation takes place in an ordinary pipe not particularly designed for solar collectors, it is considered as a very good and well documented reference basis. The numerical approach consists of an implicit, iterative discretization procedure called SIMPLER[1], originally introduced and developed by Patankar [1980]. As an alternative to the developed EPFM, this SIMPLER algorithm was additionally implemented into the new DSG simulation environment [see Hernández, 2015a]. Thereby, the rather simple extension of the simulation model in terms of the EPFM can be validated not only to real measurement data but also to a more elaborate, complex, and therefore accurate simulation model. Comparisons of both models will show the benefits and drawbacks of a more sophisticated approach including transients of the momentum conservation equation (see Section 4.2).

Table 4.2 summarizes the different concepts of the three simulation models studied and elaborated within the present thesis—PFM, EPFM and SIMPLER—relating to the solved transient conservation equations. Whereas in the PFM, only the enthalpy of the fluid flow is calculated based on the energy conservation equation, in the EPFM the enthalpy plus the mass of the fluid is calculated. SIMPLER additionally calculates the pressure field along the absorber by solving all three conservation equations. Regardless of the basic concept, all three simulation models basically start from the same simplified energy conservation equation, based on predominant assumptions found in literature. Table 4.3 summarizes these simplifications of the mathematical/physical model, particularly referencing publications of DSG models that are based on the same assumptions. The difference of the models in terms of the energy conservation equations is the way they are numerically approximated. As already derived and explained in Section 4.1.1, for the PFM only the energy conservation equation is numerically solved in a way that a steady mass conservation equation is fulfilled. The numerical solution of the EPFM and the SIMPLER algorithm will be explained in the following sections. Both approaches were implemented within the work of Hernández [2015a].

[1] Semi-Implicit Method for Pressure-Linked Equations—Revised

Table 4.2: Differences in the physical equations of the three used simulation models. Considered conservation equations and calculated variables of the plug-flow model, extended plug-flow model and the SIMPLER algorithm.

	PFM	EPFM	SIMPLER
Considered conservation equations	energy	energy mass	energy mass momentum
Calculated variables	enthalpy	enthalpy mass flow rate	enthalpy mass flow rate pressure

Table 4.3: Assumptions included in the physical and numerical approach of the three used simulation models. For every assumption, corresponding literature publications are listed using similar assumptions.

Number	Assumption	Model	Literature reference
1	one-dimensional energy balance	all three	[Walter, 2001; Hirsch et al., 2005; Lippke, 1994; Bonilla et al., 2012]
2	thermodynamic equilibrium	all three	[Walter, 2001; Hirsch et al., 2005; Lippke, 1994; Bonilla et al., 2012]
3	no slip	all three	[Walter, 2001; Hirsch et al., 2005; Lippke, 1994; Bonilla et al., 2012]
4	no heat conduction along absorber	all three	[Walter, 2001; Hirsch et al., 2005; Lippke, 1994]
5	friction work is led to fluid in terms of heat	all three	[Walter, 2001; Hirsch et al., 2005]
6	gravitational work is neglected	all three	[Walter, 2001; Hirsch et al., 2005]
7	kinematic and potential energy are neglected	all three	[Walter, 2001; Hirsch et al., 2005; Lippke, 1994; Bonilla et al., 2012]
8	no pressure–volume work	all three	[Walter, 2001; Hirsch et al., 2005]
9	steady mass balance	PFM	none
10	separate pressure calculation	PFM, EPFM	[Hirsch et al., 2005; Biencinto et al., 2016]
11	resolution of all three conservation equations	SIMPLER	[Walter, 2001]

■ 4.1.3 Extended Plug-Flow Model EPFM

The derivation of the EPFM is based on the same physical model for the energy equation as in the PFM of Equation (C.5) or used in Hirsch [2005]. Additionally, the mass conservation equation is considered. The difference of the respective simulation models merely results from differences in the discretization approach.
The mass conservation equation is defined as

$$\frac{\partial \rho}{\partial t} + \frac{\partial \rho v}{\partial x} = 0, \tag{4.4}$$

with the energy conservation equation being

$$\frac{\partial}{\partial t}(\rho h) + \frac{\partial}{\partial x}(\rho v h) = \frac{\dot{Q}}{V}. \tag{4.5}$$

The detailed numerical solution of both equations based on a finite volume method are given in Section C.2. Since this derivation is more advanced than the one for the simple PFM, the indexing is adapted according to the following definitions (see Figure 4.1): P is a control volume, with neighbor volumes E and W. The interface between E and P is

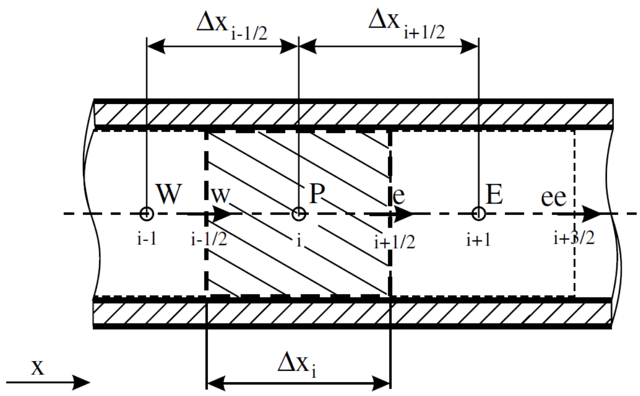

Figure 4.1: Grid structure for the numerical discretization. With the control volume, that is, node P and its neighbor volumes E and W. [Walter, 2007]

e. The interface between P and W is w. The entire absorber has a constant cross section area A. The control volume P has the length $\Delta x = e - w$ and volume $V = A \cdot \Delta x$. The final discretized form of the conservation equations therefore leads to

$$V \cdot \frac{(\rho_P^{t+1} - \rho_P^t)}{\Delta t} + \dot{m}_e^{t+1} - \dot{m}_w^{t+1} = 0 \tag{4.6}$$

for the mass and analogously for the energy balance to

$$V \cdot \frac{(\rho h)_P^{t+1} - (\rho h)_P^t}{\Delta t} + \dot{m}_e^{t+1} h_P^{t+1} - \dot{m}_w^{t+1} h_W^{t+1} = Q_{gains,n}. \tag{4.7}$$

The implicit Equation (4.6) and (4.7) can be converted to be solved without iteration[2], which reduces computational time and allows for flexible (i.e., also larger) time steps. The concept is based on an approach proposed by Seubert [2015]. From Equation (4.6) follows

$$V \cdot \frac{\rho_P^{t+1}}{\Delta t} + \dot{m}_e^{t+1} = V \cdot \frac{\rho_P^t}{\Delta t} + \dot{m}_w^{t+1}. \tag{4.8}$$

Equation (4.7) is transformed to

$$h_P^{t+1} = \frac{Q_{gains,n} + \rho_P^t h_P^t \frac{V}{\Delta t} + \dot{m}_w^{t+1} h_W^{t+1}}{\frac{V \cdot \rho_P^{t+1}}{\Delta t} + \dot{m}_e^{t+1}}. \tag{4.9}$$

The denominator of Equation (4.9) is unknown, but can be replaced by Equation (4.8), leading to

$$h_P^{t+1} = \frac{Q_{gains,n} + \rho_P^t h_P^t \frac{V}{\Delta t} + \dot{m}_w^{t+1} h_W^{t+1}}{\frac{V \cdot \rho_P^t}{\Delta t} + \dot{m}_w^{t+1}}. \tag{4.10}$$

Thereby, Equation (4.10) allows a direct calculation of h_P^{t+1} as a function of h_P^t, ρ_P^t (obtained from the previous time step already calculated) and of $\dot{m}_w^{t+1}, h_W^{t+1}$ (obtained from

[2] This is only the case when heat conduction is neglected and only convection considered with an upwind scheme. In this way, all boundary conditions are given at the ‘left’ (i.e., flow entrance) side from the control volumes and a direct calculation from ‘left’ to ‘right’ can be performed.

the previous node already calculated as well). From the enthalpy of the node P, the thermodynamic properties can be derived by

$$T_P^{t+1} = f(h_P^{t+1}, p), \tag{4.11}$$

$$\rho_P^{t+1} = f(h_P^{t+1}, p), \tag{4.12}$$

which allows solving the mass conservation Equation (4.8) as follows:

$$\dot{m}_e^{t+1} = \dot{m}_w^{t+1} - V \cdot \frac{\rho_P^{t+1} - \rho_P^t}{\Delta t}. \tag{4.13}$$

In order to simplify the indexing and nomenclature of these equations and therefore facilitate a faster comprehension, in the following the temporal indexing is adapted. The upper index of $t+1$ is subsequently omitted, whereas properties of one time step before are indicated by substituting t by 0. In this way, $\rho_P^{t+1} = \rho_P$ and $\rho_P^t = \rho_P^0$, and hence:

$$\dot{m}_e = \dot{m}_w - V \cdot \frac{\rho_P - \rho_P^0}{\Delta t}. \tag{4.14}$$

By the direct calculation of the outlet mass flow rate $\dot{m}_e^{t+1} = \dot{m}_e$ (without any iteration), the change in mass flow rate as well as the change in the node mass can be derived. This allows to appropriately reproduce the dynamics of the evaporation/condensation along an absorber tube with a limited computational effort. It thereby represents the main benefit of the introduced EPFM. Nevertheless, it still uses a steady pressure calculation by applying linear interpolation between inlet and outlet pressures. That this computationally less complex approach is valid to use for the evaluation of direct steam generating collectors is proven by comparing it to measurement data on the one hand, but also to the more complex and accurate SIMPLER algorithm on the other hand (see Section 4.2). The numerical approach of SIMPLER is presented in the following section.

■ 4.1.4 SIMPLER Algorithm

The algorithm Semi-Implicit Method for Pressure-Linked Equations—Revised (SIMPLER) is based on an approach solving the momentum conservation equation (i.e., the pressure calculation) linked to the mass conservation (i.e., the velocity calculation). It represents a very sophisticated and capable method to accurately reproduce compressible fluid flow by resolving all three conservation equations of mass, energy, and momentum. Within the present thesis, the basic principle is outlined in the following. For detailed derivations and theoretical background knowledge, refer to Hernández [2015a], Walter [2001], and Patankar [1980].

The general conservation of the one-dimensional mass, momentum, and energy is represented by the partial differential equation

$$\frac{\partial}{\partial t}(\rho\phi) = -\frac{\partial}{\partial x}(v\rho\phi) + S_\phi, \tag{4.15}$$

where ϕ may be the velocity v (for the momentum equation), the specific enthalpy h (for the energy equation) or 1 (i.e., unity, for the mass balance). S_ϕ represents the source term of the corresponding conservation equation, consisting, for instance, of incoming heat sources (e.g., by solar radiation), gravitational forces, friction losses, and so forth.

By means of a finite volume method according to the grid points and their indices defined in Figure 4.1, Equation (4.15) can be transformed to an algebraic equation, which allows to calculate ϕ by integrating the partial differential equation for the control volume P. To facilitate the discretization for $\phi \neq 0$—this is, for the energy and momentum equation—the discretized ϕ-conservation equation is subtracted from the discretized mass balance times ϕ, obtaining a general discretization equation as

$$a_{Pi}\phi_i = a_{Wi}\phi_{i-1} + a_{Ei}\phi_{i+1} + b_i, \tag{4.16}$$

with

$$\begin{aligned}
a^0_{Pi} &= \frac{\rho^0_i \cdot \Delta x}{\Delta t}, \\
a_{Wi} &= Max\left[(v\rho)_{i-\frac{1}{2}}; 0\right], \\
a_{Ei} &= Max\left[(-v\rho)_{i+\frac{1}{2}}; 0\right], \\
a_{Pi} &= a_{Wi} + a_{Ei} + a^0_{Pi} - S_{\phi,pi}\Delta x, \\
b_i &= S_{\phi,ci} \cdot \Delta x + a^0_{Pi}\phi^0_i.
\end{aligned} \tag{4.17}$$

A detailed derivation of Equation (4.16) is found in Walter [2001, pp. 11–14] and Hernández [2015a, pp. 12–14]. Equation (4.16) is based on the concept that all terms are sorted and summarized according to their lower indices (i, $i+1$, $i-1$) of ϕ. This equation has to be applied to all nodes (i.e., cells or control volumes) of the discretized absorber tube and thus allows a simple, recursive solution by means of the Tri-Diagonal Matrix Algorithm (TDMA) procedure. For details on this algorithm, refer to Patankar [1980, pp. 52–54]. For the first and final control volume of the absorber, the algebraic equations are modified according to their specific boundary values. For a general derivation of the boundary conditions, refer to Hernández [2015a] and Walter [2001]. Using the SIMPLER approach, the following two issues have to be specified.

Source term:

The source term of the transport equations mayorly influences the stability of the numerical scheme. According to Patankar [1980], it should be linearized into an always positive constant term $S_{\phi,ci}$ and an always negative proportional term $S_{\phi,pi}$. More details on the impact and the specific handling of the source term can be found in Hernández [2015a, p. 16], Walter [2001, p. 16] and Patankar [1980, p. 48].

Staggered grid:

A staggered grid should be used for the calculation of pressure in comparison to the calculation of velocities and enthalpy. Not applying a staggered grid can lead to solutions that depend on the time step or relaxation factors of the numerical scheme. Moreover, physically unrealistic solutions are possible. Therefore, pressure is calculated on a staggered grid having the interfaces of a node/cell as a center point as depicted in Figure 4.2. More detailed information is available in Hernández [2015a, p. 15], Walter [2001, p. 15] and Patankar [1980, p. 115].

Being a pressure correction procedure, SIMPLER is based on the main principle of searching for a velocity field that is fulfilling momentum and mass balance simultaneously. The

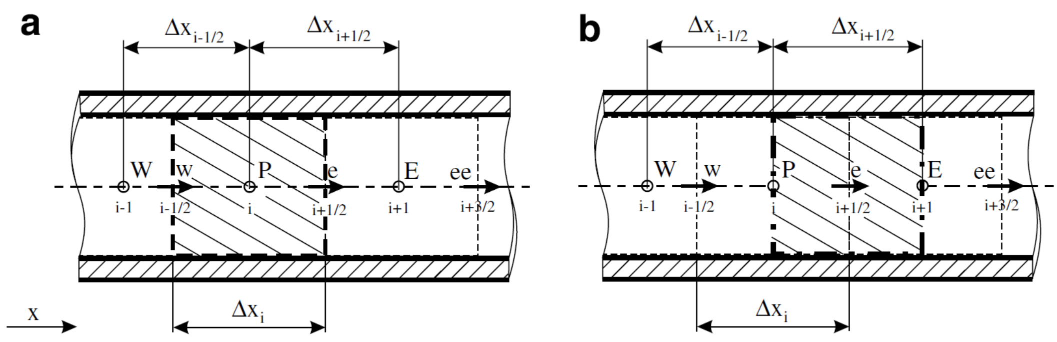

Figure 4.2: Staggered grid of the SIMPLER algorithm. Grid structure for mass and energy balance (a) and momentum balance (b). [Walter, 2007]

discretized mass conservation equation is represented by

$$\frac{(\rho_i - \rho_i^0)A_i \Delta x_i}{\Delta t} + (\rho v A)_{i+\frac{1}{2}} - (\rho v A)_{i-\frac{1}{2}} = 0. \tag{4.18}$$

According to the structure of Equation (4.16), the momentum equation is

$$a_{ei} v_{i+\frac{1}{2}} = a_{wi} v_{i-\frac{1}{2}} + b_{ei} + (p_i - p_{i+1}), \tag{4.19}$$

with the coefficients analog to the ones of Equation (4.16). In this case, no negative velocities are assumed, omitting a term of $v_{i+\frac{3}{2}}$ because $a_{eei} = 0$. Specific coefficients and boundary conditions are listed in Appendix C.4.1.

The complete iterative procedure of SIMPLER is summarized in Section C.3. It mainly consists of initially guessing a velocity field. Thereby, a guessed pressure field can be calculated. If both, pressure and velocity, fulfill the mass balance, convergence is reached and the procedure stopped. If the balance is not fulfilled, the approach allows to calculate a correction value for pressure and velocity. With the newly corrected velocity and pressure values, the energy balance can be resolved in order to update the corresponding fluid properties. The specific energy conservation equation is given by:

$$a_{hP_i} h_i = a_{hW_i} h_{i-1} + b_{hi}. \tag{4.20}$$

Its particular coefficients and boundary conditions are given in Section C.4.4. Subsequently, the corrected velocity and pressure values are again considered as guessed values and the iterative procedure started from the beginning, until both variables fulfill the mass balance.

The SIMPLER algorithm returns a state of the fluid fulfilling mass, momentum, and energy conservation. Boundary conditions are given by the inlet mass flow rate, inlet enthalpy, and outlet pressure of the absorber. SIMPLER was designed to promote physically realistic solutions. Though, it is considered a complex discretization scheme, where convergence of the algorithm is not guaranteed. Different techniques facilitate achieving convergence, such as relaxation factors or adapting spatial and time discretization to the specific simulation [Patankar, 1980, pp. 139–143]. In the following, it is checked if the

EPFM provides sufficient accuracy in comparison to the SIMPLER algorithm. To validate both simulation approaches to measurement data, pre-processing of the data is required. This is realized by the use of a steam drum model. Its concept will be explained in the subsequent section.

■ 4.1.5 Steam Drum Model

The PFM, EPFM, and SIMPLER represent different numerical approaches to simulate the fluid state along the absorber tube and specifically at the outlet of the collector. In this way, they compute outlet temperatures T_{out}, steam qualities $\dot{x}_{out}$, specific enthalpies h_{out} and mass flow rates $\dot{m}_{out}$. Direct steam generating collectors operating in recirculation mode do not produce directly 100 % saturated or superheated steam but rather a two-phase flow of water and steam with steam qualities around 0.4–0.8. This vapor–liquid mixture is fed to and separated in a subsequent steam drum. For the validation of the newly implemented numerical approaches, computed outlet fluid states should be compared to measurement data of installed collectors operating with DSG. Nevertheless, the typical variable studied—and measurable for two-phase flow—in terms of the collector outlet temperature is not characteristic, because it remains constant along the evaporation process. Distinct properties, which would allow meaningful comparisons, represent the collector outlet steam quality, enthalpy, and mass flow rate. All three variables are not measurable up to date for two-phase flow. Figure 4.3 sketches the measurands typically available for a DSG collector with steam drum. Variables in green can be measured, whereas properties in orange cannot. However, it is possible to determine these values by drawing a mass and energy balance over the steam drum, given a measurable pressure and level of the steam drum (variables marked in blue in Figure 4.3).

The model of the steam drum is derived according to Walter [2001, pp. 106–108], its implementation performed and documented within the work of Hernández and Zirkel-Hofer [2016]. The simplified mass conservation equation included in the steam drum approach is represented by

$$m_{SD} - m_{SD}^0 = \left(\dot{m}_{in,SD} - \dot{m}_{out,sum,SD}\right) \cdot \Delta t, \tag{4.21}$$

where m_{SD} is the entire mass of the fluid in the steam drum. m_{SD}^0 indicates the mass of the steam drum one time step before. $\dot{m}_{in,SD}$ is considered as the inlet to the steam drum coming from the absorber tube of the collector. $\dot{m}_{out,sum,SD}$ is defined by the sum of the mass flow rates at all other exits (or even potential additional inlets) of the steam drum. In this way, the change of mass inside the system is equal to the mass entering the system minus the mass exiting the system. m_{SD} and m_{SD}^0 can be calculated according to the measurement data by

$$\begin{aligned} m_{SD} &= m_{water} + m_{steam} \\ &= \rho_{water} \cdot V_{water} + \rho_{steam} \cdot V_{steam}, \end{aligned} \tag{4.22}$$

where the densities ρ_{water} and ρ_{steam} can be calculated using the steam drum pressure p_{SD} and assuming saturation temperature. The volume V_{water} is a function of the steam

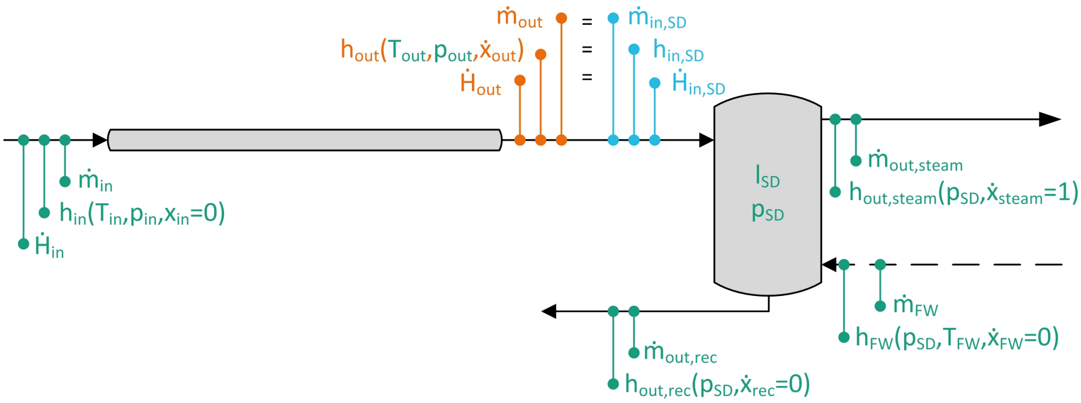

Figure 4.3: Inlet and outlet properties of a DSG collector in recirculation mode. Variables marked in green are measurable, properties in orange color are not directly measurable. Variables in blue can be determined by balancing the steam drum.

drum level.[3] The total volume V_{SD} is known. Thus, the volume of steam V_{steam} can be calculated since $V_{steam} = V_{SD} - V_{water}$. Thereby, from Equation (4.21) the inlet mass flow rate of the steam drum can be derived from

$$\dot{m}_{in,SD} = \frac{m_{SD} - m_{SD}^0}{\Delta t} + \dot{m}_{out,sum}. \tag{4.23}$$

Similarly, for the simplified energy conservation the algebraic equation is used

$$\Delta Q_{SD} = \left(\dot{H}_{in,SD} - \dot{H}_{out,sum,SD}\right) \cdot \Delta t, \tag{4.24}$$

meaning the change of enthalpy and mass inside the system is equal to the enthalpy and mass entering the system (referred to as inlet flow enthalpy $\dot{H}_{in}$) minus the enthalpy and mass exiting it. $\dot{H}_{out,sum,SD}$ can be calculated from measurement data by

$$\dot{H}_{out,sum} = \dot{m}_{out,rec} \cdot h_{out,rec} + \dot{m}_{out,steam} \cdot h_{out,steam} - \dot{m}_{FW} \cdot h_{FW}, \tag{4.25}$$

with the first term on the left being the recirculation flow, the second one the steam flow, and the third a potential feed water flow entering the steam drum. ΔQ_{SD} is calculated considering the change of enthalpy and mass of the liquid water or steam, and the pressure–volume change of the steam drum:

$$\begin{aligned} \Delta Q_{SD} =& V_D \left(p_{SD} - p_{SD}^0\right) + \left(h_{water} \cdot m_{water} - h_{water}^0 m_{water}^0\right) \\ &+ \left(h_{steam} m_{steam} - h_{steam}^0 m_{steam}^0\right). \end{aligned} \tag{4.26}$$

Therefore, from Equation (4.24) follows

$$\dot{H}_{in,SD} = \dot{m}_{SD,in} \cdot h_{SD,in} = \dot{H}_{out,sum,SD} + \frac{\Delta Q_{SD}}{\Delta t}. \tag{4.27}$$

[3] If the steam drum is considered a horizontal cylinder, $V_{water} = \left(\frac{d_{SD}}{2}\right)^2 \pi \cdot l$. For a horizontal steam drum, $V_{water} = \frac{d_{SD}}{8}(l_{tot})^2(\pi - (\sin a + a))$ with $a = 2 \cdot \sin^{-1}\left(1 - \frac{2l}{l_{tot}}\right)$. Here, d_{SD} represents the diameter of the steam drum, l the level of the steam drum, and l_{tot} the length of the cylinder/steam drum, neglecting the header geometry.

$\dot{H}_{in,SD}$ is considered equal to $\dot{H}_{out,meas} = \dot{m}_{out,meas} \cdot h_{out,meas}$, the measured collector outlet flow enthalpy, which actually is not a direct measurand but rather a determined variable from measurement data. This concept is based on the assumption that the losses between outlet of the collector and inlet of the steam drum are negligible. The same concept applies for the inlet steam drum mass flow $\dot{m}_{in,SD}$, which is assumed equal to the measured collector outlet mass flow $\dot{m}_{out,meas}$. In the following, if nothing is specifically indicated, $\dot{m}_{out}$ is considered equal to $\dot{m}_{out,meas}$ and analog for $\dot{H}_{out} = \dot{H}_{out,meas}$. By this approach, a more appropriate comparison of the different models to measurement data is available, not only comparing outlet pressures and temperatures but also the objective variable of the collector performance evaluation in terms of the collector outlet flow enthalpy.

■ 4.2 Validation of the Simulation Models

To validate the implemented simulation approaches, measurement data of collector `PTC_s1` were analyzed, because they are based on a frequently and extensively studied system used for diverse validation aspects in the broad context of DSG simulations. Three exemplary dynamic test situations at three different pressure levels were chosen as a reference:

- Large DNI jump at a pressure level of 30 bar (day `A`)
- Stepwise mass flow jumps at a pressure level of 60 bar (day `B`)
- Continuous pressure rise and moderate DNI dynamics at pressure level of 100 bar (day `C`)

In Figure 4.4 to Figure 4.6, the measurands in terms of DNI, mass flow rates, pressure, and temperatures of these exemplary days are depicted. Furthermore, the simulated versus the measured collector outlet flow enthalpy $\dot{H}_{out}$ are sketched for the different simulation models of PFM, EPFM, and SIMPLER, including measurement uncertainty bands marked in light grey.

■ 4.2.1 Comparison of EPFM to SIMPLER

For the validation of the EPFM, simulation results are compared to data simulated with the SIMPLER algorithm. Outlet flow enthalpy values of the EPFM approach $\dot{H}_{out,EPFM}$ are illustrated in comparison to calculated ones by SIMPLER $\dot{H}_{out,SIMPLER}$. Deviations between both variables for the three days in terms of the root mean square deviation as well as absolute and relative mean deviations are listed in Table 4.4. Deviations of EPFM to SIMPLER range from approximately 5–12 kW, corresponding to relative error values of around 0.2–0.3 % of the measured outlet flow enthalpy. The higher RMS of

Table 4.4: Difference between simulation results of EPFM and SIMPLER. Root mean square, absolute, and relative mean deviation for the outlet flow enthalpy $\dot{H}_{out}$ are given for the three exemplary measurement days.

Deviation	Unit	Day `A`	Day `B`	Day `C`
RMS	kW	16.2	7.7	9.6
Absolute mean	kW	7.4	4.7	5.8
Relative mean	%	0.33	0.18	0.24

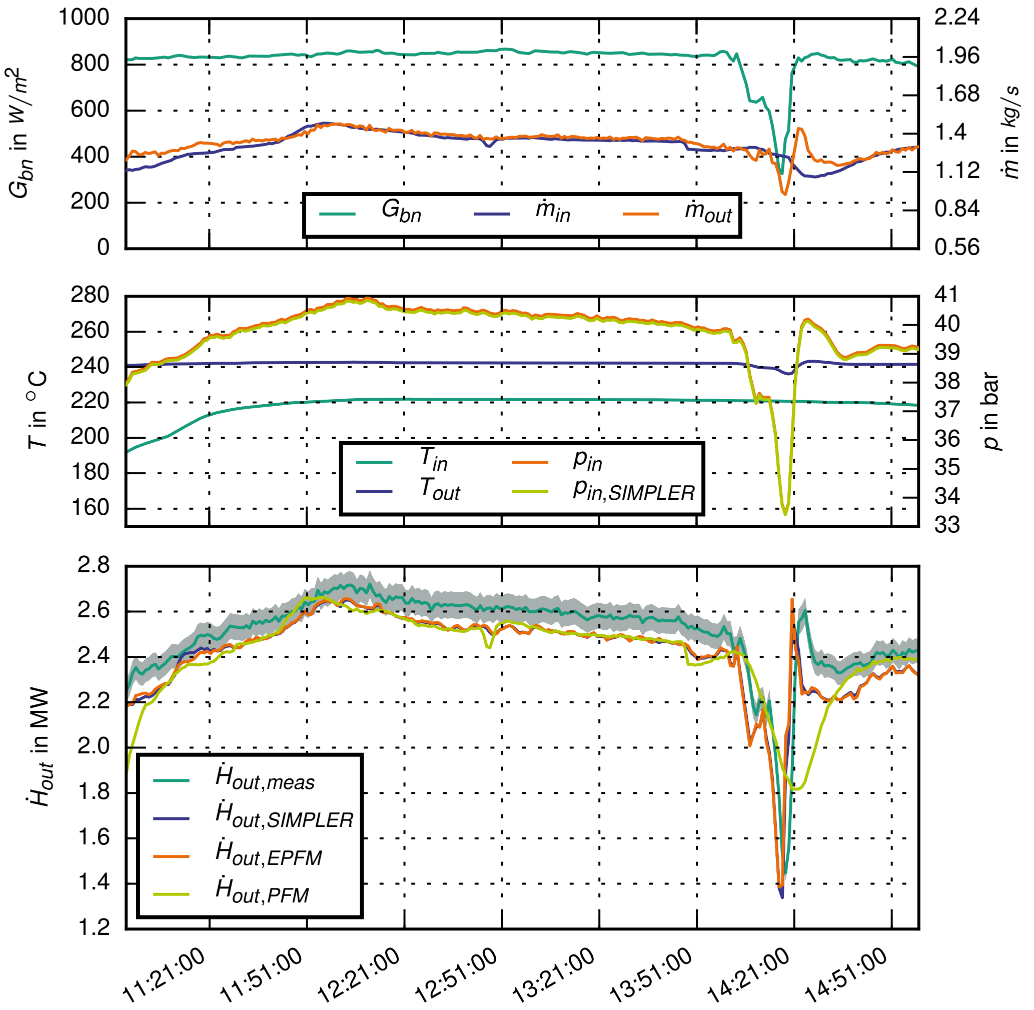

Figure 4.4: DSG measurement day A. Measurement and simulation data of exemplary test day A for collector PTC_s1. The measurement uncertainty band in terms of $U_c(\dot{H}_{out,meas}) = 2.2\,\%$ is additionally marked in light grey.

day A is resulting from the extreme DNI drop within this test day. Abrupt and large dynamics are causing higher changes in the simulated variable. Even slight temporal shifts of both simulations therefore cause larger deviation of the curves, resulting in a more pronounced RMS value. However, overall deviations of both simulation approaches are not significant. They are hardly noticeable[4] in the graphical illustration of Figure 4.4 to Figure 4.6, especially in comparison to the PFM simulated outlet flow enthalpy $\dot{H}_{out,PFM}$ or even the measured flow enthalpy $\dot{H}_{out,meas}$.

The EPFM is able to provide equal results to the more sophisticated SIMPLER approach, even though the pressure field of the EPFM is not explicitly calculated, but linearly interpolated from measurement data. The difference in the pressure calculation

[4]Only for the high dynamics at 2:21 p.m. (14:21:00 in Figure 4.4) of day A, a difference between the lila and orange line is perceivable.

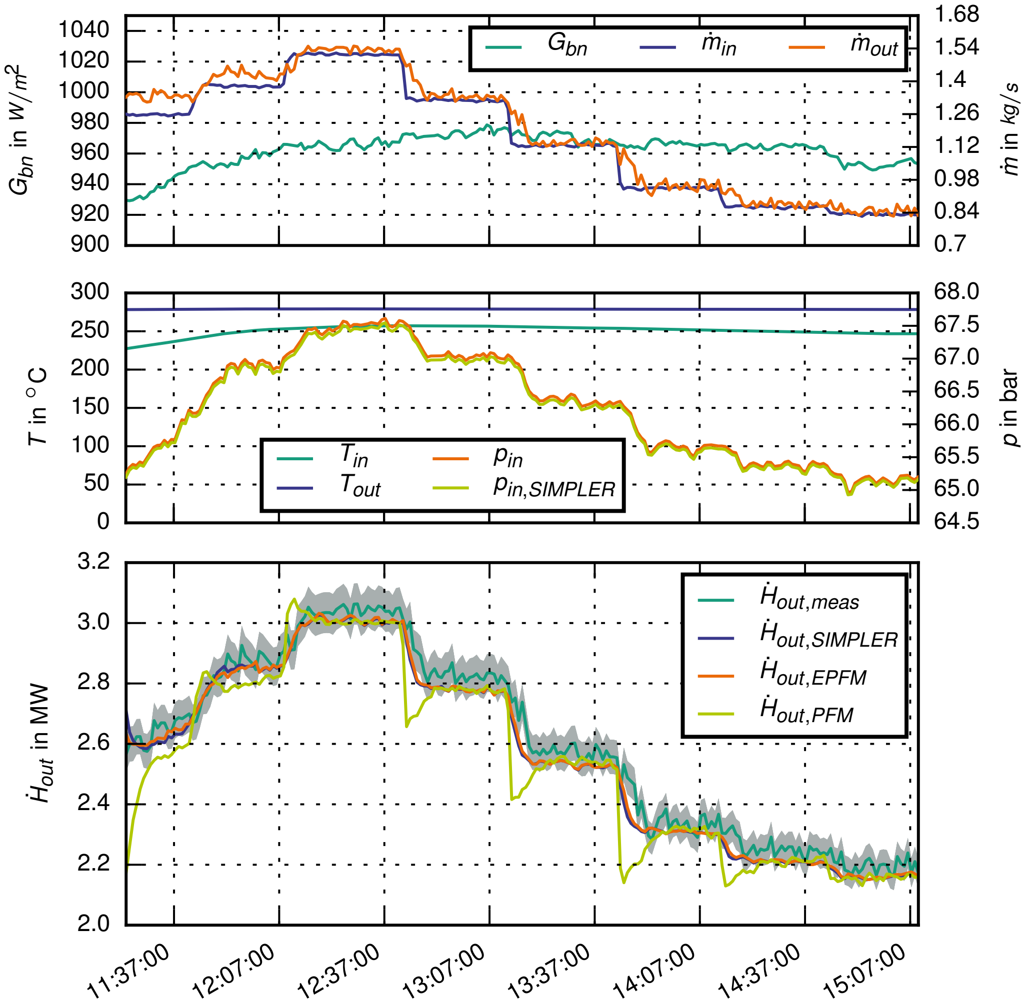

Figure 4.5: DSG measurement day B. Measurement and simulation data of exemplary test day B for collector PTC_s1. The measurement uncertainty band in terms of $U_c(\dot{H}_{out,meas}) = 2.2\,\%$ is additionally marked in light grey.

is perceivable while comparing the measured inlet pressure p_{in} with the calculated inlet pressure of SIMPLER $p_{in,SIMPLER}$ (depicted in orange and light green colored line in Figure 4.4 to Figure 4.6). The calculated inlet pressure is always smaller (approximately 0.1 bar) than the measured inlet pressure. The reason for this difference is that not every single pressure-drop effect—such as a slight inclination of the collector loop, every ball joint, interconnections between collector modules, and bendings of the tubes—is considered in the pressure-drop calculation within the SIMPLER procedure. However, the difference in inlet pressure do not substantially influence the overall simulation results in terms of the simulated outlet flow enthalpy $\dot{H}$. Moreover, a very distinct and detailed inclusion of every pressure-drop effect is not desired in the context of performance testing. Apart from the issue that detailed constructive and material data is usually not available (and in most cases a sharing and disclosure of the collector manufacturer not desired), representative testing aims at an overall balancing of the system performance rather than

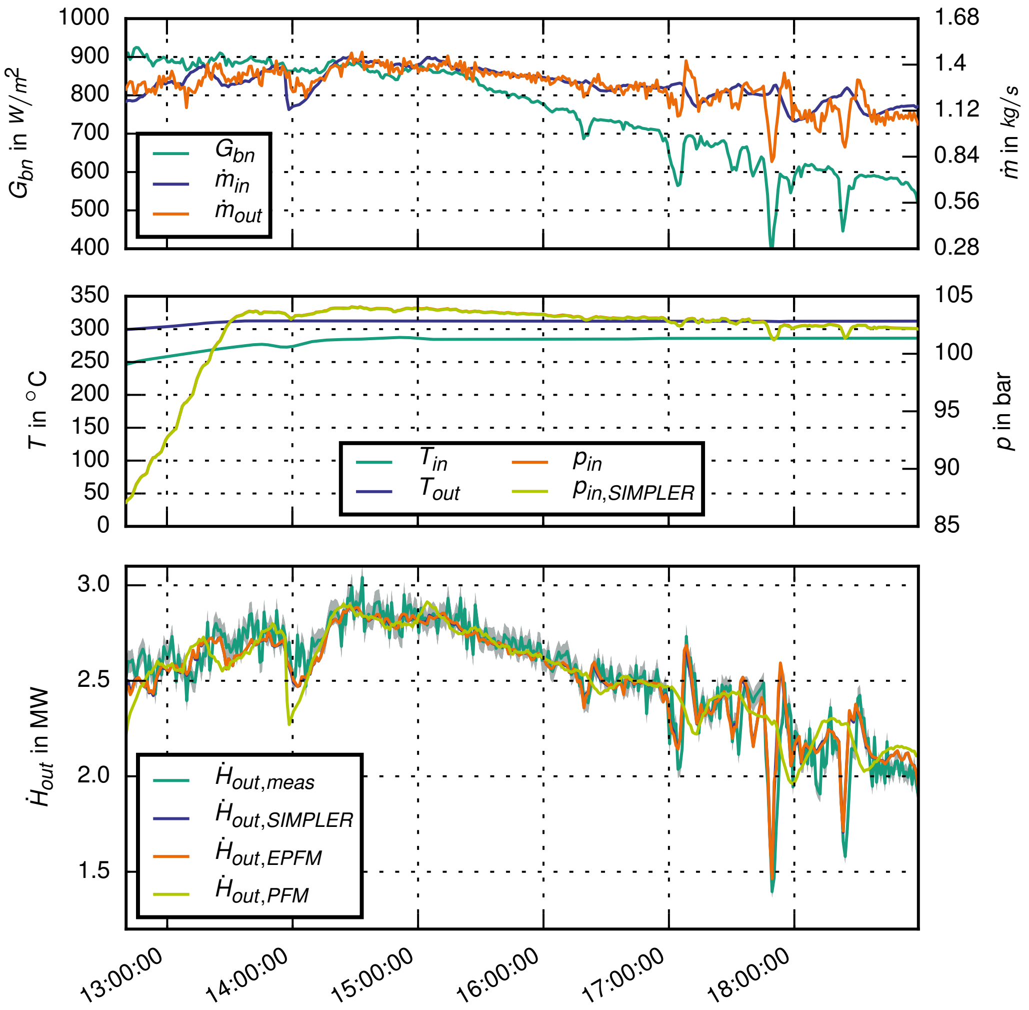

Figure 4.6: DSG measurement day `C`. Measurement and simulation data of exemplary test day `C` for collector `PTC_s1`. The measurement uncertainty band in terms of $U_c(\dot{H}_{out,meas}) = 2.2\,\%$ is additionally marked in light grey.

describing single physical effects. The collector is desired to be treated as a black box, including empirical relations with aggregated performance parameters and little details as possible. Certainly, in the case of DSG testing, the model needs to be elaborate enough to accurately reproduce the dynamics of the systems. Nevertheless, a simpler model equally reproducing the dynamics of a system is always to be favored. Furthermore, in the case of using the simulation model for testing purposes, inlet and outlet pressures are available measurands. They may reliably be included as boundary conditions for the EPFM, leading to equally accurate results as obtained from the SIMPLER procedure. Note that the suitability of the EPFM for annual yield simulations and control purposes—without measurement data as boundary conditions—needs to be further checked into more detail. For an adequate performance testing procedure, this aspect is not considered relevant.

An additional drawback of the SIMPLER approach represents its high computational expense coupled with its numerical instability. The simulation time for the SIMPLER

Table 4.5: Benefits and drawbacks of the implemented DSG simulation approaches. Comparison of capabilities and deficits of the EPFM and SIMPLER algorithm. In the context of performance testing, the disadvantage of the EPFM can be eliminated.

	Benefits	Drawbacks
EPFM	• faster computation • stable numerical scheme • less physical details required • comparable results to SIMPLER	• simplification in pressure calculation • realistic boundary condition for p_{in} required
SIMPLER	• solving of all three conservation equations • no simplification of pressure calculation • good reference bases for validation purposes	• high computational expense • numerical stability issues • high level of required details for accurate pressure calculation

is significantly larger (approximately 15 times the simulation time of PFM and eight times of the EPFM simulation time), even if parallelization of the numerical scheme is enabled. Simulations performed with EPFM are only two times slower than PFM simulations. Moreover, the complex numerical scheme of SIMPLER is still significantly less robust than both other simulation approaches. Convergence of the iterative procedure is not always reached and sensitive to the simulation time step, number of simulated nodes, boundary conditions, and high dynamics of the system. Certainly, this drawback does not represent a general limitation and may successfully be addressed with further work and time investigated in the improvement of the numerical solver. In the context of enabling a dynamic testing and evaluation of DSG collectors, and with a valuable and equally suitable alternative—the EPFM—at hand, a further elaboration of the SIMPLER algorithm is therefore not considered crucial. With regard to the purpose within the present thesis, the SIMPLER algorithm provides a valuable reference basis. A proper validation of the simplified EPFM approach is feasible, even if the numerical scheme of the SIMPLER does not stably converge for every (sometime unrealistic) boundary conditions. Instability of the algorithm solely leads to a crash of the calculation—which can be fixed by manually changing unfavorable boundary conditions such as initialization values, evaluation and simulation time step, and so forth—but does not influence the correctness of the simulation results. Consequently, the obtained reasonable results of the EPFM in comparison to the SIMPLER justify the use of the EPFM for dynamic evaluations of DSG collectors. Table 4.5 summarizes the benefits and drawbacks of both implemented procedures. Due to the advantages of the EPFM and disadvantages of the SIMPLER, coupled with the fact that the drawbacks of the EPFM do not play any role in collector testings—as measured pressure values are available—the EPFM approach is chosen for the following dynamic steam simulations.

■ 4.2.2 Comparison of PFM to EPFM/SIMPLER

When comparing the newly implemented dynamic DSG simulation approach EPFM—and equally SIMPLER—with the already existing model of the PFM, more pronounced differences are discernible. In Figure 4.4 to Figure 4.6, the specific dynamics of the variables and their effect on the simulated outlet flow enthalpy are illustrated. For day A, the reduction in incoming irradiance leads to a significant decrease of $\dot{H}_{out,meas}$, which is reproduced rather accurate by both dynamic models. The PFM, however, shows a temporal delay and reduced peaks of the dynamics. It therefore reacts with large inertia to the

Table 4.6: Difference between measurement and simulation results of PFM, EPFM and SIMPLER. Root mean square, absolute and relative mean deviation of the collector outlet flow enthalpy $\dot{H}$ are given for the three exemplary measurement days.

Deviation	Model	Unit	Day A	Day B	Day C
RMS	PFM	kW	151.0	99.4	161.8
	EPFM	kW	127.4	46.3	104.0
	SIMPLER	kW	121.6	50.1	103.3
Absolute mean	PFM	kW	105.4	70.3	108.8
	EPFM	kW	100.3	38.4	74.5
	SIMPLER	kW	99.7	41.3	74.5
Relative mean	PFM	%	4.35	2.69	4.76
	EPFM	%	4.23	1.49	3.15
	SIMPLER	%	4.18	1.60	3.15

dynamics of the system. The reason for this behavior is comprehensible: with a decreasing irradiance, the vapor quality produced in the absorber nodes is reduced. In this way, the density of the fluid within the node increases. Due to the condensation, less mass flow exits the absorber nodes, leading to a significant reduction of the collector outlet flow enthalpy. Yet, the PFM does not consider varying outlet mass flow and assumes it constant to the collector inlet mass flow rate. Thereby, the collector outlet flow enthalpy $\dot{H} = \dot{m} \cdot h$ in the case of the PFM is only reduced by the reduction of the specific enthalpy, whereas the outlet mass flow remains constant. This causes the buffering (i.e, less peak) of the PFM flow enthalpy curve in Figure 4.4. Notice that all three simulation models show a noticeable, nearly constant difference to the measured flow enthalpy $\dot{H}_{out,meas}$. All models following the same tendency for this particular day may indicate that other effects for this difference, which are not considered in the current simulation boundaries, have to be adapted. Particularly, the included, measured soiling rate—determined with high uncertainties, especially in the case of larger collector rows—may cause this absolute shift. Theses factors will be specifically evaluated within a global parameter identification procedure. For the comparison of the different models, this systematic deviation is not considered pertinent.

The PFM versus the EPFM simulation results of day B, including the inlet mass flow jumps, demonstrate the clear superiority of the dynamic models. With a decrease in the inlet mass flow rate, the steam quality in the absorber nodes increases with constant irradiance. Consequently, the density of the absorber nodes decreases with more evaporation, causing a rise in the outlet mass flow rate. Again, the PFM considers the outlet mass flow rate as constant to the inlet mass flow rate. Accordingly, the collector outlet flow enthalpy does not decrease as abrupt for the dynamic models as for the PFM.

For the third measurement day C, the pressure rise during the start-up of the collector around noon is equally simulated for all three models. Nonetheless, the DNI change in the afternoon coupled with abrupt pressure drops in the afternoon are reproduced considerably better by the dynamic models similarly to the previously studied days. In Table 4.6, the overall deviations of the simulation results of the three models compared to the measured outlet flow enthalpy are summarized. For all measurement days, the PFM performs worst. However, the deviation is not as pronounced as perceivable in the graphs. The reason for this may originate from the steady-state periods, where the PFM performs equally well. In this way, the deviations in the purely dynamic situations are averaged out. This tendency is revealed by the RMS deviation in comparison the mean absolute deviation. In the RMS calculation, outliers are weighted more than in the calculation of the mean deviation. The PFM shows significantly worse RMS values in comparison to the dynamic models (151 to 127 kW) than for the mean deviation (105 to 100 kW). Apparently, outliers—resulting from dynamic situations—appear more frequently for the PFM.

Additionally notice that deviations will always be higher for dynamic situation than for steady-state independent on the simulation model. If steady-state conditions are considered, simulated and measured data will fit better, because only slight changes occur. Higher overall dynamics of the system generally provoke higher deviations of simulated versus measured data. If large changes in $\dot{H}_{out}$ arise, even slight temporal shifts cause higher deviations, even though the general course is reproduced well. Consequently, dynamic steam evaluation will always be linked to higher RMS values due to more pronounced changes in the collector outlet flow enthalpy to be simulated.

All in all, the results confirm the value and necessity of using a dynamic DSG model to adequately reproduce the dynamics of steam generating systems. The verification of the practicability of the EPFM—in terms of lower computational cost and complexity—as well as its validated capability and reliability in reproducing dynamics prove it to be a valuable approach for the further DSG evaluation of concentrating solar collectors.

■ 4.3 Adaptation of the Evaluation Procedure

As already discussed in Section 3.2.1, so far the collector outlet temperature was considered the objective variable for the optimization procedure of the collector performance evaluation. This means that the measured outlet temperature is compared to the simulated outlet temperature computed by the simulation model (until now the PFM of ColSim). This approach is appropriate for evaluating collectors operating without phase change. However, due to the evaporation of water, the outlet temperature of the collector does not represent a distinct variable for the collector performance any more. The amount of incoming solar radiation transfered to available thermal energy (i.e., the efficiency of the collector) does not influence the outlet temperature of the fluid, as it will always be the saturation temperature of the two-phase fluid[5]. It rather effects the quantity of steam produced, that is, the outlet steam quality of the fluid. Because the steam quality of a fluid cannot be measured, two alternatives are possible for the determination of the collector performance; one for steady-state conditions of DSG collectors and the other for both, steady-state and dynamic DSG measurements.

■ 4.3.1 Adaptation to Steady-State Conditions

For steady measurement conditions, all incoming and outgoing variables and properties of the system remain constant. Therefore, the outlet steam quality of the collector can directly be calculated by relating the outlet steam mass flow of the steam drum to the inlet mass flow

$$\dot{x}_{out} = \frac{\dot{m}_{out,steam}}{\dot{m}_{in}}. \tag{4.28}$$

[5]This is only valid for pure substances and azeotropes.

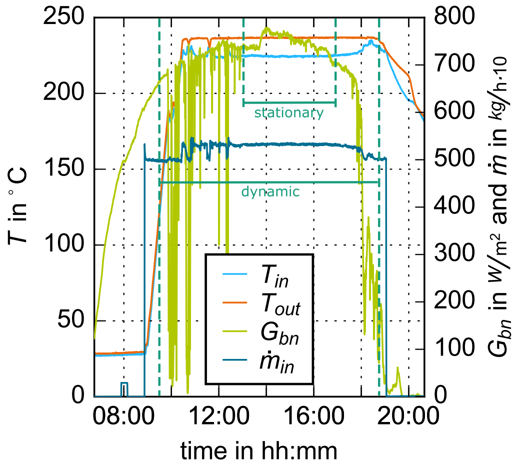

(a) Measurement day D

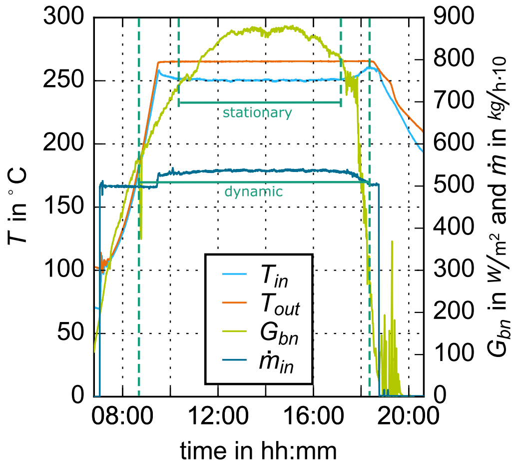

(b) Measurement day E

Figure 4.7: DSG measurement data of collector LFC_s1. Exemplary measurement days with particularly indicated steady-state and dynamic evaluation time intervals.

For steady-state conditions, the level as well as the pressure of the steam drum can be considered constant, facilitating this simple calculation. With the steam quality, the specific outlet enthalpy $h_{out}(\dot{x}, T, p)$ can be calculated, depending on the measured outlet temperature, measured outlet pressure, and calculated outlet steam quality. This specific enthalpy is considered the adapted objective variable of the optimization procedure for steady-state conditions within this thesis. Thereby, specific outlet enthalpies are simulated and compared to measured ones.

Notice that the PFM can still be applied if steady-state measurement data is available for a DSG collector. With steady-state conditions, the mass flow rates of inlet and outlet are equal and remain constant. Inevitably, the density of the outlet water–steam mixture will be lower than the one of the entering water fluid. Yet, the velocity will counterbalance this difference, since the water–steam mixture is flowing faster leading to the same mass flow rate of inlet and outlet. With constant mass flow rates, the PFM is suitable for an evaluation of steady measurement conditions, as already seen in the simulation results for the collector PTC_s1 of the previous section. The use of this concept for steady DSG measurement data is recommended, as the PFM is the most stable numerical procedure with the least computational effort.

This approach has been implemented in Nettelstroth [2015, pp. 55–59] and applied to measurement data of LFC_s1. In this test campaign, large steady-state conditions are available. All five available measurement days were included in the DSG collector evaluation. In this case, only the optical efficiency at normal incidence $\eta_{opt,0}$ was identified, because not enough temperature and incidence angle variation were available within these measurement days. A detailed study and conclusion on the testing procedure (i.e., what fluid temperatures, solar incidence angles, and so forth are required for a proper identification of those parameters) will be specifically addressed in Chapter 7.

To demonstrate the capability of the implemented approach, the results of two exemplary measurement days D and E are shown in the following. Figure 4.7 depicts the main measurement data of these test days. Approximately steady conditions only

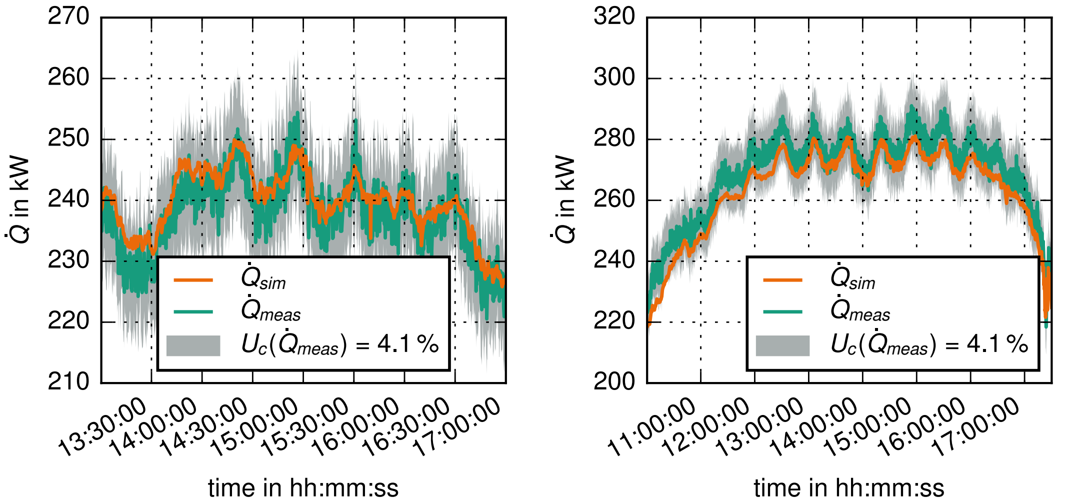

(a) Evaluation result of day D

(b) Evaluation result of day E

Figure 4.8: Steady-state evaluation results of collector LFC_s1. Simulated (marked in orange) and measured (marked in green) collector power output, obtained as a result of the adapted evaluation procedure to steady DSG measurement data.

arise between 1 p.m.–5 p.m. for D, whereas a longer steady-state interval from around 10 a.m.–5:30 p.m. is available for day E. Figure 4.8 reveals that the adaptation of the parameter identification procedure to steady DSG data was implemented successfully. Simulated and measured collector power outputs $\dot{Q}_{sim} = \dot{m}_{in} \cdot (h_{out,sim} - h_{in,meas})$ versus $\dot{Q}_{meas} = \dot{m}_{in} \cdot (h_{out,meas} - h_{in,meas})$ only differ slightly, leading to a reasonable $\eta_{opt,0}$-value and a RMS of 4.1 $^{kJ}/_{kg}$ in the specific outlet enthalpy. This corresponds to acceptable 6.0 kW of a RMS in the collector power output $\dot{Q}$ as sketched in Figure 4.8.

■ 4.3.2 Adaptation to Dynamic Conditions

For the evaluation of dynamic measurement data, the EPFM has to be used for the parameter identification procedure. Furthermore, no simple calculation of the steam quality is feasible. Instead, dynamic balancing of the steam drum as introduced in Section 4.1.5 has to be applied. As already seen in the results of the previous sections, not only the specific outlet enthalpy but also the outlet mass flow rate changes significantly for dynamic evaporation processes. On this account, the objective variable of the optimization procedure is adapted to the collector outlet flow enthalpy $\dot{H}_{out}$ for dynamic DSG evaluations. Similarly to the steady-state example, the same measurement data basis of collector LFC_s1 was chosen. Only the evaluation time intervals were extended. They are specifically marked for the two exemplary measurement days in Figure 4.7. By amplifying the evaluation interval, more disperse fluid temperatures are available. Consequently, a distinct determination of heat loss parameters is feasible for this dynamic evaluation case. The corresponding results of the adapted dynamic DSG evaluation procedure are depicted in Figure 4.9, with the simulated and measured collector power output as

$$\begin{aligned} \dot{Q}_{sim} &= \dot{H}_{out,sim} - \dot{H}_{in,meas} = \dot{h}_{out,sim} \cdot \dot{m}_{out,sim} - \dot{h}_{in,meas} \cdot \dot{m}_{in,meas}, \\ \dot{Q}_{meas} &= \dot{H}_{out,meas} - \dot{H}_{in,meas} = \dot{h}_{out,meas} \cdot \dot{m}_{out,meas} - \dot{h}_{in,meas} \cdot \dot{m}_{in,meas}. \end{aligned} \tag{4.29}$$

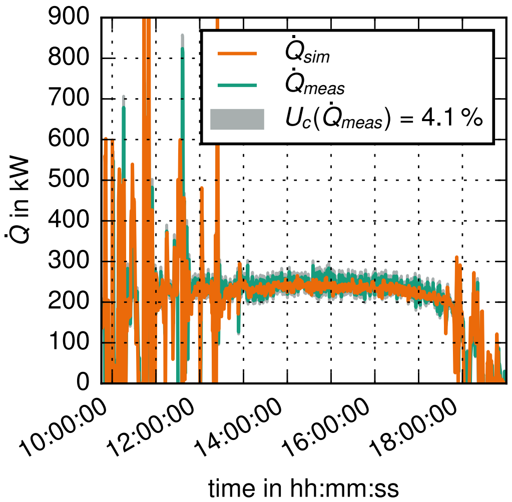

(a) Evaluation result of day D

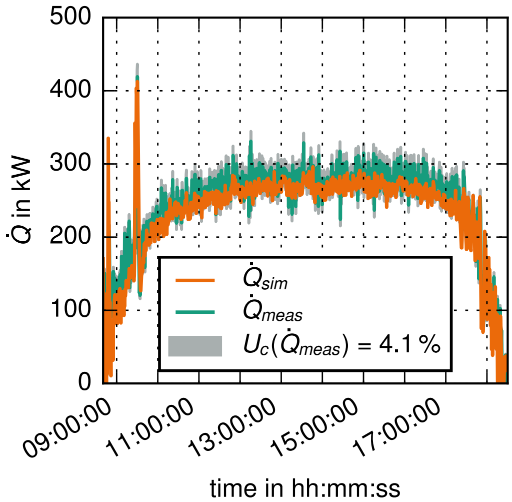

(b) Evaluation result of day E

Figure 4.9: Dynamic evaluation results of collector LFC_s1. Simulated (marked in orange) and measured (marked in green) collector power output, obtained as a result of the adapted evaluation procedure to dynamic DSG measurement data.

Identification results show that the adaptation of the parameter identification procedure in general was implemented successfully, leading to reasonable $\eta_{opt,0}$-values and heat loss parameters. Concerning the fit quality, higher deviations between measurement and simulation data of 39.7 kW in the RMS of $\dot{H}_{out}$ or $\dot{Q}$ arise. As expected, the RMS of the dynamic evaluation is considerably higher than the one for steady-state or incompressible media. DSG and dynamic measurement data are usually more error-prone, due to sensor response time. Moreover, the level sensor of the steam drum is commonly very sensitive and additionally has a large influence on the energy balance of the steam drum, because it is multiplied by the steam drum horizontal surface. This is noticeable by the noisy $\dot{Q}_{meas}$-signal. Besides, modeling of dynamic states is never as exact as for steady-state conditions or incompressible media. Peaks in the collector outlet flow enthalpy are harder to reproduce correctly, leading locally to larger deviations significantly affecting the RMS. However, as shown in Figure 4.9, the general collector behavior is reproduced correctly, in particular periods with lower dynamics. From this follows that the mean deviation of approximately 20.9 kW is considerably smaller than the RMS. It corresponds to approximately 7.8 % of the nominal collector power output, which represents an elevated but still acceptable error value, especially in comparison to a generally higher overall measurement uncertainty of approximately 4.1 %.

Note that for the evaluation of dynamic data, the capability of the classically used optimization algorithm of a least-squares fit may be limited. The optimization region may consist of diverse, rather pronounced local minima due to the harder reproduction of dynamic DSG data. Therefore, found/identified values may depend on the given starting values of the optimization procedure. For this reason, the use of a more capable global algorithm (such as genetic algorithms) is recommended, though it is less efficient and in most cases requiring more computational effort. Nevertheless, with the use of a genetic algorithm the implemented parameter identification procedure for DSG succeeds reliably, which represents the basic step for enabling performance evaluation for direct steam generating collectors.

The given example additionally reveals the valuable benefit of a dynamic evaluation procedure. With a more flexible use of measurement data, the time intervals of the measurement data can be extended so that more dispersion of the tested properties is available. In this way, a more distinct and detailed performance identification of the tested collector is feasible. Because enough information is contained in the larger data basis, less correlated and more precise optical and thermal properties can be identified. Altogether, the results proof the proposed extended dynamic testing method to be a meaningful and worthwhile procedure for DSG evaluations. An important basis is accordingly set for the steam evaluation under more flexible dynamic operating conditions, which was not available so far. The comprehensive procedure of performance evaluation and its practicability are proven and presented in Chapter 8. The following chapters will introduce diverse aspects of performance testing and data evaluation in order to enable and complete this comprehensive procedure.

Chapter 5

Statistical Methods to Assess the Identification Quality

Performance testing requires the availability of a suitable evaluation procedure in order to determine the performance parameters of a collector, which is the main focus of this thesis. An equally important element for meaningful performance testing represents the quality assessment of the determined parameters with respect to the uncertainty bands of the test results. It facilitates statements concerning how precise (with how much dispersion) and how accurate (with how much bias) the performance parameters are determined. This dispersion is caused by several uncertainty factors, such as sensor measurement uncertainty, parameter covariance, mirror soiling, tracking inaccuracies, mirror torsion, and so forth. These performance uncertainty effects cannot be prevented in collector tests, but need to be considered while reporting meaningful test results. For this reason, derived performance parameters of a thermal test campaign never comprise only one individual absolute value. They rather (and more appropriately) need to be described by an absolute value including a probability distribution instead. These uncertainty bands are commonly reported by means of confidence intervals, which allow to evaluate how much confidence to place in the performance results of the collector testing. Although several tools for parameter estimation are available (such as in our case, the software package Dakota), less attention has been paid to the proper construction of confidence intervals [Dogan, 2007, p. 415]. In common thermal collector tests, confidence calculations are seldomly addressed. If applied at all, mostly standardly implemented (mainly linear) confidence interval computations are used [see, e.g., ISO 9806, 2013, pp. 113–114]. Violations of standard assumptions make the generation of confidence intervals a similarly difficult task as identifying the best-fit parameters itself [Dogan, 2007, p. 415]. Due to the limited capacities of standard statistical inference methods, they may not be suited for every test situation. Therefore, the following chapter is dedicated to the construction of confidence intervals by implementing and comparing standard procedures to more advanced methods of statistical inference. Detailed theory, applied methods, and their specific implementation of confidence computations were published in Zirkel-Hofer et al. [2018]. Wide parts of the following chapter correspond to this publication in a slightly modified way.

■ 5.1 Basic Concept of Confidence Levels

For the computation of confidence intervals, the simulation software ColSim is denoted as the model function $f(X,\theta)$ and treated as a black box. The inputs of the model function consist of the measurement data matrix X (with entries like the inlet mass flow rate, inlet temperature, DNI, etc.) and the parameter vector θ (representing the performance parameters as $\eta_{opt,0}$, u_0, u_1, etc.)[1]. The output consists, for example, of the collector outlet temperature denoted by $y_{sim}(\theta)$. The objective of the parameter identification procedure is to fit measurement data to simulation data by minimizing the residual function of n data points

$$S(\theta) = \sqrt{\frac{1}{n}\sum_{i=1}^{n}\left(y_{meas,i} - y_{sim,i}\right)^2}, \tag{5.1}$$

where $\widehat{\theta} = \arg\min S(\theta)$ represents the best-fit estimate.

Due to associated measurement uncertainties, the measuring and gathering of data is considered a random process within the error intervals of the installed instrumentation. Because measurement data is used to generate the simulation output of ColSim, it represents a random variable as well. From the simulated and measured collector outlet variables the identification results are derived by the parameter identification procedure. Therefore, the eventual identification results—that is, the best-fit parameter vector $\widehat{\theta}$—is a (vector valued) random variable with a certain probability distribution. For the construction of confidence intervals, it is important to know how the parameter vector is distributed (e.g., normally or uniformly), what variance (standard deviation) it has, and how the best-fit estimate $\widehat{\theta}$ differs from the real parameter θ in terms of bias.

For the best-fit parameter vector of the present dynamic parameter identification procedure, none of the above information concerning the probability distributions is available. Standard approaches are based on assuming approximately linear model functions as well as normally and independently distributed error terms, enabling an approximation of the confidence intervals. Nevertheless, if assumptions are violated, approximate confidence intervals can become "essentially meaningless" [Donaldson and Schnabel, 1987, p. 80]. For this reason, several approaches have been implemented for the dynamic performance evaluation procedure to show the capabilities, differences, and deficits of the corresponding methods.

■ 5.1.1 Linearization Methods

Linearization methods represent the standardly used and predominantly implemented methods in existing software packages. The optimization software Dakota features confidence interval computation based on linearization methods [Adams et al., 2016, p. 142]. These methods assume that the error terms are normally as well as identically and independently distributed (iid)[2]. Moreover, they are based on the assumption of an approxi-

[1] Note that the parameter vector is defined intentionally with the variable θ as commonly used in stochastics. Equally, θ is commonly referred to the solar incidence angle within the area of solar technology. Be aware of this double definition to avoid confusion. In the field of confidence intervals computation, θ is always used as the parameter vector.

[2] For further explanation, refer to Section 5.1.3.

mately linear model function $f(X,\theta)$, that is,

$$f(X,\theta) \approx X^T \theta. \tag{5.2}$$

A 100(1-α) %-confidence interval for the parameter θ_j is computed by using the estimated variance–covariance matrix $\widehat{C}$ with its (j,j)-th element $\widehat{C}_{jj}$ [Donaldson and Schnabel, 1987, p. 70]:

$$\widehat{\theta_j} - \sqrt{\widehat{C}_{jj}} \cdot t_{n-p}^{1-\alpha/2} \quad \leq \quad \theta_j \quad \leq \quad \widehat{\theta_j} + \sqrt{\widehat{C}_{jj}} \cdot t_{n-p}^{1-\alpha/2}, \tag{5.3}$$

where $t_{n-p}^{1-\alpha/2}$ is the $(1-\alpha/2)$-percentile of the t-distribution with $n-p$ degrees of freedom. n represents the number of data points and p the number of parameters. The variance–covariance matrix can be approximated by different approaches using Jacobian or Hessian matrices. By comparing different approximations, Donaldson and Schnabel [1987, p. 80] recommend the use of the simplest approximation by the Jacobian with

$$\widehat{C} = \left(\frac{S(\widehat{\theta})}{n-p}\right)^2 \cdot \left(J(\widehat{\theta})^T J(\widehat{\theta})\right)^{-1}, \tag{5.4}$$

where $S(\widehat{\theta})$ is calculated according to Equation (5.1). For linear model functions, the variance–covariance matrix can be analytically calculated by means of the Jacobian matrix J of the linear model function, being $J = X$. With non-linear model functions, however, the Jacobian (or Hessian) matrix has to be approximated numerically. For more information concerning the detailed mathematical calculation, see Donaldson and Schnabel [1987, pp. 67–71].

Due to their approximation, linearization methods are simple procedures, which require little computational complexity and effort. However, they are only able to generate reliable confidence intervals if the model function can be reasonably approximated by a linear relation. Therefore, linearization methods may not always be the adequate method to use [Adams et al., 2016, p. 142], as in highly non-linear cases they generate error-prone (mostly unrealistically narrow) and hence meaningless confidence intervals [Donaldson and Schnabel, 1987, p. 80].

■ 5.1.2 Alternative, Non-Linear Methods

Alternative methods are available particularly suited for non-linear model functions, such as the likelihood ratio method or the lack-of-fit method. For the detailed approach and mathematical implementation of these methods, refer to Donaldson and Schnabel [1987, pp. 71–72].[3] Both methods are capable of providing reliable confidence regions for non-linear models, especially in comparison to the linearization methods [Donaldson and Schnabel, 1987, p. 80]. Nevertheless, they posses significant computational disadvantages. Confidence intervals may be disjoint and unbounded for non-linear models. Traceable reporting of confidence intervals via these methods can be very difficult, as the information required to reconstruct these values are excessive [Donaldson and Schnabel, 1987, p. 71]. Apart from these difficulties, the methods are computationally very expensive and only useful for a small number of parameter estimates (i.e., around 1–3 performance parameters). This presents the finally decisive aspect for the methods not being suited for

[3] For general detailed reference of non-linear regression and their statistical inference, see Seber and Wild [2005, Chp. 5] and Bates and Watts [2007].

the purposes within the present thesis. Moreover, they still assume the error terms to be normally, identically, and independently distributed, which cannot be guaranteed for the identified parameter vector generated by the dynamic parameter identification procedure.

■ 5.1.3 Bootstrapping BS

General Procedure

The method of Bootstrapping (BS) represents a powerful approach to overcome the restrictions of the standardly used methods presented above. It is considered a resampling technique, originally introduced by Efron [1979]. Since then, it has been consistently gaining popularity, especially in the area of theoretical and empirical economics [Li and Maddala, 1996, p. 116] and with computational capabilities becoming faster and cheaper [Dogan, 2007, p. 416]. An extensive overview and details concerning different approaches of bootstrapping are given in Li and Maddala [1996].

The main objective of confidence interval computation lies in the generation of a probability distribution for the identified parameter vector $\widehat{\theta}$. The basic idea behind bootstrapping consists of the following: if an infinite amount of measurement data were available, numerous, independent, and non-overlapping datasets of equal size and informative content could be selected. By performing dynamic parameter identifications of these datasets, the distribution of $\widehat{\theta}$ could therefore be simulated as sketched in Figure 5.1. With the thereby generated empirical histogram of $\widehat{\theta}$, confidence intervals of the identified performance parameters can be derived.

Infinite data are never available in reality, though, they could be approximated by a very large data basis. This is the concept behind the Random Sub-Sampling (RSS) approach introduced hereafter. However, the requirement of a large data basis is not desired nor feasible in practicable collector testing, since it exceedingly increases measurement time and effort. For this reason, the challenge of bootstrapping lies in generating artificial datasets (so-called 'bootstrap replicates'), which adequately represent the original measurement data. The (more or less correct) way of creating the bootstrap replicates—the so-called data generating process—represents the only assumption underlying the bootstrapping method. Apart from that, the error terms do not have to fulfill certain criteria (such as linear model, iid error terms, small number of parameters) in contrast to the above introduced methods of Section 5.1.1 and Section 5.1.2. On this account, bootstrapping is particularly beneficial for non-linear models and can be generally applied to diverse confidence interval problems [Dogan, 2004, p. 4].

Specific Data Generating Process

Since the capability and quality of bootstrapping highly depends on the data generating process, several approaches exist addressing the particularities of each confidence interval problem. Two main classes of resampling[4] are available for bootstrapping: the direct approach and the residual-based bootstrapping. The direct approach uses the data itself, that is, for example, in our case the outlet temperature T_{out}. The residual-based bootstrapping uses the error terms (residuals) of the parameter identification procedure, that

[4] Resampling is understood as taking the very same amount of measurement data, but sampling it in a different way by changing order and/or value by a defined procedure including random components.

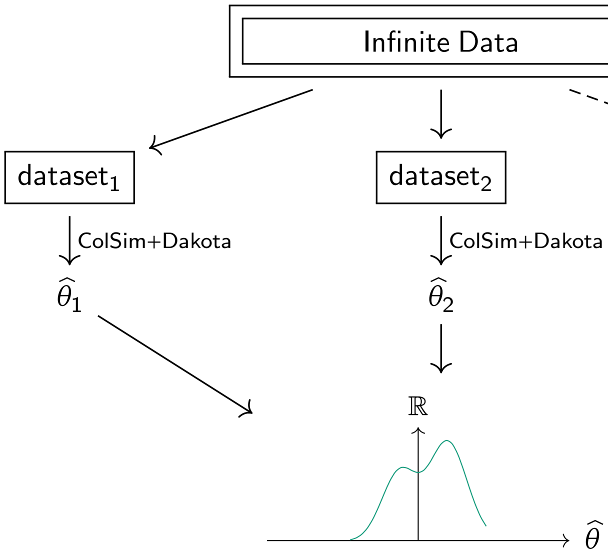

Figure 5.1: Sketch of the basic idea behind bootstrapping. By performing R identification procedures of different, independent datasets with equal informative data content, the probability distribution of the parameter vector $\widehat{\theta}$ could be approximated. [adapted from Zirkel-Hofer et al., 2018]

is, the difference of simulated versus measured objective variable, such as $T_{meas}-T_{sim}$. Direct bootstrapping methods are not suited for dynamic time-series models like the present dynamic testing procedure. The reason for this is that the resampling of the actual data—the single outlet temperature values—destroys the dynamic time-series pattern of the thermal process [Dogan, 2004, p. 4]. This time dependency in terms of the collector inertia is considered essential in dynamic evaluations to accurately reproduce dynamics of the system. Consequently, to maintain the information contained in time series, residual-based bootstrapping is chosen for the confidence interval creation [Li and Maddala, 1996, p. 127]. In this way, the remaining residuals obtained from a first parameter identification procedure are randomly resampled and added to the original measurement data (e.g., the collector outlet temperature).

Moreover, error terms of dynamic time-series models are often autocorrelated, that is, not independent. In this way, neighboring residuals assume similar values. In thermal collector testing, auto-correlation may arise due to defective tracking, soiling, temperature dependent sensor uncertainties, and many other effects. If this structure of serial correlation is not properly considered, residual-based methods can give inconsistent confidence intervals [Li and Maddala, 1996, p. 136]. A remedy is found by sampling the residuals randomly in continuous blocks of certain block length b, called the moving-block bootstrap [Kunsch, 1989]. This is the approach pursued and implemented for the confidence interval construction of the present dynamic parameter identification procedure. The specific implementation of the BS procedure will be particularly described in Section 5.2.1.

To resume, for the confidence interval generation the moving-block residual-based bootstrap was chosen based on the following aspects:

Non-linear model

With the dynamic parameter identification procedure being highly non-linear, no analytical nor linearity-approximating method is available.

Unknown parameter distribution

The probability distribution of the parameter vector is unknown, not justifying the strong assumption of a normal error distribution.

Auto-correlation of residuals

Due to the dynamic time-series model of the parameter identification procedure, auto-correlation of the residuals cannot be excluded. Consequently, the assumption of independently distributed error terms is not justified. Moreover, identically distributed error terms are little probable, because measurement uncertainties depend on the operating conditions (e.g., the measurement data input X) rather leading to unequally distributed errors.

Large parameter vector

The complexity of confidence interval construction increases with the number of performance parameters. In excessive cases (as for the angle-stepwise identification of IAM values), the number of identification parameters may rise up to around 40–80 independent variables, impeding reliable confidence interval calculation by customary methods.

Based on these criteria, bootstrapping represents a worthwhile method for confidence interval computation. For the specific computing of confidence intervals, different methods are available. They are based on the empirical histogram generated by the bootstrap. These methods are detailedly discussed in Davison and Hinkley [1997, Chp. 5]. For the present bootstrapping approach, the basic percentile method is chosen[5] based on [Davison and Hinkley, 1997, pp. 202–203]:

$$\widehat{\theta}^*_{\alpha/2} \quad \leq \quad \theta_j \quad \leq \quad \widehat{\theta}^*_{1-\alpha/2}, \tag{5.5}$$

where $\widehat{\theta}^*$ is the distribution of the identified parameter vector obtained from the bootstrap replicates. $\widehat{\theta}^*_{\alpha/2}$ and $\widehat{\theta}^*_{1-\alpha/2}$, respectively, represent the corresponding parameter values at the upper $(1-\alpha/2)$- and lower $(\alpha/2)$-bounds of the empirical histogram.

Certainly, the validity of bootstrapping results strongly depends on the adequacy of the bootstrapping procedure specifically selected for our purposes. Therefore, identification results have to be assessed cautiously. Confidence intervals for highly complex problems as in the present case, will never give perfectly correct results. They rather serve as indicative values with, however, a significantly higher informative value than confidence intervals generated by the standardly used linearization methods. To increase the reliability of the bootstrapping confidence intervals, they are compared to results obtained by an additional procedure of random sub-sampling, which will be explained in the following.

[5] as it can also be applied to confidence interval computation of the below introduced random subsampling approach and therefore guarantees a direct comparison of both

5.1.4 Random Sub-Sampling RSS

The Random Sub-Sampling (RSS) procedure consists of a self-designed approach originally proposed by Perry [2016]. It is designed to specifically address the weak point of the previously introduced bootstrapping approach, the data generating process of the bootstrap replicates. The main objective of the RSS method is therefore to verify the adequacy of the chosen residual-based moving-block procedure in order to obtain realistic confidence intervals.

Its basic approach is based on using real measurement datasets instead of artificially created datasets for the generation of parameter histograms and confidence intervals. By evaluating different measurement datasets of equal size and informative content, the main idea behind bootstrapping—as sketched in Figure 5.1—is directly realized. This means in our case that R datasets of the size of n measurement days are randomly assembled and evaluated by the dynamic parameter identification procedure. Note that overlapping of the entries is allowed, that is, one measurement day can appear in different datasets. Thereby, the histogram of Figure 5.1 consists of performance parameter vectors derived from real measurement data, representing the real dispersion of evaluated performance parameters. Consequently, the artificial data generating process of the bootstrapping method can be validated to the RSS data generation process, exclusively based on real measurement data. Calculated confidence intervals from the RSS histogram are analog to the ones of the bootstrapping approach in Equation (5.5), allowing a direct comparison of both values. Because real measurement data will never be of infinite size, random sub-sampling will create somewhat narrow confidence values. Though, RSS confidence intervals still allow a valuable verification whether the bootstrap confidence intervals are realistic or not.

One major requirement for random sub-sampling represents the availability of test data with a large data basis. Within the work of the present thesis, a vast measurement data basis is available due to the testing of collector `LFC_w2`. Certainly, large measurement data bases are not standardly available in the frame of common collector testing. For this reason, random sub-sampling is not proposed to be a standard procedure to compute confidence intervals in dynamic performance evaluations. Nevertheless, it is considered a beneficial method to verify bootstrapping results on the one hand. On the other hand, it is furthermore used to derive an appropriate testing strategy to obtain representative performance parameters with little dispersion. Random sub-sampling allows to analyze what information needs to be contained in the datasets to assure small confidence intervals. The results of this thorough analysis will be presented in Section 7.2.

5.2 Implemented Bootstrapping Approach

5.2.1 Adapted Procedure for the DT Method

The moving-block residual-based bootstrap method implemented for the dynamic performance evaluation procedure is analog to the approach of Kunsch [1989]. The procedure is based on creating and eventually evaluating R number of bootstrap replicates in order to generate a parameter distribution and their confidence intervals. The bootstrap replicates are created by randomly choosing blocks of length b of the residual vector obtained from an initial parameter identification procedure. Subsequently, the block of

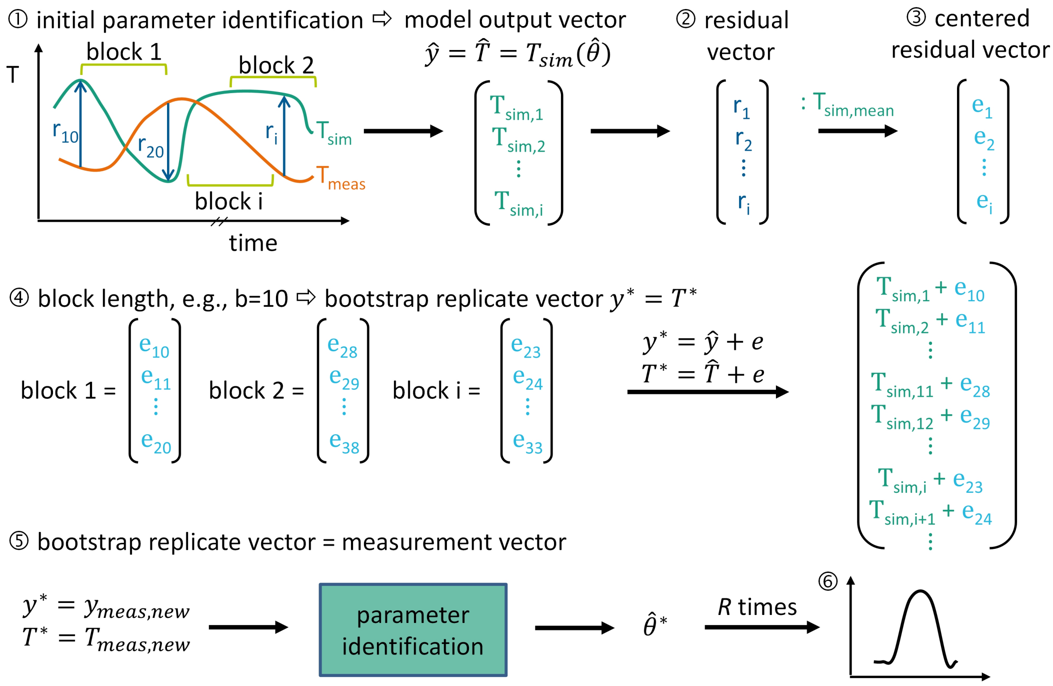

Figure 5.2: Sketch of implemented BS procedure. Sequential illustration of the main steps performed in the implemented bootstrapping procedure in order to generate a probability distribution of the initially identified best-fit parameter vector $\hat{\theta}$.

residuals are applied one after another to the original objective variable of the dataset. For incompressible media, this is the outlet temperature T_{out}, whereas for DSG, this is the specific outlet enthalpy h_{out} in case of steady-state or the outlet flow enthalpy $\dot{H}_{out}$ in case of dynamic conditions. This procedure is schematically illustrated in Figure 5.2. Additionally, the detailed procedure is outlined in the following for an exemplary dataset X with the measured output quantity $y_{meas,i}$ according to Zirkel-Hofer et al. [2018]:

① Initially, a first parameter identification of the dataset is performed yielding the estimate parameter vector $\hat{\theta}$, for which the confidence intervals are wanted. The initial parameter identification additionally provides the simulated model outputs $y_{sim,i}(\hat{\theta}) = \hat{y}_i$.

② The residuals $r_i = y_{meas,i} - \hat{y}_i$ are computed.

③ The residuals need to be centered by subtracting their mean value $e_i = r_i - \bar{r}$.

④ Bootstrap replicates y_i^* are generated by adding randomly chosen blocks of the residuals to the model outputs:

$$y_i^* = \hat{y}_i + e_i \tag{5.6}$$

⑤ The parameter identification procedure is performed for every bootstrap replicate by considering it as the new measured output quantity $y_{meas,i}$. Thereby, R different estimates of θ are obtained.

6 Empirical histograms of the estimated bootstrap parameter vectors $\widehat{\theta}^*$ are generated.

7 Confidence intervals are computed according to Equation (5.5).

8 Apart from the histograms and confidence interval computation, numerous statistics and plots are automatically produced to be able to evaluate the effect of parameter covariance and correlations of the estimates to other characteristics.

Certainly, the block length b is one parameter significantly influencing the results of the confidence intervals. For this reason, a study concerning the adequate block length was performed as presented in the following section. Though, in our present case, the block length is not considered as dominant as in other studies, because it is restricted to certain boundaries by nature. A block length of $b = 1$ represents the lower bound, implying that every data point would be independent to each other. That is, auto-correlation of the residuals would be completely ruled out—a rather unrealistic scenario. The maximum block length is represented by the minimum of data points available for one entire measurement day. Auto-correlation over more than one measurement day is not considered meaningful.

Another degree of freedom lies in the number of replicates R used to generate the bootstrapping histogram. For complex and therefore computational- and time-expensive procedures as the present dynamic parameter identification procedure, the decision of the adequate number of replicate R will always be a trade-off between accuracy and computational effort. Davison and Hinkley [1997, p. 202] advise the use of $R \geq 1000$ for confidence levels of 0.95 or 0.99, if "practically feasible". Performing 1000 parameter identification procedures may be possible for a reduced system. In this case, the number of measurement days is smaller than 10 and only the optical efficiency at normal incidence and heat loss parameters are to be determined, whereas IAM values are kept constant. For a comprehensive collector characterization including IAM values, $R \geq 1000$ is not considered practical. Therefore, the influence of R smaller than 1000 is analyzed within the subsequent section.

■ 5.2.2 Application to Measurement Data

To verify the implementation and to validate the suitability of the approach, bootstrapping was performed based on the measurement data of collector `LFC_w2`. The measurement campaign at this collector provided a large measurement data basis which is required for the validation to RSS. Moreover, it is desired to test the bootstrapping capability based on data of an LFC, because this collector type (with its specific optical characteristics) represents a significantly more complex system to evaluate than PTC. If the suitability of the introduced approach is valid for meaningful evaluations of LFCs, it will be equally possible to reliably apply it to PTCs.

Capability of BS with Reduced Model

To stepwise test the capability of the implemented bootstrapping approach, a first study was designed consisting of a reduced identification model with the three performance

Table 5.1: Summarized results and their statistical inference for reduced identification model. Statistical assessment of optical and thermal identification results based on bootstrapping, standard linearization method, and random sub-sampling for reduced identification model ($\eta_{opt,0}$, u_0/u_1).

Variable	Unit	BS	Lin. method	RSS
$\eta_{opt,0}$	%	69.31	69.52	69.49
$\sigma(\eta_{opt,0})$	%-pts.	0.56	–	0.57
$CI(\eta_{opt,0})$	%-pts.	$-0.95/+1.18$	$-0.12/+0.13$	$-1.06/+1.20$
HL_{100}	W/m	80	66	67
$\sigma(HL_{100})$	W/m	17	–	13
$CI(HL_{100})$	W/m	$-28/+33$	$-15/+15$	$-30/+26$

parameters of $\eta_{opt,0}$, u_0 and u_1. An exemplary and representative combination[6] of measurement days was chosen based on the selection of five days at different temperature levels with an evaluation time step of 15 s and a fixed reference IAM curve in 5 °-angle steps. Table 5.1 summarizes the identification results and statistical inference values for the bootstrapping approach in comparison to a standard linearization method[7] and random sub-sampling. For the bootstrapping, the block length was defined to 300 and the number of replicates fixed to 200, the same as the number of drawings within the sub-sampling procedure. In this way, the confidence interval computation of both approaches is based on a histogram consisting of 200 different values, which allows a direct comparison of both results. The indicated CI-values in Table 5.1 represent the upper and lower values to add/subtract to the identified value to get the boundaries of a 95 %-confidence interval. Experience has shown that it is not meaningful to evaluate individual heat loss coefficients but rather the combination of both[8]. Therefore, the variable HL_{100} is introduced as listed in the results table. It states the heat loss at a defined reference fluid temperature difference, in this case at 100 K. In the following, it represents the variable typical studied while analyzing heat loss within this thesis.

Concerning the absolute value of $\eta_{opt,0}$, all three procedures generate very similar results. However, the confidence intervals are differing largely when comparing the standard linearization method to the newly introduced bootstrap. While the standard method provides a value of $\eta_{opt,0}\pm0.12$ %-pts., bootstrapping computes significantly larger values of approximately $\eta_{opt,0}\pm0.95$–1.18 %-pts. A cross-validation of the bootstrap confidence intervals indicates comparable CI-values obtained from random sub-sampling around $\eta_{opt,0}\pm1.06$–1.20 %-pts. Both $\eta_{opt,0}$-histograms generated by BS and RSS are visualized in Figure 5.3. In all following histogram plots, additionally, the mean value (marked in orange dashed line) and the lower and upper confidence levels (marked in light blue dashed lines) are marked. They reveal a remarkable good agreement of both parameter distributions. Note that the RSS histogram is based on the pure analysis of real measurement data. The only limitation of this method represents the non-infinite measurement data basis potentially leading to more conservative (i.e., too narrow) confi-

[6]The specific measurement days were selected according to the findings of the derived testing strategy, which will be elaborately explained in Chapter 7.

[7]For the exemplary standard linearization method, the method customary implemented in the software package of Dakota was used, consisting of a linear approach using the Jacobian matrix. For more information, see Adams et al. [2016, p. 142].

[8]Further explanation and detailed discussion concerning this topic will be given in Section 7.1.3.

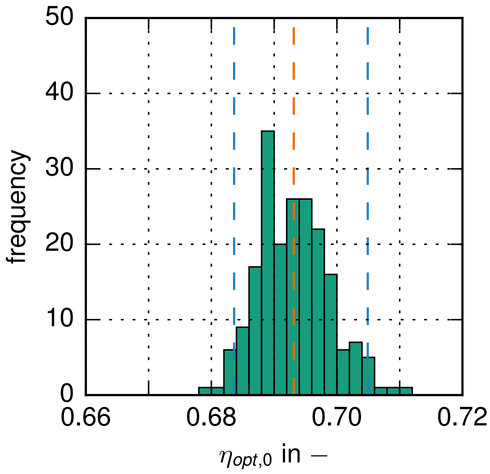

(a) BS histogram of $\eta_{opt,0}$

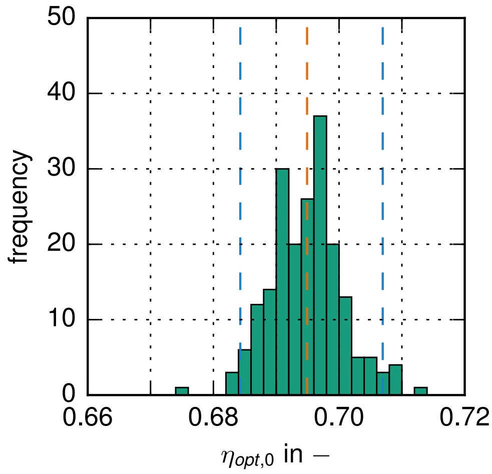

(b) RSS histogram of $\eta_{opt,0}$

Figure 5.3: Comparison of optical efficiency results for reduced identification model. Histogram of identified $\eta_{opt,0}$ based on bootstrapping (a) versus random sub-sampling (b) for reduced identification model ($\eta_{opt,0}$, u_0/u_1) with five measurement days at 15 s time step with 5 °-IAM and 200 replicates/drawings.

dence intervals. The good conformance of both advanced statistical inference procedures, however, gives a first indication that standard methods may not be suited for the present complex case of confidence interval generation in the context of dynamic performance evaluations.

The presented bootstrapping results are based on an exemplary, representative combination of measurement days. They correspond to a drawing from RSS identifying an $\eta_{opt,0}$-value near to its mean, that is, with high occurrence probability. Bootstrapping was also performed based on other initial drawings that were not as representative. These day combinations rather consisted of outliers in the probability distribution, that is, exceptions of lower probability leading to identification results at the far ends of the $\eta_{opt,0}$-histogram. In those—less probable—cases, the bootstrapping histograms do not show such a distinct distribution, but a rather disperse one leading to higher CI-values. For an additional graphical illustration, see Figure D.1 of Appendix D. Nevertheless, even in those exceptional cases the bootstrapping approach generates more realistic confidence intervals than the standard method. Moreover, the provided parameter probability distribution can be used to give potential indications on the representativeness and suitability of the data basis in order to get more consistent results. A more disperse probability (i.e., a less distinct tendency to a normal distribution) indicates a low confidence and potential correlation of the identified performance parameters. In these cases, the data basis may not be adequate enough (i.e., does not contain sufficient information) to provide meaningful results. An appropriate testing strategy in order to reduce a potential dispersion and increase confidence of the results is elaborately derived in Chapter 7.

With regard to the heat loss identification, the generated histograms show less agreement as illustrated in Figure 5.4. All three methods differ more in their absolute HL_{100}-values than for $\eta_{opt,0}$. Also the corresponding histogram of BS and RSS show larger differences (compare with Figure 5.4). The distribution is more pronounced to a normal curve for RSS than for BS heat loss results. Though, the confidence intervals of both meth-

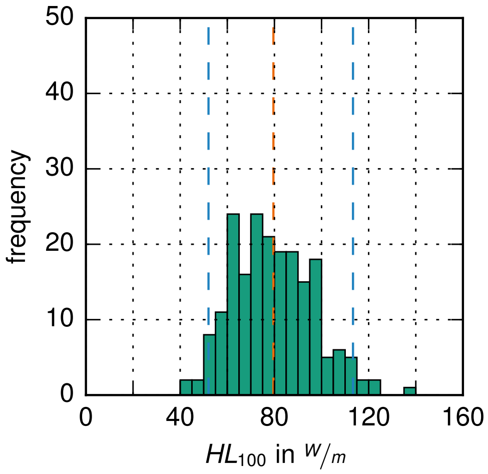

(a) BS histogram of HL_{100}

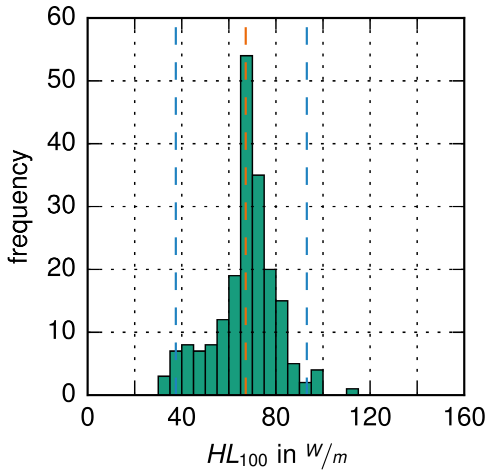

(b) RSS histogram of HL_{100}

Figure 5.4: Comparison of heat loss results for reduced identification model. Histogram of identified HL_{100} based on bootstrapping (a) versus random sub-sampling (b) for reduced identification model ($\eta_{opt,0}$, u_0/u_1) with five measurement days at 15 s time step with 5°-IAM and 200 replicates/drawings.

ods coincide acceptably. The deviations in absolute values may originate from the general difficulty of a distinct determination of the heat loss for such systems as the present studied (i.e., small-scale collector with evacuated glass envelope receiver). More information and detailed discussion concerning this aspect are given within Chapter 7. To this end, these differences do not indicate any deficits of the BS approach but more a deficit in the data selection, which does not present the focus of the current chapter.

Capability of BS with Complete Model

In a second study, the advanced capability of the bootstrapping approach was tested based on the complete identification model with the parameters of $\eta_{opt,0}$, u_0/u_1, and a stepwise IAM identification. Thereby, approximately 30 parameters have to be determined and their confidence intervals to be reliably computed. This was the final decisive reason for implementing bootstrapping, because other non-linear methods are not designed for such a large parameter number. In Table 5.2, aggregated results for the three CI-computation

Table 5.2: Summarized results and their statistical inference for complete identification model. Statistical assessment of optical and thermal identification results based on bootstrapping, standard linearization method, and random sub-sampling with complete identification model ($\eta_{opt,0}$, u_0/u_1, K_T/K_L).

Variable	Unit	BS	Lin. method	RSS
$\eta_{opt,0}$	%	68.55	68.39	68.62
$\sigma(\eta_{opt,0})$	%-pts.	1.28	-	1.34
$CI(\eta_{opt,0})$	%-pts.	$-2.39/+2.49$	$-0.46/+0.46$	$-2.83/+2.50$
HL_{100}	W/m	49	43	69
$\sigma(HL_{100})$	W/m	17	-	17
$CI(HL_{100})$	W/m	$-22/+46$	$-15/+15$	$-30/+32$

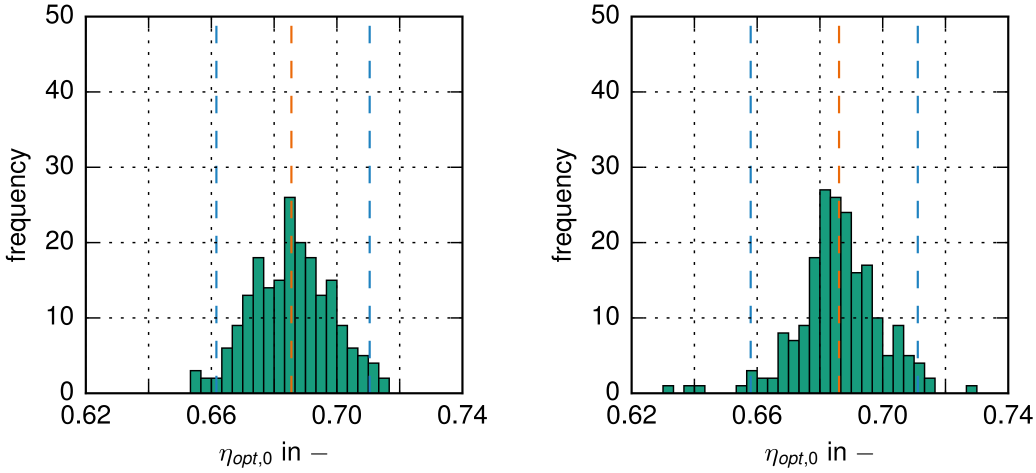

(a) BS histogram of $\eta_{opt,0}$

(b) RSS histogram of $\eta_{opt,0}$

Figure 5.5: Comparison of optical efficiency results for complete identification model. Histogram of identified $\eta_{opt,0}$ based on bootstrapping (a) versus random sub-sampling (b) for complete identification model ($\eta_{opt,0}$, u_0/u_1, K_T/K_L) with five measurement days at 15 s time step with 5 °-IAM identification.

approaches are given. The same tendency as for the reduced model can be found for the $\eta_{opt,0}$-results from the complete model. Absolute values of all three methods are very similar, whereas the CI-values of the standard method differ significantly with very narrow uncertainty bands. Comparing the histograms of $\eta_{opt,0}$, as illustrated in Figure 5.5, reveals comparable parameter distributions obtained by both sampling approaches. Only exceptional outliers of $\eta_{opt,0}$ from RSS are not reproduced by BS, but they are not considered representative. Even though the bootstrap approach generates slightly smaller CI-values than the RSS procedure—which is not entire reasonable since RSS provides slightly narrow values, that is, a minimum error bar—the results of BS are considerably more representative and accurate than the results obtained from the standard method.

Regarding identified heat loss values analog to the previous study, neither a perfectly distinct absolute value nor a normal probability distribution is discernible. For a visualization of the heat loss results, refer to Figure D.2 of Appendix D. The high dispersion of both histograms indicates once again the challenge of a proper heat loss identification.

Within the complete model, IAM values are identified stepwise for the present LFC. In Figure 5.6, scatter plots for every transversal and longitudinal angle step are sketched. This graphical illustration does not visualize the distribution of every identified IAM, but indicates the mean value (marked in orange dots) of every angle step and the dispersion within this angle step (marked in green dots). RSS provides a very sensitive dispersion of the IAM values at different angle steps. However, both methods agree remarkably well, even for specific details as a more pronounced uncertainty band for high transversal angles $K_T(85\,°)$ or lower longitudinal solar angles $K_L(15\,°)$. For a comparison of the actual shape and mean values of the corresponding IAM distribution, exemplary cases for $K_T(50\,°)$ and $K_L(10\,°)$ are appended in Figure D.3 and Figure D.4. Good conformance of the BS and RSS histograms in the mean values and even in the shape of the parameter distribution is discernible.

All in all, with regard to the very complex model of more than 30 parameters, little dispersion of the results generated by bootstrapping and computed by RSS is perceivable.

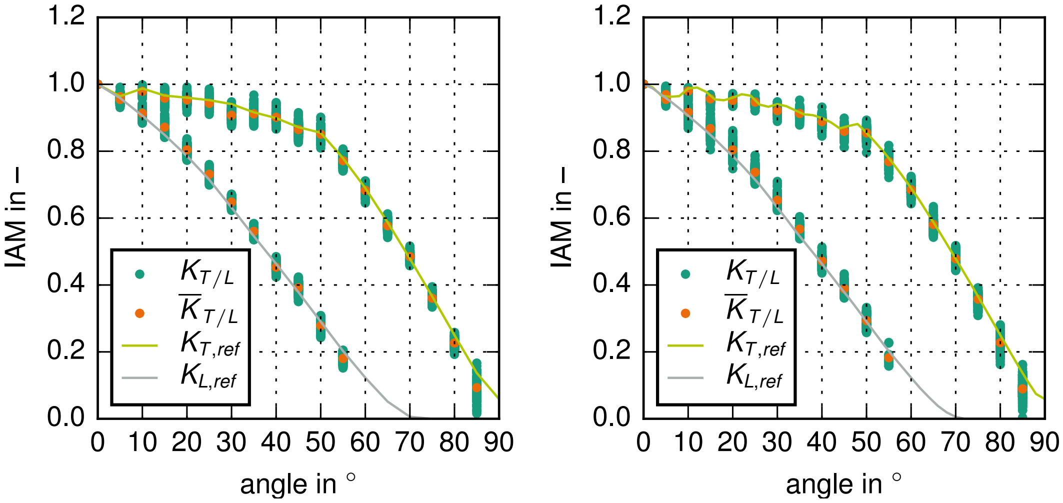

(a) BS scatter plot of IAM

(b) RSS scatter plot of IAM

Figure 5.6: Comparison of IAM results for complete identification model. IAM scatter plot based on bootstrapping (a) versus random sub-sampling (b) for complete identification model ($\eta_{opt,0}$, u_0/u_1, K_T/K_L) with five measurement days at 15 s time step with 5 °-IAM identification.

In this way, BS presents a valuable and worth-while option for an adequate confidence interval calculation, especially in comparison to standard methods. The two degrees of freedom of the bootstrap approach consist of the block length b and the number of replicates R. In the previous studies, both factors have been fixed to reasonable values ($b = 300$, $R = 200$) obtained from past experience with bootstrapping. Nevertheless, the influence of both factors will be presented in the following paragraphs.

Block Length b

The block length is a factor depending on the time step, since it defines the number of serial data points chosen for the generation of residual blocks, as illustrated in Figure 5.2. For the very same bootstrapping procedure as previously performed (the complete model with five measurement days, time step of 15 s and 5 °-IAM determination based on 200 replicates), the block length b was altered between 1, 150 and 300. A block length of 300 represents the smallest, continuous measurement time period available for this data basis. This is the upper bound for the block length. Choosing a larger block length would exclude the residuals of these measurement time periods from the generation of bootstrapping residuals, which is not desired. A block length of one represents the lower extreme of possible block lengths.

Summarized results of the block length study are given in Table 5.3. They reveal a very dominant influence of the block length. Especially in the case of $b = 1$ the results differ largely. Figure 5.7 furthermore depicts the corresponding IAM identification results, which clearly reveal very narrow uncertainty bands computed with a block length equal one (for the scatter plot of $b = 300$ see Figure 5.6(a)). The results indicate the prevailing effect of auto-correlation of the time-series data. In the case of $b = 1$, auto-correlation of the data is not considered. Every obtained residual from the initial parameter optimization procedure is subsequently used individually—and not in serial form as with longer block lengths—in the generation of bootstrap replicates. Thereby, the bootstrap results

Table 5.3: Influence of bootstrap block length on confidence interval computation. Summarized identification and statistical inference results depending on the block length b for five measurement days at 15 s time step with 5°-IAM identification.

Variable	Unit	Block length 1	Block length 150	Block length 300
$\eta_{opt,0}$	%	68.37	68.41	68.55
$\sigma(\eta_{opt,0})$	%-pts.	0.21	1.19	1.28
$CI(\eta_{opt,0})$	%-pts.	$^{-0.39}/_{+0.38}$	$^{-2.71}/_{+2.38}$	$^{-2.39}/_{+2.49}$
HL_{100}	$^{W}/_{m}$	44	48	49
$\sigma(HL_{100})$	$^{W}/_{m}$	3	14	17
$CI(HL_{100})$	$^{W}/_{m}$	$^{-6}/_{+6}$	$^{-19}/_{+35}$	$^{-22}/_{+46}$

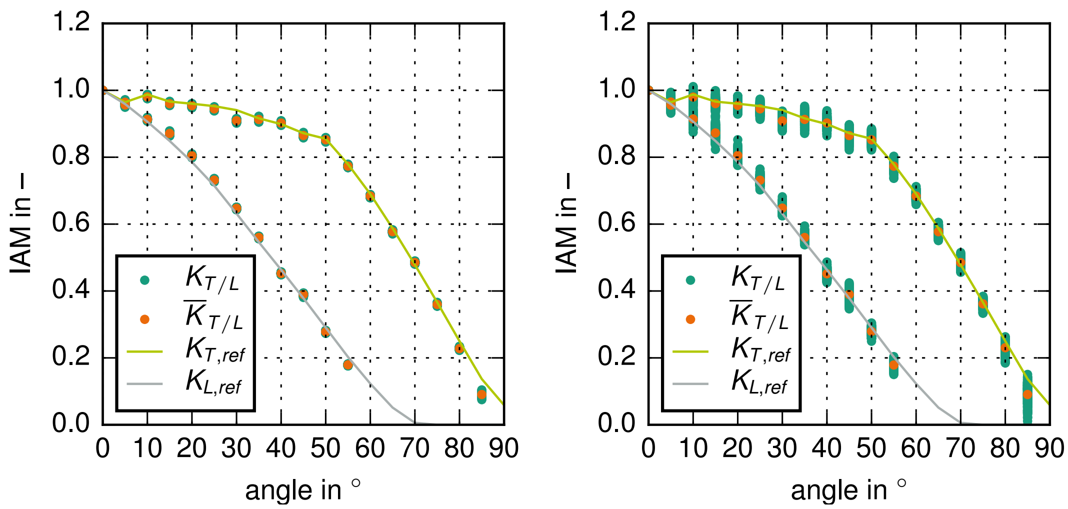

(a) IAM scatter plot with $b = 1$ (b) IAM scatter plot with $b = 150$

Figure 5.7: IAM bootstrapping results at different block lengths. IAM scatter plot based on bootstrapping with block length $b = 1$ (a) and $b = 150$ (b) for five measurement days at 15 s time step with 5°-IAM identification.

resemble the results of standard linearization methods. Since standard methods equally do not consider auto-correlation of the data basis, they provide similar narrow confidence intervals as a block length $b = 1$. In comparison to the actual confidence intervals obtained from RSS, they are clearly not representative for this measurement data basis. If auto-correlation of the time-series data is considered, confidence levels computed by bootstrapping show significantly more realistic values. Additionally, they more appropriately reflect the influence and error propagation of measurement uncertainties than standard confidence methods[9]. The difference between block length of 150 to 300 is not as noticeable as the difference to a block length equal one. This shows that the consideration of this effect of auto-correlation is very important for an adequate confidence interval computation. Causes for auto-correlation may originate, for instance, from defective tracking, soiling, wind inducing torsion of the mirrors and many other uncertainty sources that may effect the performance of the collector, but cannot be explicitly simulated. Because a block length $b = 300$ implies the least deviations to the corresponding RSS results, this value

[9]Compare to results of Chapter 6.

was chosen as an adequate reference value. If confidence intervals were based on other block lengths, they would show slightly differing results. In comparison to the standard methods, however, BS confidence intervals will clearly outperform them in any chosen block length case considering auto-correlation of the data (i.e., $b \gg 1$).

Number of Bootstrap Replicates R

The previous studies were based on 200 bootstrap replicates. It represents the maximum of bootstrap replicates feasible to evaluate within a reasonable computational time with common computation equipment. However, in literature a recommendation of $R = 1000$ is given in the case of being practically feasible [Davison and Hinkley, 1997, p. 202]. For this reason, an exemplary comparison of BS results for the reduced model was performed based on 200 and 1000 replicates. The results are summarized in Table 5.4, corresponding histograms of $\eta_{opt,0}$ depicted in Figure 5.8. Even if the bootstrapping approach is based on a significantly larger number of replicates, nor the absolute results neither the confidence intervals change substantially. Certainly, the histograms based on $R = 1000$ show larger frequency values, as they consist of more individual results. However, the

Table 5.4: Influence of number of replicates on confidence interval computation. Summarized identification and statistical inference results based on 200 versus 1000 replicates for five measurement days at 15 s time step and 5 °-IAM.

Variable	Unit	$R = 200$	$R = 1000$
$\eta_{opt,0}$	%	69.31	69.40
$\sigma(\eta_{opt,0})$	%-pts.	0.56	0.52
$CI(\eta_{opt,0})$	%-pts.	$^{-0.95}/_{+1.18}$	$^{-1.03}/_{+0.99}$
HL_{100}	$^{W}/_{m}$	80	82
$\sigma(HL_{100})$	$^{W}/_{m}$	17	17
$CI(HL_{100})$	$^{W}/_{m}$	$^{-28}/_{+33}$	$^{-31}/_{+37}$

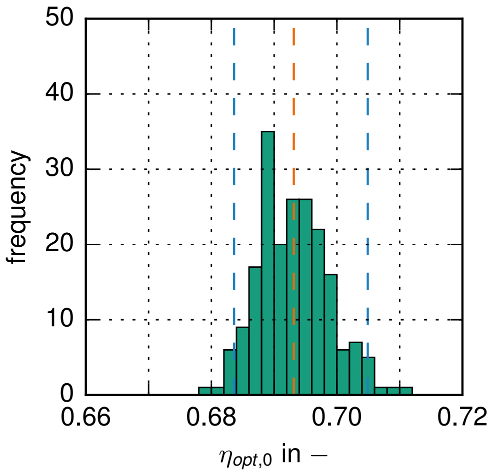

(a) $\eta_{opt,0}$-histogram with $R = 200$

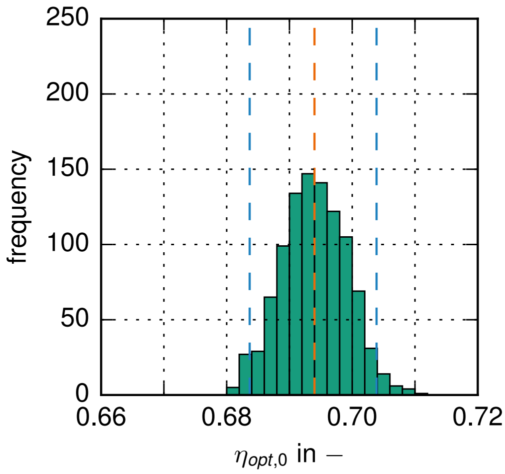

(b) $\eta_{opt,0}$-histogram with $R = 1000$

Figure 5.8: Bootstrapping results of optical efficiency based on different numbers of bootstrap replicates. $\eta_{opt,0}$-histogram based on $R = 200$ (a) and $R = 1000$ (b) bootstrap replicates for five measurement days at 15 s time step with 5 °-IAM.

shape and distribution of the identification results does not change noticeable (compare with Figure 5.8). Thereby, bootstrapping based on a considerably smaller computational effort of $R = 200$ is providing comparable results to those of $R = 1000$. Because the number of replicates equal 1000 implies an excessive computational cost, it is not considered manageable, reasonable nor necessary. The results reveal that BS based on the reduced number of replicates is equally suitable for providing representative results in the present application of confidence interval computation for dynamic performance evaluations.

Conclusion on BS Approach

In the previous sections, the bootstrap method was introduced, implemented, its capabilities demonstrated, and the results verified to real data obtained by random sub-sampling of a large measurement data basis. The validation of BS to RSS demonstrated comparable capabilities of bootstrapping, even if for this procedure significantly less measurement data and informative content is required. Results proved the bootstrapping approach to be a powerful tool, generating considerably more representative and therefore reliable confidence intervals than the customary methods. In this way, bootstrapping represents a valuable means of statistical inference—an aspect until now not yet thoroughly studied nor commonly available in thermal collector testing. It is considered a key feature of the enhanced dynamic evaluation method of this thesis, since it may provide improved information concerning parameter distribution, uncertainty bands, covariance, and hence the validity of identified performance parameters.

Chapter 6

Measurement Instrumentation

Measurement instrumentation and its uncertainties considerably influence recorded measurement data and thereby the identified performance parameters of a test collector. For this reason, a profound study concerning the influence of measurement instrumentation and uncertainties was performed. Details of this broad uncertainty study were published within Zirkel-Hofer et al. [2016]. Wide parts of the following chapter correspond to this publication in a restructured, summarized, or slightly modified way.

The quality of installed measurement equipment greatly influences the reliability and therefore the representativeness of the test results. For this reason, details on the measurement instrumentation recommended for the testing of low-temperature solar collectors are already given in the testing standard ISO 9806 [2013]. Due to the larger dimensions of concentrating collectors and thus different working temperatures and mass flow rates, these recommendations cannot be directly applied for the testing of concentrating solar collectors. A comprehensive literature review on uncertainty analysis for solar collector testing compiled in Zirkel-Hofer et al. [2016, pp. 300–301] revealed that this aspect has been sparsely addressed until now. Only in Janotte [2012], an elaborate uncertainty study is included particularly focusing on PTCs installed in large solar fields operating with thermal oil. However, adequate measurement instrumentation and its associated uncertainties are considered a crucial aspect to increase the reliability of performance tests. Uncertainty values are required to assess acceptable fit qualities of the parameter identification procedure. Moreover, uncertainty examinations are particularly relevant for in situ tests, in which the choice of measurement instrumentation has to be adapted to the specific measurement situation on-site.

For larger systems as concentrating collectors, in general two major measurement concepts can be applied, comprising intrusive or clamp-on measurement instrumentation. For a detailed discussion and characteristics concerning different measurement approaches, refer to Janotte and Zirkel-Hofer [2018]. Clamp-on instrumentation provides the advantage of reduced leakage risk and inference with the regular system operation, because intrusion to the hydraulic circuit is not necessary for the proper sensor installation. However, clamp-on sensors are usually less precise and accurate if they are not specifically calibrated to determined measurement conditions (such as fluid temperatures, mass flow rates, HTFs, and geometrical properties as piping diameter and wall thickness). Moreover, a proper calibration of sensors may be very challenging and time-consuming. In contrast, intrusive measurement sensors can be flexibly and easily adapted to the measurement conditions on-site in order to obtain high accuracy and precision measurement data. Yet for the sensor installation, the hydraulic circuit has to be intruded, interrupting regular operation and increasing leakage risk. Another option represents the use of already built-in sensors, mainly installed for operation and control purposes of the facility. However, independent data recording can hardly be assured, which is crucial for impartial certification procedures. Moreover, build-in sensor mostly imply higher measurement uncertainties. External sensor installation is accordingly advised for independent collector testing. A good selection of measurement instrumentation will therefore always be a trade-off between feasibility, cost of the instrumentation, and its associated uncertainties. In order to facilitate a simple, fast, and meaningful selection of measurement equipment, a comprehensive uncertainty study is presented in the following.

6.1 Measurement Uncertainty

The approach of calculating measurement uncertainty is based on the "Guide to the Expression of Uncertainty in Measurement" GUM [JCGM, 2008]. Because GUM represents an abstract instruction to uncertainty calculations, adaptations to the specific measurement situation need to be applied. For the derivation of the detailed methodology pursued within the present thesis, refer to Zirkel-Hofer et al. [2016, pp. 301–303]. In this publication, the basics of uncertainty calculations are introduced and applied to line-concentrating solar collectors.

6.1.1 Uncertainty Calculation for Line-Concentrating Solar Collectors

In the context of performance testing, the parameter of interest mainly represents the collector power output $\dot{Q}$. This quantity is not measured directly, but actually calculated with the help of several input measurands via the previously introduced formula:

$$\dot{Q} = \dot{m}_{in} \cdot c_p \cdot (T_{out} - T_{in}) = \dot{m}_{in} \cdot c_p \cdot \Delta T. \tag{6.1}$$

In the case of steam generating collectors in recirculation mode, the formula has to be adapted according to:

$$\dot{Q}_{DSG} = \dot{m}_{steam} \cdot h_{evap}(p_{SD}) + \dot{m}_{in} \cdot c_p \cdot (T_{sat}(p_{SD}) - T_{in}), \tag{6.2}$$

with $\dot{m}_{steam}$ being the steam mass flow exiting the steam drum, h_{evap} being the evaporation enthalpy at the steam drum pressure p_{SD}, and T_{sat} the corresponding saturation temperature. Similarly, uncertainty values can be studied for the thermal collector efficiency η or, in case of DSG, the collector outlet flow enthalpy $\dot{H}_{out}$. Explanations and specific equations concerning those variables can be found in Section E.1 of Appendix E.

Note that the calculated quantities have to be understood as instantaneous values of power at exemplary, pre-defined, and steady conditions. The following uncertainty calculations therefore reflect the pure effect of measurement uncertainties. In contrast, resulting uncertainties of the global performance evaluation procedure including uncertainties of simulation, measurement, and regression fit of a complete set of measurement data were previously studied in Chapter 5.

Standard Uncertainty

Every measurand contributing to the power output $\dot{Q}$ is associated with diverse uncertainty factors. To determine the standard uncertainty of a measurand, every uncertainty effect is added up, irrespective of whether it is estimated or extracted from a technical data sheet. Uncertainty effects contributing to a standard uncertainty of a measurand may be the sensor uncertainty itself and additional uncertainties associated with the entire measurement chain, such as data logging, display accuracy, long-term stability, non-linearity, temperature dependencies, and so forth. Sensor standard uncertainty with its different contributing effects for the evaluated test collectors within the present thesis are listed in Section B.2.

Combined Uncertainty

In general, for a given quantity of interest $Y = f(X_1, \ldots, X_n)$ that is a function of the measurands $X_1, \ldots, X_n$, the standard combined uncertainty $u_c(Y)$ is calculated via the Gaussian error propagation law[1]:

$$u_c^2(Y) = \sum_{i=1}^{n} \left(\frac{\partial Y}{\partial X_i} \right)^2 \cdot u^2(X_i). \tag{6.3}$$

This value represents the standard deviation of the distribution of Y. Directly applying the Gaussian law to Equation (6.1) yields the combined uncertainty

$$u_c^2(\dot{Q}) = \left(\frac{\partial \dot{Q}}{\partial \dot{m}} \right)^2 \cdot u^2(\dot{m}) + \left(\frac{\partial \dot{Q}}{\partial c_p} \right)^2 \cdot u^2(c_p) + \left(\frac{\partial \dot{Q}}{\partial \Delta T} \right)^2 \cdot u^2(\Delta T) \tag{6.4}$$

and analogously applying it to Equation (6.2) provides

$$\begin{aligned} u_c^2(\dot{Q}_{DSG}) = & \left(\frac{\partial \dot{Q}_{DSG}}{\partial \dot{m}_{steam}} \right)^2 \cdot u^2(\dot{m}_{steam}) + \left(\frac{\partial \dot{Q}_{DSG}}{\partial h_{evap}} \right)^2 \cdot u^2(h_{evap}) + \\ & + \left(\frac{\partial \dot{Q}_{DSG}}{\partial \dot{m}_{in}} \right)^2 \cdot u^2(\dot{m}_{in}) + \left(\frac{\partial \dot{Q}_{DSG}}{\partial c_p} \right)^2 \cdot u^2(c_p) + \\ & + \left(\frac{\partial \dot{Q}_{DSG}}{\partial T_{sat}} \right)^2 \cdot u^2(T_{sat}) + \left(\frac{\partial \dot{Q}_{DSG}}{\partial T_{in}} \right)^2 \cdot u^2(T_{in}). \end{aligned} \tag{6.5}$$

To be able to utilize Equation (6.4) and Equation (6.5), the standard uncertainties of the variables $\dot{m}_{in}$, c_p, ΔT as well as $\dot{m}_{steam}$, h_{evap}, and T_{sat} have to be determined. However, these computations depend on whether the variables are measured directly or are themselves calculated quantities. This is, for example, the case of measuring volume flow rather than mass flow (where $\dot{m} = \rho \cdot \dot{V}$) or for the steam properties $h_{evap} = f(p_{SD})$ and $T_{sat} = f(p_{SD})$. In these cases, the error propagation formula has to be applied again until arriving at directly measured quantities.

To ensure a correct calculation of uncertainty values, the appropriateness of simplifying assumptions commonly applied to uncertainty calculations of collector power output was confirmed in Zirkel-Hofer et al. [2016, pp. 304–305]. In particular, it was demonstrated that sophisticated computational techniques, which account for non-linearity and covariance in the variables of these equations, do not significantly improve simplified calculations that neglect these effects. These findings justify the use of the above introduced simplified uncertainty equations of Equation (6.4) and Equation (6.5).

[1] with $u^2(X_i)$ being normally distributed

Expanded Uncertainty

Combined uncertainty can be translated into the language of confidence intervals. Assume that Y is normally distributed with standard deviation $u_c(Y)$, and let y be some measured instance of Y. Then, the interval $y \pm k \cdot u_c(Y)$ represents an approximate 95 % confidence interval for measurand Y when we set the coverage factor $k = 2$. The value $U_c(Y) = k \cdot u_c(Y)$ is called the expanded (or overall) uncertainty and is only meaningful when the coverage factor is specified. Equally to the 95 %-confidence levels computed by the bootstrapping or random sub-sampling approach in Chapter 5, all expanded uncertainty figures within the present thesis are reported with the coverage factor $k = 2$.

Incorporated Uncertainty of Fluid Properties

The heat capacity $c_p(T_m)$ is calculated as a polynomial function of the mean fluid temperature T_m, as is the density of the heat transfer fluid $\rho(T_m)$, which is required when the volume flow is measured rather than directly measuring mass flow. Importantly, there is an element of uncertainty in these fluid property calculations that arises from uncertainty regarding the equations used to determine them. This uncertainty should be factored into the calculation of $u(c_p)$. The magnitude of this uncertainty greatly depends on the fluid used: the evaluation of the fluid properties of water are extremely sophisticated, leading to small uncertainties (approximately 0.02 % [ISO 9806, 2013]), whereas for thermal oil and other heat transfer media, the uncertainty is more pronounced (approximately, e.g., 1–3 % for thermal oil [Solutia, 1998]). Even though the uncertainty of water and steam properties are small, the same concept is applied for the evaporation enthalpy $h_{evap}(p_{SD})$ and saturation temperature $T_{sat}(p_{SD})$, which are considered polynomial functions depending on the measured steam drum pressure. The profound concept of including errors in the fluid property equations can be found in Zirkel-Hofer et al. [2016, pp. 302–303]. Specifically applied formulas are given in Equation (E.7) to Equation (E.10) of Appendix E.

■ 6.1.2 Application to Evaluated Test Collectors

Uncertainty results in Zirkel-Hofer et al. [2016, p. 304] revealed a relevant influence of operating conditions on the expanded uncertainty of the power output and therefore to the performance evaluation in general. For this reason, appropriate operating conditions for the uncertainty calculation of the evaluated test collectors have to be chosen. Only representative reference conditions allow meaningful assessments of associated uncertainties of the collector tests. Consequently, nominal operating conditions of the evaluated test collectors were considered within the measurement uncertainty computations. Table E.2.1 lists the selected temperature, mass flow, pressure, and irradiance conditions for the uncertainty assessment of the evaluated test collectors. Calculations are based on the sensor standard uncertainties given in Section B.2. Corresponding absolute and relative uncertainties of the collector power output are summarized in Table 2.2.

■ 6.1.3 Uncertainty Case Study

For future collector tests, in order to facilitate a faster assessment and accordingly an easier selection of measurement instrumentation, a comprehensive uncertainty case study was performed. To this end, exemplary measurement instrumentation typically installed for collector testing (intrusive and clamp-on) or maintenance and operation were analyzed. In this context, not only standard uncertainties of individual sensors were evaluated but also their impact on expanded uncertainty values of collector efficiency and power. The study indicates which sensors are dominating the overall uncertainty values and may thus be worthwhile to install or to improve.

The results concerning the influence of operating conditions in Zirkel-Hofer et al. [2016] particularly revealed that a clamp-on measurement approach may be adequate for large-scale power plant collectors. Yet, it may induce excessively high uncertainty values for the evaluation of small-scale process heat collectors. Thus, to draw general conclusions about the quality of specific measurement instrumentation setups, more than one fixed base case of operating conditions should be considered to account for the entire spectrum of line-concentrating solar collectors. Consequently, the uncertainty case study was conducted based on two operational reference cases. They consist of a linear Fresnel process heat collector operated with pressurized water and a large-scale solar-field loop of parabolic trough collectors with thermal oil. Their specific properties are listed in Table 6.1[2]. Both cases adequately cover the complete range of collector types and operating conditions typically involved in the field of line-concentrating solar collectors.

To be able to assess the suitability of individual measurement instrumentation, a base case of measurement instrumentation was taken as a reference basis. Subsequently, the effect of changing a single sensor while keeping the other sensors constant was studied. Detailed sensor uncertainties can be found in Zirkel-Hofer et al. [2016, p. 311]. The selected sensors represent standard measurement instrumentation typically available and installed for performance testing or for operation and control purposes.

For the **temperature measurement**, five different temperature sensors with their respective standard uncertainty $U(T)$ were considered:

- **PtAC:** calibrated Pt-100 sensor (reference basis),
- **PtA:** non-calibrated Pt-100 class A sensor,
- **PtB/10:** non-calibrated Pt-100 sensor class 1/10-B,
- **Ptclamp:** Pt-100 sensor mounted as a clamp-on sensor,
- **PtclampCr:** relative calibrated Pt-100 sensor mounted as a clamp-on sensor.

Concerning the **mass flow measurement**, four different technologies were studied with the following naming:

[2]For technical data of the used heat transfer fluids, such as density and heat capacity, see ISO 9806 [2013, p. 109] for water and Solutia [1998] for thermal oil VP1.

Table 6.1: Characteristics of the operational reference cases within the uncertainty case study. Two collector sizes with typical operating conditions are considered. [adapted from Zirkel-Hofer et al., 2016]

Variable	Unit	Small-scale	Large-scale
Collector		LFC	PTC
HTF		water	thermal oil
T_{in}	°C	150	290
T_{out}	°C	170	390
$\dot{m}$	kg/s	0.97	6.87
G_{bn}	W/m^2	850	850
$\dot{Q}$	kW	84	1664
η	–	0.66	0.65

- **USinC:** calibrated ultra-sonic in-line sensor (reference basis),
- **USin:** non-calibrated ultra-sonic in-line sensor,
- **Cor:** Coriolis flow meter,
- **USclamp:** ultra-sonic clamp-on sensor.

Analogously, two different sensors with their respective standard uncertainties $U(G_{bn})$ were chosen for the **irradiance measurement**:

- **Ph1st:** first class pyrheliometer (reference basis),
- **PnSM:** pyranometer with shadow mask.

The results of the comprehensive study for both cases of small-scale and large-scale collectors are depicted in Figure 6.1. A detailed discussion of the particular results and their absolute values is presented in Zirkel-Hofer et al. [2016, pp. 305–308].

The case study shows that high-accuracy and high-precision sensors are particularly beneficial for small-scale systems, because smaller collectors are more sensitive to higher uncertainties of measurement instrumentation. This becomes particularly important for temperature measurements, since they represent a major contributor to the uncertainty of the collector power output. Standardly installed temperature sensors for operation and control (such as the PtA-sensor) yield high uncertainty values and accordingly impede reliable test results for small-scale systems. In the studied case of an LFC process heat collector with an efficiency of 66.0 %, by installing a PtA-sensor with an expanded, combined efficiency uncertainty of 2.8 %-pts., the measured efficiency performance may vary between 63.2 % and 68.8 %. Measurements with these uncertainty values may certainly provide valuable indications on the approximate collector efficiency. However, these error bands are still too high for collector certification purposes, where precise results are requested. For this reason, the standardly installed instrumentation for control purposes should not be used for representative collector testing, and the use of higher-quality sensors is essential. To reduce the overall uncertainty for small-scale collectors, it is therefore worthwhile to improve the accuracy of these sensors, for example, by calibrating them.

The overall uncertainty values of large-scale collectors are more robust against individual sensor uncertainty. Uncertainties in power and efficiency in large-scale collectors are proportionally much smaller than for small-scale collectors. Even higher temperature uncertainties may still allow a rather decent identification of the collector performance for large-scale systems. Thus, clamp-on instrumentation can present a viable alternative to intrusive measurement instrumentation for larger systems. The same applies for higher uncertainties of the mass flow rate. In this context, Coriolis sensors lead to the best test results, because they directly measure mass flow rather than volume flow rates. However, other alternatives—such as in-line ultra-sonic sensors—may achieve similar uncertainty values and may come at lower costs and susceptibility. Conversely, uncertainty in heat capacity greatly contributes to both power and efficiency uncertainties in large-scale collectors. This implies the importance of additionally measuring this fluid property for a proper performance evaluation of a collector with less-defined heat transfer media, such as thermal oil or molten salt. Irradiance measurements considerably influence thermal efficiency uncertainty in both small- and large-scale systems. Consequently, for meaningful collector tests and especially for certification purposes, high-quality irradiance instrumentation is required.

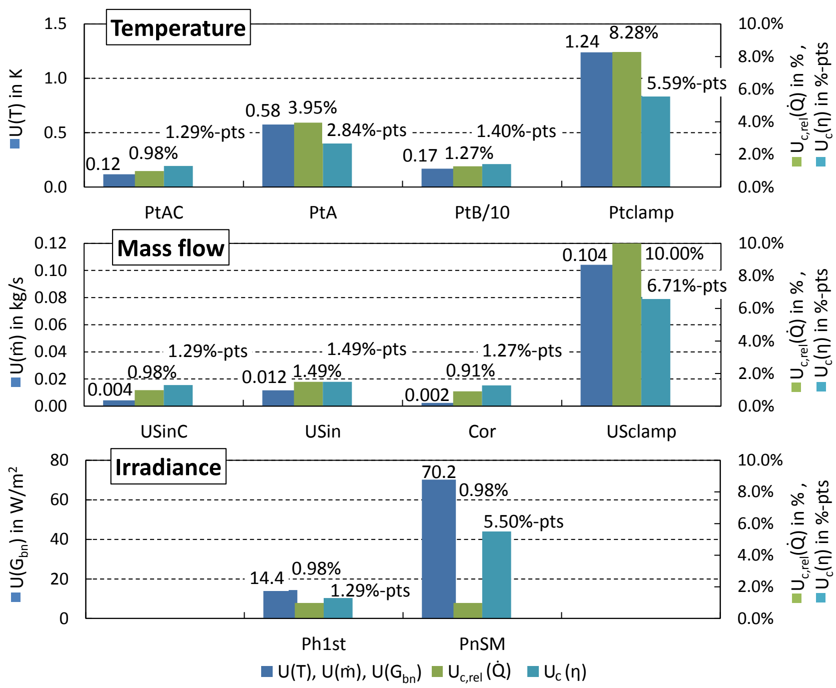

(a) Case of small-scale collector

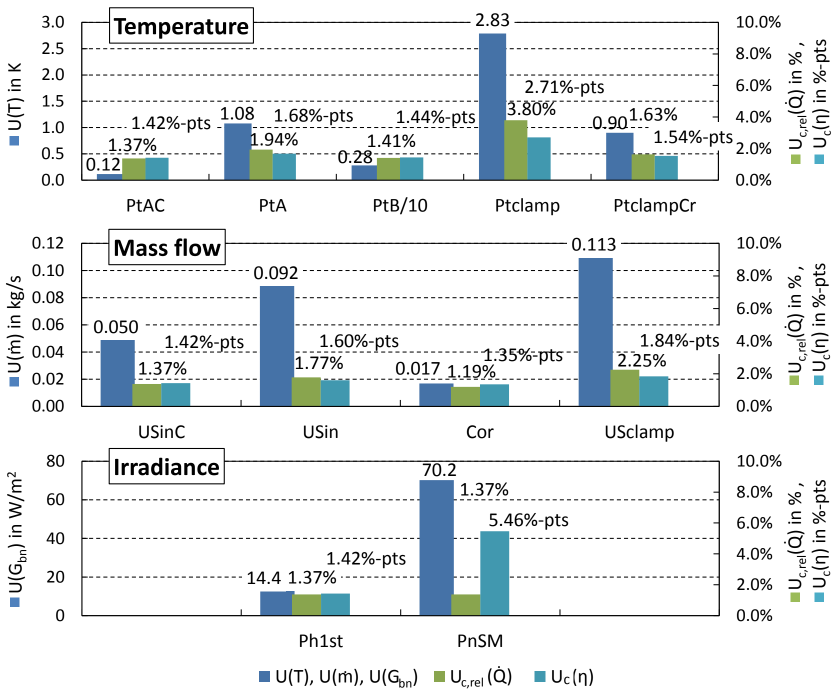

(b) Case of large-scale collector

Figure 6.1: Results of uncertainty case study. Sensor uncertainty $U(T)$, $U(\dot{m})$, $U(G_{bn})$ (in dark blue) and its impact on the overall relative power uncertainty $U_{c,rel}(\dot{Q})$ (in green) and efficiency $U_c(\eta)$ (in turquoise). For the studied cases, only one sensor is changed while the remainder of the instrumentation is kept constant to the base case (consisting of a PtAC temperature sensor, a USinC mass flow sensor, and a Ph1st irradiance sensor). Different operating conditions of small-scale (a) and large-scale (b) collectors are considered. [adapted from Zirkel-Hofer et al., 2016]

■ 6.2 Recommendations for the Measurement Instrumentation Selection

■ 6.2.1 Recommended Selection Procedure

Based on the thoroughly elaborated methodology in Zirkel-Hofer et al. [2016] and the uncertainty case study, the following procedure for a selection of adequate measurement instrumentation is suggested. The recommended procedure for how to use the compiled methodology and its results at the beginning of a planned collector testing phase consists of the following steps:

(1) Identify average values of operating conditions of the collector under test, such as mean mass flow rate, inlet and outlet temperatures, and heat capacity of the heat transfer medium. Take average values of incoming irradiance depending on the potential location of the testing. From these data, deduce potential collector power output and efficiency:

$$\text{test collector} \Rightarrow \overline{T}_{test}, \overline{\dot{m}}_{test}, \overline{c_p}_{test} \Rightarrow \overline{\dot{Q}}_{test}, \overline{\eta}_{test}$$

(2) Compare mean values of operating conditions to the cases of the uncertaitny case study listed in Table 6.1.

$$\overline{T}_{test}, \ldots, \overline{\dot{Q}}_{test} \approx / \not\approx \overline{T}_{study}, \ldots \overline{\dot{Q}}_{study}?$$

CASE (2.1): Operating conditions are close to the small-scale or large-scale test case.

- For an assessment of already installed instrumentation, compare installed sensor standard uncertainty values $U(sensor)$ (e.g., $U(T)$) to the indicated case study values to obtain an estimation of the induced uncertainty values on power and efficiency:

  $$U(T)_{test} \approx U(T)_{study} \Rightarrow U_c(\dot{Q})_{test} \approx U_c(\dot{Q})_{study}$$

  As previously stated, in most cases, commonly installed sensors for operation and control do not satisfy collector testing requirements.
- If induced uncertainties are too high or no instrumentation available, take the results in Figures 6.1(a) and 6.1(b) and their discussion as a reference for the selection of instrumentation. For reliable collector qualification, higher-quality sensors, such as calibrated PtAC- or PtB/10 temperature sensors, are recommended.

CASE (2.2): Operating conditions differ significantly from the studied test cases.

- Determine the associated sensor standard uncertainty and its effect on combined uncertainty of power and efficiency to assess instrumentation already installed:

  $$\text{sensors} \Rightarrow U(T)_{test} \xrightarrow[operating\ conditions]{methodology} U_c(\dot{Q})_{test}$$

- If induced uncertainties are too high or no instrumentation available, take the standard uncertainty of exemplary sensors (e.g., the recommended temperature sensors PtAC or PtB/10 of the case study). Evaluate the associated power and efficiency uncertainty for the designated collector test according to the given operating conditions in order to determine whether uncertainties are in an acceptable range:

  $$U(T)_{study} \xrightarrow[operating\ conditions]{methodology} U_c(\dot{Q})_{test}$$

3 Decide as a compromise between feasibility, cost of the instrumentation setup, and minimum of associated sensor uncertainty to obtain significant and reliable collector test results.

■ 6.2.2 Conclusions Concerning Measurement Instrumentation

In general, the study confirms the relation of higher uncertainties of measurands leading to higher overall performance uncertainties and accordingly to less significant test results. Nevertheless, the extra cost and effort have to be carefully weighed against the associated precision enhancement. For this reason, this comprehensive study provides valuable indications for future in situ collector testing with respect to the type of instrumentation advisable to select, given certain boundary conditions. It furthermore shows how to proceed when selecting new measurement instrumentation for in situ testing: merely using standard sensors designed for operation and control or solely using the same instrumentation of a different collector testing does not ensure significant test results. A successful testing requires a rechecking of collector performance uncertainties and shows the indispensability of detailed uncertainty analysis in the context of reliable performance evaluations. For this reason, the general methodology of uncertainty calculation for line-concentrating collectors was elaborated in detail, as presented in Zirkel-Hofer et al. [2016]. Besides, by including two exemplary operational reference cases, the present uncertainty study provides helpful orientation for the complete spectrum of line-concentrating solar collectors: a sensor with a similar standard uncertainty as a sensor studied within Section 6.1.3 will very likely have similar influence on the test results. In the case of a measurement situation being very different from the exemplary cases studied within this publication, the thoroughly introduced methodology can still be applied. The analysis therefore provides a good reference point for the decision if more precise (and hence, in most cases, more expensive) measurement instrumentation is decisively improving the quality of test results and is hence worth the investment. It is designed such that the results are also transferable to other testing situations, which are not specifically studied. The presented systematic uncertainty case study thus serves as a guideline for the selection of appropriate measurement instrumentation. It furthermore demonstrates the relevance of properly selecting measurement instrumentation for reliable performance testing.

Chapter 7

Testing Strategy

With the general enhancement of the DT method and its specific advancements concerning DSG collectors, confidence intervals, and measurement instrumentation in Chapter 3 to Chapter 6, a universally applicable evaluation procedure for the performance testing of line-concentrating collectors is enabled. In order to warrant an identification of representative and dependable performance parameters, the testing strategy represents a further key element for the performance testing. An appropriate testing strategy is defined by particular information contents that need to be contained in the measurement data basis in order to assure a good evaluation quality. The information content can be influenced by particular operating conditions during the tests. Besides the aspects within the previous chapters, the testing strategy ensures that not merely one best-fit parameter set of the specifically evaluated data basis is determined, but a parameter set that is generally valid and therefore representative for the entire collector system under test. This is considered essential for performance testing aiming at collector certifications. A good evaluation quality leads to the determination of reliable and significant performance results, which are defined by the following two aspects:

Small confidence intervals

The smaller the statistical variance (i.e., the potential dispersion of every single identified performance parameter), the more meaningful and hence dependable the test results.

Minimal parameter correlation

While simultaneously deducing more than one performance parameter of a collector, parameter correlation between the identified parameters may arise. For example, if a collector is measured at one temperature level and one solar incidence situation only, thermal and optical parameters cannot be identified independently. A high heat loss of the collector coupled with a high optical efficiency would lead to the same measured collector power output as the opposite case of low heat loss coupled with a low optical efficiency. In this case, independent identification of optical and thermal performance parameters is not possible and parameter correlation severely dominating the evaluation results. Certainly, in the context of a reliable and comparable performance testing, this parameter correlation is not desired nor acceptable and needs to be reduced to a minimum possible, if not even prevented at all.

These two quality criteria of the identification results are influenced by the information content included in the evaluated measurement data. In the case of the previously introduced example of parameter correlation, several temperature levels could decrease the correlation as more information is provided allowing to separate the effects of heat loss from the optical performance. In the following sections, a suitable testing strategy is derived by analyzing which factors (i.e., which information contents) substantially influence—and which factors do not affect—the quality and hence the significance of identification results. For the derivation of a suitable testing strategy two approaches are pursued: while in the first part in Section 7.1 artificial measurement data is generated and evaluated to assure a broad and systematic variation of the information content, in Section 7.2 real measurement data of a large data basis is processed.

Both concepts possess several valuable benefits justifying its application in the context of deriving an appropriate testing strategy, which are summarized in Table 7.1. The most important advantage of artificial data represents the possibility of creating a vast and systematic variation of information content, allowing to specifically in- or exclude factors and enabling a proper differentiation of the studied effects. Moreover, when real measurement data are evaluated, they are compared to simulated data obtained from a simulation model. Even if the simulation model is very elaborated, it will never reproduce reality 100 % correctly. By taking artificially created measurement data, effects arising from a potential shortcoming of the chosen simulation model can be eliminated. The exclusion of this error source is desired to comprehensively understand the impact of selected datasets and their characteristics. Though, this aspect additionally imposes the major drawback of artificial data, because reality is only approximated when using artificial data. The validity of the artificial data is limited to the capability of the simulation model to reproduce reality. Nevertheless, artificial data present a good starting basis for comprehensive studies, giving valuable indications on dominating factors and relations.

In addition, for artificial data the 'true' performance reference values are available allowing an unbiased and correct assessment of the studied factors. For real measurement data instead, the true solution is never known for certain. Already determined performance parameters of a well-investigated, real collector could be taken as a true reference solution. Yet, parameters derived from physical modeling of a collector may not adequately enough describe a complex reality. Similarly, parameters derived from other testing methodologies are limited by measurement uncertainty and inadequate testing methodology. When evaluating real measurement data, one of these aspects will always bias the assessment of the results. In contrast, for artificial data, the true values are distinctly known, because they are originally set when creating them. The pros and cons of artificial and real measurement data show that both concepts complement each other valuably for the derivation and validation of a testing strategy. They particularly address and alleviate the drawbacks of each other. When studying real measurement data, every effect occurring in reality is included, allowing for a cross-validation of the conclusions obtained from the artificial data evaluation. In this way, the simplified model of the artificial data can be cross-checked for significant deviations to reality. Certainly, the variation of information content will never be as large and distinct for real measurement data as for artificial ones. For this reason, not every individual conclusion will be cross-checked to reality. However, the verification and therefore confirmation of some major conclusions is regarded valuable enough to judge on the representativeness and reliability of other conclusions drawn from artificial data.

Table 7.1: Benefits and drawbacks of the validation of a testing strategy with artificial and real measurement data. Both concepts complement each other.

Data	Benefits	Drawbacks
Artificial data	broad systematic variation	approximation of reality
	specific in-/exclusion of effects	limited, not proven validity
	good indications on dominating factors and relations	
	known true reference values	
	no error source from deviations of simulation to reality	
Real data	inclusion of all effects present in reality	no broad systematic variation
	verification of conclusions from artificial data	unknown true reference values

■ 7.1 Analysis of Artificial Measurement Data

■ 7.1.1 Theoretical Concept

Creation of Artificial Data

Artificial measurement data were generated using ColSim's PFM[1], that means, the same simulation model which is used for the parameter identification procedure. For fixed (and therefore known) performance values of an exemplary LFC[2] the outlet temperature of the collector is simulated. Afterwards, the simulated outlet temperature is considered as a measured outlet temperature of the collector during a subsequent identification procedure. For 'perfect' measurement data, identification results of artificially created measurement data should match identically to the fixed performance parameters at the beginning. Depending on the fixed performance parameters as well as on the set of weather data and operating conditions of the simulated collector, different properties of the measurement data are defined. The concept of artificial measurement data were implemented and part of its evaluation realized within the work of Nettelstroth [2015]. The following characteristics[3] of the artificial measurement data were created and their effect evaluated in subsequent parameter identifications:

Heat transfer fluid:

Two different HTFs were considered in the generation of artificial measurement data to be able to cover the entire temperature range that concentrating collectors are typically working in. Pressurized water was taken for simulations below 240 °C with a pressure level of 45 bar to avoid vaporization of the fluid. Molten salt was taken for the simulation of higher temperatures up to approximately 550 °C[4]. Moreover, the respective HTF implies the scale of the collector: water is used in a small-scale process heat collector, whereas molten salt is used in a large-scale col-

[1]The physical model and numerical scheme of the PFM is elaborately derived in Section C.1.

[2]The testing strategy based on artificial data could also be investigated on the basis of a PTC. As the performance evaluation is more complex for LFCs, parameter correlation is expected to have a higher influence on the testing of LFCs. Results and conclusions of the parameter correlation and identification quality may be transferable to dynamic PTC testing as well.

[3]The characteristics of the data were chosen on typical collectors designs, heat transfer fluids, working temperatures, mass flow rates, solar irradiance, and their dynamics prevailing in common collector operations.

[4]The commonly used HTF of thermal oil as studied in Chapter 6 only allows an operation up to approximately 400 °C. To be able to study the maximum feasible temperature range, molten salt was chosen for the following analysis.

lector rather designed for electricity generation. Thereby, the collector apertures and lengths vary between the two distinguished HTF cases[5].

Receiver type:

Two LFC receiver types were evaluated considering different amounts of heat loss. One receiver is showing heat loss values similar to an evacuated receiver, for example, consisting of an evacuated glass tube absorber with secondary mirror, in the following referred to as *evac*. The other receiver presents heat loss values similar to those of a non-evacuated receiver, featuring a secondary mirror with an absorber enclosed by a glass tube without vacuum. This case is referred to as *non-evac*. An exemplary illustration of both receiver configurations is given in Figure A.2 (cases a and b). Due to convective heat loss, the *non-evac* receiver design has a significantly higher heat loss than the *evac* one, especially at higher fluid temperatures (as already discussed in Section 3.3).

Temperature setting:

To analyze the effect of fluid temperature characteristics, measurement data were created with three different inlet temperature courses:

- constant inlet temperature,
- quick inlet temperature rise at a noon,
- and a temperature curve with gradually increasing inlet temperature before noon and decreasing inlet temperature after noon.

Mass flow setting:

Similarly to the temperature setting, the effect of the mass flow course on the collector performance was evaluated by generating measurement data with:

- controlled (i.e., varying) inlet mass flow rate and hence constant outlet temperature and
- constant inlet mass flow rate and hence varying outlet temperature of the collector.

DNI dynamics:

Different dynamics in the DNI course were analyzed, which are describing how much the DNI changes throughout an entire day (from morning to evening). Mainly three different cases were differentiated: entire sunny days (cloudless), days with few clouds (partly clouded) and days with highly alternating periods of clouds and sun (cloudy). For an exemplary illustration of the artificial days, refer to Figure 7.5.

Temperature level:

Each base day characterized by the previously introduced categories was simulated for different inlet temperature levels. For the HTF water, four to five different temperature levels were considered between 50–240 °C. For molten salt, three to four different temperature levels were implemented between 250–550 °C.

Day of year:

The occurring incidence angles of each identification day define the identifiable IAM values of a collector. It is assumed that they also influence the quality of the

[5]Summarized settings for the two reference collectors are given in Table F.1.1

identifications. Thus, artificial measurement data were created on different days throughout the year. The specific locations of the collectors are listed in Table F.1.1.

Noise level:

A limited precision and accuracy of the measurement instrumentation leads to real measurement data being affected by uncertainties. This effect was included in the artificial data evaluation by applying different noise levels to the simulated measurement data. The defined noise levels 0 %, 0.1 %, and 0.5 % represent a random relative error that is applied to the value of the simulated outlet temperature T_{out} in each time step.[6] Moreover, artificial noise is added on the measured inlet temperature, DNI, and mass flow rate. Table 7.2 gives an overview on the applied relative noise values for all four variables. The relative noise level of the objective variable T_{out} (0 %, 0.1 %, and 0.5 %) is used as a reference naming for all evaluations. The error linked to the different noise levels shall represent realistic measurement uncertainties associated with measurements in collector testing.

The randomly applied noise leads to a statistical variation of the generated datasets, even though they are based on the same initial characteristics. This randomly produced difference is referred to as different 'forks' of the same base day. It was observed that these differences have a perceivable influence on the identification results. An example for this is given in Figure 7.1. For ten different forks n, the error $\varepsilon_{rel}(\eta_{opt,0})$ is depicted, defined as the deviation between the identified parameter $\eta_{opt,0}$ and its true value, which will be explained in detail in the following paragraph. It shows how the mean of the errors varies with the number of forks. Note that the identification procedure (i.e., the optimization algorithm) works completely deterministic. This means that the repetition of one identification from one fork always leads to the very same results. Accordingly, the differences sketched in Figure 7.1 are produced solely by the randomly applied noise. In the given example, forks 1 and 10 produce extremely bad results, with a deviation to the true value larger than 1.8 %, while the best case of fork 6 entails an error of smaller than 0.1 %. The mean of all forks is approximately 1.0 %. With the objective of reducing these uncertainties introduced by the noise as well as getting distinct and representative results, a number of ten forks was chosen. In this way, each identification was simulated ten times and in most cases the mean of the resulting error used for subsequent evaluations and interpretations. For a detailed derivation and justification for using the particular number of ten forks, see Section F.2. It was chosen as a compromise between manageable computational expense and accuracy/representativeness of the corresponding results.

[6]Detailed results of a study with noise applied on merely the collector outlet temperature are given in Nettelstroth [2015].

Table 7.2: Defined reference noise levels and their applied random relative noise values. Noise values of the temperature variables are taken for the reference naming of the noise levels.

Variable	Reference noise level 0.1 %	Reference noise level 0.5 %
T_{in}	0.1 %	0.5 %
T_{out}	0.1 %	0.5 %
$\dot{m}$	1 %	3 %
G_{bn}	3 %	5 %

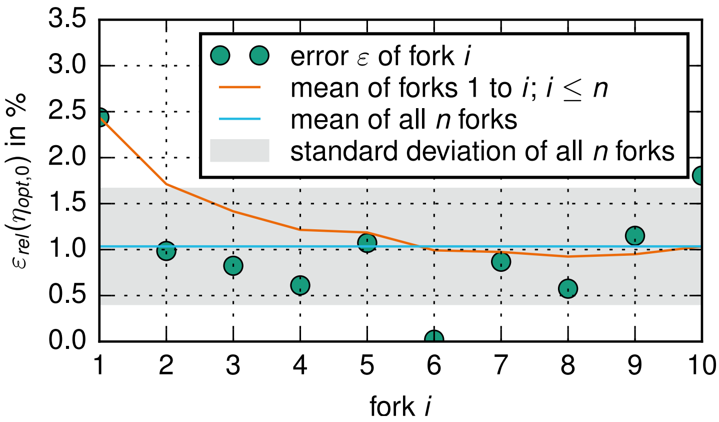

Figure 7.1: Error values for the ten forks of one exemplary identification case based on the noise level of 0.5 %. The deviation of identified versus true value in terms of the specific error value $\varepsilon_{rel}(\eta_{opt,0})$ of each fork is displayed and its statistics given concerning the mean value and the standard deviation of the errors for all ten forks.

The artificially created measurement data, corresponding to the previously introduced categories for the operating conditions (temperature, mass flow, and DNI setting as well as temperature levels), are taken as base days and can be evaluated as single days only or in combination with each other. An overview on the characteristics of these base days is given in Appendix G.

For the HTF water, 27 different base days with different temperature, mass flow, and irradiance settings were generated. 122 diverse combinations of these measurement days were identified. These identifications were performed for the two receiver types and the three noise levels, which equals to a total number of 732 different identifications. Each of these was performed one time per fork, with a number of ten forks yielding to 7320 identifications.

For the HTF molten salt, the same procedure was performed with 72 base days and 83 different combinations of these, resulting in $83 \cdot 2 \cdot 3 = 498$ different identifications (and thus 4980 forks of identifications). To be able to focus on the effects of thermal identification quality, both studies with water and molten salt are based on identifying $\eta_{opt,0}$ and both heat loss coefficients u_0/u_1, while the IAM values are kept constant to their reference values. Thereby, a separation of aspects influencing the thermal identification quality to effects dominating the IAM identification quality is possible.

Additionally, to particularly address factors dominating the identification quality of the IAM, a third study was performed including an identification of $\eta_{opt,0}$ and IAM values, but keeping the heat loss coefficients constant to their reference values (both cases evac and non-evac). This study is based on 24 base days of different settings with 51 diverse combinations of those measurement days throughout the year, providing a total sum of $51 \cdot 2 \cdot 3 \cdot 10 = 3060$ different identification results to evaluate. Identification results of these different measurement days and their combinations are taken as a basis for the conclusions concerning the parameter correlation and quality of measurement data.

Assessment of Identification Quality

The artificial data are designed to study the factors that are influencing the quality of identified parameters. To assess the positive or negative influence of certain factors, a measure of this identification quality has to be defined. In general, the identification quality is considered as the deviation between the identified and the true performance parameters. The present concept of error calculation is analog to the one introduced in Nettelstroth [2015, pp. 15–16;33]. For the evaluated collector and its artificially created measurement data, the true values of the performance parameters—that is, the originally fixed parameters while creating/simulating the data—are summed in Table 7.3. Assumed heat loss coefficients represent realistic values for an evacuated or non-evacuated receiver tube. They were determined by calculations with the TRM introduced in Section 3.3. Incorporated IAM values are illustrated in Figure A.5.

For the optical efficiency at normal incidence $\eta_{opt,0}$, the corresponding error function $\varepsilon_{rel}(\eta_{opt,0})$ is defined as:

$$\varepsilon_{rel}(\eta_{opt,0}) = \frac{\left|\eta_{opt,0,ident} - \eta_{opt,0,true}\right|}{\eta_{opt,0,true}}. \tag{7.1}$$

Note that in most cases when such an error is referred to, the mean value of this error over all ten forks is meant, otherwise it will be specifically indicated. It describes the relative deviation of the identified value to the true value.

The same concept could be applied for the heat loss coefficients u_0 and u_1. Since the comparison of every individual coefficient is not considered meaningful nor expedient, a different approach was pursued. An agglomerated error value of $\varepsilon(u_0, u_1)$ was introduced that combines both heat loss parameters. It describes the root mean square error of a heat loss curve based on the identified values for u_0 and u_1 to the heat loss curve based on the true values. The agglomerated heat loss error is computed as a root mean square of the heat loss deviation at four evenly distributed temperatures T_i along the complete, relevant temperature interval for this fluid. This relevant interval is defined from 1–240 °C for the HTF water and from 250–550 °C for molten salt. Equivalent to the heat loss, the unit of the error value is W/m. The relative mean absolute error $\varepsilon_{rel}(u_0, u_1)$ is computed analog by dividing the heat loss deviation by the true heat loss at each T_i [Nettelstroth, 2015, p. 16]:

$$\varepsilon(u_0, u_1) = \sqrt{\frac{\sum_{i=0}^{4} \Delta\dot{Q}_{HL}(T_i)^2}{4}} \tag{7.2}$$

Table 7.3: Original values of the performance parameters for the artificially generated measurement data. The originally set values are considered the 'true' reference values for the error calculation.

Parameter	Unit	Evac receiver	Non-evac receiver
$\eta_{opt,0,true}$	-	0.65	0.65
$u_{0,true}$	$W/m{\cdot}K$	0.039948	0.8615
$u_{1,true}$	$W/m{\cdot}K^2$	0.0010661	0.0017020

and

$$\varepsilon_{rel}(u_0,u_1) = \sqrt{\frac{\sum_{i=0}^{4}(\Delta\dot{Q}_{HL}(T_i)/\dot{Q}_{HL,true}(T_i))^2}{4}} \tag{7.3}$$

with

$$\begin{aligned}\Delta\dot{Q}_{HL}(T_i) &= \dot{Q}_{HL,ident}(T_i) - \dot{Q}_{HL,true}(T_i) = \\ &= (u_{0,ident} - u_{0,true})\cdot T_i + (u_{1,ident} - u_{1,true})\cdot T_i^2.\end{aligned} \tag{7.4}$$

In order to measure the quality of IAM identification, a similar concept was applied. Equivalent to the calculation of an agglomerated error for a heat loss curve, the identified IAM curve is compared to the true one. Since the IAM of an LFC is defined at a discrete number of angle steps n, deviations at every specific angle step are computed. To generate the agglomerated error value, the relative deviation for every angle step is taken and the root mean square over all angle steps calculated by:

$$\varepsilon_{rel}(K_L) = \sqrt{\frac{\sum_{i=0}^{n}(\Delta K_L(i)/K_{L,true}(i))^2}{n}}, \tag{7.5}$$

$$\varepsilon_{rel}(K_T) = \sqrt{\frac{\sum_{i=0}^{n}(\Delta K_T(i)/K_{T,true}(i))^2}{n}} \tag{7.6}$$

with

$$\Delta K_{L/T}(i) = K_{L/T,ident}(i) - K_{L/T,true}(i). \tag{7.7}$$

[adapted from Nettelstroth, 2015, p. 15–16;33]

■ 7.1.2 Study of General Aspects

While analyzing the results of the broad artificial data evaluation in detail, several conclusions were drawn regarding general aspects influencing the quality of identified parameters, which will be referred to with the capital letter of '**G**'. Thermal conclusions will be marked with the capital letter of '**T**', whereas conclusions concerning the optical identification quality will be marked by the letter '**O**'. A summary on all drawn conclusions will be given at the end of this chapter in Section 7.3.

General Identification Quality

To get an overall impression of the identification quality, mean values of all performed identification over all collector operating conditions, day combinations, noise levels, and forks were calculated for the different receiver designs and HTFs. The overall results are listed in Table 7.4, including mean error values and their respective standard deviations. Independent on the specific design and heat transfer fluid, the results clearly indicate that the error values of the heat loss are predominantly higher than the optical error values. In the best case, $\eta_{opt,0}$ can be determined on average with a deviation of 0.17 %, showing no significant difference for an evac or non-evac receiver design. The values are slightly

Table 7.4: Overview on mean error values over all collector operating conditions, day combinations, noise levels, and forks. Mean errors and standard deviations are differentiated according to the receiver design and used heat transfer fluid.

HTF	Error	Unit	Evac		Non-evac	
			mean	σ	mean	σ
Water	$\varepsilon_{rel}(\eta_{opt,0})$	%	0.17	0.26	0.17	0.24
	$\varepsilon_{rel}(u_0, u_1)$	%	128.8	247.5	9.1	22.6
Molten salt	$\varepsilon_{rel}(\eta_{opt,0})$	%	0.21	0.34	0.25	0.42
	$\varepsilon_{rel}(u_0, u_1)$	%	10.2	20.5	2.1	5.6

larger for molten salt than for water, which may be associated to a higher absolute noise due to higher mean working temperatures for molten salt. Regarding the heat loss quality, particularly the case of an evacuated receiver tube operating with water entails excessive error values of approximately 129 %, which is clearly not acceptable for a proper collector testing. For other configurations, the heat loss error terms are not as pronounced as for this particular case, but still consistently show larger values than for $\eta_{opt,0}$. This already indicates in general the issue of a correct heat loss identification—especially for collectors featuring a generally low heat loss level—which has already been addressed in Chapter 3 and will be specifically elucidated in the following sections.

The reason for the generally worse identification quality of the heat loss in comparison to $\eta_{opt,0}$ may originate from the derivation of both parameters from the collector power output $\dot{Q}$. However, the contribution of the optical input to the power output is a lot higher than the share of the heat loss, particularly depending on the evaluated case. Collectors with higher fluid temperatures as in the case of molten salt or for non-evacuated receivers present a larger share (approximately 15–30 % of $\dot{Q}$) than collectors using water featuring an evacuated receiver (approximately 1–6 % of $\dot{Q}$). The smaller the contribution to the collector power output, the higher the heat loss identification is affected by the associated noise. This leads to a less distinct heat loss determination, because the error values are more pronounced (higher noise-to-signal ratio). Even though receiver configurations, heat transfer fluids, and operating conditions change for different collector tests, the share of optical input will always be higher than the heat loss. Consequently, the heat loss will always be the more critical parameter to correctly determine for concentrating systems.

Conclusion G 1:

> The optical efficiency at normal incidence $\eta_{opt,0}$ can be identified more accurately than the heat loss parameters.

Influence of Noise

To study the effect of the induced noise on the artificial measurement data, the previously introduced results can be split up according to their noise levels. In order to summarize the results, only two exemplary cases of an evacuated receiver with water and a non-evacuated one operating with molten salt are listed in Table 7.5[7]. The results generally indicate the relation of larger noise inducing higher error values in thermal and optical parameters. To evaluate the results more distinctly, direct comparisons of all individual

[7] Both cases reflect the lower and upper extrema of possible heat loss amounts, even though—particularly the salt/non-evac case—they do not represent a typical receiver configuration installed in reality.

Table 7.5: Dependency of heat loss and optical identification quality on noise level. Mean error values over all measurement days and forks are split up according to their noise level. Results for two exemplary cases of an evac water collector and a non-evac molten salt collector are shown.

Error	Noise level	Unit	Water/evac	Molten salt/non-evac
$\varepsilon_{rel}(\eta_{opt,0})$	0 %	%	0.01	0.07
	0.1 %	%	0.13	0.24
	0.5 %	%	0.37	0.46
$\varepsilon_{rel}(u_0, u_1)$	0 %	%	7.1	0.5
	0.1 %	%	91.5	1.7
	0.5 %	%	284.8	4.1

parameter identifications were additionally performed. This means that for an evaluation based on the same data basis, receiver configuration, and heat transfer fluid, the mean identification results of all forks for a separate noise level of 0 %, 0.1 %, and 0.5 % were compared to each other. For the error of $\eta_{opt,0}$, in 94.5 % of the 118 evaluated water/evac cases the 0.5 % noise level caused worse results than 0.1 % noise, which performed worse than the 0 % noise level. For molten salt/non-evac, 89 % of the 83 comparisons fulfilled this criterion of $\varepsilon_{rel}(0\,\%) < \varepsilon_{rel}(0.1\,\%) < \varepsilon_{rel}(0.5\,\%)$. Concerning the quality of heat loss identification, 99.6 % of the water/evac comparisons fulfilled the latter criterion, while for molten salt/non-evac 92.8 % of the identifications performed better for 0.5 % noise than for 0.1 % or 0 % noise level. For the cases where a lower noise level showed better error values than a higher noise level, the absolute error values mostly were small and showed little difference to each other. The same tendency was found for the study including an identification of IAM values. The corresponding results can be found in Table F.4.1 of Appendix F.

Note that in the case of not applying noise to the artificial data (i.e., in the case of perfect measurement data), the heat loss of a water/evac-collector can only be determined with an accuracy of 7 %. Hence, even for perfect conditions in theory, this configurations shows to be particularly challenging. Accordingly, this will be even more difficult in practice. This emphasizes the importance of an adequate testing strategy to avoid disproportional error values. The large influence of noise—which is comparable to noise induced by the measurement uncertainty associated to the instrumentation of a test site—univocally shows the substantial relevance of reducing the measurement uncertainty to a minimum possible. As already addressed in Chapter 6, measurement uncertainty should therefore be treated with great caution before installing equipment, recording, and evaluating measurement data for reliable performance testing.

Conclusion G 2:

> The stronger the noise, that is, the larger the associated measurement uncertainty of the installed instrumentation, the worse the identification quality.

Influence of Number of Measurement Days

While analyzing the identification results in detail, the tendency of significantly decreasing error values with increasing number of measurement days becomes discernible. Table 7.6 lists the mean error values over all forks, noise levels, and operating conditions of the measurement days. Error values of $\eta_{opt,0}$ and heat loss are split for water and

Table 7.6: Dependency of heat loss and optical identification quality on number of measurement days. Mean error values and standard deviations over all forks, noise levels, and operating conditions are differentiated according to the number of included measurement days in the corresponding evaluation.

HTF	Number of days	Unit	$\varepsilon_{rel}(\eta_{opt,0})$	$\sigma(\varepsilon_{rel}(\eta_{opt,0}))$	$\varepsilon_{rel}(u_0, u_1)$	$\sigma(\varepsilon_{rel}(u_0, u_1))$
Water	1	%	0.27	0.41	214.2	446.4
	2	%	0.19	0.26	60.6	128.7
	3	%	0.18	0.26	70.1	152.3
	4	%	0.12	0.17	44.8	96.8
	5	%	0.11	0.14	36.6	72.9
	>6	%	0.08	0.08	18.0	31.1
Molten salt	1	%	0.53	0.77	20.1	35.2
	2	%	0.19	0.26	3.4	5.4
	3	%	0.18	0.24	5.5	9.7
	>4	%	0.18	0.25	2.1	3.3

salt depending on the number of included measurement days in the evaluation. With an increasing number of measurement days, the identification quality of $\eta_{opt,0}$ increases on average from 0.27 % to 0.08 % for water and from 0.53 % to 0.18 % for salt. The improvement is even more pronounced for the heat loss identification quality from 214.2 % to 18.0 % and from 20.1 % to 2.1 % for water and salt, respectively. A slight increase of the heat loss error values for three days disrupts the general tendency, which may originate from unfavorable temperature conditions. Apparently, they are specifically dominant within this category of three measurement days, as only a small number of identifications with three days were performed in comparison to other number of days. Consequently, the indicated mean value of this category is considered unrepresentative not invalidating the overall tendency. Additionally, this trend can be confirmed by the overall results of the third study including an IAM identification. For the particular values, refer to Table F.4.2 of Appendix F.

However, note that an increasing number of measurement days mostly comes along with an increasing amount of information content included in the measurement data, which could also provoke the improvement of the identification quality. To isolate the effect of merely increasing the number of measurement points without increasing the information content, the following comparison was conducted: an identification of two exemplary molten salt days `Y1` and `Y2` operating at constant fluid inlet temperature of approximately 440 °C and 470 °C is compared to an identification of solely one measurement day `Y3`—with the same irradiance and mass flow settings as `Y1` and `Y2`—featuring a temperature jump around noon from an inlet temperature level of 440 °C to 470 °C. Thereby, the collector outlet temperature course of `Y3` is very similar to the one of `Y1` before and to `Y2` after noon. Comparing the mean results over all forks of an identification of `Y1Y2` to `Y3` at the different noise levels, receiver types, and different base days shows that in all of the identified 36 cases, two days are identified better than one day only. Even though in the identification `Y1Y2` already existing information is repeated, the identification quality increases. [Nettelstroth, 2015, p. 23–24]

Conclusion G 3:

> The more days, the more data points provide a more stable information content, which results in a better identification quality.

Until now, mean error values of $\eta_{opt,0}$ and heat loss were analyzed. Table 7.6 additionally shows values of standard deviations σ for the corresponding error values. Analog to the error values, with an increasing number of measurement days, the standard deviations decrease. Contradictions to this tendency are corresponding to the previously explained minor exceptions. The values of standard deviation provide a means for assessing the dispersion of the error values and hence of the identification results. While the error values indicate a potential bias of the results (i.e., by indicating the accuracy), standard deviation allows to assesses their precision. With an decreasing standard deviation, the results obtained from the different identifications are less disperse. Consequently, the induced noise has less influence on the results, enabling a more stable and consequently more representative identification of performance parameters. For a detailed analysis concerning the specific number of required measurement days, refer to Section 7.2.4.

Conclusion G 4:

> The more days, the less the identification quality (precision and accuracy) is affected by associated noise in terms of measurement uncertainty.

■ 7.1.3 Study Concerning Heat Loss Identification Quality

Identification results of conclusion **G 1** discussed in Section 7.1.2 already indicated that the heat loss is considerably more difficult to correctly determine in comparison to the optical efficiency at normal incidence. Based on these findings, the particular influences on the heat loss identification quality is analyzed into more detail within the present section.

Influence of Heat Loss Amount

A comparison of the heat loss identification quality $\varepsilon_{rel}(u_0, u_1)$ of an evac versus a non-evac receiver, as already compiled in Table 7.4, explicitly points out the relation of decreasing heat loss error with increasing amount of overall heat loss. This tendency is equally valid for a comparison between the heat transfer fluids: for water, $\varepsilon_{rel}(u_0, u_1)$ results in 127.8 % for evac and 9.1 % for non-evac, while for molten salt error values of 10.22 % arise for evac and 2.1 % for non-evac. The lower the heat loss (irrespective whether resulting from lower fluid temperatures or different receiver configuration), the lower its share to the measured collector power output, the more pronounced the associated measurement uncertainty on the absolute heat loss value, and consequently the less accurate the identification result. Moreover, the effect of higher standard deviations results in a higher dispersion of the results.

Conclusion T 1:

> The higher the amount of overall heat loss, the better the heat loss identification quality.

The above conclusion particularly reveals the challenge of determining correct heat loss values for the specific case of an evac collector operated with water at low temperatures. The overall heat loss curve of the collector represents an intrinsic property of the system under test, which cannot be influenced during testing. Nevertheless, the heat loss identification quality can be considerably enhanced if the temperature level is increased (which

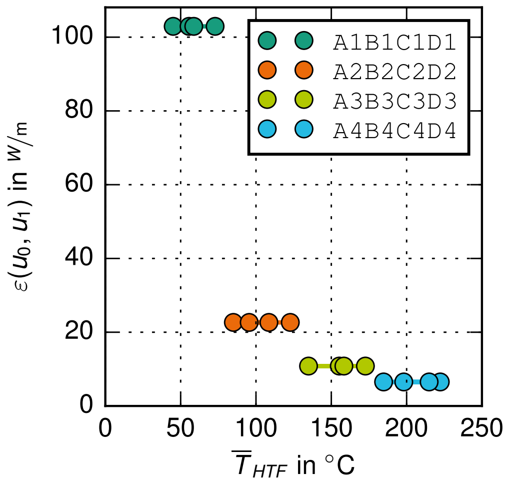

(a) Evac receiver

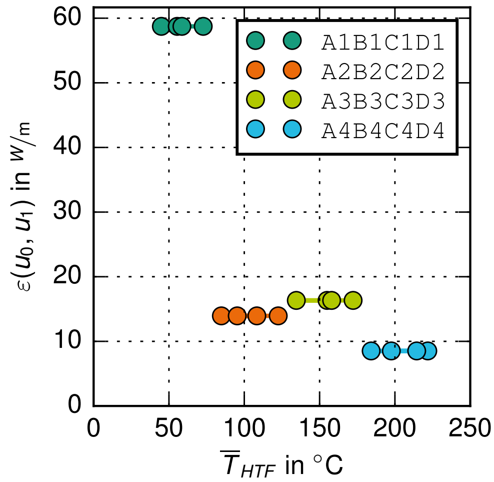

(b) Non-evac receiver

Figure 7.2: Exemplary heat loss identification results depending on the temperature level. The absolute heat loss error $\varepsilon(u_0, u_1)$ is considered as a mean value over all forks for an exemplary combination of days `ABCD` with water at a noise level of 0.5 % and different fluid temperatures.

implicitly results in a higher amount of heat loss as well). This tendency can be derived by directly comparing the mean results over all forks of equal measurement days at different temperature levels. In Figure 7.2, the results are depicted for one exemplary identification case consisting of a combination of four different water days[8] `ABCD` evaluated at different temperature levels `A1B1C1D1` to `A4B4C4D4`. The corresponding numbers 1–4 indicate the temperature level of 50 °C, 100 °C, 150 °C, and 200 °C respectively. It shows the distinct improvement of the heat loss identification quality at higher temperatures, which is more pronounced for evac than for non-evac. Because absolute heat loss values are already higher for non-evac, an increase of heat loss with higher fluid temperature does not affect the results as much as in the case of evac.

Comparing all identified day combinations at different temperature levels, for water, 92.9 % of the 42 different cases confirm this tendency. Similarly, 83.3 % of the 72 comparisons with molten salt support the relation of decreasing error with increasing fluid temperature. The slightly lower value of molten salt may arise from a smaller temperature range between 410–550 °C, whereas the temperature range for water is noticeable higher between 50–240 °C. Thus, the increase in heat loss is not as pronounced for molten salt than for water, leading to minor exceptions to the found tendency. However, in most cases disrupting the general trend[9], error values are very small and similar to each other. All in all, the results support the following implicit conclusion of **T 1**:

Conclusion T 1.1:

The heat loss identification quality increases with a higher fluid temperature level.

[8] with the different characteristics according to Table G.0.1

[9] as similarly for the non-evac case of `A3B3C3D3` depicted in Figure 7.2(b).

Particularly, the results depicted in Figure 7.2(a) illustrate the issue of heat loss identification for an evac collector with low temperatures as raised in Section 3.1. With maximum fluid temperatures of approximately 90–140 °C, the mixture of cases `A1B1C1D1` and `A2B2C2D2` may be comparable to the test conditions of `LFC_w1`. Even for artificial measurement data, where no effects of reality may interfere the identification results, a correct and distinct identification was not feasible with absolute error values between 22–100 W/m as depicted in Figure 7.2(a).

Excursus on reference error values for heat loss identification

To be able to assess and classify the resulting heat loss error values, a means is required to state the maximum limit for acceptable heat loss error. With the objective of defining such a reference value, the following thought was pursued: the potential minimum of (in practice) possible measurement uncertainty of the collector power output (in W), as introduced in Chapter 6, is translated into heat loss values by dividing them by the respective length of the reference collector (to obtain W/m). In this way, the associated magnitude of power uncertainty is considered to directly influence the uncertainty of heat loss. As this value is obtained from steady error-propagation calculations, it reflects the uncertainty for one measurement data point only. By combining several data points in the evaluation procedure, the error is considered to be averaged and should consequently decrease. It therefore represents a maximum limit of associated measurement uncertainty (under the condition that correlation does not dominantly influence model parameters). Values lower than this value are regarded as realistic and desirable to achieve[10]. By this approach, a reference value of 10 W/m for small-scale collectors (water case) and 16 W/m for large-scale collectors (molten salt case) arise. Both values will serve in the following as rough indications for the classification of absolute heat loss errors. For the detailed calculation, see Section F.3 of Appendix F.

The reference value of 10 W/m indicates that for concentrating collectors an acceptable heat loss identification is only possible (according to Figure 7.2(a)) with fluid temperatures above 150 °C. If already in theory—by evaluating artificial measurement data—a distinct identification of heat loss values is difficult, it will even be more difficult in real collector testing.

Note that until now, overall error values of the heat loss identification over the entire temperature range were analyzed and no absolute values of u_0 and u_1 were compared. Past evaluations of absolute values have shown that several pairs of heat loss coefficients u_0/u_1 describe the absolute heat loss curve over the fluid temperature range very similar, provoking a remarkable correlation of the two parameters. As a result, the corresponding error values are similar as well. To demonstrate this correlation, individual identification results of u_0 and u_1 are sketched in Figure 7.3. Hereby, the particular results of all ten forks are depicted in contrast to the results illustrated before, which consisted of mean values over all ten forks. The contour plot in the background of the figures depicts the corresponding heat loss error $\varepsilon(u_0, u_1)$ at this coordinate [Nettelstroth, 2015, p. 28]. The previously introduced reference value is taken as an upper limit for the contour plot. Thereby,

[10]Note that the introduction of this reference value does not claim universal validity nor absolute guarantee of appropriateness for this comparison. It merely represents an attempt of deriving a means to somehow classify the complex issue of heat loss error by introducing a rough indication value.

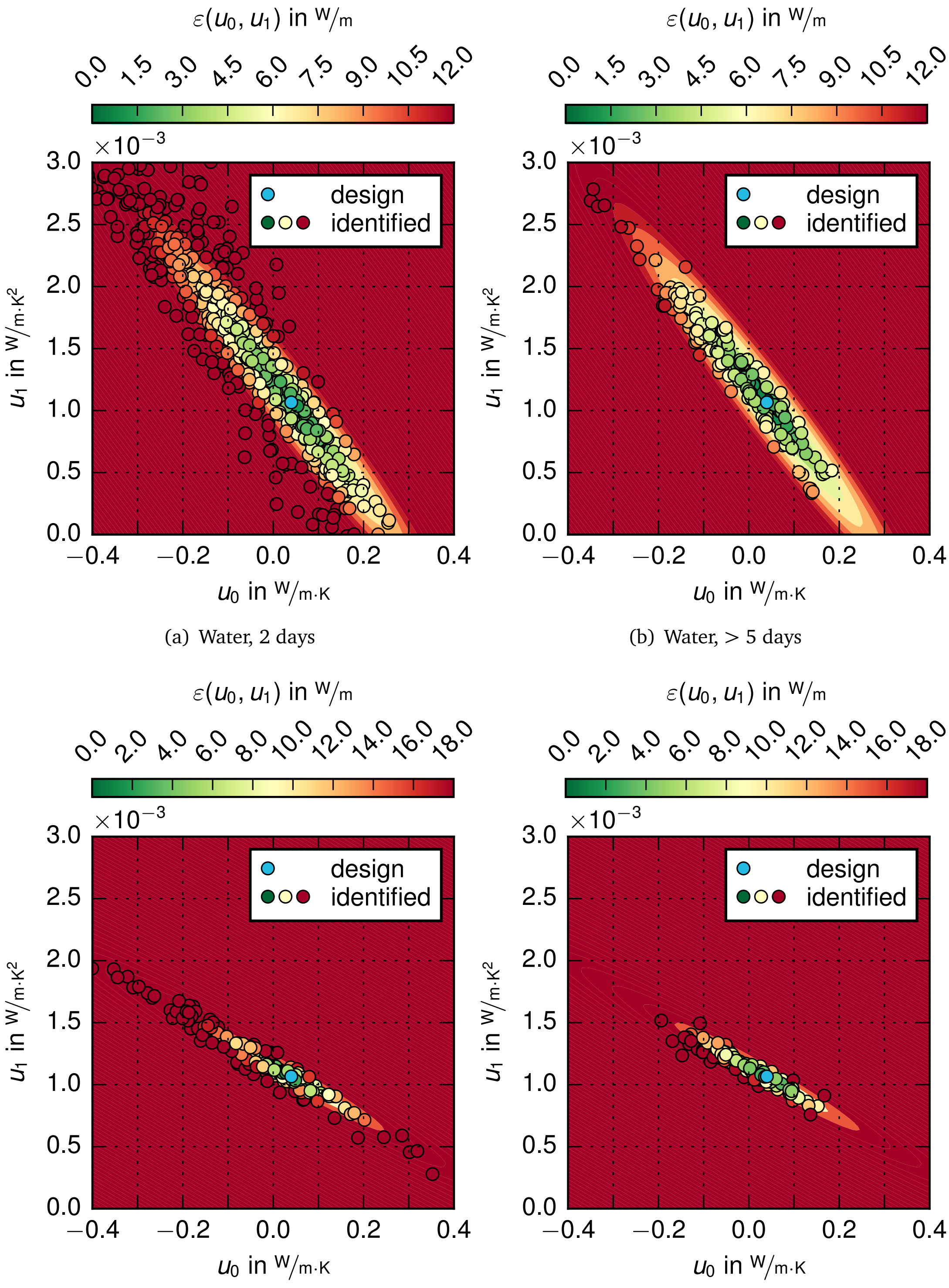

(a) Water, 2 days

(b) Water, > 5 days

(c) Molten salt, 2 days

(d) Molten salt, > 4 days

Figure 7.3: Illustrated correlation of identified heat loss coefficients for different evaluations. u_0- versus u_1-values for all identifications of evac at a noise level of 0.5 % are depicted. The rows show the results for water (a,b) and salt (c,d), whereas the columns represent the number of included measurement days of 2 (a,c), >5 (b), and >4 (d). The background contour plot indicates $\varepsilon(u_0,u_1)$. [updated from Nettelstroth, 2015, p. 29]

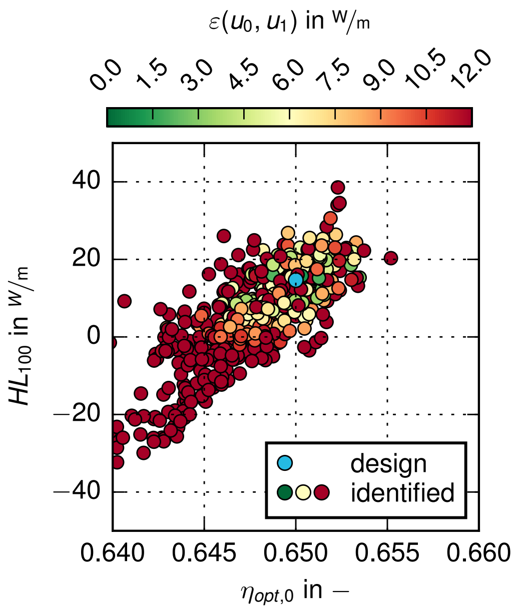

(a) 2 measurement days

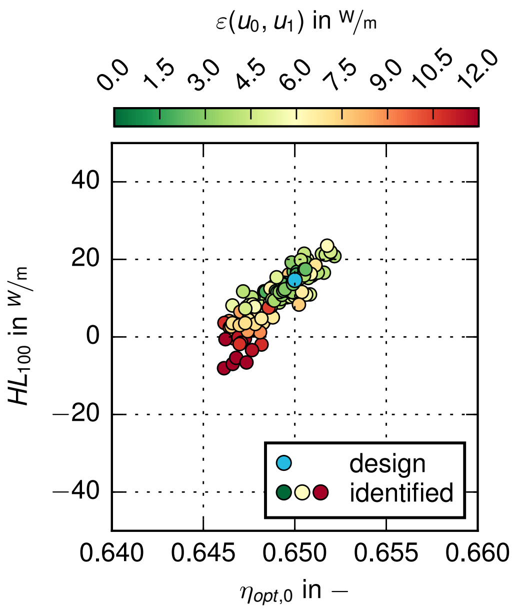

(b) >5 measurement days

Figure 7.4: Correlation of identified efficiency and heat loss for all identifications of water, evac at a noise level of 0.5 %. $\eta_{opt,0}$ versus HL_{100}-results are given for a number of included measurement days of 2 (a) and >5 (b) with coloring of data points according to the absolute heat loss error $\varepsilon(u_0, u_1)$.

the resulting color valley indicates acceptable heat loss identification results. Comparing the different HTFs shows that the arising correlation is more pronounced for water than for molten salt. It thereby illustrates the positive effect of higher absolute heat loss. For water, a wider band of acceptable identification results is discernible, allowing seemingly implausible negative u_0-values, which are however leading to small—but realistic—heat loss values. By increasing the number of measurement days (as already seen in conclusion **G 3**), the identification results reduce their dispersion and gather within the yellow/green valley of acceptable heat loss values. However, correlation of u_0/u_1 can be minimized, but hardly avoided. As a result, individual parameter values of heat loss coefficients are not recommended to be compared, but rather the parameter pair and the implied values. For this reason, it was chosen to evaluate overall heat loss error values in terms of $\varepsilon(u_0, u_1)$ and $\varepsilon_{rel}(u_0, u_1)$.

Conclusion T 1.2:

> The lower the amount of overall heat loss, the harder a distinct identification of the heat loss value and uncorrelated heat loss parameters.

To study the further correlation of optical and thermal performance parameters, it was accordingly considered more meaningful to compare $\eta_{opt,0}$-values with absolute heat loss values at a certain reference temperature instead of directly comparing $\eta_{opt,0}$ to individual u_0 or u_1. The correlation of optical efficiency at normal incidence versus absolute heat loss are depicted in Figure 7.4. In this case, the variable HL_{100} represents the corresponding heat loss of u_0/u_1 at a reference fluid temperature difference of 100 K. The coloring of data points according to the corresponding heat loss error illustrates: the more precise the heat loss is identified, the more precise $\eta_{opt,0}$ is determined as well. Furthermore, the results clearly point out that the correlation of $\eta_{opt,0}$ and HL_{100} can be significantly decreased, as in the given example, by increasing the number of measurement days. However, parameter correlation cannot be prevented completely, as even for a good heat loss identification (as marked in Figure 7.4(b) by green dots) a slight correlation remains associated to the induced measurement uncertainties. The results reveal the issue of a simultaneous deduction of performance parameters from thermal testing: a 100 % distinct separation can merely be achieved, because even for theoretical results (based on artificial data) a correlation cannot be completely prevented. However, correlation can be reduced to a minimum, allowing meaningful and dependable performance evaluations. Consequently, this drawback is considered to be acceptable with regard to the powerfulness and practicability of the introduced methodology. Certainly, special care has to be applied in thermal collector testing, paying particular attention to a proper selection and installation of measurement instrumentation, as well as an appropriate testing strategy in order to minimize potential error sources. Only in this way, the evaluation procedure is stabilized and may provide representative and reliable performance parameters. Be aware that identified parameter values are only valid as a conjunction and should therefore never be reported nor assessed individually. Equally, the valid or tested temperature range should be specifically indicated.

Influence of DNI

Previous results showed that a good heat loss identification quality positively influences the reduced error of $\eta_{opt,0}$ as well. For this reason, further factors are studied to potentially improve the heat loss results and therefore the overall identification quality. With regard to the incoming solar irradiance to the test collector, the impact of DNI dynamics dG_{bn}/dt were analyzed. For molten salt, three different irradiance levels of measurement data were created: a cloudless day, a day partly clouded, and a predominantly overcast day throughout the entire day (see Figure 7.5). Evaluations were performed based on the very same combination of base days, receiver configuration, and noise levels but with varying characteristics of DNI dynamics. In 84.7 % of the 192 compared cases, the days with higher dynamics provoked a better identification result of $\eta_{opt,0}$ as a cloudless day. For the heat loss identification quality, 87.6 % of the comparisons showed better results with increasing dynamics. This may indicate that with increasing dynamics, the variation of the outlet temperature is more pronounced, therefore comprising more information at different temperatures.

However, caution is recommended with this interpretation for two reasons. First, an increase of DNI dynamics only results in a slight improvement of the identification quality, in an exemplary best case for $\varepsilon_{rel}(\eta_{opt,0})$ from approximately 0.5 % to 0.1 %. Second, this effect is only perceptible for higher noise levels. In the case of no noise, only 57 % of the cases confirm this relation, while it is more pronounced in >90 % of the cases for 0.5 %-noise level. This tendency may be linked to the associated relative noise applied during the creation of artificial data. As a result of increasing dynamics in DNI, the daily mean values of DNI decreases (compare to Figure 7.5) from values of approximately 900 W/m^2 to values of 550 W/m^2. Because the noise is applied relatively to the variable, cloudless days are provoked with higher noise than days with higher DNI dynamics. Analog to conclusion **G 2** of Section 7.1.2, this may affect the validity of the found tendency. Fur-

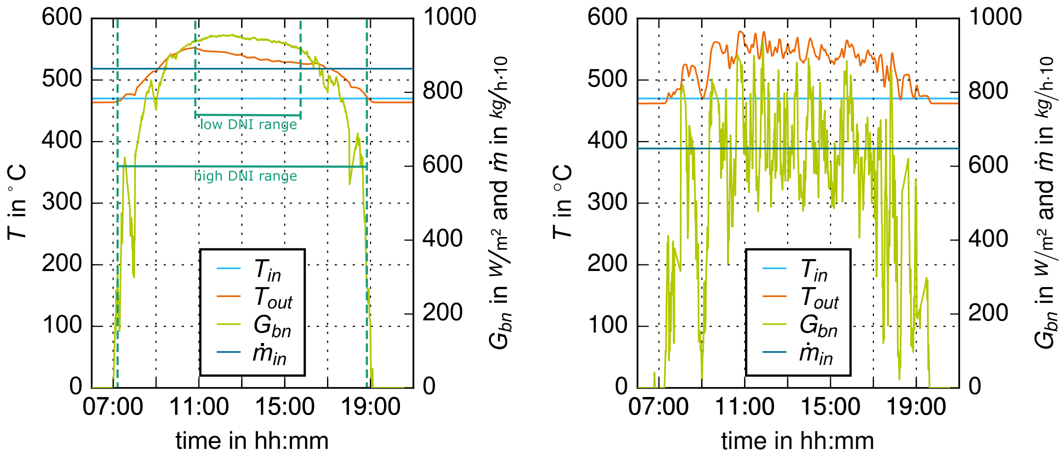

(a) cloudless measurement day (b) partly clouded measurement day

Figure 7.5: Exemplary artificial measurement days comprising different DNI dynamics. Data of a cloudless measurement day (a) show smaller fluctuations than for a partly clouded day (b). [adapted from Nettelstroth, 2015, p. 26]

thermore, note that the concept of artificial data creation does not include the aspect commonly found in reality of a higher measurement uncertainty for lower irradiance values. While the tendency of a positive effect of DNI dynamics cannot be verified for sure, a negative influence cannot be stated either. In this way, the results indicate that data with higher DNI dynamics do not necessarily imply worse identification quality. Consequently, completely steady-state DNI conditions are not required for a meaningful collector test, as desired for dynamic, outdoor, in-situ performance evaluations. This is valid under the mentioned condition of equal irradiance uncertainty $u(G_{bn})$, which is not always valid in practice for extreme cases. A more elaborate analysis concerning this aspect in reality is given in Section 7.2.4.

In addition to the DNI dynamics, the influence of the DNI range was analyzed. For this reason, results for a typical DNI course of a complete, cloudless measurement day, including sunrise and sundown with collector warm-up and shutdown, were compared to completely steady DNI conditions at one constant DNI level. The latter corresponds to measurement periods as exemplarily depicted in Figure 7.5(a) between 11 a.m. and 4 p.m. For this particular study, noise was applied only on the variables of outlet temperature and irradiance. Table 7.7 summarizes the corresponding results. They reveal that steady-state DNI data (=low range) imply a larger error value, for both optical and thermal parameters. Nevertheless, this tendency has to be treated with some degree of care as well. The reduction of the artificial measurement days to periods of approximately solar noon comes along with a reduction of available measurement points. Analog to conclusion **G 3**, this could lead to a reduction of identification quality, because less (even if repeated) information content is available. However, similar to the DNI dynamics, the results indicate that constant DNI levels (resulting in steady-state collector operating conditions) are not considered a requirement for meaningful performance testing. To the contrary, they might actually induce a negative effect with less accurate and less precise identification results. Therefore, measurement data of an entire day, including periods of

Table 7.7: Influence of DNI range on identification quality. A constant DNI level (=low range) is compared to a cloudless DNI course of an entire day (=high range). Results are considered as mean values over all operating conditions, day combinations, forks, and noise levels.

Receiver	Variable	Unit	Constant DNI level (=low DNI range)	Cloudless DNI day course (=high DNI range)
Evac	$\varepsilon_{rel}(\eta_{opt,0})$	%	0.92	0.18
	$\varepsilon(\eta_{u_0,u_1})$	W/m	28.5	13.8
Non-evac	$\varepsilon_{rel}(\eta_{opt,0})$	%	1.03	0.13
	$\varepsilon(\eta_{u_0,u_1})$	W/m	32.5	12.6

warm-up and cool-down of the collector with lower DNI values are valid and even recommended to use, as they do not interfere and potentially even improve the quality and robustness of the evaluation results.

Conclusion T 2:

Varying DNI range and dynamics do not interfere with an accurate and precise identification quality of heat loss and optical efficiency.

Influence of Operating Conditions

Similar to the dynamics in DNI, the influence of operating conditions on the identification quality was analyzed. As introduced in Section 7.1.1, different inlet temperature settings were compared: constant temperature, quick temperature rise, and gradual temperature curve over the entire day. Meanwhile the other boundaries such as the heat transfer fluid, combination of days, temperature levels, and noise were kept constant. For example, three water days with noise level 0.5 % at maximum temperature level with constant temperature are compared to three water days with noise level 0.5 % at the same maximum temperature level with a quick temperature rise. Under the condition of a constant mass flow rate, changes in inlet temperature lead to changes in the outlet temperate course. In 52 % of the 42 comparisons performed, a constant inlet temperature was identified better than a temperature jump. Similarly, 64 % of 42 comparisons lead to a better result of a constant inlet temperature in comparison to a smooth temperature in-/decrease. In 55 %, the temperature jump improved the heat loss identification quality compared to a smooth temperature curve. Thereby, the results slightly do not favor a smooth inlet temperature course. Though, the present values do not allow any distinct statement concerning a positive or negative influence of inlet temperature settings.

In the case of a controlled mass flow rate, the outlet temperature is controlled to a constant value. For this operating strategy, in 79 % of the 48 comparisons a constant inlet temperature provides better results than a temperature jump. A smooth temperature curve results in a better heat loss identification quality in 65 % of the compared cases with a constant inlet temperature, as well as in 90 % of the comparisons with a temperature jump. In contrast to the results of a constant mass flow rate, they reveal a slight favoring of a smooth inlet temperature curve, impeding the derivation of an unambiguous tendency.

Concerning the effect of mass flow rate, in 41 % of the 45 performed comparisons the constant mass flow rate shows better results than the controlled one. Again, no clear trend is discernible. All in all, the analysis of operating conditions points out the marginal influence of operating conditions on the identification quality. Consequently, under the assumption of independent measurement uncertainty, no specific operating conditions are required for an accurate, precise, and stable performance evaluation.

Conclusion T 3:

Neither the course of mass flow rate within the measurement data, nor the course of fluid temperatures largely influence the identification quality.

Another factor potentially impacting the heat loss identification quality represents the temperature span of fluid temperatures included in the identifications. Accordingly, measurement day combinations were compared featuring one high temperature level (such as the already above introduced case of `A4B4C4D4`) with day combinations comprising different temperature level as exemplarily `A4B4C1D1`. In 83 % of the 18 comparisons for water, the heat loss error improved with an increasing temperature span by including a higher and lower temperature level in the evaluation. For molten salt, in 96.6 % of 30 compared cases a higher temperature span showed a better heat loss quality than a lower one.

Note, however, that the improvement of identification quality is not as dominant as the effect of the temperature level itself as concluded in **T 1.1**. The reason for salt revealing a more distinct result than water may originate from a different starting value of temperature spans. While the temperature span at the higher temperature level for `A4B4C4D4` amounts approximately 15–20 K for salt, it already amounts approximately 45 K in the case of water. Thereby, the effect of increased temperature span of `A4B4C1D1` is more pronounced for molten salt than for water. In the water case, the starting point is already more elevated. Nonetheless, both, water and molten salt identification quality, improve by an increasing temperature span, even though the effect is not as significant as others. Consequently, if feasible in practice, a higher temperature span positively influences the accuracy of heat loss identification, but does not present neither a necessary nor a sufficient condition.

Conclusion T 4:

Of subordinate importance, the condition of a larger temperature span slightly improves the heat loss identification quality.

■ 7.1.4 Study Concerning Optical Identification Quality

Influence of Minimum Fluid Temperature

Analog to the previous analysis, the effect of the temperature span on the quality of identifying $\eta_{opt,0}$ was evaluated. Accordingly, for 88.9 % of the 18 compared cases, the optical efficiency at normal incidence improved when using water, while only 53.3 % of the 30 comparisons showed the same tendency for molten salt. In the case of water, comprising a higher temperature range—this is equivalent to lower minimum fluid temperatures—mainly decreases error values of $\eta_{opt,0}$. However, in a best case, the improvement is less pronounced from exemplary 0.3 % to 0.1 %. For molten salt, no distinct tendency is discernible. As a result, a lower minimum fluid temperature improves the optical identification quality, but is not as dominant as to require it for an adequate performance testing. In view of the current testing standard ISO 9806 [2013, p. 51], which demands a testing of $\eta_{opt,0}$ at near-ambient temperature conditions of ±3 K, the present results do not support this strict condition. If feasible in practice, a lowest fluid temperature as possible is recommended. Though, a specific fulfillment of particularly distinct near-ambient fluid temperatures is not required for concentrating collectors. Because concentrating collectors comprise a lower heat loss compared to the optical input, an extrapolation of $\eta_{opt,0}$ from non-zero heat loss conditions at higher fluid temperatures seems to still provide accurate results. Concerning the validity of this conclusion drawn from artificial data, a cross-check with real measurement data is certainly advised as given in Section 7.2.1.

Conclusion O 1:

> The temperature range and accordingly the minimum fluid temperature do not significantly affect the identification of $\eta_{opt,0}$.

Influence on IAM Identification Quality

Concerning the quality of IAM identification, a separate study was designed using molten salt as a heat transfer fluid. The main reason for choosing molten salt instead of water lies in the faster computation time, originating most probably from a simpler and consequently faster library of fluid properties [Nettelstroth, 2015, p. 31]. The general aspects as number of measurements days and noise levels also apply for this study. Specific results are given in Section F.4 of Appendix F.

As previously discussed in conclusion **G 3** of Section 7.1.2, the combination of measurement days improves the identification quality of $\eta_{opt,0}$ and heat loss. This is equally valid for an identification of IAM. For the identification of values for every specific incidence angle, the occurrence and distribution of incidence angles are supposed to be similarly crucial. Commonly, a collector test is performed within one continuous measurement time period. That is why a study was performed comparing results from one measurement week during summer (Case a) with one measurement week during autumn (Case b). Figure 7.6 illustrates the respective longitudinal and transversal IAM errors for

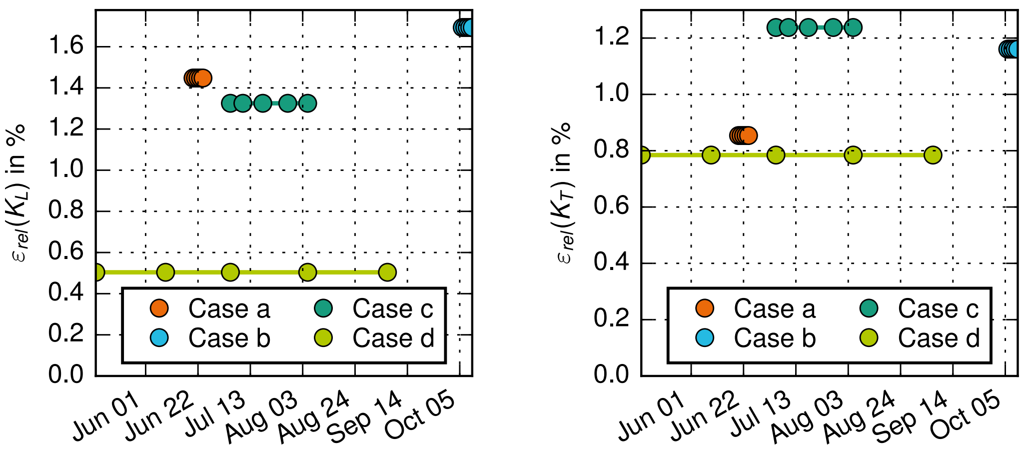

(a) Longitudinal IAM error

(b) Transversal IAM error

Figure 7.6: IAM identification quality including continuous versus discontinuous days within different seasons. Exemplary mean longitudinal (a) and transversal (b) IAM identification error over all forks with evac and 0.5 %-noise level for different combinations of measurement days.

both weeks[11]. As a reference, two exemplary cases of more spread measurement days between July to August (Case c) and May to September (Case d) are sketched as well. The results clearly indicate that the week in June performs significantly better than the week in October. The discontinuous day combinations follow the same tendency with better results than the measurement week in October. Moreover, they principally show a slightly better identification than the summer week as well. To better understand the found tendency, the included angle spread of the different measurement days was analyzed as given in Figure 7.7. The remarkable difference between days in October and days in June is that the days in October merely comprise any θ_{LS}-values equal to zero (just for really high θ_T). As a result, longitudinal angles from zero to approximately 35 ° only occur at one specific other transversal angle. This may cause correlated longitudinal and transversal IAM values, since always the very same specific angle pairs arise. For the measurement week in summer, two measurement points at a longitudinal angle of zero appear, which may cause a significantly more stable quality of IAM determination. For the occurring angle pairs (θ_T, θ_{LS}), if one of the angles is zero, the other can be distinctly determined. The correlation of both parameters may therefore decrease with more data at one angle equal to zero. According to this relation, is seems plausible that the identification quality increases for both discontinuous measurement day combinations. In these cases, both angles are very well spread more or less over a wide angle space featuring several zero-intersection points. In this way, a specific longitudinal angle arises with different transversal angles, reducing correlation and hence improving the identification quality. Note that merely the transversal error for the case of discontinuous days from July to August is worse than the measurement week in summer, contradicting the previous conclusion. The reason for this originates from the very large transversal angles greater than 80 °. In this angle bin, only few data points are available. Consequently, measurement uncertainty (in terms of the applied noise) may cause severe deviations to the true value. If this angle bin is excluded from the error calculation, $\varepsilon_{rel}(K_T)$ improves to approximately 0.77 % confirming the above drawn conclusion.

All in all, to improve the IAM identification quality a wide spread of incidence angle pairs over the entire angle space is recommended. Therefore, summer periods should be preferred when continuous measurement periods are required. Attention should be paid that measurements comprise enough data at zero incidence angle for longitudinal and transversal direction. Even if data in autumn may provide valuable angle information at higher values increasing the length of the identifiable IAM curve, they are not suited on their own to properly characterize the angle dependency of a collector. To reduce correlation and stabilize the evaluation results, summer measurement periods are therefore advised. To further assure a good characterization of angle dependency, if feasible, a combination of data of two measurement periods may present a valuable option as well.

Conclusion O 2:

> The more spread the angle pair of (θ_T, θ_{LS}) and the more data available at zero incidence of one angle, the higher the optical identification quality and lower the correlation of longitudinal and transversal IAM parameters.

[11]Notice that the occurring incidence angles during summer and autumn strongly depend on the location (in this case: Spain) and the orientation (in this case: 17 ° to West) of the collector under test. The findings of the present analysis apply to other test situations as well, as long as analog incidence angle situations are determined.

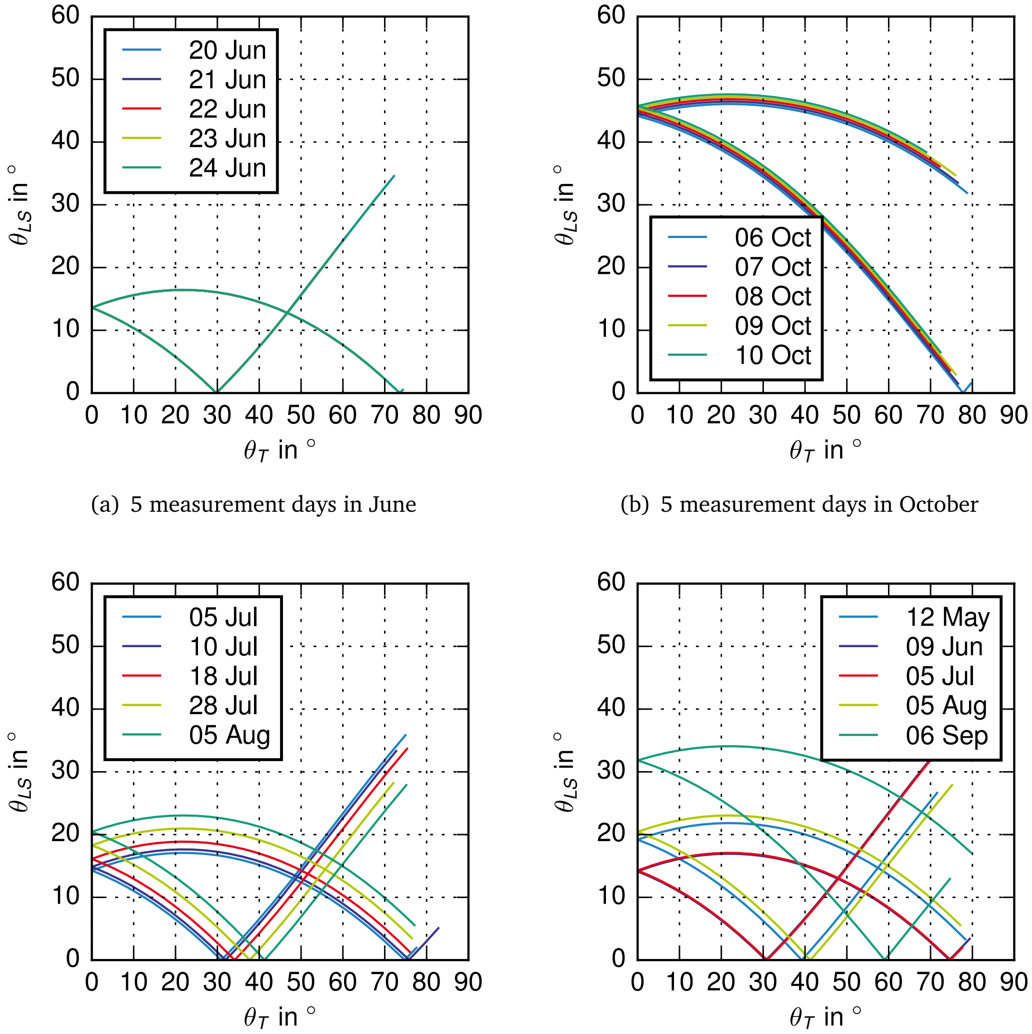

(a) 5 measurement days in June

(b) 5 measurement days in October

(c) 5 measurement days in July to August

(d) 5 measurement days in May to September

Figure 7.7: Occurring angles of incidence for exemplary identifications. Angles θ_T versus θ_{LS} of five measurement days in June (a), October (b) July to August (c) and May to September (d).

■ 7.2 Validation to Real Measurement Data

To increase the dependability of the conclusions derived from the artificial data analysis in Section 7.1, they were additionally validated by detailedly studying real collector data of a large measurement data basis. The data originate from the measurement campaign at collector LFC_w2 ranging from March to October of the corresponding test year. Details of this collector are summed in Table 2.2. The entire measurement data basis was evaluated by means of random sub-sampling as introduced in Section 5.1.4. To address the relevant aspects of a testing strategy, several different studies were performed and their conclusions are presented in the following. At the end of this chapter, a summary of those conclusions will be given in Section 7.3. Due to the powerful capabilities of RSS, some of the studies not only allow for conclusions concerning the testing strategy, but additionally entail aspects of an evaluation strategy as well (which will be marked with the capital letter of '**E**'). However, both aspects on how to test (i.e., how to gather measurement data) and how to evaluate the collector data, are considered important elements in the context of reliable and representative performance testing.

■ 7.2.1 Reduced Study without Identification of IAM

Due to the stepwise identification of IAM values for an LFC collector, the evaluation complexity rises from only three identification parameters without IAM identification to around 30–100 parameters including IAM identification (depending on the angle step size of the IAM curve). To be able to separate effects associated to the IAM identification from aspects concerning the general evaluation and thermal parameters, in a first study (similar to the proceeding for the artificial data evaluation) the optical efficiency at normal incidence $\eta_{opt,0}$ and the heat loss parameters u_0/u_1 were evaluated.

Heat Loss Model

Already in Hofer et al. [2015a] problems with a proper identification of heat loss parameters for concentrating process heat collectors were reported. Accordingly, in the artificial data evaluation significant correlation of heat loss parameters was revealed. For this reason, an initial study was designed to show if the heat loss model using both coefficients is appropriately describing the heat loss of the collector, or if it is over-parametrized and the use of merely one heat loss parameter recommended. Therefore, three evaluations were performed: one identifying both coefficients u_0/u_1, one only identifying u_0 and a third one identifying only u_1. For all three cases, $\eta_{opt,0}$ was determined as well. Every evaluation was based on the identical RSS procedure including the very same data basis of randomly chosen ten days. This means that the ten measurement days to be evaluated were randomly chosen (in this case 500 times) once for all three cases and only the identification procedure (with or without including the determination of u_0 or u_1) was changed in order to allow a direct comparison of the results. Table 7.8 lists the mean RMS value and its mean standard deviation σ(RMS) for the three studies. They show that the identification of both coefficients u_0/u_1 entails the lowest RMS values, that is, the best fit between simulated and measured data. Even though the RMS is only slightly better for the heat loss model with both coefficients, the use of only one parameter does not present any additional advantage. While comparing every single identification, in some cases the model u_0 outperforms the model u_1 and vice-versa, but both models always fall behind or present equal results as the model u_0/u_1. As there is no discernible reason for reducing

Table 7.8: RSS results for an identification of different heat loss models. An identification of both heat loss coefficients u_0/u_1 shows the lowest RMS value, while the other models do not comprise any additional advantage.

Model		u_0/u_1	u_0	u_1
Mean RMS	K	0.2941	0.2982	0.2951
Mean σ(RMS)	K	0.0652	0.0652	0.0655

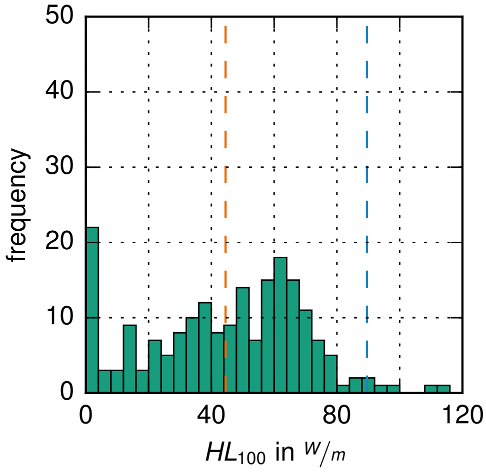

(a) Histogram plot of HL_{100}

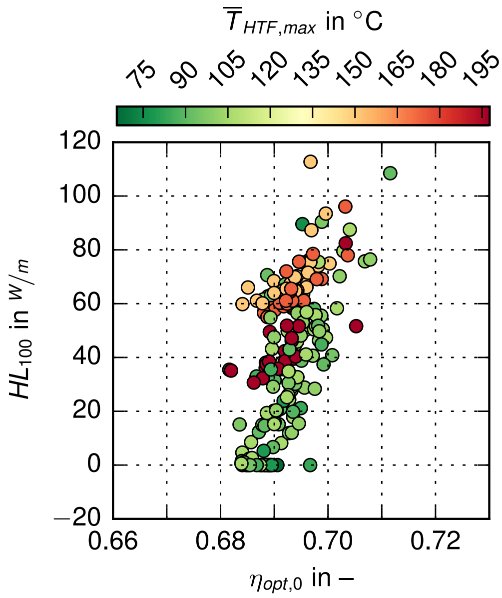

(b) Covariance plot of $\eta_{opt,0}$ vs. HL_{100}

Figure 7.8: RSS results for reduced study without IAM identification. Histogram of identified heat loss HL_{100} at 100 K fluid temperature difference (a) and covariance plot of identified $\eta_{opt,0}$ versus HL_{100} with coloring of data points by maximum fluid temperature level (b).

the heat loss model, in the further evaluations always both heat loss parameters u_0/u_1 were identified.

Having a look at the dispersion of the heat loss as depicted in Figure 7.8(a)[12], the poor and hence insignificant identification of heat loss becomes apparent. This is conform to the conclusion **T 1** of Section 7.1.3, as the present collector consists of a process heat collector with an evacuated glass tube absorber featuring small overall heat loss values and therefore deteriorating heat loss identification results. Furthermore, results depicted in Figure 7.8(b) particularly verify conclusions **T 1.1** and **T 1.2**, as it shows the evident correlation of $\eta_{opt,0}$ versus the collector heat loss (in this case at 100 K). The lower the overall heat loss of a receiver, the less the heat loss contributes to the objective function of the collector power output and the more difficult its correct and distinct identification (**T 1.2**). The coloring of the data points according to the maximum fluid temperature level reveals the fact that the higher the fluid temperature level, the better—less disperse and more distinct—the heat loss identification results (**T 1.1**).

Temperature Level Criteria

All outliers of the heat loss identification in Figure 7.8(b), and especially those with an unrealistic value of zero heat loss, share the property of a very low maximum fluid tem-

[12] Equally to the value in the artificial data evaluation, the shown variable HL_{100} refers to a summarized value of u_0 and u_1 by calculating the heat loss with both coefficients at a specified reference fluid temperature difference, in this case at 100 K.

Table 7.9: Effect of including a maximum fluid temperature selection criterion within the RSS procedure. All values are considered as mean values over all randomly drawn datasets.

Variable	Unit	With T_{max}-criterion	Without T_{max}-criterion
$\eta_{opt,0}$	%	69.3	69.3
$\sigma(\eta_{opt,0})$	%-pts.	0.4	0.5
$CI(\eta_{opt,0})$	%-pts.	$-0.8/+0.8$	$-0.9/+1.1$
HL_{100}	W/m	60	44
$\sigma(HL_{100})$	W/m	13	25
$CI(HL_{100})$	W/m	$-25/+24$	$-44/+46$
HL_{150}	W/m	129	87
$\sigma(HL_{150})$	W/m	27	53
$CI(HL_{150})$	W/m	$-52/+37$	$-87/+83$
HL_{200}	W/m	223	144
$\sigma(HL_{200})$	W/m	50	96
$CI(HL_{200})$	W/m	$-92/+68$	$-144/+152$

perature level[13]. For this reason, selection criteria have been added to the random subsampling procedure. While nine of the ten days are still randomly chosen of the measurement data basis, one measurement day (i.e., the tenth) has to fulfill certain temperature criterion. For the following study, the criterion was set to a maximum outlet fluid temperature of greater than 150 °C. Table 7.9 represents the results of the study including and not including a temperature criterion in the RSS procedure based on 200 random drawings. While the identification quality of the optical efficiency $\eta_{opt,0}$ is only slightly improved by the newly introduced selection criterion, this effect dominates the heat loss quality. Both, standard deviation σ and confidence intervals CI, are significantly improved, allowing a more distinct identification of heat loss parameters (from 25 to 13 W/m in $\sigma(HL_{100})$). Figure 7.9(a) in comparison to Figure 7.8(a) illustrates this improvement, since the histogram of identified heat loss HL_{100} tends to a better defined normal distribution.

However, correlation of $\eta_{opt,0}$ and HL_{100} cannot be completely ruled out as depicted in Figure 7.9(b). The higher the identified heat loss, the higher the identified optical efficiency at normal incidence. An additional evaluation was performed analog to the study including the temperature selection criterion and considering the very same measurement data basis, but only identifying thermal parameters u_0/u_1 (and keeping $\eta_{opt,0}$ constant). It showed an equally pronounced dispersion of heat loss. This implies that the indistinct identification of heat loss parameters does not originate from the correlation of optical and thermal parameters, but rather from a different source as, for example, the measurement uncertainty. To enable a maximum reference value for acceptable heat loss identification quality, the proceeding as proposed in the excursus of Section 7.1.3 was followed. It takes into account the actual error propagation of the measurement uncertainty of the collector under test as detailedly described in Chapter 6. In this way, a reference standard deviation of 22 W/m for the heat loss identification quality of this collector can be derived[14]. In comparison to the mean standard uncertainty of $\sigma(HL_{100})$ with a value of 13 W/m, the dispersion might have to be accepted, particularly as the error values are already—as desired—considerably smaller than the maximum acceptable reference value.

[13]The maximum fluid temperature level is calculated by taking the maximum of the daily mean outlet fluid temperatures of all randomly chosen measurement days, i.e., 'level' refers to the daily mean of the outlet fluid temperature.

[14]For the complete derivation of the exact value, see Section F.3 of Appendix F.

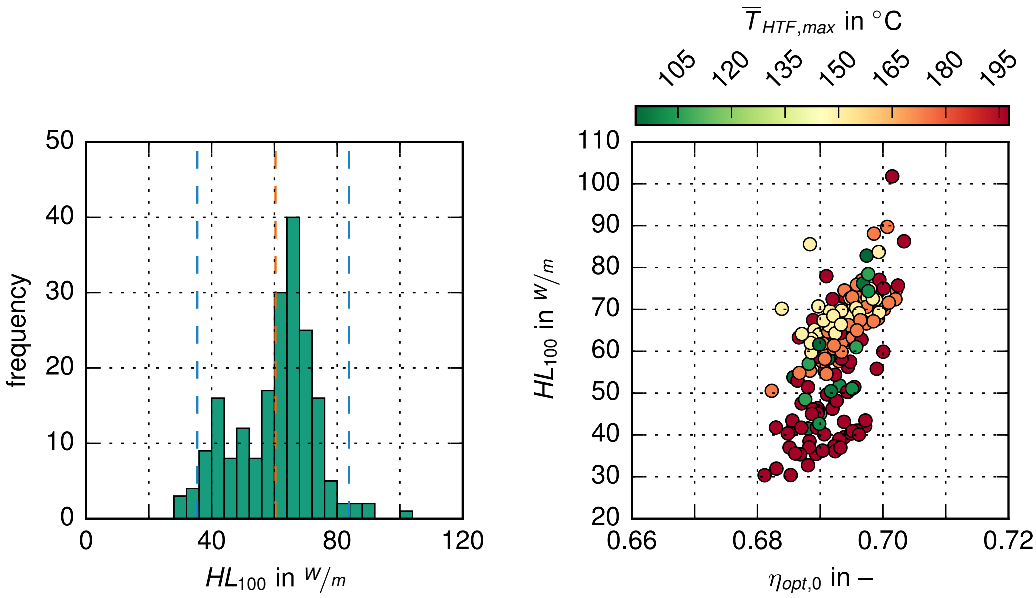

(a) Histogram plot of HL_{100} (b) Covariance plot of $\eta_{opt,0}$ vs. HL_{100}

Figure 7.9: RSS results including a maximum fluid temperature selection criterion. Histogram of identified heat loss HL_{100} at 100 K fluid temperature difference (a) and covariance plot of identified $\eta_{opt,0}$ versus HL_{100} with coloring of data points by maximum fluid temperature level (b).

Note that the acceptable standard uncertainty and dominant improvement of confidence intervals is only valid for the heat loss at a fluid temperature difference of 100 K. The standard uncertainty for HL_{150} entails a higher value of 27 W/m slightly above the limit of the maximum acceptable reference value (see Table 7.9). Moreover, the corresponding heat loss histogram shows ambiguous values and does not tend to a normal distribution. This higher dispersion may have to do with the prevailing fluid temperatures for the heat loss identification. The mean value over all RSS identifications of the maximum temperature level lies around 169 °C. This implies that on average the maximum available temperature level is approximately 169 °C, representing the upper temperature edge of the tested heat loss curve. The fluid temperature of 169 °C is more or less equivalent to a temperature difference of 150 K (considering a mean ambient temperature of 20–30 °C), which is the basis for the calculation of HL_{150}. Seemingly, the heat loss at the upper edge of the available fluid temperatures is characterized according to the maximum induced measurement uncertainty (i.e., the reference standard deviation). Similar results are discernible for HL_{100} without the T_{max}-criterion: here, the mean value of the maximum temperature level is approximately 130 °C. This is more or less equivalent to a temperature difference of 100 K (considering a mean ambient temperature of 20–30 °C), which is the basis for the calculation of HL_{100}. HL_{100} is likewise identified according to the maximum reference measurement uncertainty of 25 W/m, showing an indistinct histogram (compare to Figure 7.8(a)).

Certainly, these results are not satisfactory and illustrate in a practical way the challenge of heat loss identification for systems with large optical input and low thermal loss. As the heat loss represents a minor part of the optically gained power, it is less character-

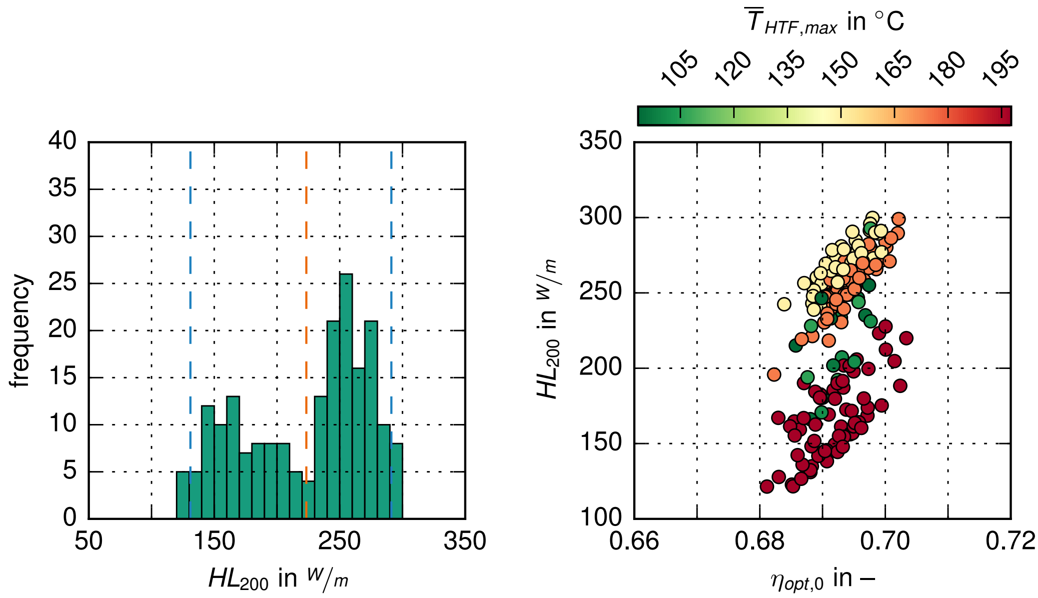

(a) Histogram plot of HL_{200} (b) Covariance plot of $\eta_{opt,0}$ vs. HL_{200}

Figure 7.10: RSS results including a maximum fluid temperature selection criterion for HL_{200}. Histogram of identified heat loss HL_{200} at 200 K fluid temperature difference (a) and covariance plot of identified $\eta_{opt,0}$ versus HL_{200} with coloring of data points by maximum fluid temperature level (b).

istic to the collector power output and problems with a distinct determination arise. With low fluid temperatures the measurement uncertainty of the system is so dominant that no clear characterization is possible. Only by increasing the working fluid temperature, the heat loss increases (and its respective share to the collector power output), minimizing the influence of measurement uncertainty. Consequently, not only the heat loss at higher temperatures (e.g., HL_{150}) is identified better, but also the heat loss identification quality at lower temperatures improves significantly. This implies that a good quality of higher-temperature heat loss has a positive effect on the quality of heat loss at lower temperatures as well. While the maximum edges of a tested fluid temperature range are dominated by the maximum corresponding measurement uncertainty, the middle part of the temperature range may be determined more robust. This is conform to conclusion **T 1.1** as with higher temperature levels, the overall identification quality is enhanced.

Caution has to be applied, when heat loss is extrapolated to temperature levels larger than the maximum edges tested, which is demonstrated by the results of HL_{200} depicted in Figure 7.10. Similar to the histogram of HL_{150}, the identified heat loss at 200 K entails a broad dispersion. Particularly, Figure 7.10(b) shows the error-prone effect of extrapolation. Only for the points marked in deep red, fluid temperatures of larger than 200 °C are available. All other data points represent extrapolated values from lower fluid temperatures significantly shifted to higher heat loss values than apparently real. Be aware, while a higher fluid temperature still dominantly increases the identification quality for HL_{200}, it does not positively influence HL_{100} anymore (compare Figure 7.10(b) to Figure 7.9(b)). With the temperature selection criterion, for HL_{100} enough information is

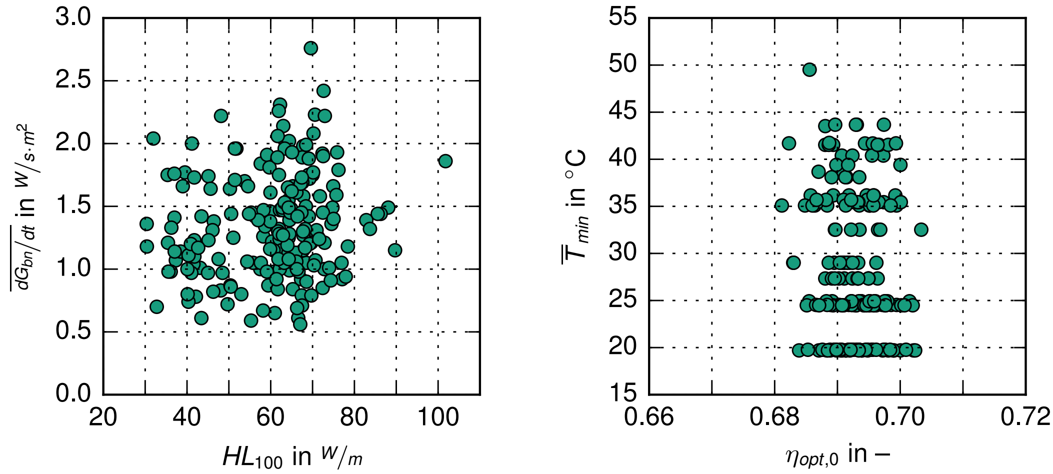

(a) Covariance plot of HL_{100} vs. $\overline{dG_{bn}/dt}$ (b) Covariance plot of $\eta_{opt,0}$ vs. $\overline{T}_{min}$

Figure 7.11: Influence of operating conditions on the RSS identification results. Covariance of heat loss versus mean DNI dynamics (a) and $\eta_{opt,0}$ versus mean minimum fluid temperature (b) based on RSS including a T_{max}-criterion.

available to adequately describe this value. All in all, the results confirm the validity of conclusion **T 1**, particularly emphasizing the dominant effect of **T 1.1**.

Furthermore, the present study allows to verify conclusions concerning the DNI dynamics and minimum fluid temperature included in the evaluation data. In Figure 7.11(a), the mean DNI dynamics of the evaluated measurement days are sketched with respect to the identified heat loss HL_{100}. Confirming conclusion **T 2** of Section 7.1.3, no clear tendency between dynamics in irradiance and identified heat loss is discernible. The same applies for values of $\eta_{opt,0}$, which is not particularly illustrated, but shows a similar graph to Figure 7.11(a). The dispersion of identified parameters is not influenced by dynamics in irradiance, approving the use of dynamic measurement data for accurate and representative performance testing. The requirement of the testing standard to determine $\eta_{opt,0}$ at near-ambient conditions was additionally checked for real data of concentrating collectors. Figure 7.11(b) confirms the tendency found in conclusion **O 1** of Section 7.1.4: near-ambient minimum fluid temperatures do not influence the dispersion of identified $\eta_{opt,0}$. Independent if fluid temperatures around ambient temperature exist in the evaluated measurement data, $\eta_{opt,0}$ is identified within a certain dispersion. Certainly, a wide span of temperature levels assures a robust determination of a more representative heat loss curve. Yet, results indicate that the inclusion of merely warm-up measurement periods with initially lower fluid temperatures is equally suited for process heat collectors operating with water as strictly fulfilling long-period, near-ambient test conditions. Note, however, that in the present case the level of minimum fluid temperature is never above 50 °C. This implies that conclusion **O 1** cannot be entirely validated for collectors exclusively working at higher fluid temperatures above 200 °C as in the case of collectors operating with molten salt or thermal oil. Nevertheless, a complete invalidation of conclusion **O 1** for high-temperature collectors is not expected, since the artificial data analysis indicates an opposite tendency.

7.2.2 Advanced Study with Identification of IAM

Evaluation with and without IAM Identification

Similarly to the previous analysis, a more advanced study was performed including an identification of IAM values. Therefore, the random sub-sampling procedure without the temperature selection criterion of the previous analysis was taken as a reference data basis and only the parameters to identify were adapted. This means that the very same drawings of randomly chosen measurement days as used for the results in Figure 7.9 and Table 7.9 without T_{max}-criterion were taken. The difference consists in amplifying the number of identified parameters from $\eta_{opt,0}$ and u_0/u_1 to $\eta_{opt,0}$, u_0/u_1, and all stepwise IAM values. This allows for a direct comparison of results including and not including an IAM identification as summarized in Table 7.10.

The results show that the absolute value of $\eta_{opt,0}$ decreases with an identification of the IAM. This is comprehensible, as the mean IAM value (especially in longitudinal direction K_L) is remarkably larger than the ray-traced reference IAM included in the evaluation without IAM identification. Therefore, the lower $\eta_{opt,0}$-value balances out the differences in the K_L-values. Concerning the identified heat loss, results reveal very similar absolute values, error values of standard deviation, and confidence intervals. Merely values for the standard deviation $\sigma(\eta_{opt,0})$ are significantly larger when identifying IAM values than without. A reason for this might have to do with the quality of identifying the IAM values. With the IAM being more disperse, the dispersion of $\eta_{opt,0}$-values increases as well. Influencing factors to the IAM identification quality are analyzed in Section 7.2.4.

Temperature Level Criteria with IAM Identification

To improve the identification quality of the heat loss parameters, the maximum fluid temperature selection criterion as proposed in the previous section was included into the RSS procedure involving an identification of IAM values. Because an IAM identification consists of numerous identified $K_T(\theta_T)/K_L(\theta_{LS})$-parameters (one for each transversal and one for each longitudinal angle bin), a new agglomerated variable $MURD$ (Mean Unsigned Relative Deviation) is introduced to provide a means to assess the overall quality of K_T/K_L. For example, the $MURD_{M,T}$-value consists of the mean unsigned relative deviation over all angle bins to its respective mean $\overline{K}_T$-value. This means that for each specifically identified $K_T(\theta_T)$-value, the deviation to its mean $\overline{K}_T(\theta_T)$ over all RSS iden-

Table 7.10: Comparison of RSS identification results of reduced study to advanced study including IAM identification. All values are considered as mean values over all randomly drawn datasets.

Variable	Unit	With IAM identification	Without IAM identification
$\eta_{opt,0}$	%	68.15	69.3
$\sigma(\eta_{opt,0})$	%-pts.	1.0	0.5
$CI(\eta_{opt,0})$	%-pts.	$-2.0/+2.0$	$-0.9/+1.1$
HL_{100}	W/m	47	44
$\sigma(HL_{100})$	W/m	24	25
$CI(HL_{100})$	W/m	$-47/+46$	$-44/+46$
HL_{200}	W/m	173	144
$\sigma(HL_{200})$	W/m	100	96
$CI(HL_{200})$	W/m	$-173/+200$	$-144/+152$

Table 7.11: Effect of including a maximum fluid temperature selection criterion within the RSS procedure with IAM identification. All values are considered as mean values over all randomly drawn datasets.

Variable	Unit	With T_{max}-criterion	Without T_{max}-criterion
$\eta_{opt,0}$	%	68.3	68.15
$\sigma(\eta_{opt,0})$	%-pts.	0.9	1.0
$CI(\eta_{opt,0})$	%-pts.	$-1.4/+2.0$	$-2.0/+2.0$
HL_{100}	W/m	62	47
$\sigma(HL_{100})$	W/m	14	24
$CI(HL_{100})$	W/m	$-25/+27$	$-47/+46$
HL_{200}	W/m	233	173
$\sigma(HL_{200})$	W/m	53	100
$CI(HL_{200})$	W/m	$-86/+82$	$-173/+200$
$MURD_{M,T}$	%	1.6	1.9
$\sigma(MURD_{M,T})$	%-pts.	0.8	0.8
$MURD_{M,L}$	%	1.9	2.5
$\sigma(MURD_{M,L})$	%-pts.	1.1	1.4

tifications of this angle bin is calculated. Then, the mean of this deviation is taken over all angle bins as defined by[15]:

$$MURD_{M,T} = \frac{1}{n} \cdot \sum_{i=0}^{n} \frac{|K_T(\theta_{T,i})_{ident} - K_{T,i}(\theta_T)_{mean}|}{K_{T,i}(\theta_T)_{mean}}, \tag{7.8}$$

with n being the number of bins and i being the i-th angle bin. The calculation is analog for longitudinal values.

In Table 7.11, the results of this study are summarized. They show that the inclusion of the temperature selection criterion does merely influence the identification quality for $\eta_{opt,0}$. However, similar to the reduced study, the quality of heat loss identification is significantly improved from a standard deviation of 24 W/m to only 14 W/m with a T_{max}-criterion. This implies that conclusion **T 1** is also valid for identifications including a determination of IAM-values. All other drawn conclusions and detected aspects in the previous study apply to the study with IAM identification as well. Regarding the IAM identification quality, the T_{max}-criterion slightly improves the error values in terms of $MURD$ and $\sigma(MURD)$. Nevertheless, a mean deviation of IAM values of approximately 1.6–2.5 % in $MURD$ still allows for improvements of the identification quality. The relevant factors will be derived in the following Section 7.2.3 and Section 7.2.4.

General Remarks

For an identification of performance parameters including a determination of IAM values, the correlation of thermal and optical parameters unexpectedly vanishes as illustrated in Figure 7.12(a). However, the correlation does not completely disappear, but rather shifts to a correlation of IAM values and $\eta_{opt,0}$ as exemplarily depicted for the longitudinal IAM at 10° in Figure 7.12(b). Coloring of the results according to the $MURD$-value indicates

[15] The approach of calculating the $MURD$-value is comparable to the calculation of $\varepsilon_{rel}(K)$ as introduced in the artificial data evaluation in Equation (7.6). However, the concept of $MURD$ is based on the calculation of mean errors, while ε_{rel} is based on taking the root mean square error value. Both concepts have their own advantages. Whereas the root mean square is more suitable and meaningful to perform statistical inference, mean errors are considered to enable better traceability and rating of the real collector results.

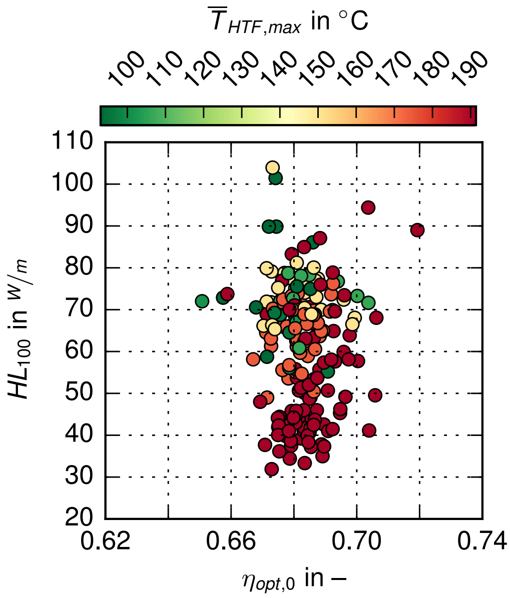

(a) Covariance plot of $\eta_{opt,0}$ vs. HL_{100}

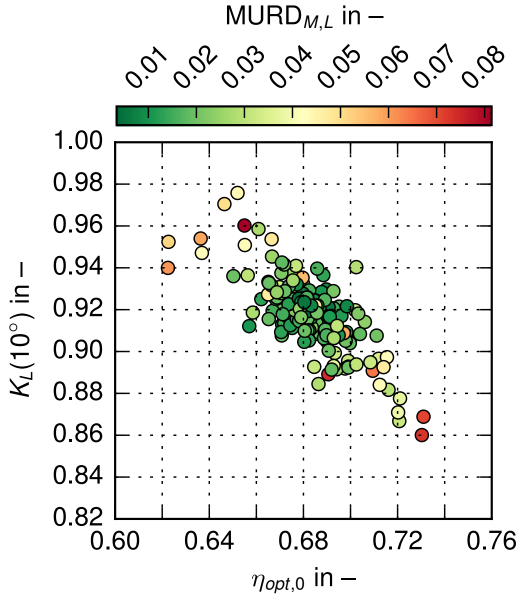

(b) Covariance plot of $\eta_{opt,0}$ vs. $K_L(10°)$

Figure 7.12: Covariance plots for RSS results with IAM identification and T_{max}-criterion. Covariance between $\eta_{opt,0}$ and heat loss disappears (a), whereas covariance between $\eta_{opt,0}$ and IAM values arises (b).

that the correlation and dispersion of the $\eta_{opt,0}$-values may be reduced when improving the quality of the IAM identification.

■ 7.2.3 Influence of Evaluation Time Step and IAM Angle Step

The main objective of the derivation of a testing strategy is to find relevant factors (i.e., necessary information content included in the measurement data) influencing the identification quality. To make sure that these effects of measurement data to the IAM quality are not superimposed by intrinsic properties such as angle step and evaluation time step, the following sections are dedicated to study those effects.

IAM Angle Step

The influence of the IAM angle step size was analyzed by performing six different evaluations based on the very same RSS measurement data basis: IAM values were identified with an angle step size of 2 °, 5 °, and 10 °. Moreover, the concept was studied of parameterizing the longitudinal IAM value. Thereby, the number of identified parameters significantly decreases (especially in the case of a very fine IAM curve of 2 °), since the longitudinal IAM is not described by discrete angle steps anymore but rather by a polynomial function. For the present case, a polynomial degree of three is chosen, analog to Equation (A.5), resulting in four IAM parameters to be identified. The transversal IAM is still determined in discrete values with an angle step size of 2 °, 5 °, and 10 °, because its staggered shape cannot be correctly approximated by a polynomial function.

Table 7.12: Influence of IAM angle step on the identification quality. All values are considered as mean values over all randomly drawn datasets.

Variable	Unit\Angle step	Including angle-stepwise K_L 2°	5°	10°	Including parametrized K_L 2°	5°	10°
$\eta_{opt,0}$	%	68.4	68.7	67.5	68.3	68.5	67.3
$\sigma(\eta_{opt,0})$	%-pts.	0.7	0.6	0.6	0.5	0.5	0.6
$CI(\eta_{opt,0})$	%-pts.	−1.2/+1.2	−1.1/+1.1	−1.0/+1.1	−1.0/+1.0	−0.9/+1.0	−1.0/+1.0
HL_{100}	W/m	61	61	62	63	63	63
$\sigma(HL_{100})$	W/m	12	12	12	12	12	12
HL_{200}	W/m	236	236	236	238	239	239
$\sigma(HL_{200})$	W/m	45	45	46	48	47	47
$MURD_{M,T}$	%	1.3	1.6	1.1	1.3	1.6	1.2
$\sigma(MURD_{M,T})$	%-pts.	0.6	0.8	0.6	0.6	0.9	0.6
$MURD_{M,L}$	%	1.1	1.3	1.0	0.7	0.5	0.4
$\sigma(MURD_{M,L})$	%-pts.	0.4	0.7	0.5	0.4	0.3	0.3
RMS	K	0.2416	0.2441	0.2476	0.2442	0.2468	0.2503

Table 7.12 summarizes the results of the angle-step RSS study. Concerning the identification quality of $\eta_{opt,0}$, all three discrete angle step sizes show very similar results. The parametrization of K_L improves both, standard deviation and confidence intervals of $\eta_{opt,0}$. Note that the error values of an angle step of 10° are remarkably favoring, however, a shift of absolute $\eta_{opt,0}$-values is discernible. The reason for this shift lies in the large angle bin of 10° provoking identified angle grid points far apart. For the calculation of specific IAM values in between two grid points interpolation is used. However, the IAM values at zero incidence are defined per default equal to one: $K_{T/L}(0°) = 1$. In the case of large angle bins such as, for example, 10°, this necessarily fixed grid point is valid for angles from 0–5°. The fixed reference value is consequently larger than the actual value corresponding to angles of 0–5°. For a graphical illustration of this issue see Figure F.1 of Appendix F. As a consequence, lower values of $\eta_{opt,0}$ originate from this systematic error source. With a finer angle resolution this effect is minimized and the error source eventually removed. On this account, the use of an angle step size of 10° is not recommended for small-scale LFC or collectors comprising significant change within very small incidence angles.

Referring to the heat loss identification quality, the results show equal values: no effect of changing angle step size nor a parametrization is significant. With respect to the IAM identification quality, note that the listed $MURD$-values have to be studied with some degree of caution, because they might not be completely representative for this particular comparison of different angle steps. The $MURD$-values indicate the deviation of the identified values to their respective mean values, not including the effect of a finer description of the IAM curve. For an angle step size of 10°, the $MURD$-values show the smallest IAM deviations. However, the very rough description of the curve implies a systematic shift of $\eta_{opt,0}$-values. For this reason, the use of 10°-IAM angle step should be applied with care and is not recommended for collector testing similar to the present analysis (i.e., collectors featuring larger IAM changes for small incidence angles). An indication for this systematic error might additionally be the slightly larger RMS of identifications with 10°, which implies that the fit of measured to simulated data is not as good as for smaller angle steps. For both longitudinal and transversal IAM, a finer description with 2°-angle step improves the identification quality in comparison to 5°, favoring an identification with 2°-IAM values.

Note, however, that the finer the angle step, the larger the number of parameters to be identified and the significantly larger the computational effort. Moreover, for 2°-angle steps, the density of data points within one bin is less than for 5°, making an identification with 5° more robust and stable. Consequently for identifications with 2°, special attention is advised that every angle bin consists of enough and reliable measurement points (further explanation will be given in Section 7.2.4). To avoid critical densities a larger number of measurement days is usually required, increasing again the computational effort.[16]

Alleviation of this issue can be found by parameterizing the longitudinal IAM according to Equation (A.9) of Section A.2, as commonly done for PTCs. Results indicate that a parametrization significantly improves the quality of longitudinal IAM identification, whereas no effect can be found for the transversal IAM. Moreover, smaller standard deviations indicate a more stable evaluation by parametrization in longitudinal direction. In addition, it comprises the advantage of reduced number of identification parameters and therefore decreased computational complexity. In this way, an identification of 2°-angle step with parametrized longitudinal IAM presents a valuable evaluation option. It couples accurate transversal and longitudinal identification quality with reduced computation effort and a significantly more robust evaluation procedure. Still, caution is recommended that enough data points for transversal IAM values are available for a 2°-identification. However, experience in collector evaluation has shown that transversal densities are less critical than particularly longitudinal ones, which are prevented by the parametrization. Note that a parametrization is only useful if no atypical IAM errors arise for a determined angle step, reducing the fit quality of the evaluation. For a detection of atypical errors, a stepwise identification is therefore advised.

Conclusion E 1:

> The smaller the angle step, the more accurate the IAM determination under the condition of sufficiently available data point densities. Parametrization of longitudinal IAM values provides accurate and robust results with less computational effort.

Evaluation Time Step

Measurement data is recorded in a given time step, mostly defined by the capability of the data acquisition system. For the evaluation, measurement data is usually averaged to a defined evaluation time step. To analyze the influence of the evaluation time step on the identification results, a study was performed with four different evaluation time steps of 5 s, 15 s, 30 s, and 60 s. Analog to the previous studies, the measurement data basis consists of the very same RSS for every time step. In this case, 200 drawing of 10 days were performed. What changes between the different evaluations is the time step of the included measurement data according to their averaged values of the respective time step. Moreover, the simulation time step is adapted depending on the data time step. In Table 7.13, an overview of the results for the time-step study is given.

[16] This found tendency of favoring an angle step of 2° may contradict the conclusions drawn in Nettelstroth [2015, p. 40] at first sight. Though, the results cannot be directly related to each other, as in the mentioned study angle step sizes of 1° and 5° were compared based on a small number of measurement days. Here, the effect of a more stable and robust identification of 5° compared to an even finer resolution with 1° becomes dominant. The lower identification quality may arise from critical data point densities for the finer resolution. However, the results of this study confirm the remark of advised caution with higher angle resolutions.

Table 7.13: Influence of evaluation time step on the identification quality. All values are considered as mean values over all randomly drawn datasets.

Variable	Unit	5 s	15 s	30 s	60 s
$\eta_{opt,0}$	%	67.9	68.4	68.9	67.8
$\sigma(\eta_{opt,0})$	%-pts.	1.0	0.9	1.1	1.0
$CI(\eta_{opt,0})$	%-pts.	$-1.8/+1.7$	$-1.7/+2.0$	$-2.1/+2.5$	$-1.9/+2.0$
HL_{100}	W/m	55	61	68	56
$\sigma(HL_{100})$	W/m	15	17	20	15
$MURD_{M,T}$	%	1.8	1.9	2.3	1.9
$\sigma(MURD_{M,T})$	%-pts.	0.8	0.9	1.0	0.8
$MURD_{M,L}$	%	2.0	1.9	1.9	2.1
$\sigma(MURD_{M,L})$	%-pts.	1.2	1.1	1.1	1.3
RMS	K	0.3359	0.2809	0.3316	0.4710

With regard to standard deviations and $MURD$-values of the different time steps, no clear and distinct tendency can be found. All evaluations show more or less similar and somehow equivalent results. Merely, absolute values of $\eta_{opt,0}$ and heat loss differ slightly; however, no coherence can be found. Regarding RMS-values of the data fit, the evaluation with 60 s entails the largest value with certain distance to the others. This might give an indication that with a larger time step dynamics of the system cannot be reproduced as accurate as with smaller time steps. Though, error values and standard deviations do not show excessive values either, which would justify not using this time step. This implies that for the dynamic evaluation procedure all studied time steps are valid to use. The decision of a time step is rather influenced by a compromise between accuracy of reproducing dynamics of the system, computational effort, and influence of inaccuracies of measurement data. For this reason, 15 s as an evaluation time step was chosen for the present case. In this way, the dynamics of the system can be properly reproduced. Moreover, measurement inaccuracies of the data recorded in 5 s-intervals are slightly averaged, making the evaluation procedure more robust. Additionally, with a time step of 15 s, the computational effort is significantly reduced in comparison to a simulation time step of 5 s. For other collector tests (for example in the case of a recorded time step of 5 s not being available) other evaluation time steps between 5 s and 60 s are equally valid to be used.

Conclusion E 2:

> An evaluation time step in the range of 5–60s does not significantly influence the identification quality. The evaluation time step has rather to be chosen as a compromise between accuracy and computational effort in dependence on the available data recording capabilities.

■ 7.2.4 Influence of Number of Measurement Days

Number of Data Points

The previous studies were designed based on a large number of measurement days (around 10 to 15 days), to make sure enough data is available not influencing the actually studied effect. Artificial data evaluation has already given indications that the number of measurement days, or rather the number of measurement data points, is highly affecting the overall identification results. Based on this fact, a study was performed to analyze

Table 7.14: Influence of number of measurement days/data points on the identification quality. All values are considered as mean values over all randomly drawn datasets.

Number of measurement days		3–5 d	5–7 d	8–10 d
Equiv. number of data points		6,000–9,000	11,000–14,000	16,000–19,000
Equiv. number of hours		25–37 h	45–58 h	66–80 h
Variable	Unit			
$\eta_{opt,0}$	%	68.7	68.4	68.3
$\sigma(\eta_{opt,0})$	%-pts.	1.6	1.2	1.1
$CI(\eta_{opt,0})$	%-pts.	$-3.3/+3.1$	$-2.0/+2.6$	$-2.5/+2.0$
HL_{100}	W/m	66	65	66
$\sigma(HL_{100})$	W/m	21	17	16
$MURD_{M,T}$	%	2.4	2.1	1.8
$\sigma(MURD_{M,T})$	%-pts.	1.1	0.8	0.8
$MURD_{M,L}$	%	2.0	1.7	1.5
$\sigma(MURD_{M,L})$	%-pts.	1.2	1.0	0.7

the influence of the number of measurement days in detail. It was designed to be able to evaluate the minimum of required measurement days necessary to obtain reliable and representative identification results with acceptable error values. Initial data analysis has shown that the number of measurement days is not a fully characteristic variable. Depending on the weather conditions, the information contained in one measurement day highly varies. For sunny days, numerous data points are available, whereas for partly clouded days the number decreases sometimes considerably. In unfavorable cases, several days with little data points are selected, which show different error values than the selection of the same number of days with numerous data points. For this reason, it was decided to rather take the actual number of available measurement data points as a selection criterion for the RSS. Three introduced categories of number of data points (6,000–9,000, 11,000–14,000 and 16,000–19,000 with a time step of 15 s) are equivalent to more or less 3–5, 5–7, and 8–10 measurement days with a range of 25 to 80 hours of measurement data. Table 7.14 lists the results of the RSS study based on 200 random drawings for each category with an identification of IAM values in 2° (without parametrization) including T_{max}-criterion for a potentially proper heat loss identification.

The results show a clear tendency of consistently decreasing error values for all identified parameters with increasing number of data points. This relation verifies conclusion **G 3** of Section 7.1.2. Particularly, results based on 3–5 days entail high error values for optical efficiency and IAM. Therefore, this small amount of measurement days is not recommended for meaningful and dependable performance testing. Whereas the improvement of identification quality from 3–5 days to 5–7 days is significant, the differences of error values are not that pronounced between 5–7 and 8–10 days. For an overview of induced confidence intervals of the IAM, Figure 7.13 illustrates the scatter plot of every sub-sampled data basis with its respective identified IAM values. In this case identification results of 3–5 days are sketched in comparison to results of 8–10 days. In both examples, the rough IAM curve is discernible. However, the shape is more pronounced (especially the staggered shape of the transversal IAM) for a large measurement data basis of 8–10 days as indicated by the lower $MURD$-values.

Even though results significantly improve by the number of data points, error values between 1.5–1.8 % of $MURD$ for longitudinal and transversal IAM are not entirely satisfying. Maximum $MURD$-values even reach 4–6 % of mean deviation. The sketched IAM error bars in Figure 7.13(b) demonstrate these higher deviations for large transversal an-

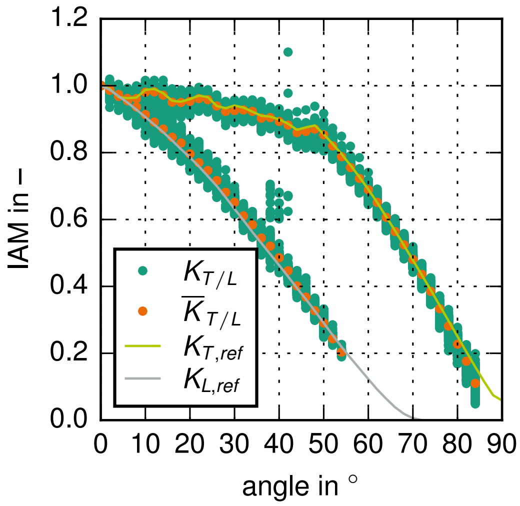

(a) IAM scatter plot for 3–5 d

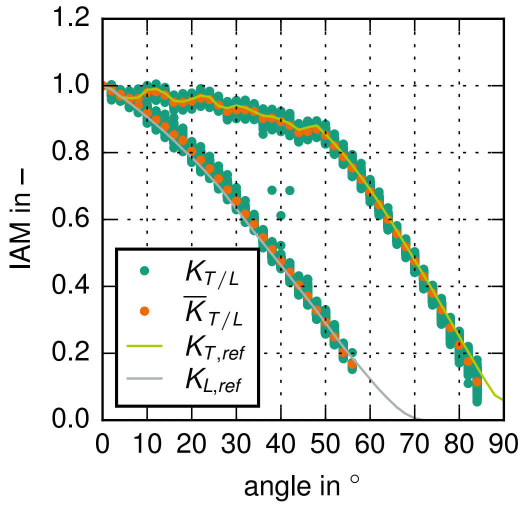

(b) IAM scatter plot for 8–10 d

Figure 7.13: IAM identification results of RSS study depending on number of measurement days. Scatter plot of identified IAM-values for every randomly chosen dataset selecting 3–5 measurement days (a) and 8–10 measurement days (b).

gles and small longitudinal as well as harsh outliers for intermittent longitudinal values. For this reason, further factors are analyzed in the following in order to increase the IAM identification quality.

Factors Improving the IAM Identification Quality

While analyzing the effects improving the IAM quality, it was recognized that the averaging property of the $MURD$ does not efficiently allow to assess detailed factors. The comprehensive study of the results showed that high $MURD$-values were caused by single defective regions rather than a complete erroneous IAM curve. As $MURD$ is designed to take the mean over all angle bins, it is considered more expedient to analyze discrete IAM values and their dispersion. In this way, two influencing factors were found: the number of data points corresponding to one angle bin, as well as the mean DNI available for these data points. Especially at the edges of certain testing periods—mostly in the early morning or late evening—small DNI values may contribute to disperse and therefore erroneous IAM identifications, if they solely contribute to the angle bin without higher DNI values. To understand the significant influence of both factors, the following exemplary sub-sample shall illustrate the relation of both mean irradiance and number of data points (also referred to as frequency). For this sub-sample, high deviations to the corresponding mean values arise for θ_T from 30–55 ° and 80–85 °. All IAM values in longitudinal direction entail larger deviations, with particularly pronounced errors larger than 5 % for θ_{LS} from 35–50 °. Figure 7.14 depicts the mean irradiance and frequency in a histogram over all identified angle bins for transversal and longitudinal solar angle. They show that for certain angles the frequency or the mean DNI is significantly lower than for others. For the longitudinal solar angle between 40–48 °, little data points are available, sometimes coupled with low irradiance, sometimes not. For high transversal angles the number of

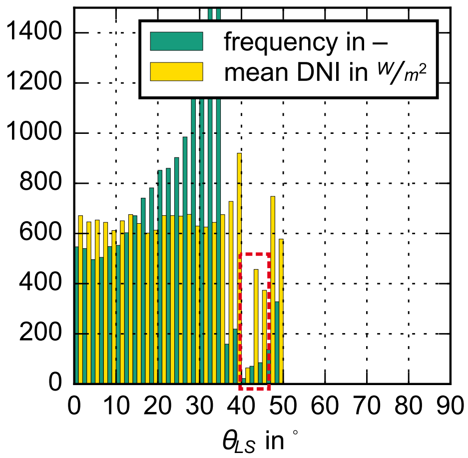

(a) Longitudinal solar angle θ_{LS}

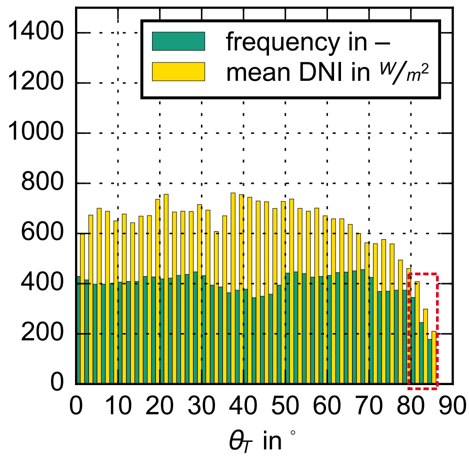

(b) Transversal angle θ_T

Figure 7.14: Mean DNI and number of data points for every angle bin of the exemplary sub-sample. Histogram of mean irradiance and number of data points for identified longitudinal solar angle θ_{LS} (a) and transversal angle θ_T (b).

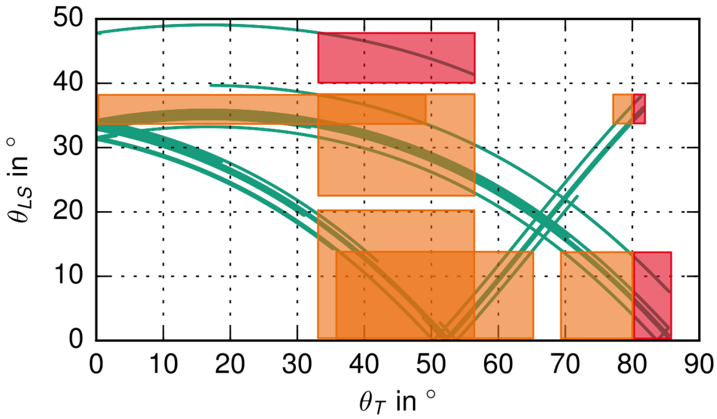

Figure 7.15: Incidence angle pairs for the exemplary sub-sample. Highlighted regions correspond to regions directly (marked in red) and indirectly (marked in orange) affected by small data point frequency or low mean DNI.

data points is acceptable (greater than approximately 100), but mean DNI values are lower than 400 W/m^2. Both factors unequivocally cause the large error values of approximately 6–15 % of deviation to the mean value of these angle bins. In addition, they influence other angle regions of IAM identification as well, where their effect is having impact. These regions are the ones defined by the coupled angle pairs of (θ_T/θ_{LS}). In Figure 7.15, the angle combinations of the exemplary sub-sample are depicted with red highlighting of the defective regions by poor mean DNI and data-point frequency. Additionally, the impact of these error-prone regions to other coupled angles is marked in orange. Apart from the regions marked in red, the regions where two of the orange regions overlap correspond to the same regions of the IAM curve entailing high error values. This indicates that angle regions that are coupled with regions including both transversal and longitudinal errors are faulty as well. Certainly, the illustration represents an extraordinary bad case, but shows the dominant influence of the DNI and the number of data points. Not only the angles directly affected by unsatisfying DNI and data frequency, but also coupled angles are erroneous and eventually affecting the global identification quality. The coupling and hence the error propagation can be decreased, if angle pairs are well spread over the entire angle spectrum (which is conform to conclusion **O 2** of Section 7.1.4). Nevertheless, an inclusion of error-prone regions has to be prevented in the first place. Therefore, a new criterion for the proper IAM identification is introduced as explained in the following.

■ 7.2.5 Data Frequency and DNI Criteria

To increase the IAM identification quality, evaluation criteria were introduced so that the randomly selected measurement data basis of every sub-sample satisfies acceptable irradiance and number of data points for every identified angle bin. In the present case, only angle bins with a larger mean DNI than 400 W/m^2 as well as a data point frequency larger than 100 were permitted in the identification procedure. Apart from this change, the very same data basis as in the previous study was taken to allow for direct comparisons. Note that the chosen frequency value is certainly to some degree coherent with the total number of data points. For 3–5 days, only around 9.000 individual data points are available. With 42 angle bins in transversal direction, the probability of certain angle bins to exhibit a small data frequency is higher than for more measurement days included in the evaluation procedure. This may cause the worse IAM identification quality for less measurement days. The mean data frequency per bin for 3–5 days lies around 200 (with 42 angle bins and 9.000 data points). Taking into account that some angles are occurring more often with values significantly larger than 200 (compare with Figure 7.14(b)), low and maybe critical density of certain bins smaller than 100 can be easily reached with a small number of measurement days available.

By introducing the new criterion, the quality of identifying $\eta_{opt,0}$ is slightly improved from a standard deviation of 1.14 %-pts. to 1.09 %-pts. As expected, the heat loss identification quality is not affected by the DNI and frequency criterion. However, the IAM quality is significantly better for this RSS study than for the previous analysis without criterion. For transversal incidence angles, the maximum $MURD_T$-deviation improves from 4.4% to 2.5%, which corresponds to an improvement of the mean $MURD_T$-value over all RSS identifications from 1.8 % to 1.0 %. Similarly, maximum $MURD_L$-deviations decrease from 6.3% to 2.8%, corresponding to mean values improving from 1.54 % to 1.2 %. Further evaluations have shown that the particular value of mean DNI may range between 350–400 W/m^2 to entail the positive effect on the overall identification quality. Analog, data point frequencies between 50–100 lead to comparable improvements. Thereby, the results show that apart from the already concluded wide angle spread for a good identification quality (according to **O 2** of Section 7.1.4), in reality two more aspects of mean DNI and data point frequency have to be considered. Note that the mean-DNI criterion is certainly linked to the fact that measurement data of lower irradiance values are associated with a higher uncertainty than high irradiance values. Ensuring a higher mean-DNI per bin consequently mitigates the influence of this uncertainty source.

Conclusion O 3:

IAM values can only be identified for angle bins fulfilling the criteria of a specific minimum mean DNI and data point frequency. This is considered a necessary condition for acceptable IAM identification quality in particular, but overall identification quality in general as well.

■ 7.2.6 General Remark and Conclusion

In the artificial data evaluation, continuous measurement days within a week were checked for their suitability for representative performance testing. A similar analysis was performed including real measurement data. For the complete data basis of collector `LFC_w2` always ten continuous measurement days were evaluated. Results showed a similar tendency as found for the artificial data evaluation: a measurement period in summer is outperforming the measurement period in autumn since the probability and occurrence of zero incidence angles is less for autumn days than for summer days (compare to Figure 7.16(a))[17].

For an adequate decoupling of IAM values, a wide spread of the angle pairs is required. Thereby, transversal incidence angles do not only occur with one other specific longitudinal angle. Moreover, angle points coupled with a corresponding zero angle point, for example ($\theta_T = 0°, \theta_{LS} = x°$) or ($\theta_T = y°, \theta_{LS} = 0°$), ensure a distinct and uncoupled determination of IAM values at x° or y° incidence angle (i.e., $K_T(y)$ and $K_L(x)$). Even though the days in autumn present a wide range of identifiable θ_{LS}-values resulting in a long identified IAM curve, they comprise the drawback of little zero-intersection points. The results unequivocally show this effect provoking a severe correlation of the identification results (compare to Figure 7.16(b)).

[17] Be aware that this relation is depending on the location of the collector and its orientation (in this case Central Europe with orientation of 20° West). For other test locations and orientations the period equivalent to the here mentioned summer period has to be determined accordingly.

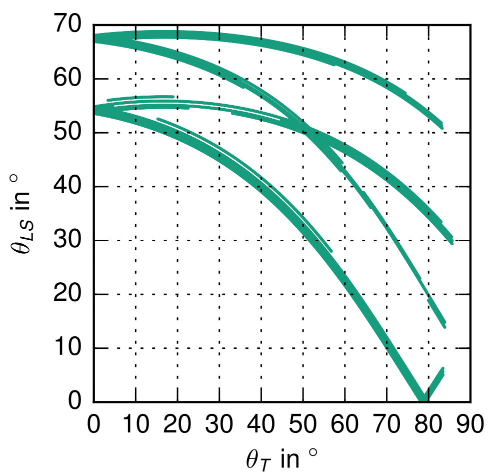

(a) Angle combination θ_T vs. θ_{LS}

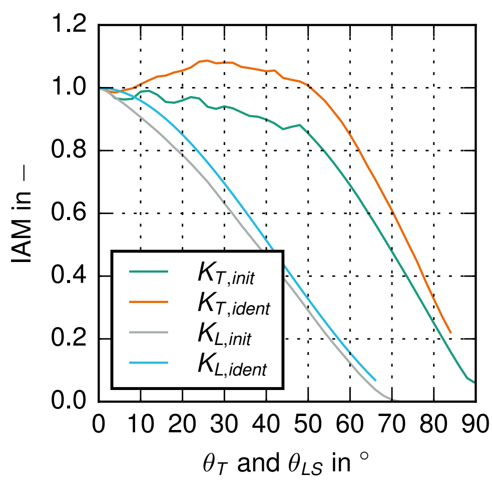

(b) Identified K_T/K_L-values

Figure 7.16: Exemplary results of a continuous measurement period in autumn. Available angle pair combination θ_T versus θ_{LS} (a) of the exemplary continuous day identification and its identified IAM results (b).

All in all, the results reveal that a continuous measurement test period is in principle feasible for an accurate and representative IAM determination if enough data points are available fulfilling the introduced mean-DNI and frequency criterion. Moreover, the conditions of sufficient zero-intersection points for a distinct IAM identification has to be met. Days in autumn comprise the benefit of larger θ_{LS}-values, but share the relevant drawback of featuring little zero-intersection points. Only considering autumn days in the evaluation will lead to correlated results. However, including them additionally to a measurement period in summer, as, for example, in two discontinuous measurement periods represents a valuable option. A compromise may also present a measurement period in the late summer, where acceptable zero-intersection points and enough angle spread for decoupled IAM values are available including higher θ_{LS}-values.

■ 7.3 Recommendation for Testing and Evaluation Strategy

An elaborate derivation of a testing and evaluation strategy was presented within the previous sections. Table 7.15 summarizes the drawn conclusions from the artificial and real data evaluation and the recommendations they involve.

Table 7.15: Summary on conclusions and recommendations concerning an appropriate testing and evaluation strategy. Short descriptions of the conclusions including the recommendations they involve are given with indications if they are drawn from artificial or real data analysis.

Index	Short description of conclusion	Art.	Real	Recommendation
G 1	$\eta_{opt,0}$ is identified more accurate than the heat loss	✓		• follow the subsequently given recommendations to improve $\eta_{opt,0}$-quality
G 2	stronger noise induces worse identification	✓		• minimize measurement uncertainty by installing high-quality instrumentation
G 3	more evaluation days lead to a better identification	✓	✓	• test during a measurement period as long as possible, at least > 8 full days
G 4	more evaluation days lead to results less affected by noise	✓		• with more measurement days effects of less good instrumentation may be compensated
T 1	higher heat loss leads to a better heat loss identification	✓	✓	• perform tests at higher fluid temperatures, if feasible
T 1.1	higher fluid temperatures lead to a better heat loss identification	✓	✓	• perform tests at higher fluid temperatures, if feasible
T 1.2	low heat loss leads to a higher probability of correlated parameters	✓	✓	• perform tests at higher fluid temperatures, if feasible; always report identified parameters as a conjunction
T 2	DNI range and dynamics show no significant effect on identification quality of heat loss and optical efficiency	✓	✓	• no requirements concerning conditions of DNI range&dynamics
T 3	mass flow and temperature course show no significant effect on identification quality	✓		• no requirements concerning operating conditions
T 4	wider temperature span slightly improves heat loss identification quality	✓		• test at a wide distribution of fluid temperatures, if feasible
O 1	minimum fluid temperature does not significantly affect $\eta_{opt,0}$	✓	✓	• near-ambient fluid temperatures are not strictly required, include them if feasible
O 2	more spread angle pairs and occurring zero incidence angles lead to better results and minimize parameter correlation	✓	✓	• test at one continuous measurement period in late summer or more discontinuous measurement periods, if feasible
O 3	criteria of mean DNI and frequency values for all identified angle bins need to be fulfilled		✓	• only include angles to identify which fulfill the criteria
E 1	evaluation time step between 5–60 s shows no significant influence on identification quality		✓	• evaluate at 15-s time step, if available, otherwise all time steps <60 s are acceptable
E 2	decision of identified angle step involves a compromise between accuracy, number of available measurement days and computation effort		✓	• avoid evaluating with 10 ° IAM angle step; 2–5 ° are recommended if sufficient data densities are available; if not, check for parametrized K_L

Chapter 8

Application and Validation of the Elaborated Testing Procedure

Results of the previous chapters have shown that reliable performance testing with the objective of a collector certification requires a high quality, large quantity, and broad information content of the measurement data basis. The elaborated dynamic testing method can also be applied in a less complex context for simpler performance checks, involving less requirements concerning the measurement data basis. It allows, however, a general study of the collector performance, supporting design and development of the product or enabling an identification of misbehaviors.

While Chapter 6 and Chapter 7—concerning measurement instrumentation and testing strategy—focus on certification aspects, the following chapter comprises a comprehensive application of the elaborated method addressing both aspects: certification and performance checks. It is structured to show the general capability of the DT method, its limits, and potential for different collector types and systems under test.

Until now, the test collector `LFC_w2` was extensively studied in the previous chapters. The collector `LFC_w2` served as a reference basis, revealing a successful implementation of the different individual elements for this particular test case. To combine all addressed and elaborated elements of the dynamic testing method, an exemplary, overall proceeding for an ideal collector test and evaluation—according to the recommendations of this thesis—is outlined in the following section. It is based on the measurement campaign at collector `LFC_w2`. To furthermore assure a broad validity of the elaborated method beyond this particular test case of `LFC_w2`, the developed models and procedures were additionally applied to diverse other test situations. They include different locations, heat transfer media, collector types, and scales as well as measurement conditions. An overview of the characteristics of the test collectors is given in Table 2.2. Results of these test collectors will be discussed in a summarized way, focusing on challenging issues of the specific test cases. This ensures the universal applicability of the enhanced dynamic testing method of this thesis and demonstrates its specific capabilities.

8.1 Recommended Overall Proceeding for Collector Test and Evaluation

In order to assure meaningful performance evaluations, diverse already addressed aspects have to be considered as a conjunction. A recommended, overall proceeding is outlined using the example of test collector LFC_w2. For this collector, a vast, high-quality, and therefore nearly ideal measurement data basis is available. The fulfillment of the proposed proceeding will generate reliable evaluation results, which are valid within the framework of representative collector tests for certification purposes. An ideal collector test and evaluation includes three main parts concerning preparation & testing, data evaluation, and reporting of results, which will be discussed in the following.

Preparation & Testing

Reliable collector testing requires an appropriate preparation and execution of the measurement campaign, considering the following aspects:

Selection of measurement instrumentation:
High-quality measurement equipment provides data associated with low measurement uncertainties, which are required for meaningful, uncorrelated test results. Specific recommendations are elaborately given in Section 6.2. This was assured for collector LFC_w2 by installing measurement instrumentation similar to the studied—and recommended—base case of Section 6.1.3. In this way, an exemplary collector power output uncertainty of 0.5 kW, that is, 1.65 % (2σ) was achieved.

Measurement period:
According to the derived testing strategy summarized in Table 7.15, an evaluation of more than 8–10 measurement days is recommended. A measurement period should therefore at least comprise two measurement weeks. For collector LFC_w2, a vast data basis is available for investigation purposes. This represents a unique advantage, but does not reflect realistic test conditions. For this reason, an exemplary data basis reduced to ten days recorded within a period of six weeks was selected for illustration purposes. This is considered a long but practicable period assuring a representative evaluation of all collector parameters.

Supervision of measurements:
During the test campaign, cleaning of the collector should be performed in order to minimize error sources and warrant accurate and precise evaluation results. If regular cleaning is not possible, reflectance measurements should be performed on regular basis as to ensure a proper assessment of soiling rates. Moreover, regular checking and maintenance of the system is recommended. Thereby, potential failure can be detected and quickly solved in order to prevent potential biasing of the test results. These conditions were fulfilled for collector LFC_w2.

Fluid temperature level:
For a significant heat loss identification, high fluid temperatures need to be included, especially in the case of evacuated absorber tubes. Consequently, for collector LFC_w2, measurement days were selected comprising fluid temperatures up to 225 °C.

Operating conditions:
No specific constraints of operating conditions have to be addressed concerning mass flow rate, fluid temperature, and solar irradiance. Certainly, only data of a

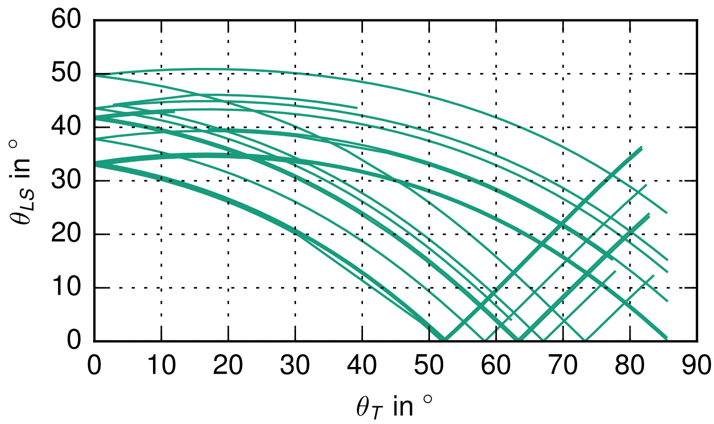

Figure 8.1: Incidence angle pairs for the exemplary measurement data basis of `LFC_w2`. Occurring pairs of transversal and longitudinal solar incidence angles.

collector in operation and in focusing mode are meaningful to evaluate. Chosen time periods of the collector `LFC_w2` were selected accordingly.

Solar incidence:
Particularly for LFCs, a wide spread of incidence angles needs to be assured to properly identify IAM values. This requirement is fulfilled by the exemplarily chosen ten measurement days of `LFC_w2`, as sketched in Figure 8.1.

Data Evaluation

A significant evaluation of recorded measurement data is recommended as follows:

Time and angle step:
According to Table 7.15, time and IAM step have to be selected depending on the measurement situation and extent of available data basis. The decision is based on a compromise between desired resolution of IAM, available information content (data points), computational capabilities, and accuracy of the results. For the exemplary evaluation of collector `LFC_w2`, the ten measurement days were evaluated with a time step of 15 s to correctly reproduce the dynamics of the system. The IAM was identified stepwise for transversal and longitudinal direction with angle steps of 2 °.

Irradiance and frequency criteria:
The derivation of the testing strategy in Section 7.2.5 showed that IAM angle bins of low irradiance and number of data points need to be excluded from the data evaluation. They may severely corrupt identification results. Computing of the corresponding values before starting the identification procedure is therefore essential. Figure 8.2 illustrates the corresponding irradiance and data point frequency for collector `LFC_w2`. It reveals that only transversal angles $\theta_T \leq 80\,°\mathrm{C}$ can be evaluated. Moreover, the angle bin of $\theta_{LS} = 46-48\,°$ needs to be excluded from the evaluation procedure due to low irradiance values.

Evaluation procedure:
With a limited measurement data base—as the present exemplary case—

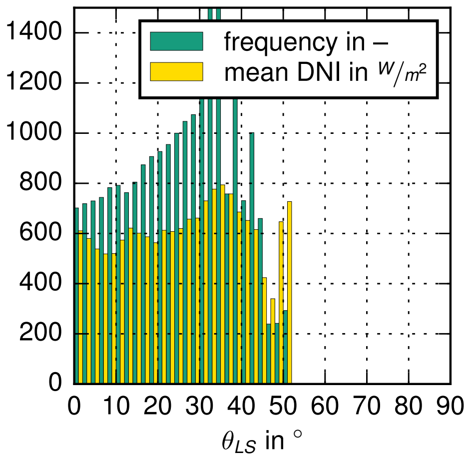

(a) Longitudinal solar angle θ_{LS}

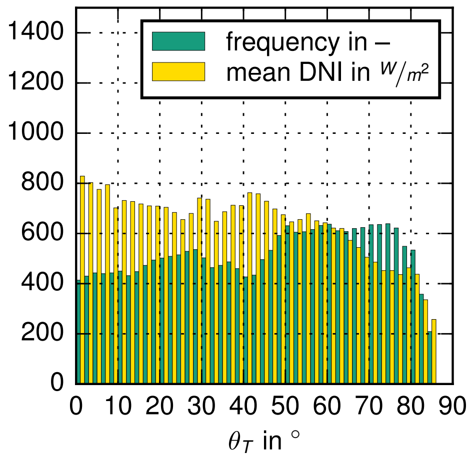

(b) Transversal angle θ_T

Figure 8.2: Mean DNI and number of data points for every angle bin of the exemplary dataset of LFC_w2. Histogram of mean irradiance and number of data points for identified longitudinal solar angle θ_{LS} (a) and transversal angle θ_T (b).

bootstrapping calculations are advised as enabled within this thesis. They facilitate a valuable assessment of the identification quality and allow to judge on the confidence of the performance parameters. Statistical inference computations are considered a key feature of the proposed evaluation procedure in order to warrant a meaningful reporting of test results. Thereby, confidence levels of the identified performance results are available.

Reporting of Results

With the instrumentation installed, data recorded, selected, and evaluated, the identified performance results of the test collector need to be adequately reported according to the following indications:

Parameter conjunction:
Main premise is the reporting of all evaluated test results as a conjunction. Even though diverse aspects to reduce parameter correlation are considered, correlation cannot be prevented for sure. For this reason, parameters should never be indicated individually but the complete set of derived performance parameters.

Absolute values, standard deviation, and confidence intervals:
A meaningful reporting of test results comprises absolute values, including their standard deviation and confidence intervals. An exemplary tabular reporting of the identification results for the evaluated data basis of test collector `LFC_w2` is given in Table 8.1. For the heat loss, the individual coefficients are of less significance than overall heat loss values and their confidence. For this reason, the reporting of the introduced HL-values is recommended. The corresponding fluid temperature difference (e.g., 100 K, 150 K, 200 K) should be chosen according to prevailing fluid temperatures of the test. For collector `LFC_w2`, HL_{100} was chosen. IAM values should be reported in a separate table or graphically illustrated. The indication

Table 8.1: Recommended way of reporting evaluation results. Absolute values and confidence levels in terms of CI-values and standard deviation for the exemplary evaluation of collector `LFC_w2`.

Variable Unit	$\eta_{opt,0}$ %-pts.	u_0 $W/m{\cdot}K$	u_1 $W/m{\cdot}K^2$	HL_{100} W/m	IAM %
Absolute value	67.8	0.7481	0.0005	80	see Figure 8.3(a)
σ	0.8	0.12	0.0007	6	see Figure 8.3(a)
CI	$-1.54/+1.72$	$-0.2865/+0.1503$	$-0.0005/+0.0016$	$-13/+11$	see Figure 8.3(a)
$MURD_{M,T}$	–	–	–	–	0.83
$MURD_{M,L}$	–	–	–	–	0.66

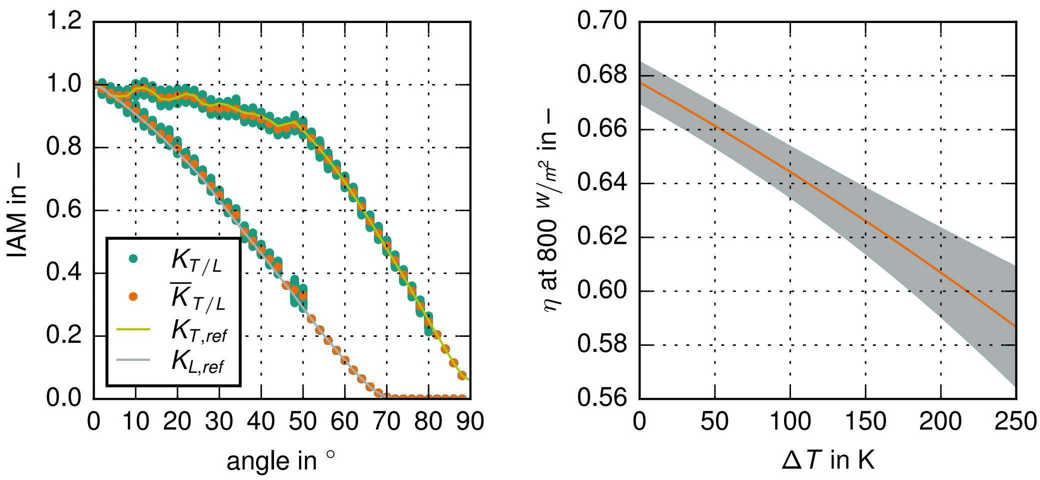

(a) IAM scatter plot (b) Instantaneous efficiency curve

Figure 8.3: Exemplary evaluation results for collector `LFC_w2`. Bootstrapping scatter plot of identified IAM-values (a) and instantaneous efficiency curve including associated uncertainties (1σ) marked in gray based on the BS parameter standard deviation (b).

of $MURD$-values allows a fast assessment of the overall IAM identification quality. Concerning a practical and meaningful assessment of individual IAM results for every angle step, the graphical representation by means of a scatter plot as depicted in Figure 8.3(a) is recommended. A graphical representation of the bootstrap parameter distribution of $\eta_{opt,0}$ and HL_{100} certainly reveals valuable information, but is not considered essential to report. Apart from these basic plots, the implemented enhanced dynamic performance evaluation procedure allows for a graphical representation of a vast amount of different options. They are meant to study particularly influencing factors, resulting parameter dispersion, and their correlation, similar to the covariance graphs shown in Chapter 7.

Instantaneous efficiency curve:

To assure a joint reporting and illustration of the identified optical and thermal parameters, an instantaneous efficiency curve is commonly presented as depicted in Figure 8.3(b) [analog to ISO 9806, 2013, p. 60, Eq. 20]. It illustrates the overall collector efficiency η under normal solar incidence (i.e., $K_T, K_L = 1$) at a defined irradiance level[1] (in this case 800 W/m^2), depending on the temperature difference of the heat transfer fluid according to

$$\eta = \eta_{opt,0} - u_0 \cdot \frac{l_{abs}}{A_{ap} \cdot G_{bn}} \cdot \Delta T - u_1 \cdot \frac{l_{abs}}{A_{ap} \cdot G_{bn}} \cdot \Delta T^2. \tag{8.1}$$

The associated uncertainty of the curve (marked in gray color) is calculated via the Gaussian error propagation law by:

$$u_c^2(\eta) = \sigma^2(\eta_{opt,0}) - \sigma^2(u_0) \cdot \left(\frac{l_{abs} \cdot \Delta T}{A_{ap} \cdot G_{bn}}\right)^2 - \sigma^2(u_1) \cdot \left(\frac{l_{abs} \cdot \Delta T^2}{A_{ap} \cdot G_{bn}}\right)^2. \tag{8.2}$$

It thereby includes the standard deviations σ obtained by the bootstrapping procedure as listed in Table 8.1.

Range of validity:

Indicating the range of validity of the derived performance parameters is considered a substantial aspect in order to report comparable results and avoid misinterpretation. For the exemplary evaluation of collector `LFC_w2`, heat loss coefficients u_0/u_1 are valid in the range of $T_{HTF} \in [30; 225]\,°C$. For the IAM identification, K_T is valid for $\theta_T \in [0; 80]°$ and K_L for $\theta_{LS} \in [0; 50]°$.

Measurement uncertainty:

Associated measurement uncertainties have to be stated for a consistent reporting of test results. In the given example of collector `LFC_w2`, the collector power output uncertainty amounts 0.5 kW/1.65 %(2σ).

Fitting quality:

Finally, indications on the fitting quality should be provided. The RMS value of the fitting procedure is to be stated. The present exemplary identification leads to a RMS of 0.26 K. The graphical illustration of simulated versus measured objective variable allows a fast and rough assessment, as exemplary depicted for collector `LFC_w2` in Figure 8.4.

Validation sequence:

If enough measurement data is available, a cross-check of the identified parameters by means of a validation sequence is recommended. This increases the reliability of the derived performance results. It comprises a simulation of an additional measurement period based on the finally reported performance parameters of the collector. This measurement period may not be included in the original data set of the evaluation procedure. Typically, the RMS of the collector power output is stated. Deviations of simulation to measurement should be of the same magnitude as the original fitting quality. For collector `LFC_w2`, numerous validation sequences are available. Associated deviations are of a similar magnitude than the RMS of the identification procedure in the range between 0.14–0.32 K.

[1] Be aware that in this case the irradiance is referred to direct normal irradiance G_{bn}, since concentrating collectors only use this proportion of the global irradiance. This allows for meaningful comparisons between concentrating collectors. However, when comparing them to different collector types—in particular to those that are able to use a proportion of diffuse irradiance—an appropriate reference irradiance has to be selected.

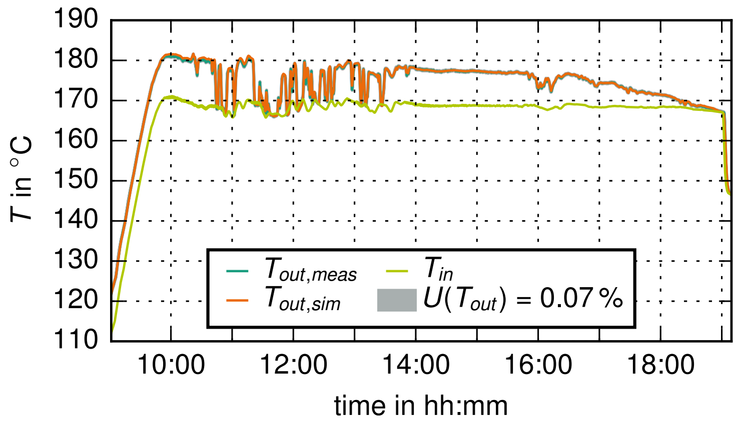

Figure 8.4: Fitting quality of exemplary identification day for collector LFC_w2. Inlet temperatures (marked in light green) and simulated versus measured outlet temperatures (marked in orange vs. dark green color) are illustrated. The dark green line of $T_{out,meas}$ is hardly perceivable. The implied small difference of $T_{out,sim}$ vs. $T_{out,meas}$ leads to a good fit quality of 0.26 K in the RMS.

The above indications concerning an adequate overall proceeding represents the ideal case of collector performance testing. It is therefore especially suited for collector certification purposes. However, ideal test conditions are not always existent and—depending on the objective of the collector test—not always desired nor necessary. The developed dynamic performance evaluation method of this thesis is equally capable of providing informative and meaningful results for other test situations. It is especially useful for on-site, in situ testing, where strict operating and test conditions cannot be fulfilled. In this way, an evaluation of test data recorded with standard measurement equipment is feasible, since associated bootstrapping confidence intervals indicate a potentially higher dispersion of the identified results. These aspects will be particularly addressed in the following sections.

Note that certainly the main objective of the elaborated procedure is the derivation of absolute performance values. Yet, due to non-disclosure agreements absolute values of the test collectors may not be reported, but are equally not considered relevant within the scope of this thesis. The exemplary evaluations are rather meant to prove the practicability and capacity of the developed method. They should especially show the unique and very potential feature of confidence computation as well as DSG evaluation. For this reason, only confidence intervals will be stated in the following. Furthermore, indications will be given, whether absolute values are within the expected range.

■ 8.2 Application to Collectors Operating Without Phase Change

■ 8.2.1 Process Heat Collectors

Collector LFC_w1

The linear Fresnel collector LFC_w1 consists of a small-scale, evacuated-tube collector, operating with pressurized water at a production site of an end user. It therefore represents

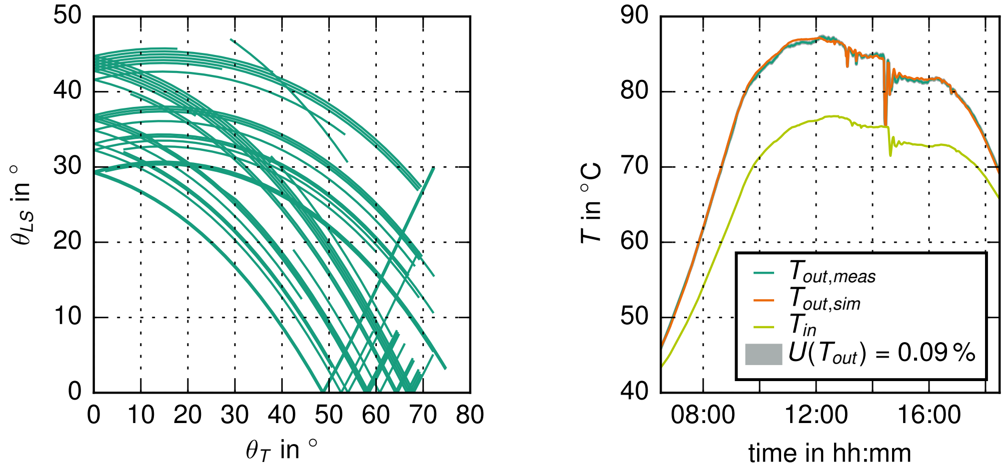

(a) Incidence angle pairs θ_{LS} vs. θ_T

(b) T_{meas} vs. T_{sim}

Figure 8.5: Characteristics of measurement data basis and evaluation results for `LFC_w1`. Occurring pair of transversal and longitudinal solar incidence angles (a) and simulated versus measured objective variable T_{out} of validation sequence (b).

a classical in situ test situation where the generated solar heat is permanently used as process heat of a production line. Interference with the process is consequently not possible, involving less operating flexibility in terms of potential measurement conditions. For this reason, only smaller fluid temperatures to a maximum of 160 °C are available. As already seen in Chapter 7, lower fluid temperatures of an evacuated receiver lead to a high correlation and insignificant identification of heat loss parameters. For this reason, only optical parameters are meaningful to identify in this case.

Several data points of this measurement basis were already included in the validation of the QDT with the DT method in Section 3.1. The entity of the available data basis consists of 22 measurement days, with approximately 145 h of usable data. Thereby, a vast and widespread angle information content is accessible as depicted in Figure 8.5(a). In Table 8.2, the corresponding identification results of the complete data basis are summarized. Absolute IAM and efficiency values agree well with the previous evaluations in Section 3.1. Bootstrapping CI-intervals (with 95 % confidence) and standard deviations of the identified $\eta_{opt,0}$ as well as $MURD$-values of IAM indicate small uncertainty bands of the identification results. This is conform with the high-quality measurement instrumentation and regular cleaning and maintenance of the test collector reducing potential error sources. It moreover underlines this requirement for a proper identification of IAM values, especially in the case of LFCs. Their optical behavior is more complex and therefore more sensitive to identify than for PTCs.

For this exemplary case, the identified angle step size of the IAM was set to 5 °. An evaluation with 2 ° and polynomial longitudinal IAM shows similar identification values. However, a parametrization of longitudinal IAM fits the curve to a certain shape. Thereby, potential misbehaviors at specific incidence angles[2] can be recognized harder, only by a potential higher RMS of the objective function. As a consequence, stepwise IAM iden-

[2]originating, for example, from tracking errors, unexpected blocking and shading of mirrors or shutdown, partly defocussing at a certain incidence situation, etc.

Table 8.2: Confidence intervals of identification results for collector `LFC_w1`. Confidence levels in terms of CI-values and standard deviation for $\eta_{opt,0}$ and $MURD$-values for longitudinal and transversal IAM.

Variable Unit	$\sigma(\eta_{opt,0})$ %-pts.	$CI(\eta_{opt,0})$ %-pts.	$MURD_{M,T}$ %	$MURD_{M,L}$ %	RMS(T_{out}) K
Value	0.65	$-1.23/+1.17$	0.75	0.47	0.28

tification provides valuable information, particularly in the case of performance checks. Especially, when large measurement data basis are available, stepwise identification is recommended. Nevertheless, with a small data basis at hand, parametrization of the IAM provides a good means for accurate and less error-prone evaluations.

To verify the identified results, a validation sequence was selected. It consists of a measurement day not included in the previous evaluation. A subsequent simulation of this measurement day with fixed performance parameters to the previously identified values leads to a RMS of the objective function—in terms of simulated versus measured outlet temperatures—of 0.30 K. An exemplary illustration of this validation sequence is given in Figure 8.5(b). The resulting RMS value is conform to the RMS value of the original evaluation of 0.28 K. It corresponds to a mean deviation of the collector power output $\dot{Q}$ of 0.93 kW. With respect to a nominal power output of approximately 50 kW, this deviation is considered acceptable.

All in all, the evaluation of `LFC_w1` proves the capability of the DT method for an accurate IAM identification for LFCs. With the enhancement of the evaluation procedure including bootstrapping computations, valuable information is accessible. Small dispersion of the confidence intervals indicate a high confidence of identified parameters. It additionally demonstrates the remaining challenge of significant heat loss identification. This aspect will be particularly addressed within the following collector test.

Collector `LFC_w3`

The linear Fresnel process heat collector operating with pressurized water `LFC_w3` represents a rather challenging system under test. On the one hand, the installed measurement instrumentation is not designed for certification purposes but rather for operation and control. The irradiance measurement equipment consists of an uncalibrated pyrheliometer entailing higher measurement uncertainties. Moreover, the collector is not regularly cleaned and the soiling rate non-regularly to rarely measured. These test conditions are not particularly favoring an IAM identification of an LFC. For this reason, the focus was put on a determination of thermal performance parameters and optical efficiency. Nevertheless, an identification of IAM values was feasible and gives valuable indications on potential low-performance incidence angles (e.g., where the tracking is not working perfect).

On the other hand, even the thermal evaluation cannot be applied straight away for collector `LFC_w3`, because the receiver consists of a multi-tube absorber with a glass plate cover. Commonly, no detailed simulation of every particular geometric detail and its fluid flow effect is desired. On this account, the receiver is consequently treated as a black box, consisting of one absorber tube with an equivalent diameter to the multiple tubes. In this

Table 8.3: Confidence intervals of identification results for collector LFC_w3. Confidence levels in terms of CI-values and standard deviation for $\eta_{opt,0}$ and HL_{150}.

Variable	$\sigma(\eta_{opt,0})$	$CI(\eta_{opt,0})$	$\sigma(HL_{150})$	$CI(HL_{150})$	RMS(T_{out})
Unit	%-pts.	%-pts.	W/m	W/m	K
Value	0.80	$-1.55/+1.38$	75	$-140/+140$	0.71

way, the standard PFM of ColSim[3] can be used for the evaluation. A large measurement data basis (around 26 days with 115 h of measurement data) with a wide variation of available fluid temperatures between 10–200 °C, however, facilitates a significant heat loss identification.

Confidence intervals and standard deviations of the identified optical and thermal parameters are given in Table 8.3. Absolute values coincide well with estimated values obtained from ray tracing or physical modeling of heat loss[4]. They reveal larger confidence intervals, with a standard deviation of 0.8 %-pts. for $\eta_{opt,0}$ and 75 W/m for the heat loss at a fluid temperature difference of 150 K. Both lead to a higher RMS of the objective function T_{out}. The arising deviations may originate from the higher measurement uncertainty as well as a less perfect reproduction of the dynamics of a multi-tube receiver in comparison to a simpler one-tube model. However, the limited precision of reproducing dynamics is not considered decisive. For a visualization of the fitting quality, see Figure 8.6(a) with depicted measured versus simulated outlet temperatures. The standard deviation of the heat loss value HL_{150} at 150 K fluid temperature difference corresponds to a standard deviation of the overall collector heat loss of approximately 1.5 kW. In comparison to the nominal collector power output of 65 kW, this error value of 2.3 % is considered reasonable.

A validation sequence of one measurement day not included in the original evaluation procedure—which is simulated with the identified performance parameters—leads to similar error values. For the objective variable T_{out}, the RMS is 0.53 K, corresponding to a mean deviation of the collector power output of around 4.5 kW.

Altogether, the evaluation of collector LFC_w3 demonstrates a feasible and reasonable identification of heat loss parameters. This is conform to the conclusion **T1** drawn in Chapter 7. With a more pronounced heat loss, a distinct identification of thermal performance parameters is achievable, even though higher measurement uncertainties are associated. It moreover shows that the applied black-box approach including a simpler simulation model for a more complex receiver configuration provides appropriate results. The procedure will therefore very likely be applicable for other, similar receiver designs as well.

■ 8.2.2 Power Plant Collector Loop

Collector PTC_o1

The measurement conditions of the parabolic trough power plant loop PTC_o1 represent a classical, large-scale, on-site performance test situation. Measurement data of this test loop are recorded by standardly installed measurement instrumentation for operation and

[3] as derived in Section C.1

[4] by means of the introduced TRM in Section 3.3

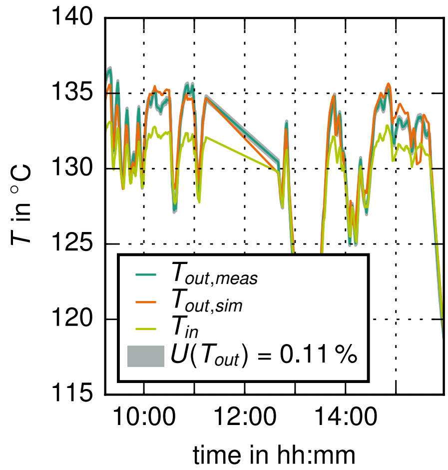

(a) collector LFC_w3

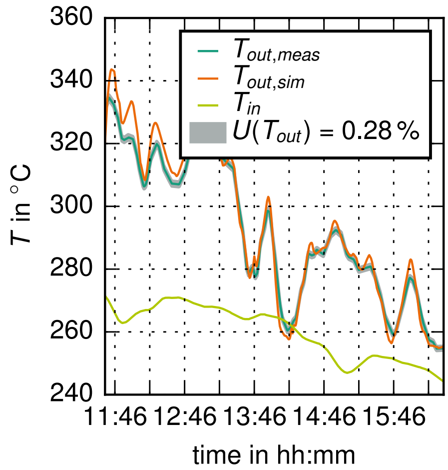

(b) collector PTC_o1

Figure 8.6: Exemplary fitting quality of the data evaluation. Simulated versus measured collector outlet temperatures for collector LFC_w3 (a) and PTC_o1 (b).

control within one large solar field. It consists as a whole of more than 30 loops under operation for several years. Flexibility of data and corresponding process conditions are therefore limited. Data were facilitated for four exemplarily selected days under normal solar field operating conditions.

Table 8.4 lists the confidence intervals and standard deviations of the identified performance parameters for this data basis. Absolute values are conform with known reference values for this well-investigated collector type. Results indicate significantly larger confidence intervals for this test situation of 2.65 %-pts. for the standard deviation of $\eta_{opt,0}$ or 38 W/m for HL_{300}. Additionally, the IAM for this parabolic trough was identified by means of a polynomial curve fit in longitudinal direction with a mean accuracy of 0.6 %. The large dispersion of the bootstrapping results reveals lower confidence of the identified performance parameters originating from the following deficits in:

Measurement instrumentation:

Installed sensors are designed for operation and control purposes, mostly not directly mounted at the exact entrance and exit of the collector loop. Irradiance sensors are commonly installed near the control facilities and not at the near side of the particular loop under investigation. For dynamic passages of clouds, this may influence the results due to a local distance between test loop and irradiance sensor. Moreover, thermal oil as a heat transfer fluid incorporates unquantifiable uncertainty sources. As already discussed in Chapter 6, a less exact definition of thermal properties is available. Additionally, altering of the fluid cannot be assessed inducing unknown error sources.

Simulation modeling:

Dynamic simulations are performed for one continuous absorber tube. Geometric details like ball joints and bends of connection tubes between modules—which are particularly characteristic for parabolic trough loops consisting of several collector modules—are not explicitly included. Due to those connective parts, higher inertia

Table 8.4: Confidence intervals of identification results for collector PTC_o1. Confidence levels in terms of CI-values and standard deviation for $\eta_{opt,0}$ and HL_{300} as well as $MURD$-values for longitudinal IAM.

Variable Unit	$\sigma(\eta_{opt,0})$ %-pts.	$CI(\eta_{opt,0})$ %-pts.	$\sigma(HL_{300})$ W/m	$CI(HL_{300})$ W/m	$MURD_{M,L}$ %	RMS(T_{out}) K
Value	2.65	−4.84/+4.72	38	−63/76	0.6	3.08

of the system arise in reality than for the simulated continuous absorber tube. This aspect is particularly affecting the capability of reproducing the fluid flow behavior accurately as exemplarily depicted in Figure 8.6(b). Simulation results react too fast (with too little inertia) to high dynamics. However, the overall tendency is reproduced correctly.

Data basis:

A small data basis of merely four days involves little information of the system under investigation. Correlation of performance parameters cannot be ruled out leading to a higher dispersion of identification results. If particular parameters are fixed to constant reference values, confidence intervals of remaining parameters are reduced.

The given results show that the data basis and measurement conditions of this test loop are not suited for a reliable collector certification. Several profound investigations have already been performed (and are still ongoing) addressing the mentioned deficits in order to overcome the induced limitations for representative performance testing of large solar field (see, e.g., Janotte [2012]). However, these aspects are considered beyond the scope of the present thesis.

Nevertheless, the dynamic evaluation of collector PTC_o1 still allows for performance checks of this system. For this test case, no steady-state data are available. Even with spare—merely dynamic—data, a fast, simple, and informative performance assessment of the loop is achievable. This particularly challenging test condition demonstrates the valuable capacity and high relevancy of the elaborated dynamic testing procedure of this thesis. Note that the standard deviation of 2.65 %-pts. is high but not completely excessive and meaningless. Similarly, the heat loss of the system is characterized with reasonable accuracy (with respect to the mentioned limitations): a standard deviation of 38 W/m corresponds to a standard deviation of the overall collector heat loss of approximately 22.8 kW. This is equivalent to around 3.0 % of the nominal collector power output of 750–850 kW. Besides, the dynamic evaluation may also reveal particular misbehavior at certain incidence angle situations, especially if the IAM is identified stepwise for the case of parabolic troughs.

All in all, the application of the dynamic testing method to the large-scale parabolic trough power plant loop demonstrates the general capability of the DT method. Even though no steady-state data is available, a study of the collector performance is feasible, providing valuable information. The results underline the importance of the measurement equipment and data basis for a meaningful performance test. They furthermore confirm the general applicability of the DT method for diverse systems at different scales, heat transfer media, and collector types. Particular potential for improvement is pointed out with respect to certification aspects of these larger systems, which is not the focus of the present thesis.

■ 8.3 Application to Collectors Operating with Steam

■ 8.3.1 Parabolic Trough Collector

Collector `PTC_s1`

Measurement data of the direct steam parabolic trough loop `PTC_s1` were already taken for the main validation of the newly implemented dynamic steam simulation models EPFM and SIMPLER. Details on the fitting quality of measurement to simulation data for exemplary days are given in Section 4.2. The entire data basis of collector `PTC_s1` consists of nine measurement days in recirculation mode leading to a fit quality of the objective variable $\dot{H}_{out}$ of 61.9 kW. Confidence intervals and standard deviations of the identified parameters generated by bootstrapping are listed in Table 8.5. Even though DSG evaluations entail higher RMS values of the objective function, standard deviations and confidence intervals are not excessively high. This indicates that outliers in the fit—which are dominating the RMS—are not having a similar dominant effect on the eventual identification result.

Notice, however, that the generation of accurate confidence intervals by the bootstrapping procedure has proven to be more demanding for steam generating collectors than for the other evaluated cases. As already pointed out in Section 4.3, global optimization procedures, such as genetic algorithms, revealed to perform better and more accurate than standard local algorithms. However, the use of the genetic algorithm has proven to be of limited meaning for the computation of confidence intervals. Genetic algorithms possess the property of being less sensitive to noise within the optimization procedure. Yet, this sensitivity is desired when applying bootstrapping calculations. This implies that a plausibility check of confidence result is essential. For this reason, in the present case, the genetic algorithm was applied for the first evaluation in order to find the global minimum. The subsequent bootstrapping was then based on the application of the commonly used least-squares algorithm with starting values neat the global optimum. Thereby, a realistic dispersion of the induced uncertainties of the identification results is available.

Note that independent of the reported confidence levels, a distinct and uncorrelated identification of optical and thermal parameters was considered a challenging task for this collector test case. Absolute $\eta_{opt,0}$-values mostly showed higher values than realistic ones. A source for this discrepancy may lie in the soiling of the collector. It was not cleaned regularly, but merely its soiling rate determined by means of reflectance measurements of the mirrors. An elaborated and standardized procedure to adequately assess soiling is currently under investigation and not yet available. For this reason, included soiling

Table 8.5: Confidence intervals of identification results for collector `PTC_s1`. Confidence levels in terms of CI-values and standard deviation for $\eta_{opt,0}$ and HL_{250} as well as $MURD$-values for longitudinal IAM.

Variable Unit	$\sigma(\eta_{opt,0})$ %-pts.	$CI(\eta_{opt,0})$ %-pts.	$\sigma(HL_{250})$ W/m	$CI(HL_{250})$ W/m	$MURD_{M,L}$ %	RMS$(\dot{H}_{out})$ kW
Value	0.77	−1.52/+1.52	25	−71/+26	0.5	62

rates of the collector are error-prone, since only a mean value of several measurements at different mirror segments are taken for the complete loop. Furthermore, measurements are not available for every test day requiring interpolation between soiling measurement days. This is causing an additional uncertainty source, because wind, rain, and other ambient conditions may interrupt the linear soiling behavior between days. Since included cleanliness values range between 76–97 %, soiling measurements may significantly influence determined optical efficiency values. This might be one reason for encountered difficulties in identifying uncorrelated heat loss parameters of this collector. Even though higher fluid temperatures (and therefore higher heat loss) are available, a remarkable correlation of optical and thermal parameters arises. However, heat loss amounts only around 5 % of collector power output. Errors in the soiling rate coupled with higher measurement uncertainties in DSG systems and less accurate curve fits for highly dynamic situation might therefore affect the heat loss and IAM identification quality for this test collector.

■ 8.3.2 Linear Fresnel Collector

Collector LFC_s1

The linear Fresnel steam collector LFC_s1 already served as a starting point for the adaptation of the optimization procedure to direct steam collectors. Steady-state evaluations in comparison to dynamic evaluations indicated a successful implementation of the procedure and already pointed out the benefit of a dynamic steam evaluation procedure. By being able to include dynamic measurement data, a determination of heat loss performance is feasible. Fitting qualities of measured versus simulated collector power outputs $\dot{Q}$ are given in Figure 4.9 of Section 4.3 for two exemplary measurement days. Table 8.6 additionally summarizes corresponding confidence intervals and standard deviations of identified optical and thermal performance parameters generated by bootstrapping. Absolute values are corresponding well to estimated values obtained from ray tracing and physical modeling of heat loss. While for the steady-state evaluation only small confidence levels appear, they are more pronounced for the dynamic case. This represents a reasonable tendency as with increasing dynamics, higher errors in measurement data as well as in the simulation accuracy arise.

Even more than the previous DSG evaluation, the computation of confidence intervals by bootstrapping for this collector has shown to be a highly challenging task. The application of a combination of genetic and least-squares optimization did not always succeed reliably for this collector evaluation. A reason for this might be the extraordinary objective function with numerous and pronounced local minima. A cause for this may lie in the soiling rates of different days that do not match to each other. As a consequence, an application of the least-square algorithm regularly lead to an identification of unrealistic local minima, even with starting values nearer to the global minimum. Remedy was found by applying a genetic algorithm with restricted parameter space. Applying genetic algorithms with very large parameter space either require excessively high computational cost and time not feasible for bootstrapping of 200 replicates. Or, equal best-fit individuals are surviving more generations leading to the very same final value of convergence, even though slight changes in the RMS occur. By limiting the parameter space, convergence is facilitated with the procedure being more sensitive to noise. Certainly, caution is required in order to prevent an artificial limitation to unrealistic narrow distributions. Nevertheless, applying a genetic algorithm for the bootstrap approach may

Table 8.6: Confidence intervals of identification results for collector LFC_s1. Confidence levels in terms of CI-values and standard deviation for $\eta_{opt,0}$ and HL_{250}.

Variable	$\sigma(\eta_{opt,0})$	$CI(\eta_{opt,0})$	$\sigma(HL_{250})$	$CI(HL_{250})$	RMS($\dot{H}_{out}$) / RMS(h_{out})
Unit	%-pts.	%-pts.	W/m	W/m	kW / kJ/kg
Dynamic	0.7	$-1.68/+0.95$	27	$-89/+101$	40
Steady-state	0.15	$-0.29/+0.21$	–	–	3981

imply histograms not tending to the commonly expected normal distribution but rather disperse and discrete bins with several identifications of the same value. The cause for this is the afore mentioned inheritance approach of evolutionary algorithms. It leads to the same best-fit descendants in noisy environments, which cannot be ruled out completely by limiting the parameter space.

Altogether, the evaluation of this collector has shown that attention has to be paid when computing confidence intervals for DSG collectors, because it still does not present a fully automated procedure yet. The results moreover underline the importance of plausibility checks of results, whether bootstrap computations succeed well. Nevertheless, generated confidence intervals allow a valuable rating of the identification results, especially in comparison to standard linear methods providing unrealistically narrow confidence levels.

■ 8.4 Remaining Challenges

Previous results indicate that the correlation of identified parameters represents a notable issue, for which no general recipe may be applied to universally avoid or even exclude it from test results. It rather has to be accepted as a side aspect of thermal characterization procedures, where performance parameters are deduced simultaneously from the very same thermal test campaign (i.e., from the same measurement data basis). This issue can be avoided by a separate testing of individual parameters, as for example proposed by Valenzuela et al. [2014]. However, this requires interfering to the process conditions of the system under test to be able to isolate specific parameters to be determined. This approach may be very time-consuming, if feasible at all for on-site measurements. It is furthermore not conform to the strategy and philosophy pursued by in situ testing, where an intrusion to the normal operation of the system under test is not desired. Additionally, the higher flexibility of a simultaneous thermal characterization of systems by means of a dynamic on-site test method are considered significantly more valuable than the remaining challenge of parameter correlation. Besides, the amount and weight of occurring correlation can be influenced in order to reduce its effect.

Evaluations have shown that correlation is dominantly arising within tests where a small data basis is available. With little information content—particularly where information is not doubled—correlation of the identified parameters increases. Analogously, the number of required measurement days depends on the focus and objective of the corresponding evaluation. The larger the number of performance parameters wished to determine and the higher the desired confidence, the larger the required measurement data basis and information content necessary. That means, it has to be decided if only a rough performance check with larger acceptable confidence intervals is desired, or a generally valid, detailed certification is aimed at. The other way around, the amount of available measurement data defines the manner of possible identification results (i.e., if one parameter with high confidence may be determined or more parameters with less confidence and potential correlation).

Concerning the particularities of DSG collectors, sensor precision and high dynamics of the system still present a challenging aspect. Steam measurements are generally associated with higher uncertainties, decreasing the accuracy of adequately reproducing the steam dynamics of the system under test. Moreover, experience has indicated that especially the limited precision of the level sensor is highly influencing an accurate balancing of the steam drum. Slight changes in the level implicate a rather pronounced change of mass flow rates and enthalpies. A more precise level measurement concept (or even a volumetric measurement approach) would therefore considerably enhance the reliability of the measurement results. Accordingly, lower dynamics in the system generally favor a meaningful assessment of the system. They imply smaller measurement uncertainties as well as a better reproduction of the dynamics by the simulation models. Thereby, a better fitting quality is achievable, resulting in higher confidence of the evaluation results.

Error values and confidence intervals of dynamic measurements will probably always be larger than for steady-state conditions. Nevertheless, steady-state conditions may be time-consuming, if attainable at all. With the dynamic steam evaluation method at hand, strict limitations to purely steady conditions can be overcome. An accurate steam performance assessment will therefore always be a compromise between flexibility of the test conditions and accuracy of the results. However, already including slight dynamics significantly enhances the meaningfulness and practicability of DSG collector tests. Moreover, for a rather sensitive DSG collector testing, well-defined collector conditions, regular cleaning, and generally smaller systems under test favor a reliable performance evaluation, because potential error sources are significantly reduced. For certification purposes of steam systems, though, mentioned limitations of the procedure still have to be particularly addressed. Yet, the elaborated approach is considered a valuable feature particularly suited for fast and simple performance checks of DSG systems.

Altogether, experience of diverse collector performance evaluations has shown that the testing and subsequent evaluation is and potentially will never be a fully automated procedure. An adequate evaluation of measurement data is always linked to a considerable effort of working with the data. Filtering of obvious measurement errors or potential periods of high uncertainties (such as low irradiance values) and exclusion of discrepancies in measurement data represents an important task before a final evaluation. Thereby, a detailed study and plausibility checks of the corresponding data points and time intervals will always be a necessary condition for a correct determination of performance parameters. However, with the diverse elaborated elements of the dynamic evaluation method at hand, good tools are existent to study and detect potential error sources within the evaluation procedure. They considerably enhance the testing procedure leading to an easier as well as more trust- and meaningful performance evaluation. In this way, a reliable assessment of collector performance is facilitated.

Chapter 9

Conclusion of Procedures and Results

9.1 Summary

Within this thesis, a comprehensive approach of dynamic performance testing and evaluation procedure for line-concentrating solar thermal collectors is elaborated. The substantial and main benefit of dynamic testing represents its possible application to on-site, in situ measurements, where no strict limitations to distinct measurement conditions are given. However, a literature review and survey among a representative group of the CSP community show that a dynamic testing method for performance tests is not yet commonly available nor universally elaborated for concentrating collectors in general. Especially for larger systems predominantly tested in outdoor facilities—as the case for concentrating collectors—dynamic testing is considered a relevant and valuable option. Thereby, a significant reduction of testing time and effort is expected.

To prove the general viability of the proposed Dynamic Testing (DT) method, it is validated in a first step to the Quasi-Dynamic Testing (QDT) procedure of the current testing standard ISO 9806 [2013]. Equivalence in identified performance results for one exemplary test collector demonstrate the general reliability of the alternative testing approach. Furthermore, particularities of the DT method, especially in comparison to the QDT method, are addressed: differences in the objective function of the optimization procedure, recommendations concerning algorithm settings, and appropriate heat loss models of concentrating collectors in general and for linear Fresnel collectors in particular are given.

The suggested testing procedure includes an expansion of the DT method to collectors generating direct steam in recirculation mode. Because compressible heat transfer media show different fluid behavior than incompressible fluids, an adaptation of the dynamic simulation model is required. In this way, the standardly used discretization in terms of the Plug-Flow Model (PFM) is extended to a newly proposed Extended Plug-Flow Model (EPFM) approach. The simple adaptation is accordingly validated to a more detailed—and more computational time expensive—SIMPLER model for direct steam generation. The successful implementation of both new dynamic steam simulation models and a justification for using the simpler and faster EPFM model could be demonstrated. Moreover, testing of DSG collectors involves an adoption of the optimization procedure.

Due to differences in available sensors and measurement points within the tested steam system, the data processing as well as the objective function of the optimization approach need to be adjusted. Applying the newly introduced procedure to exemplary data of a DSG test collector confirms the viable implementation of the dynamic steam evaluation approach.

An important element of the evaluation procedure represents the computation of meaningful confidence intervals. They facilitate an assessment of identification results. However, statistical inference still represents a seldomly addressed aspect, commonly not available in thermal collector testing. Therefore, valuable information is generated concerning the confidence and reliability of performance parameters via two different approaches of bootstrapping and random sub-sampling. Standard confidence methods are proven to fail for the application within the present context of dynamic performance evaluation. By the alternative approaches good means are additionally enabled for appropriately detecting potential error sources in the evaluation procedure.

Confidence levels of identified performance parameters may considerably be influenced by the quality of measurement instrumentation. For this reason, a detailed investigation of appropriate measurement equipment and their associated measurement uncertainties is presented. Their exemplary effect on collector performance measurements and derived collector power outputs show that the suitability of measurement equipment strongly depends on the operating conditions of the test situation. As a result, no generally valid recommendation concerning specific instrumentation is possible. Nevertheless, the results illustrate that smaller systems under test tend to be more sensitive to measurement uncertainties, especially concerning temperature and irradiance measurements. The presented systematic uncertainty case study furthermore serves as a guideline for the selection of appropriate measurement instrumentation. The analysis is designed such that the results are also transferable to other testing situations, which are not specifically studied within the present thesis.

To increase the representativeness and reliability of identification results, a comprehensive derivation of an appropriate testing strategy is additionally included. It is based on artificially created measurement data to provide a broad study of potential effects influencing the meaningfulness of evaluation results. Drawn conclusions are moreover validated by analyzing real measurement data of a large data basis in order to double check significant effects to reality. Both studies reveal that no particularly set operating conditions of mass flow and temperature course are required. However, the available range of fluid temperatures does significantly influence heat loss identification and its correlation to optical parameters. Higher fluid temperatures and amounts of overall heat loss favor a distinct identification. Concerning the IAM identification, results show that a wide-spread incidence angle distribution is essential, especially in the case of LFCs. Besides, for stepwise IAM identifications, attention has to be paid to sufficient values of mean DNI levels and number of data points available for the specific angle bins. Generally, a larger extent of available data improves the overall identification quality as more information content is implied.

As a last step, the general applicability of the comprehensive procedure is verified. Evaluated test collectors imply different heat transfer fluids (pressurized water, thermal oil, and steam) at different collector scales (small-scale process heat and large-scale power plant collectors) of different types (parabolic trough and linear Fresnel collectors) as well as diverse locations and measurement conditions. Exemplary evaluations of the variety of test collectors succeed well and thereby demonstrate a broad validity of the developed alternative testing method.

■ 9.2 Overall Conclusions and Outlook

The present thesis introduces an enhanced dynamic performance testing and evaluation method. It is regarded a valuable alternative to overcome the limitations of the normative quasi-dynamic testing method, particularly in the context of testing larger systems as line-concentrating solar collectors. Since its equivalence to the testing standard is confirmed, it therefore represents a powerful tool addressing diverse aspects of a comprehensive collector characterization. Main findings of the work within this thesis substantially contributed to a best practice guideline jointly compiled by Fraunhofer ISE and DLR concerning 'Dynamic in situ Performance and Acceptance Testing (DisPAT) of Line-Concentrating Collectors and Solar Fields' [Janotte and Zirkel-Hofer, 2018]. This guideline is currently under external, international review and is expected to be available by end of 2017.

The proposed procedure is equally suited for certification purposes as well as simple and fast performance checks. The capability of the procedure and the significance of its test results strongly depend on the quality of measurement instrumentation and evaluated data basis. If high confidence of the test results is desired, standard instrumentation for operation and control may not be particularly suited. Lower sensor precision and accuracy, however, are appropriate for rough and fast performance checks. They are regarded useful, if not even essential, for the development and improvement of new products and designs. High quality instrumentation favor the representativeness of results associated with low uncertainty bands. This represents a necessary requirement for certification purposes. Moreover, high precision sensors are particularly beneficial for an accurate IAM identification for LFCs. This collector type with its complex optical characteristics—by implicating a stepwise IAM identification—has shown to be sensitive to higher measurement uncertainties.

Besides, emerging parameter correlation of test results can be reduced by higher measurement quality. Nevertheless, detailed studies have revealed that parameter correlation cannot be completely ruled out in thermal collector testing with a simultaneous derivation of optical and thermal parameters. The proposed testing strategy provides a guideline for mitigating this aspect. However, evaluation experience has shown that it is strongly recommended to always report test results as a conjunction of all parameters. An extraction of single parameters may therefore lead to erroneous interpretations of the specific performance parameter out of its original context. For example, a high optical efficiency coupled with low heat loss is superior to an equal optical efficiency coupled with an excessively high heat loss. A separate reporting of only the optical efficiency values would therefore be misleading. Correlation of identified parameters may be significantly improved with a larger data basis available. If doubled information is contained in the data basis, the evaluation procedure is considerably stabilized, generating more representative results less sensitive to measurement errors. An inclusion of higher error-prone data (e.g., low irradiance periods) is generally acceptable, as long as they are not prevailing particular characteristic test situations. In this way, low irradiance values may be included if similar data with more reliable irradiance levels are available.

Potential error sources are additionally given by the soiling rate of the mirrors. For higher confidence of the test results, soiling of the mirror rows should be avoided in general. If a regular cleaning during measurement periods is not feasible, an assessment of the soiling rate by reflectance measurements is strongly advised. Results have shown that the inclusion of mean values remarkably improves identification results, but does not lead to completely satisfactory results so far. A universally valid and completely characteristic assessment of soiling rates for larger systems represents an ongoing research activity. It is not yet adequately elaborated, especially for certification purposes. A reliable and meaningful methodology for determining representative soiling rates is however not considered trivial. In order to increase the flexibility and benefit of in situ measurements, it is regarded an important aspect and worthwhile to further investigate.

A similar and still challenging element of collector testing represents the performance evaluation of DSG collectors. By enabling a dynamic reproduction of steam generating collectors and an adequate identification of its performance parameters, a big improvement concerning the applicability of the present dynamic test method is achieved. Nevertheless, limited precision of the measurement instrumentation imply lower fit qualities as well as higher uncertainty values. They arise even for good measurement conditions as given in the well-studied DISS steam test loop of the PSA. For certification purposes, they are however not yet considered sufficient. Experience showed that the larger and complex the steam network, the more probable potential error sources which may not be taken into account in the evaluation procedure. DSG performance identification revealed to be particularly sensitive to soiling rates demanding advanced optimization approaches. Collector certification based on dynamic steam evaluations therefore requires regular cleaning and higher steam measurement precision. Standardly installed sensors indicated to be insufficient, if high confidence of the test results is aimed at. Particularly, a steam quality measurement device would considerably improve the test results, which is currently not available. Improving the level measurement of the steam drum represents a beneficial option to further investigate in order to increase the identification quality. By extending the dynamic test method to an evaluation of direct steam collectors, a viable procedure is accessible. For collector certification, further investigation in appropriate sensors and testing strategies is advised to make performance evaluation more stable. Nonetheless, the introduced procedure is already presenting a valuable and meaningful tool for performance checks of steam generating systems.

Analogously, the elaborated DT method may be adequately applied for performance checks under non-perfect measurement conditions. They are exemplarily given for test situations implying low quality instrumentation, a small data basis, or with little temperature and angle information. Still, the proposed methodology and procedure allows for brief studies of the collector behavior. It thereby permits statements concerning rough performance values, identifying potential error sources and misbehaviors. In this way, design enhancements and development of new products is supported enabling a simple and quick assessment of novelties.

All in all, a first utility and applicability of the elaborated dynamic testing procedure is proven within this thesis, especially in the context of meaningful performance checks. In order to increase the reliability of the method with regard to certification purposes, a further application to more collector systems of diverse scales, types, and configurations is regarded essential. A wide and numerous application of the alternative method would continually confirm its functional capability. This will facilitate an ongoing improvement and consequent stabilization of the test procedure on its way to a commonly accepted alternative procedure included in the relevant testing standards.

For instance, the dynamic procedure could potentially be used as well for CPC collectors or other low-concentrating collector designs. Similarly, the methodology is expected to viably work for larger configurations (i.e., fields) of low-temperature collectors as flat plate or vacuum tube collectors. Both applications share the property of being hardly suited for indoor laboratory testing and therefore require in situ characterization. Certainly, with the proposed procedure and methodology at hand, a good basis is existent for a simple and successful adaption of the procedure to those particular test situations. As already indicated in the exemplary collector evaluations, the present procedure is also applicable for larger loops and fields of line-concentrating solar collectors. However, for a more distinct system characterization, a further adaption of the modeling approach is recommended. Thereby, the particularities of larger systems under test are expected to be reproduced more accurately. In view of the emerging and currently multiply investigated technology of solar tower power plants, the elaborated methodology may represent a beneficial and viable basis for an extended application to those systems as well. Further detailed research on adaptations and advancement of this procedure are regarded an important step towards performance testing of solar towers eventually confirming its viability.

In general, the work of the present thesis represents a valuable basis for the universal testing of less standardized and new technologies of larger scale. Furthermore, regarding already more established solar thermal technologies, the proposed procedure proves to be a powerful and beneficial extension of the current testing standard to more complex test situations. They are predominantly arising within on-site measurements targeting at in situ certification. Flexible and simultaneously reliable certification procedures are considered crucial for the further establishment of solar thermal technologies and their global acceptance.

Bibliography

Adams, B. M., Ebeida, M. S., Eldred, M. S., Jakeman, J. D., Maupin, K. A., Monschke, J. A., Swiler, L. P., Stephens, J. A., Vigil, D. M., Wildey, T. M., Bohnhoff, W. J., Dalbey, K. R., Eddy, J. P., Hooper, R. W., Hu, K. T., Hough, P. D., Ridgway, E. M., and Rushdi, A. (2016). Dakota, a multilevel parallel object-oriented framework for design optimization, parameter estimation, uncertainty quantification, and sensitivity analysis: Version 6.5 User's Manual.

ASTM E 905 – 87 (2007). Standard Test Method for Determining Thermal Performance of Tracking Concentrating Solar Collectors.

Bates, D. M. and Watts, D. G. (2007). *Nonlinear regression analysis and its applications*. Wiley-Interscience paperback series. Wiley, New York and Chichester.

Beichelt, F. E. and Montgomery, D. C. (2003). *Teubner-Taschenbuch der Stochastik: Wahrscheinlichkeitstheorie, Stochastische Prozesse, Mathematische Statistik*. Vieweg+Teubner Verlag, Wiesbaden.

Biencinto, M., González, L., and Valenzuela, L. (2016). A quasi-dynamic simulation model for direct steam generation in parabolic troughs using TRNSYS. *Applied Energy*, 161:133–142.

Bonilla, J., Yebra, L. J., and Dormido, S. (2012). Chattering in dynamic mathematical two-phase flow models. *Applied Mathematical Modelling*, 36(5):2067–2081.

Büchner, D. (2014). *Analysis and Development of a Method for Determining the Performance of Concentrating Solar Collectors*. Master's Thesis (not published), ENSE3, Grenoble.

Büchner, D. and Hofer, A. (2015). Parameter Identification for Linear Fresnel Collectors Using ColSim and Dakota: Internal Documentation at Fraunhofer ISE.

CEN and CENELEC (2006). Internal regulations - Part 4 certification - The keymark system.

Davison, A. C. and Hinkley, D. V. (1997). *Bootstrap methods and their application*. Cambridge University Press, Cambridge.

Dogan, G. (2004). Confidence interval estimation in system dynamics models: Bootstrapping vs. likelihood ratio method. In *Proceedings of the 22nd International Conference of the System Dynamics Society*. Oxford, UK.

Dogan, G. (2007). Bootstrapping for confidence interval estimation and hypothesis testing for parameters of system dynamics models. *System Dynamics Review*, 23(4):415–436.

Donaldson, J. R. and Schnabel, R. B. (1987). Computational Experience with Confidence Regions and Confidence Intervals for Nonlinear Least Squares. *Technometrics*, 29(1):67.

Dow (1997). Dowtherm A – Heat Transfer Fluid: Product Technical Data.

Duffie, J. A. and Beckman, W. A. (2013). *Solar engineering of thermal processes*. John Wiley & Sons.

Eck, M., Zarza, E., Eickhoff, M., Rheinländer, J., and Valenzuela, L. (2003). Applied research concerning the direct steam generation in parabolic troughs. *Solar Energy*, 74(4):341–351.

Efron, B. (1979). Bootstrap Methods: Another Look at the Jackknife. *The Annals of Statistics*, 7(1):1–26.

Elsafi, A. M. (2015). On thermo-hydraulic modeling of direct steam generation. *Solar Energy*, 120:636–650.

Feldhoff, J. F., Eickhoff, M., Keller, L., Alonso, J. L., Meyer-Grünefeldt, M., Valenzuela, L., Pernpeintner, J., and Hirsch, T. (2014). Status and First Results of the DUKE Project – Component Qualification of New Receivers and Collectors. *Energy Procedia*, 49:1766–1776.

Feldhoff, J. F., Hirsch, T., Pitz-Paal, R., and Valenzuela, L. (2015). Transient Models and Characteristics of Once-through Line Focus Systems. *Energy Procedia*, 69:626–637.

Fernández-García, A., Sutter, F., Martínez-Arcos, L., Sansom, C., Wolfertstetter, F., and Delord, C. (2017). Equipment and methods for measuring reflectance of concentrating solar reflector materials. *Solar Energy Materials and Solar Cells*, 167:28–52.

Fernández-García, A., Zarza, E., Valenzuela, L., and Pérez, M. (2010). Parabolic-trough solar collectors and their applications. *Renewable and Sustainable Energy Reviews*, 14(7):1695–1721.

Fischer, S., Heidemann, W., and Müller-Steinhagen, H. (2003). Collector parameter identification - Iterative methods versus multiple linear regression. In International Solar Energy Society -ISES-, editor, *ISES Solar World Congress*. International Solar Energy Society (ISES).

Fischer, S., Heidemann, W., Muller-Steinhagen, H., Perers, B., Bergquist, P., and Hellstrom, B. (2004). Collector test method under quasi-dynamic conditions according to the European Standard EN 12975-2. *Solar Energy*, 76(1-3):117–123.

Fischer, S., Lüpfert, E., and Müller-Steinhagen, H. (2006). Efficiency testing of parabolic trough collectors using the quasi-dynamic test procedure according to the European Standard EN 12975. In *SolarPACES 2006, 13th Solar Power And Chemical Energy Systems International Symposium*.

Forristall, R. (2003). Heat transfer analysis and modeling of a parabolic trough solar receiver implemented in engineering equation solver.

Heimsath, A., Bern, G., van Rooyen, D., and Nitz, P. (2014a). Quantifying Optical Loss Factors of Small Linear Concentrating Collectors for Process Heat Application. *Energy Procedia*, 48(0):77–86.

Heimsath, A., Cuevas, F., Hofer, A., Nitz, P., and Platzer, W. J. (2014b). Linear Fresnel collector receiver: Heat loss and temperatures. *Energy Procedia*, 49(0):386–397.

Hernández, E. L. (2015a). *Extension of a Simulation Software for Line-Concentrating Solar Collectors to Direct Steam Generation*. Bachelor's Thesis, Karlsruhe Insitute of Technology, Karlsruhe.

Hernández, E. L. (2015b). Summary of Some Models for Direct Steam Generation: Internal Documentation at Fraunhofer ISE.

Hernández, E. L. and Zirkel-Hofer, A. (2016). Steam Drum Type Documentation: Internal Documentation at Fraunhofer ISE.

Hertel, J. D., Martinez-Moll, V., and Pujol-Nadal, R. (2015). Estimation of the influence of different incidence angle modifier models on the biaxial factorization approach. *Energy Conversion and Management*, 106:249–259.

Hirsch, T. (2005). *Dynamische Systemsimulation und Auslegung des Abscheidesystems für die solare Direktverdampfung in Parabolrinnenkollektoren*, volume 535 of *Fortschritt-Berichte / 06 / VDI*. VDI-Verl., Düsseldorf.

Hirsch, T., Feldhoff, J. F., Hennecke, K., and Pitz-Paal, R. (2014). Advancements in the Field of Direct Steam Generation in Linear Solar Concentrators—A Review. *Heat Transfer Engineering*, 35(3):258–271.

Hirsch, T., Steinmann, W., and Eck, M. (2005). Simulation of transient two-phase flow in parabolic trough collectors using Modelica. In Schmitz, G., editor, *4th International Modelica Conference*, pages 403–412.

Hofer, A., Büchner, D., Heimsath, A., Fahr, S., Kramer, K., Platzer, W., and Scholl, S. (2015a). Comparison of Two Different (Quasi-) Dynamic Testing Methods for the Performance Evaluation of a Linear Fresnel Process Heat Collector. *Energy Procedia*, (69):84–95.

Hofer, A., Cuevas F., Heimsath A., Nitz P., Platzer W., and Scholl S. (2015b). Extended heat loss and temperature analysis of three linear Fresnel receiver designs. *Energy Procedia*, (69):424–433.

Hofer, A., Valenzuela, L., Janotte, N., Burgaleta, J. I., Arraiza, J., Montecchi, M., Sallaberry, F., Osório, T., Carvalho, M. J., Alberti, F., Kramer, K., Heimsath, A., Platzer, W., and Scholl, S. (2016). State of the art of performance evaluation methods for concentrating solar collectors. In *AIP Conference Proceedings 1734*, volume 1734, page 020010, Melville, New York. AIP Publishing.

Horta, P., Brunner, C., Muster-Slawitsch, B., and Zipf, V. (2017). Solar Heat for Industrial Processes: current status and perspectives of an untapped potential (submitted and under review in Solar Energy Journal).

Horta, P. and Osorio, T. (2013). Optical Characterization Parameters for Line-focusing Solar Concentrators: Measurement Procedures and Extended Simulation Results. *Energy Procedia*, 49:98–108.

IAPWS (1997). Release on the IAPWS Industrial Formulation 1997 for the Thermodynamic Properties of Water and Steam (IAPWS-IF97).

IAPWS (2003). Uncertainties in Enthalpy for the IAPWS Formulation 1995 for the Thermodynamic Properties of Ordinary Water Substance for General and Scientific Use (IAPWS-95) and the IAPWS Industrial Formulation 1997 for the Thermodynamic Properties of Water and Steam (IAPWS-IF97).

Industrial Solar GmbH (2017). Technical Data - Industrial Solar linear Fresnel collector LF-11.

ISO 9806 (2013). Solar energy - Solar thermal collectors - Test methods ISO 9806:2013(E).

ISO 9806 (2017). Solar energy - Solar thermal collectors - Test methods ISO 9806:2017(E).

Janotte, N. (2012). *Requirements for representative acceptance tests for the prediction of the annual yield of parabolic trough solar fields*. Berichte aus der Energietechnik. Shaker, Aachen.

Janotte, N., Feckler, G., Kötter, J., Decker, S., Herrmann, U., Schmitz, M., and Lüpfert, E. (2014). Dynamic Performance Evaluation of the HelioTrough® Collector Demonstration Loop–Towards a New Benchmark in Parabolic Trough Qualification. *Energy Procedia*, 49:109–117.

Janotte, N., Lüpfert, E., and Pitz-Paal, R. (2012). Acceptance testing and advanced evaluation strategies for commercial parabolic trough solar fields. In *SolarPACES 2012, 18th Solar Power And Chemical Energy Systems International Symposium*.

Janotte, N., Meiser, S., Krüger, D., Lüpfert, E., Pitz-Paal, R., Fischer, S., and Müller-Steinhagen, H. (2009). Quasi-dynamic analysis of thermal performance of parabolic trough collectors. In *SolarPACES 2009, 15th Solar Power And Chemical Energy Systems International Symposium*.

Janotte, N. and Zirkel-Hofer, A. (2018). Dynamic in situ Performance and Acceptance Testing of Line-Concentrating Collectors and Solar Fields (DisPAT): Best Practice Guideline (to be published, currently under external review).

JCGM (2008). Evaluation of measurement data — Guide to the expression of uncertainty in measurement (GUM); Joint Committee for Guides in Metrology (JCGM) 100.

Kearney, D. (2011). Utility-scale parabolic trough solar systems: Performance acceptance test guidelines, April 2009 - December 2010.

Kong, W. Q., Wang, Z. F., Fan, J. H., Bacher, P., Perers, B., Chen, Z. Q., and Furbo, S. (2012a). An improved dynamic test method for solar collectors. *Solar Energy*, 86(6):1838–1848.

Kong, W. Q., Wang, Z. F., Li, X., and Xiao, N. (2012b). Theoretical analysis and experimental verification of a new dynamic test method for solar collectors. *Solar Energy*, 86(1):398–406.

Krüger, D., Krüger, J., Pandian, Y., O'Connell, B., Feldhoff, J. F., Karthikeyan, R., Hempel, S., Muniasamy, K., Hirsch, T., Eickhoff, M., and Hennecke, K. (2012). Experiences with Direct Steam Generation at the Kanchanaburi Solar Thermal Power Plant. In *SolarPACES 2012, 18th Solar Power And Chemical Energy Systems International Symposium*.

Kunsch, H. R. (1989). The Jackknife and the Bootstrap for General Stationary Observations. *The Annals of Statistics*, 17(3):1217–1241.

Lauterbach, C., Schmitt, B., Jordan, U., and Vajen, K. (2012). The potential of solar heat for industrial processes in Germany. *Renewable & Sustainable Energy Reviews*, 16(7):5121–5130.

Lecheler, S. (2011). *Numerische Strömungsberechnung: Schneller Einstieg durch ausführliche praxisrelevante Beispiele*. Studium. Vieweg + Teubner, Wiesbaden, 2nd edition.

Li, H. and Maddala, G. S. (1996). Bootstrapping time series models. *Econometric Reviews*, 15(2):115–158.

Linstrom, P. J. and Mallard, W. G. (1997). NIST Chemistry WebBook, NIST Standard Reference Database 69.

Lippke, F. (1994). *Numerische Simulation der Absorberdynamik von Parabolrinnen-Solarkraftwerken mit direkter Dampferzeugung*. VDI Verlag, Düsseldorf.

Lobón, D. H., Baglietto, E., Valenzuela, L., and Zarza, E. (2014a). Modeling direct steam generation in solar collectors with multiphase CFD. *Applied Energy*, 113:1338–1348.

Lobón, D. H., Valenzuela, L., and Baglietto, E. (2014b). Modeling the dynamics of the multiphase fluid in the parabolic-trough solar steam generating systems. *Energy Conversion and Management*, 78:393–404.

Lovegrove, K. and Stein, W. (2012). *Concentrating solar power technology: Principles, developments and applications*, volume number 21 of *Woodhead Publishing series in energy*. Woodhead Publishing, Oxford and Philadelphia.

McIntire, W. R. (1982). Factored approximations for biaxial incident angle modifiers. *Solar Energy*, 29(4):315–322.

Mertins, M. (2009). *Technische und wirtschaftliche Analyse von horizontalen Fresnel-Kollektoren*. Dissertation, Universität Karlsruhe, Karlsruhe.

Moya, S. L., Valenzuela, L., and Zarza, E. (2011). Numerical study of the thermal-hydraulic behavior of water-steam flow in the absorber tube of the DISS system using RELAP. In *SolarPACES 2011, 17th Solar Power And Chemical Energy Systems International Symposium*.

Muschaweck, J. and Spirkl, W. (1993). Dynamic solar collector performance testing. *Solar Energy Materials and Solar Cells*, 30(2):95–105.

Nayak, J. K. and Amer, E. H. (2000). Experimental and theoretical evaluation of dynamic test procedures for solar flat-plate collectors. *Solar Energy*, 69(5):377–401.

Nettelstroth, J. (2015). *Advancement of a dynamic method for determining the performance of linear concentrating solar collectors*. Master's Thesis, Universität Stuttgart, Stuttgart.

Nettelstroth, J. and Hofer, A. (2016). A dynamic method for determining the performance of linear concentrating solar collectors: Extended documentation of the dynamic parameter identification method with Dakota and ColSim: Internal Documentation at Fraunhofer ISE.

Osório, T. and Carvalho, M. J. (2014). Testing of solar thermal collectors under transient conditions. *Solar Energy*, 104:71–81.

Patankar, S. V. (1980). *Numerical heat transfer and fluid flow*. Series in computational methods in mechanics and thermal sciences. Hemisphere Pub. Corp. and McGraw-Hill, Washington and New York.

Perers, B. (1993). Dynamic method for solar collector array testing and evaluation with standard database and simulation programs. *Solar Energy*, 50(6):517–526.

Perers, B. (1997). An improved dynamic solar collector test method for determination of non-linear optical and thermal characteristics with multiple regression. *Solar Energy*, 59(4-6):163–178.

Perers, B. (2011). Experiences and lessons learned from 30 years of dynamic collector testing, modelling and simulation. In *ISES Solar World Congress 2011*, Germany. International Solar Energy Society.

Perry, S. (2016). Internal discussion at Fraunhofer ISE on the correct computation of confidence intervals and their validation for the dynamic parameter identification procedure.

Perry, S. (2017). Artificial Weather: Quantifying the Error - Mathematical Proof of Using 10 Forks: Internal Documentation at Fraunhofer ISE.

Platzer, W., Heimsath, A., and Hülsey, H. (2009). Parameter identification technique for the determination of optical efficiency of concentrating collectors. In *SolarPACES 2009, 15th Solar Power And Chemical Energy Systems International Symposium*.

Rao, S. S. (2009). *Engineering optimization: Theory and practice*. Wiley, Hoboken (N.J.), 4th edition.

Rojas, D., Beermann, J., Klein, S. A., and Reindl, D. T. (2008). Thermal performance testing of flat-plate collectors. *Solar Energy*, 82(8):746–757.

Sallaberry, F., Valenzuela, L., de Jalón, A. G., Leon, J., and Bernad, I. D. (2016). Towards standardization of in-site parabolic trough collector testing in solar thermal power plants. In *AIP Conference Proceedings 1734*, volume 1734, page 130019, Melville, New York. AIP Publishing.

Seber, G. A. F. and Wild, C. J. (2005). *Nonlinear regression*. Wiley series in probability and statistics. Wiley, Hoboken, NJ.

Serrano-Aguilera, J. J. and Valenzuela, L. (2016). Transient validation of RELAP5 model with the DISS facility in once through operation mode. In *AIP Conference Proceedings 1734*, volume 1734, page 040006, Melville, New York. AIP Publishing.

Seubert, B. (2015). Internal discussion on the adaptation of the Fraunhofer ISE inhouse simulation software ColSim to dynamic DSG simulations.

Solutia (1998). Therminol VP1 – Technical Data Sheet: Vapour Phase, Liquid Phase, Heat Transfer Fluid.

Teske, S. and Leung, J. (2016). Solar Thermal Electricity: Global Outlook 2016: Jointly prepared by European Solar Thermal Electricity Association (ESTELA), Greenpeace International and SolarPACES.

Ulbrich, M. (2012). *Nichtlineare Optimierung*. Mathematik kompakt. Birkhäuser, Basel.

Valenzuela, L., López-Martín, R., and Zarza, E. (2014). Optical and thermal performance of large-size parabolic-trough solar collectors from outdoor experiments: A test method and a case study. *Energy*, 70:456–464.

Valenzuela, L., Zarza, E., Berenguel, M., and Camacho, E. F. (2005). Control concepts for direct steam generation in parabolic troughs. *Solar Energy*, 78(2):301–311.

VDI-GVC (2010). *VDI Heat Atlas: Verein Deutscher Ingenieure, VDI-Gesellschaft Verfahrenstechnik und Chemieingenieurwesen (CVG)*. Springer Verlag, Berlin and Heidelberg, 2nd edition.

Walter, H. (2001). *Modellbildung und numerische Simulation von Naturumlaufdampferzeugern*, volume 457 of *Fortschritt-Berichte // VDI Reihe 6, Energietechnik*. VDI-Verl., Düsseldorf.

Walter, H. (2007). Dynamic simulation of natural circulation steam generators with the use of finite-volume-algorithms – A comparison of four algorithms. *Simulation Modelling Practice and Theory*, 15(5):565–588.

Weißmüller, C., Frenz, H., Krämer, E., Adelmann, J., Malitte, H.-J., and Triebel, J. (2012). Proficiency Test - QAiST testing of solar collectors and solar systems 2010-2011: Final Report.

Wittwer, C. (1999). *ColSim - Simulation von Regelungssystemen in aktiven solarthermischen Anlagen*. Dissertation, Universität Karlsruhe, Karlsruhe and Germany.

Wittwer, C., Hube, W., Schossig, P., Wagner, A., Kettner, C., Mertins, M., and Rittenhofer, K. (2001). ColSim - A new simulation environment for complex system analysis and controllers. In *7th Conference of Internation Building Performance Simulation Association (IBPSA)*, pages 237–244. The International Building Performance Simulation Association (IBPSA).

Xu, L., Wang, Z., Li, X., Yuan, G., Sun, F., Lei, D., and Li, S. (2014). A comparison of three test methods for determining the thermal performance of parabolic trough solar collectors. *Solar Energy*, 99:11–27.

Xu, L., Wang, Z. F., Li, X., Yuan, G. F., Sun, F. H., and Lei, D. Q. (2013). Dynamic test model for the transient thermal performance of parabolic trough solar collectors. *Solar Energy*, 95:65–78.

Xu, L., Wang, Z. F., Yuan, G. F., Li, X., and Ruan, Y. (2012). A new dynamic test method for thermal performance of all-glass evacuated solar air collectors. *Solar Energy*, 86(5):1222–1231.

Xu, R. and Wiesner, T. F. (2015). Closed-form modeling of direct steam generation in a parabolic trough solar receiver. *Energy*, 79:163–176.

Zahw, T. Y. (2014). *Heat loss sensitivity analysis of different linear Fresnel collector receiver configurations*. Master Thesis, Universität Kassel, Cairo University, Kassel, Cairo.

Zarza, E., Valenzuela, L., León, J., Hennecke, K., Eck, M., Weyers, H. D., and Eickhoff, M. (2004). Direct steam generation in parabolic troughs: Final results and conclusions of the DISS project. *Energy*, 29(5–6):635–644.

Zirkel-Hofer, A., Perry, S., Fahr, S., Kramer, K., Heimsath, A., Scholl, S., and Platzer, W. (2016). Improved in situ performance testing of line-concentrating solar collectors: Comprehensive uncertainty analysis for the selection of measurement instrumentation. *Applied Energy*, 184:298–312.

Zirkel-Hofer, A., Perry, S., Fahr, S., Kramer, K., Heimsath, A., Scholl, S., and Platzer, W. (2018). Confidence Interval Computation Method for Dynamic Performance Evaluations of Solar Thermal Collectors. *Solar Energy*, 162:585–596.

Appendix A

Basics and Particularities of Line-Concentrating Solar Collectors

A.1 General Characteristics

By tracking their mirror lines according to the sun position, line-concentrating solar thermal collectors reflect the incoming solar radiation onto a focal line. As only parallel, uni-directional radiation can be reflected onto a specific target, merely Direct Normal Irradiance (DNI)—with the variable G_{bn}—is converted to heat, whereas diffuse irradiation G_d cannot be used. Line-concentrating collectors are characterized by their simple modularity: depending on the installed length of the system, the power of the system can be adapted. Moreover, scalability presents an additional advantage: depending on the design of the collector (i.e., in terms of collector aperture areas) they can be used for different applications, ranging from solar process heat integration to power plant electricity generation. Line-concentrating collector can be differentiated into Parabolic Trough Collectors (PTCs) and Linear Fresnel Collectors (LFCs), featuring different optical and thermal characteristics.

A.1.1 Parabolic Trough Collectors

Parabolic trough collectors consist of parabolically shaped primary mirrors, reflecting the solar radiation onto an evacuated absorber tube (see Figure A.1(a)). With changing sun position, the entire parabolic collector is tracked, requiring a moving absorber tube with flexible and mobile interconnections in form of ball joints. Tracking gear and structure of the collector are designed to withstand high wind loads, as the completely tracked mirror line is exposed to potential wind. The aperture plane of a parabolic trough collector is parallel to its rotation axis and determined by the outer linear edges of the parabolic reflector. It is in a fixed relation to the rotating reflector, but changes position and orientation relative to the ground depending on the tracking position.

A.1.2 Linear Fresnel Collectors

Linear Fresnel collectors consist of several long and narrow reflector lines, only slightly bent due to their back structure (see Figure A.1(b)). Tracking is performed of all mirror lines collectively but not of the complete collector aperture. The reflectors focus on an

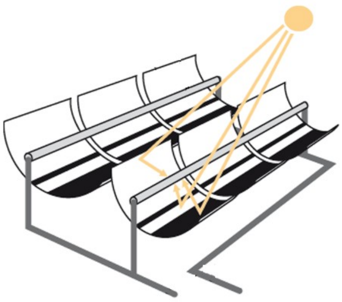

(a) Parabolic trough collector

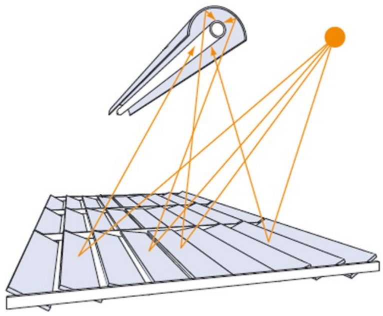

(b) Linear Fresnel collector

Figure A.1: Sketches of line-concentrating solar thermal collectors. PTC (a) with parabolically shaped mirrors, evacuated absorber tube as receiver and completely tracked collector; LFC (b) with narrow, slightly bent mirror lines, receiver with secondary reflector and tracking of every individual mirror line. © www.solarpraxis.de, M. Römer

elevated long linear tower receiver running parallel to the reflector rotational axis [Lovegrove and Stein, 2012, pp. 153–154]. This allows the installation of a fixed absorber tube with no moving parts. For this reason, LFCs are particularly well suited for the generation of direct steam, since no sensitive high pressure moving parts have to be implemented.

As the ideal geometry of a parabola is only approximated by the Fresnel design, optical losses are more pronounced compared to parabolic trough collectors. Nevertheless, with an adapted receiver design, optical loss is reduced. A secondary mirror installed at the back of the fixed absorber tube reflects the scattered radiation from the primary mirror field a second time to the absorber tube in order to increase the overall optical efficiency. Receiver designs of LFCs are diverse: ranging from one tube to multiple tubes, with evacuated glass envelope or non-evacuated glass plate cover. For an exemplary illustration of diverse LFC receiver designs, see Figure A.2.

Because only the individual single mirror line is turned, less wind loads are affecting the mirrors, steel structure, and tracking gears. By all this, LFCs show a significant potential of cost reductions. Moreover, as there are less reflector areas exposed to wind, higher concentration ratios are feasible. The collector aperture plane is defined by the axes of the corresponding mirror lines (coplanar by construction). The aperture plane of a linear Fresnel collector does not change with the sun position and is fixed relative to the ground. However, LFCs are less commercially installed than parabolic trough systems. [Lovegrove and Stein, 2012, pp. 153–154]

A.2 Optical Properties

A.2.1 Optical Efficiency

The optical efficiency η_{opt} represents an aggregated optical performance value including all optical attenuation factors from the incoming solar radiation to the absorber surface. It therefore depends on geometric parameters such as the concentration ratio and intercept factor, material parameters like absorptance, emittance, and transmittance of the

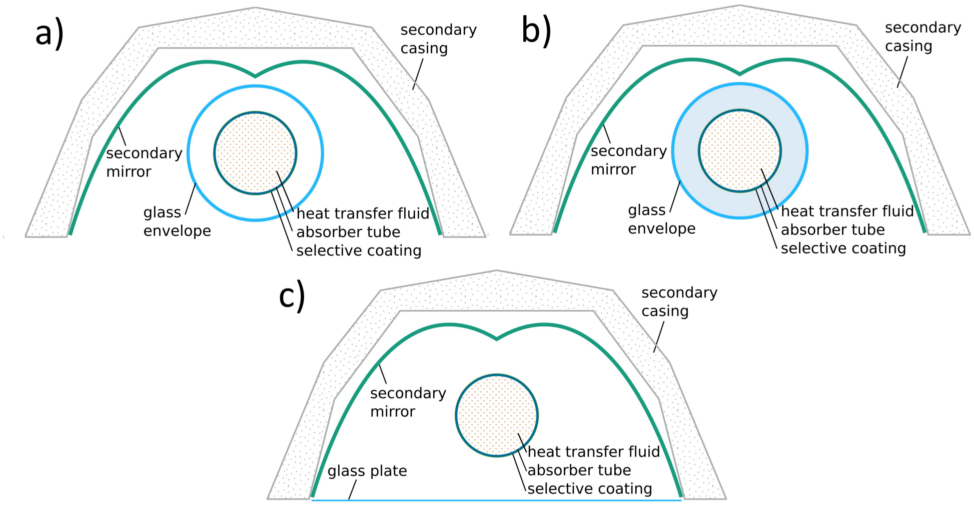

Figure A.2: Exemplary illustration of diverse LFC receiver designs. LFC receiver configuration with non-evacuated glass envelope and secondary mirror (a), evacuated glass envelope and secondary mirror (b), or non-evacuated receiver with absorber tube, glass plate cover and secondary mirror (c). [Hofer et al., 2015b]

mirrors/glass surfaces, ambient parameters such as soiling, as well as effects occurring from a non-perpendicular solar incidence. Accordingly, the optical efficiency is defined as the ratio between the incident radiant solar power absorbed by the receiver $\dot{Q}_{abs}$ and the potentially useful radiant solar power

$$\eta_{opt} = \frac{\dot{Q}_{abs}}{A_{Ap} \cdot G_{bT}}, \tag{A.1}$$

with the following relation between the direct irradiance on the tilted collector surface G_{bT} and the direct normal irradiance G_{bn}:

$$G_{bT} = G_{bn} \cdot cos\theta_i. \tag{A.2}$$

In Equation (A.2), θ_i represents the incidence angle, that is, the angle between the normal of the collector plane and the local solar vector $\vec{v}_s^*$, as sketched in Figure A.3[1]. Note that for LFCs with a fixed horizontal aperture plane, G_{bT} is equivalent to the direct horizontal irradiance G_{bh} and the incidence angle θ_i corresponds to the solar zenith angle θ_z.

The optical efficiency is commonly described as a product of different factors like optical efficiency at normal incidence $\eta_{opt,0}$, incidence angle modifier K_b, soiling factor f_{soil}, focus factor f_{focus}, and end loss f_{end} according to

$$\eta_{opt} = \eta_{opt,0} \cdot K_b \cdot (1 - f_{soil}) \cdot f_{focus} \cdot f_{end}, \tag{A.3}$$

where f_{soil} represents the soiling rate of the mirrors, which is inversely related to the cleanliness of the reflectors f_{clean}. The cleanliness of the primary mirrors and the absorber

[1]Note that this definition of θ_i contradicts the common definition of θ_i for LFCs. For a detailed justification and derivation, see Equation (A.6) and its following explanations.

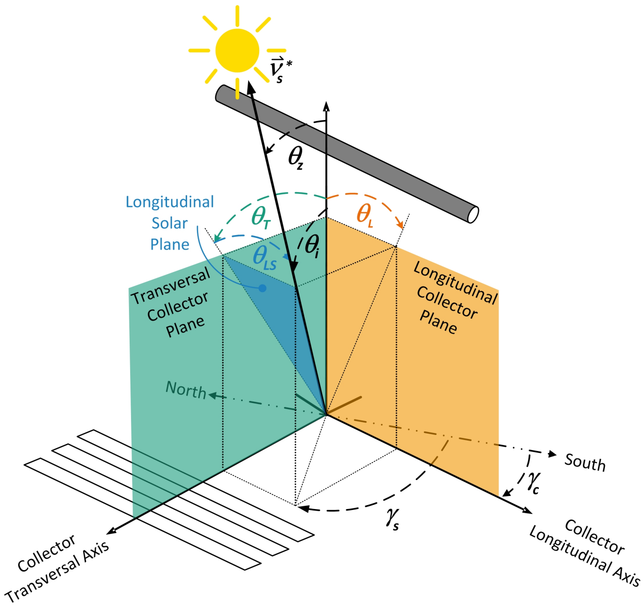

Figure A.3: Sketch of defined solar incidence angles on an LFC. The incidence angle θ_i of the collector depends on the local sun vector $\vec{v}_s^*$ defined by the collector orientation γ_c, the collector inclination β, the solar zenith angle θ_z and the solar azimuth angle γ_S; for collectors with a horizontal aperture plane θ_i=θ_z.

tubes may be determined by reflectance measurements (for an overview on common procedures see Fernández-García et al. [2017]). f_{focus} consists of the factor indicating the percentage of mirrors in focus, that is, in track mode. The individual meaning of the other parameters will be explained in the following.

■ A.2.2 Optical Efficiency at Normal Incidence

The optical efficiency at normal incidence $\eta_{opt,0}$ is defined as the optical efficiency of the system with the solar radiation normal to the aperture plane of the collector. It is furthermore defined for a perfect clean collector (assuming $f_{soil} = 0$) with no external shadow on the collector aperture. For parabolic trough collectors, it is commonly referred to as 'peak optical efficiency', as it represents the maximum of the optical efficiency possible for PTCs.

■ A.2.3 IAM and its Solar Angle Definition

The Incidence Angle Modifier (IAM) of a collector describes the change of optical efficiency depending on the direction of the solar beam incident on the collector plane. For the diffuse irradiance, it is commonly considered a constant. For concentrating collectors in particular, it is considered negligible (K_d =0), because the ability to use diffuse irradiance is insignificant (for more information and verification refer to Section 3.1.1 and Hofer et al. [2015a, pp. 90–91]).

Concerning the use of direct solar irradiance, K_b is defined as the ratio between the optical efficiency at a certain incidence situation (with the local sun beam vector $\vec{v}_s^*$ on the collector aperture plane) and the optical efficiency at normal incidence

$$K_b(\vec{v}_s^*) = K_b(\theta_z, \gamma_s, \gamma_c, \beta) = \frac{\eta_{opt}(\vec{v}_s^*)}{\eta_{opt,0}}. \tag{A.4}$$

In particular, the IAM includes the angular dependence of optical properties as well as geometric effects, such as blocking and shading of the reflector lines, which vary with the angle of incidence on the system. The local sun beam vector $\vec{v}_s^*$ depends on the global sun beam vector $\vec{v}_s$, which is characterized by the sun position in terms of the solar zenith angle θ_z and the solar azimuth angle γ_s as well as the collector orientation γ_c and inclination β. To facilitate a comparison of the IAM values independent on the location and specific implementation of the collector (as orientation and inclination), the local sun beam vector is commonly split up into a transversal and longitudinal part with reference to the two collector planes as sketched in Figure A.3. In literature and testing standards [e.g., ISO 9806, 2013], the incidence angle modifier $K_b(\vec{v}_s^*)$ is commonly defined depending on the transversal angle θ_T and longitudinal angle θ_L, that is, the local sun beam vector is split up into θ_T as the transversal and θ_L as the longitudinal part. Note that this already includes a mathematical approximation of the local sun beam vector, as $\vec{v}_s^*$ is not distinctly and mathematically correctly defined by the angle pair (θ_T,θ_L):

$$K_b(\vec{v}_s^*) \approx K_b(\theta_T, \theta_L). \tag{A.5}$$

This approximation might be valid for low-temperature collectors, but is not suited for concentrating solar collectors. Therefore, the use of the mathematically correct relation for splitting the local sun beam vector into its transversal and longitudinal part is suggested [Mertins, 2009]

$$K_b(\vec{v}_s^*) = K_b(\theta_T, \theta_{LS}), \tag{A.6}$$

where θ_{LS} consists of the angle between the solar vector and the transversal plane, which represents the mathematically correct longitudinal proportion of the solar vector.[2] The following three aspects illustrate why the use of θ_{LS} is recommended:

- For certain angle situation, as exemplified in Figure A.4(a), the angle pair (θ_T, θ_L) does not distinctly define the sun vector $\vec{v}_s^*$. In contrast, the angle pair (θ_T, θ_{LS}) does.
- For high transversal incidence situations as depicted in Figure A.4(b), the difference between the value of θ_{LS} and θ_L becomes significant. The value of θ_L would erroneously imply a large incidence angle in longitudinal direction. For these incidence situations, only the transversal part implies high incidence angles, whereas the longitudinal proportion (as seen by the value of θ_{LS}) does not. This results in a significant underestimation of the IAM and hence the collector performance as

$$\theta_{LS} \ll \theta_L \Longrightarrow K_L(\theta_{LS}) \gg K_L(\theta_L). \tag{A.7}$$

[2]Note that the use of θ_{LS} was originally introduced for LFCs by Mertins [2009] with the variable θ_i. However, this angle definition contradicts the commonly used definition of the solar incidence angle θ_i (angle between the solar vector and the collector normal) for parabolic trough as well as low-temperature collectors. For this reason, another variable is introduced to avoid misunderstanding and create a harmonized nomenclature valid for all line-concentrating collectors. As θ_{LS} lies in the longitudinal solar plane (and not as θ_T and θ_L in the transversal or longitudinal collector plane) the subscript LS was added analog to the commonly used θ_L. It therefore consists of the longitudinal proportion of the solar vector, representing the mathematically correct corresponding to θ_L.

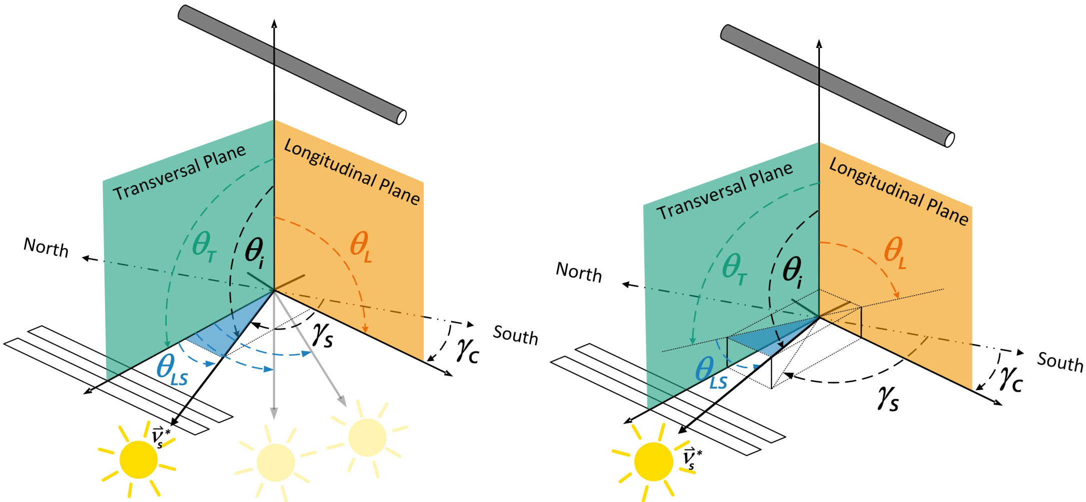

(a) Transversal and longitudinal angles of 90°

(b) Large transversal angles

Figure A.4: Exemplary solar incidence situations showing the issue and difference of using θ_L instead of θ_{LS}. In (a) only the angle pair of θ_T and θ_{LS} distinctly describes the solar vector; (b) shows an exemplary incidence situation, where the differences of θ_L and θ_{LS} are significant.

- In the case that the cosine loss is included into the IAM—what is commonly done for LFCs and will be explained in the following subsection of 'Cosine Loss'—the use of θ_L leads to erroneous values as

$$cos(\theta_i) = cos(\theta_T) \cdot cos(\theta_{LS}) \neq cos(\theta_T) \cdot cos(\theta_L). \tag{A.8}$$

Particular Use of the IAM

In the case of parabolic trough collectors, the collector is tracked along the longitudinal axis according to the sun position. For a perfect tracking, this implies that the transversal angle θ_T is always zero. For this reason, the IAM for parabolic trough is only one-dimensional, as non-normal solar incidence just occurs in longitudinal direction ($K_b(\vec{v}_s^*)$ $= K_b(\theta_{LS}) = K_b(\theta_i)$). Because the incidence angle modifier for parabolic troughs resembles a cosine-shape function, it may be approximated by polynomial relations in general form

$$K_b(\theta_i) = a_0 + a_1\theta_i + a_2{\theta_i}^2 \tag{A.9}$$

or in a more specific form as suggested by Valenzuela et al. [2014]

$$K_b(\theta_i) = 1 - \frac{b_1}{cos(\theta_i)} \cdot \theta_i - \frac{b_2}{cos(\theta_i)} \cdot {\theta_i}^2. \tag{A.10}$$

An exemplary graphical representation of the IAM shape is given in Figure A.5(a).

For LFCs, the mirror lines are collectively tracked, with a fixed collector aperture plane (commonly with no inclination in the horizontal plane). Therefore, both longitudinal and transversal parts of the IAM have to be considered by the use of a two-dimensional

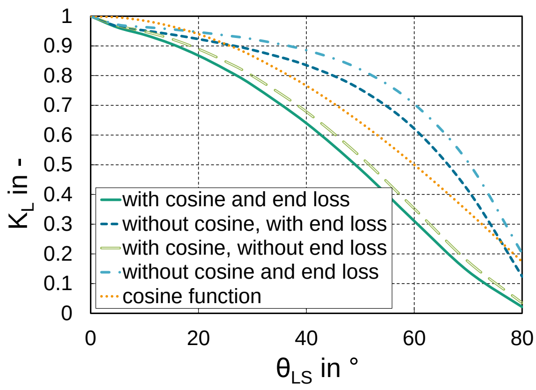

(a) Longitudinal IAM K_L

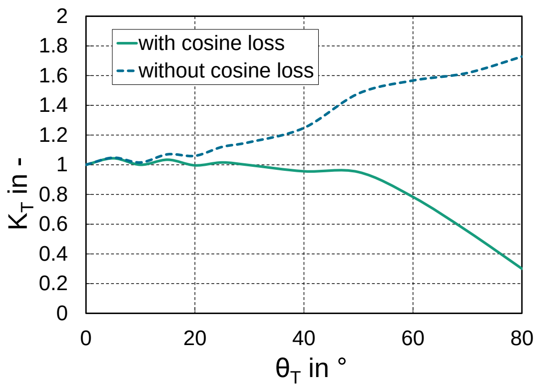

(b) Transversal IAM K_T

Figure A.5: Exemplary illustration of diverse IAM curves in- or excluding cosine and end loss. Exemplary longitudinal (a) and transversal (b) IAM curve particularly illustrating the effect of cosine loss and end loss. Exemplary values are based on Industrial Solar GmbH [2017].

or biaxial IAM. The surface of the IAM can be approximated by factorizing it into its transversal and longitudinal part K_T and K_L as originally introduced by McIntire [1982]. Note that from the very beginning this factorization, which allows a simplified use of the biaxial IAM, was linked to the use of the approximated solar vector by means of the angle pair (θ_T, θ_L), that is,

$$K_b(\vec{v}_s^*) \approx K_T(\theta_T) \cdot K_L(\theta_L). \tag{A.11}$$

Several studies [Mertins, 2009; Horta and Osorio, 2013; Hertel et al., 2015] have shown that the factorization in terms of

$$K_b(\vec{v}_s^*) \approx K_T(\theta_T) \cdot K_L(\theta_{LS}) \tag{A.12}$$

is describing the angular behavior of a collector more accurately.

Whereas the curve of the longitudinal IAM for linear Fresnel collectors might be approximated by a polynomial function as in the common case of parabolic trough, the transversal IAM shows a staggered shape. This particular behavior, caused by the alternated shading of the receiver on the reflector lines, can only be described accurately by a stepwise function with as many parameters as angle steps. An exemplary illustration of longitudinal and transversal IAM can be found in Figure A.5. Both particularities (two-dimensional and staggered-shape IAM) contribute to the fact that the angular performance of an LFC cannot be directly evaluated according to the MLR approach of the current testing standard. This is opposite to the case of parabolic troughs. For the evaluation with the QDT method, an iterative extension is required to be able to determine both longitudinal and transversal IAM as proposed in Section 3.1. For the DT method, significantly more parameters have to be determined for LFCs than for PTCs, leading to a more sophisticated evaluation procedure in terms of parameter correlation, confidence interval computation, and definition of testing strategy with stepwise IAM.

Cosine Loss

The cosine loss is defined by the reduction of the available solar irradiance due to non-normal incidence of the sun beams on the collector[3]. Consequently, the effective aperture area of the collector is reduced by the cosine of the incidence angle

$$A_{eff} = A_{Ap} \cdot cos(\theta_i) \Longrightarrow G_{bT} = G_{bn} \cdot cos(\theta_i). \tag{A.13}$$

Due to the single axis tracking of the parabolic trough collectors, cosine loss only arises in longitudinal direction. It is commonly—analog to low-temperature collectors—considered a separate factor of the IAM. Due to the two-dimensional incidence angle behavior of LFCs, the cosine loss arises in both transversal and longitudinal direction. For LFCs, the cosine loss is typically included in the incidence angle modifier K_b, that is, manufacturers usually report IAM values including the cosine loss. In this way, the IAM values only have to be multiplied by the direct normal irradiance G_{bn}. For a graphical representation of the different IAM curves with and without cosine loss, see Figure A.5. Notice that significant error may arise by factorizing a two-dimensional IAM including the cosine loss—as commonly done for LFCs—in dependence on θ_L instead of θ_{LS} since

$$\begin{aligned} \underbrace{K_b \cdot cos(\theta_i)}_{K_{b,LFC}} &= K_T \cdot K_L \cdot cos(\theta_i) \\ &= \underbrace{K_T \cdot cos(\theta_T)}_{K_{T,LFC}} \cdot \underbrace{K_L \cdot cos(\theta_{LS})}_{K_{L,LFC}} \\ &\neq K_T \cdot cos(\theta_T) \cdot K_L \cdot cos(\theta_L). \end{aligned} \tag{A.14}$$

This underlines the recommendation of using the angle pair of (θ_T, θ_{LS}) for a proper description of the angular behavior of the optical efficiency. The cosine loss may be accounted for separately with the use of G_{bT} as a reference irradiance. When the direct normal irradiance G_{bn} is applied for the evaluation, the cosine loss is a factor included in the IAM. Until now, no clear distinction between IAM definitions with and without including cosine loss have been defined. Mostly the very same variable is used for both definitions. Therefore, reporting IAM values needs particular specification, whether cosine loss is included or not (i.e., if the values are referred to direct normal irradiance G_{bn} or direct irradiance on collector aperture G_{bT}).

End Loss

Another angle-dependent optical loss source represents the end loss. It is caused by a finite length of the collector at non-normal incidence of the sun beams. Thereby, the end of the collector facing the sun is partly not irradiated, whereas at the far end of the collector—not facing the sun—part of the solar irradiation is concentrated beyond the end of the linear receiver as depicted in Figure A.6. The end loss can be analytically calculated. In a simplified form, the end loss can be defined for parabolic troughs by the length of the collector l_c, the aperture width w_{Ap}, the focal length f, and $\theta_{LS} = \theta_i$ according to Duffie

[3]Depending on the studied system, the cosine loss can also be defined referring to the non-normal incidence on the individual mirrors. In case of collector testing, the reference system consists of the entire collector and its collector aperture plane.

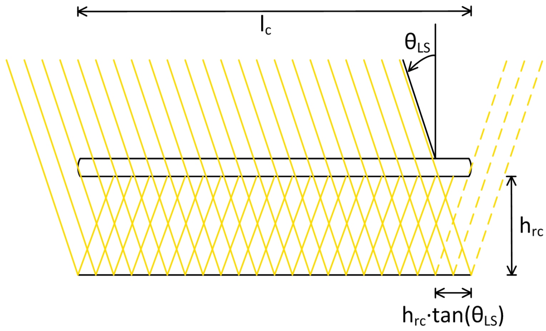

Figure A.6: Sketch of end loss for line-concentrating solar collectors. End loss occurs at non-normal incidence of sun beams due to shaded and not irradiated parts at the ends of the collector. [adapted from Heimsath et al., 2014a]

and Beckman [2013, p. 362]

$$f_{end} = 1 - \frac{f}{l_c} \cdot \left(1 + \frac{w_{Ap}^2}{48 \cdot f^2}\right) \cdot tan(\theta_i). \tag{A.15}$$

For LFCs, the end loss calculation has to be adopted due to the large collector width w_c in comparison to the height of the receiver from the primary field h_{rec} according to Heimsath et al. [2014a]

$$\begin{aligned} f_{end} &= 1 - \frac{h_{eff}}{l_c} \cdot tan(\theta_{LS}), \\ h_{eff} &= \sqrt{\left(\frac{w_c}{4}\right)^2 + h_{rec}^2}. \end{aligned} \tag{A.16}$$

For details on the specific derivation, see the corresponding sources. Similarly to the cosine loss, the end loss is still not consistently used and may therefore (or not) be included in a reported IAM value. In Figure A.5, the effect of end loss is additionally sketched. If end loss is considered a separate factor, the incidence angle modifier refers to a theoretically infinite collector. This allows a comparison of different systems with collectors of different length. When end loss is included in the IAM, it is not generally applicable but only valid for the specific length of the reported collector. IAM values derived by thermal collector testing will always include end loss, since a test of an infinite length is not feasible in practice. However, IAM values for infinite length may be determined when the test results are corrected by the above introduced relations of Equation (A.15) or Equation (A.16).

Note that no common nor standardized proceeding is defined so far for the in- or exclusion of cosine and end loss in the IAM. This implies that it is not specifically defined how to properly report IAM values, including or excluding these loss factors. For all cases, usually the same variable K_b is used. Therefore, special attention has to be paid when using externally reported IAM values. For this reason, it is highly essential to repeatedly check what exact value is indicated and to always specifically indicate which loss factors are included or not. The present thesis follows the common habit of the community by reporting IAM values including end loss. For PTCs, cosine loss is excluded, while for LFCs cosine loss is included in the given IAM values. Deviations to this proceeding will be particularly indicated.

A.3 Thermal Behavior

A.3.1 Heat Loss Parameters

The thermal performance of a collector is typically described by two aggregated heat loss parameters accounting for the (mean) fluid temperature and the ambient temperature as, for example, in the QDT equation [ISO 9806, 2013]

$$\dot{Q}_{HL} = c_1 \cdot (T_m - T_{amb}) + c_2 \cdot (T_m - T_{amb})^2 . \tag{A.17}$$

For the DT method, the heat loss is referred to every discretized node n of the absorber tube leading to

$$\dot{Q}_{HL,n} = u_0 \cdot \left(T_{HTF,n} - T_{amb}\right) + u_1 \cdot \left(T_{HTF,n} - T_{amb}\right)^2 . \tag{A.18}$$

Note that two different parameter variables for the heat loss are chosen intentionally for the QDT and DT method, because c_1 and c_2 refer to the aperture area of the collector with the unit $W/K{\cdot}m^2$, whereas u_0 and u_1 refer to the receiver length with the unit $W/K{\cdot}m$. The power of the polynomial describing the heat loss is currently discussed within different standardization working groups. An approach of using the temperature difference to the power of four is proposed by Valenzuela et al. [2014] in order to account for the predominant radiative effects for high-temperature concentrating collectors. This aspect is illuminated in greater detail within Section 3.3. Concerning the heat loss determination within the present thesis, the commonly used potency of two is used.

Notice that while referring heat loss to fluid temperatures, the thermal resistance between absorber surface and inner fluid is accounted for in the optical efficiency at normal incidence $\eta_{opt,0}$. To avoid this inaccuracy, heat loss can be referred to surface temperatures. As surface temperatures are difficult to measure exactly and representatively, these imprecisions are commonly accepted in performance measurements provided that the heat conversion is good. In the testing standard for low temperature collectors, this effect is considered by multiplying $\eta_{opt,0}$ with the collector efficiency factor F' and hence identifying the product of both $\eta_{0,b} = F' \cdot \eta_{opt,0}$ (referred to as conversion factor). For concentrating collectors in contrast, this term is usually neglected assuming good heat conversion and therefore the F'-factor tending to unity. For example, Duffie and Beckman [2013, p. 332] indicate a F'-factor for concentrating collector of 0.984. In these cases, $\eta_{0,b} \approx \eta_{opt,0}$ is considered. Special attention should be paid when using steam as a heat transfer fluid, as heat transfer coefficients might be small.

A.3.2 Heat Transfer Fluid

Process conditions of the test facilities and therefore collector output performance strongly depend on the Heat Transfer Fluid (HTF) used. For low-temperature collectors, commonly pressurized water is used. For higher working temperatures, alternatives as thermal oil, molten salt, or steam are used.

In steam generating systems, water is partially or fully evaporated while flowing through the absorber tube. For a proper assessment of those systems, specific issues have to be considered concerning the measurement concept of a two-phase flow. In order to quantify the thermal collector power output, outlet conditions such as steam mass flow and enthalpy have to be determined. Specific steam enthalpies in turn depend on the temperature, pressure, and steam quality of the fluid. In general, two-phase flow as well as pure steam are more complex to measure in comparison to common measurements of liquid fluids. Special care has to be applied when selecting and installing steam measurement instrumentation concerning associated uncertainties.

In comparison to water, single-phase fluids such as thermal oil or molten salt are not that well-studied and investigated. Therefore, physical properties of these HTFs are not characterized as accurately as for water. Moreover, the characterization of HTF aging still presents a challenging aspect. However, for reliable performance testing, the physical properties of the fluids are of great importance in order to evaluate system performance according to the generated collector power output. Specific heat capacities are required for deriving the collector power output (or useful heat generated by the collector) depending on the measured fluid temperatures. A reliable, precise, and accurate determination of heat capacities as a function of fluid temperatures is therefore essential. Besides, fluid densities are of great significance when volume flow rates are measured instead of a direct measurement of mass flow rates. As the use of direct mass flow meters (such as a Coreolis flow meter) is not always applicable, density of the heat transfer fluid needs to be determined accurately and its uncertainty included in error calculations (for more information on the effect of measurement uncertainties see Chapter 6). Implemented fluid libraries used within the evaluation procedure are based on IAPWS [1997] for water/steam or technical data sheets for other media (see exemparily Dow [1997]; Solutia [1998]).

Appendix B

Further Details on Evaluated Test Collectors

B.1 Exemplary Sketches of Test Facilities

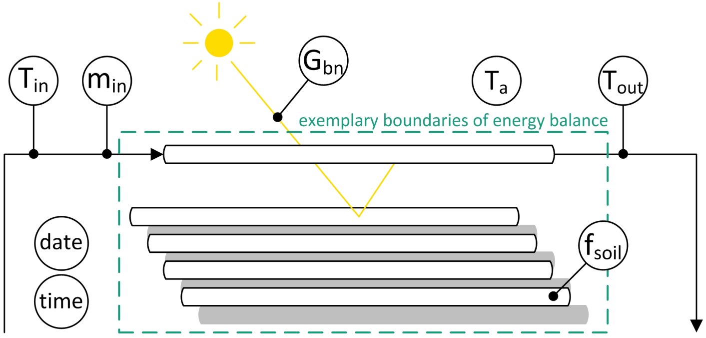

(a) Exemplary plant schematic of test collectors LFC_w1, LFC_w3 and LFC_w3

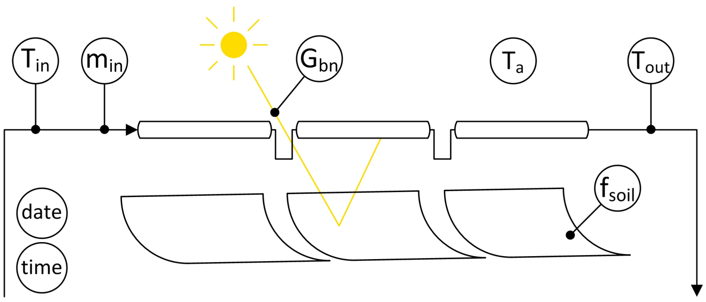

(b) Plant schematic of solar field loop PTC_o1

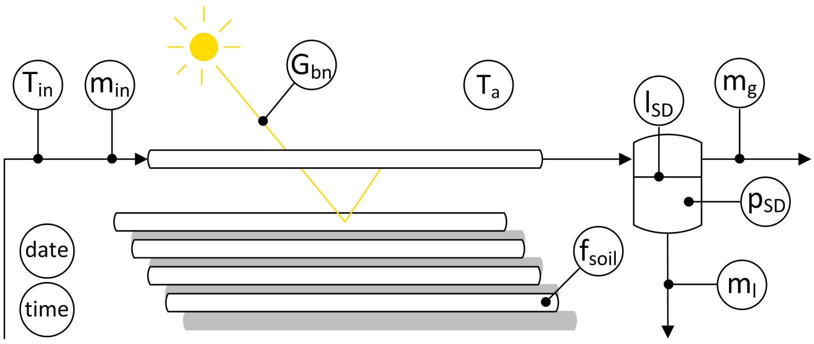

(c) Plant schematic of test collector LFC_s1

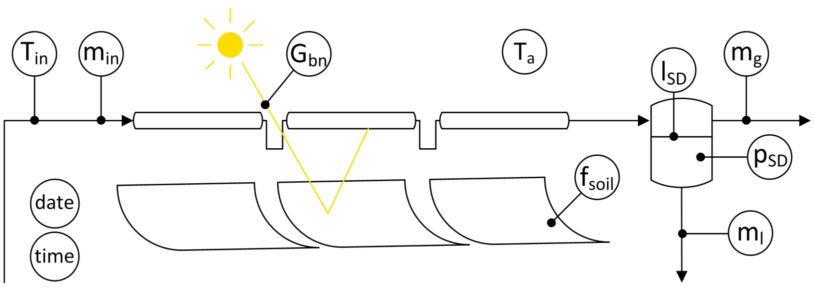

(d) Plant schematic of test loop PTC_s1

Figure B.1: Sketches of evaluated test collectors. Schematic illustration of evaluated test collectors LFC_w1, LFC_w3 and LFC_w3 in (a), solar field loop PTC_o1 in (b) as well as DSG test facilities LFC_s1 in (c) and PTC_s1 in (d).

■ B.2 Measurement Instrumentation of Test Collectors

Table B.2.1: Measurement uncertainty of test collector `LFC_w1`. Uncertainty factors and their distribution associated with temperature and mass flow measurement.

Temperature Sensor

Uncertainty factor		Value	Distribution	Source
Calibration	reference sensor	0.02 K	normal (2σ)	calibration certificate
Data logger		0.0996 K	uniform	calibration certificate
Display accuracy		0.0005 K	uniform	calibration certificate
Max. deviation		0.05 K	normal (2σ)	calibration certificate
Long-term stability		0.01 K	uniform	estimation test lab

Volume Flow Sensor

Uncertainty factor		Value	Distribution	Source
Calibration	reference sensor	0.02 %	normal (2σ)	calibration certificate
Max. deviation		0.27 %	normal (2σ)	calibration certificate
Data logger		0.1 %	uniform	data sheet
Long-term stability		0.3 %	uniform	estimation test lab

Table B.2.2: Measurement uncertainty of test collector `LFC_w2`. Uncertainty factors and their distribution associated with temperature and mass flow measurement.

Temperature Sensor

Uncertainty factor		Value	Distribution	Source
Calibration	reference sensor	0.02 K	normal (2σ)	calibration certificate
Data logger		0.0996 K	uniform	calibration certificate
Display accuracy		0.0005 K	uniform	calibration certificate
Max. deviation		0.05 K	normal (2σ)	calibration certificate
Long-term stability		0.01 K	uniform	estimation test lab

Mass Flow Sensor

Uncertainty factor	Value	Distribution	Source
Sensor	0.64 %	normal (1σ)	data sheet
Data logger	0.1 %	uniform	data sheet
Long-term stability	0.3 %	uniform	estimation test lab

Table B.2.3: Measurement uncertainty of test collector `LFC_w3`. Uncertainty factors and their distribution associated with temperature and mass flow measurement.

Temperature Sensor

Uncertainty factor	Value	Distribution	Source
Sensor	1/10(0.3+0.005·T)	uniform	data sheet
Data logger	0.0996	uniform	estimation test lab
Display accuracy	0.0005	uniform	estimation test lab
Long-term stability	0.01	uniform	estimation test lab

Mass Flow Sensor

Uncertainty factor	Value	Distribution	Source
Sensor	1.0 %	normal (1σ)	data sheet
Data logger	0.1 %	uniform	data sheet
Long-term stability	0.3 %	uniform	estimation test lab

Table B.2.4: Measurement uncertainty of test collector `LFC_s1`. Uncertainty factors and their distribution associated with temperature, pressure, and mass flow measurement.

Temperature Sensor

Uncertainty factor	Value	Distribution	Source
Sensor	1.5 K	uniform	data sheet

Pressure Sensor Steam Drum

Uncertainty factor	Value	Distribution	Source
Sensor stability	0.15 bar	uniform	data sheet
Temperature effect	0.002 %	uniform	data sheet

Steam Mass Flow Sensor

Uncertainty factor	Value	Distribution	Source
Sensor	0.0011 kg/s	normal (1σ)	calculated from data sheet

Inlet Mass Flow Sensor

Uncertainty factor	Value	Distribution	Source
Sensor	0.0125 kg/s	normal (1σ)	calculated from data sheet

Table B.2.5: Measurement uncertainty of test collector `PTC_s1`. Uncertainty factors and their distribution associated with temperature, pressure, and mass flow measurement.

Temperature Sensor

Uncertainty factor	Value / K	Distribution	Source
Sensor	1 K	uniform	data sheet

Steam Drum Pressure

Uncertainty factor	Value	Distribution	Source
Sensor accuracy	0.5 %	uniform	data sheet
Channel accuracy	0.06 %	uniform	data sheet

Steam Mass Flow

Uncertainty factor	Value	Distribution	Source
Sensor accuracy	1.6 %	uniform	data sheet
Channel accuracy	0.06 %	uniform	data sheet

Inlet Mass Flow

Uncertainty factor	Value	Distribution	Source
Sensor accuracy	1.6 %	uniform	data sheet
Channel accuracy	0.2 %	uniform	data sheet

Table B.2.6: Measurement uncertainty of test collector `PTC_01`. Uncertainty factors and their distribution associated with temperature and mass flow measurement.

Temperature Sensor

Uncertainty factor	Value / W	Distribution	Source
Sensor	0.15+0.002·T	uniform	data sheet
Data logger	0.0996	uniform	estimation test lab
Display accuracy	0.0005	uniform	estimation test lab
Long-term stability	0.01	uniform	estimation test lab

Mass Flow Sensor

Uncertainty factor	Value / W	Distribution	
Sensor	1.0 %	uniform	estimation

Appendix C

Complements to the DSG Simulation Models

C.1 Derivation of the PFM Equation

Starting from the one-dimensional, homogeneous energy equation

$$\begin{aligned}\frac{d}{dt}(E) &= \frac{\partial}{\partial t}(E) + \frac{\partial}{\partial x}(vE) \\ &= \rho v g \sin(\delta) - \frac{\partial}{\partial x}(vp) - \frac{\partial}{\partial x}(\tau v) - \dot{q} - \frac{\partial}{\partial x}(\lambda \frac{\partial T}{\partial x}),\end{aligned} \tag{C.1}$$

with the variables

$E = E_{in} + E_{kin} + E_{pot}$	$=$ the total energy with v being the velocity of the fluid,
$\rho v g \sin(\delta)$	$=$ gravitational force with collector tilt δ,
$\frac{\partial}{\partial x}(vp)$	$=$ work due to pressure change,
$\frac{\partial}{\partial x}(\tau v)$	$=$ work by friction force,
$\dot{q}$	$=$ local radiative heat exchange,
$\frac{\partial}{\partial x}(\lambda \frac{\partial T}{\partial x})$	$=$ heat conduction.

The absorber tube is considered horizontal with no inclination omitting gravitational force. Moreover, heat conduction along the absorber tube is neglected, because temperature gradients in longitudinal direction are very small especially when evaporation takes place [Lippke, 1994]. This results in

$$\frac{\partial}{\partial t}(E) = -\frac{\partial}{\partial x}(vE) - \frac{\partial}{\partial x}(vp) - \dot{q} - \frac{\partial}{\partial x}(\tau v). \tag{C.2}$$

The energy lost due to friction will be transformed to heat, so that both factors are combined within the heat-exchange term [Hirsch et al., 2005]:

$$\frac{\partial}{\partial t}(E) = -\frac{\partial}{\partial x}(vE) - \frac{\partial}{\partial x}(vp) - \dot{q}. \tag{C.3}$$

Kinetic and potential energy are neglected, leading to $E = E_{in} = \rho h - p$ and therefore

$$\frac{\partial}{\partial t}(\rho h) - \frac{\partial}{\partial t}(p) + \frac{\partial}{\partial x}(v \rho h) = -\dot{q}. \tag{C.4}$$

The time derivative of the pressure (pressure–volume work) will be neglected as well, so that

$$\frac{\partial}{\partial t}(\rho h) + \frac{\partial}{\partial x}(v \rho h) = -\dot{q}. \tag{C.5}$$

Equation (C.5) represents the basic mathematical/physical model of the PFM. For the purpose of discretization, this equation is simplified further by applying the product rule:

$$\rho \frac{\partial h}{\partial t} + \underbrace{h \frac{\partial \rho}{\partial t} + h \frac{\partial \rho v}{\partial x}}_{=h \cdot mass\ balance=0} + v \rho \frac{\partial h}{\partial x} = -\dot{q}. \tag{C.6}$$

The marked term with brackets is equal to the product of enthalpy times the mass balance, which equals zero. Therefore,

$$\rho \frac{\partial h}{\partial t} + v \rho \frac{\partial h}{\partial x} = -\dot{q}. \tag{C.7}$$

Multiplying with the cross section area A, we obtain

$$\rho A \frac{\partial h}{\partial t} + \dot{m} \frac{\partial h}{\partial x} = -A \cdot \dot{q}. \tag{C.8}$$

In ColSim, the solution of Equation (C.8) is discretized with equidistant temporal (Δt) and spacial (Δx) mesh size. Considering $-A \cdot \dot{q} = {}^{\Delta x \cdot A \cdot q}/_{\Delta x \cdot \Delta t} = {}^{V \cdot q}/_{\Delta x \cdot \Delta t} = {}^{Q_{gains,n}}/_{\Delta x \cdot \Delta t}$, with $Q_{gains,n} = Q_{abs,n} - Q_{HL,n}$ per node n, results in the final non-discretized plug-flow equation

$$A\rho \frac{\Delta h}{\Delta t} + \dot{m} \frac{\Delta h}{\Delta x} = \frac{Q_{gains,n}}{\Delta t \Delta x}. \tag{C.9}$$

Backward differencing in time and upwind differencing in spatial direction is applied, leading to the final difference equation used in ColSim's PFM [analog to Wittwer, 1999]

$$m_{node}(h_n^t - h_n^{t-1}) = -\dot{m}^t(h_n^t - h_{n-1}^t)\Delta t + Q_{gains,n}. \tag{C.10}$$

Equation (C.10) is equivalent to Equation (4.3).

■ C.2 Derivation of the EPFM Equation

For the derivation of the EPFM, we start from the same mathematical model for the energy equation as in the PFM of Equation (C.5) or used in Hirsch [2005]. Additionally, the mass conservation equation is considered. The derivation of both equations is analog to the one presented in Hernández [2015b].
The mass conservation equation is defined as

$$\frac{\partial \rho}{\partial t} + \frac{\partial \rho v}{\partial x} = 0, \tag{C.11}$$

with the energy conservation equation being

$$\frac{\partial}{\partial t}(\rho h) + \frac{\partial}{\partial x}(\rho v h) = \frac{\dot{Q}}{V}. \tag{C.12}$$

To facilitate the numerical solution, similarly to the PFM, the mass flow rate is introduced by

$$\dot{m} := A\rho v, \tag{C.13}$$

where A is the cross-sectional area of the pipe, which is assumed to be constant. Replacing ρv with $\dot{m}/A$, the following equations are obtained, which are the starting equations for the finite volume method:

$$\frac{\partial \rho}{\partial t} + \frac{1}{A}\frac{\partial \dot{m}}{\partial x} = 0, \tag{C.14}$$

$$\frac{\partial}{\partial t}(\rho h) + \frac{1}{A}\frac{\partial \dot{m}h}{\partial x} = \frac{\dot{Q}}{V}. \tag{C.15}$$

For the finite volume approach, the following definitions are used (see Figure 4.1): P is a control volume, with neighbor volumes E and W. The interface between E and P is e. The interface between P and W is w. Through the entire absorber we have a constant area A. The control volume P has the length $\Delta x = e - w$ and volume $V = A \cdot \Delta x$. Equation (C.14) and (C.15) are integrated over the volume $[w, e]$ and over the time interval $[t, t + \Delta t]$:

$$\int_w^e \int_t^{t+\Delta t} \frac{\partial \rho}{\partial t}\,\mathrm{d}t\,\mathrm{d}x + \frac{1}{A}\int_t^{t+\Delta t}\int_w^e \frac{\partial \dot{m}}{\partial x}\,\mathrm{d}x\,\mathrm{d}t = 0, \tag{C.16}$$

$$\int_w^e \int_t^{t+\Delta t} \frac{\partial}{\partial t}(\rho h)\,\mathrm{d}t\,\mathrm{d}x + \frac{1}{A}\int_t^{t+\Delta t}\int_w^e \frac{\partial}{\partial x}(\dot{m}h)\,\mathrm{d}x\,\mathrm{d}t = \int_t^{t+\Delta t}\int_w^e \frac{\dot{Q}}{V}\,\mathrm{d}x\,\mathrm{d}t. \tag{C.17}$$

The time derivative is integrated exact over time and the space derivative exact over space:

$$\int_w^e \left(\rho^{t+1} - \rho^t\right)\,\mathrm{d}x + \int_t^{t+\Delta t} (\dot{m}_e - \dot{m}_w)\,\mathrm{d}t = 0, \tag{C.18}$$

$$\int_w^e \left((\rho h)^{t+1} - (\rho h)^t\right)\,\mathrm{d}x + \frac{1}{A}\int_t^{t+\Delta t} ((\dot{m}h)_e - (\dot{m}h)_w)\,\mathrm{d}t = \int_t^{t+\Delta t}\int_w^e \frac{\dot{Q}}{V}\,\mathrm{d}x\,\mathrm{d}t. \tag{C.19}$$

Following the work of Patankar [1980, pp. 56–58], a fully implicit scheme is assumed for the mass flow rate (i.e., $\int_t^{t+\Delta t} \dot{m}\,\mathrm{d}t \approx \dot{m}^{t+1}\Delta t$) and for the energy flow rate (i.e., $\int_t^{t+\Delta t} \dot{m}h\,\mathrm{d}t \approx \dot{m}^{t+1}h^{t+1}\Delta t$). Moreover, the value of ρ and of ρh at the center of the volume serves as an average over the entire node P (i.e., $\int_w^e \rho\,\mathrm{d}x \approx \rho_P \Delta x$, $\int_w^e \rho h\,\mathrm{d}x \approx \rho_P h_P \Delta x$), leading to

$$\Delta x \cdot (\rho_P^{t+1} - \rho_P^t) + \frac{\Delta t}{A}(\dot{m}_e^{t+1} - \dot{m}_w^{t+1}) = 0, \tag{C.20}$$

$$\Delta x \left((\rho h)_P^{t+1} - (\rho h)_P^t\right) + \frac{\Delta t}{A}\left((\dot{m}h)_e^{t+1} - (\dot{m}h)_w^{t+1}\right) = \int_t^{t+\Delta t}\int_w^e \frac{\dot{Q}}{V}\,\mathrm{d}x\,\mathrm{d}t. \tag{C.21}$$

Applying an upwind scheme for the energy equation [see Patankar, 1980, pp. 83–85], this gives $h_w \approx h_W$ and $h_e \approx h_P$:

$$\Delta x \left((\rho h)_P^{t+1} - (\rho h)_P^t\right) + \frac{\Delta t}{A}\left(\dot{m}_e^{t+1}h_P^{t+1} - \dot{m}_w^{t+1}h_W^{t+1}\right) = \int_t^{t+\Delta t}\int_w^e \frac{\dot{Q}}{V}\,\mathrm{d}x\,\mathrm{d}t. \tag{C.22}$$

Multiplying Equation (C.20) and (C.22) with $A/\Delta t$ and defining $Q_{gains,n} := A/\Delta t \cdot \int_t^{t+\Delta t} \int_w^e \frac{\dot{Q}}{V}\, dx\, dt$, we obtain

$$V \cdot \frac{(\rho_P^{t+1} - \rho_P^t)}{\Delta t} + \dot{m}_e^{t+1} - \dot{m}_w^{t+1} = 0, \tag{C.23}$$

$$V \cdot \frac{(\rho h)_P^{t+1} - (\rho h)_P^t}{\Delta t} + \dot{m}_e^{t+1} h_P^{t+1} - \dot{m}_w^{t+1} h_W^{t+1} = Q_{gains,n}. \tag{C.24}$$

Equation (C.23) and (C.24) are equivalent to Equation (4.6) and (4.7)

■ C.3 Main Procedure of SIMPLER

The SIMPLER procedure is based on the general discretized conservation equations as given in Equation (4.16). The specific equations and their particular coefficients are given in Section C.4.

(1) Starting from a guessed velocity field v^*, a pseudo-velocity $\tilde{v}$ is calculated according to

$$\tilde{v}_{i+\frac{1}{2}} = \frac{\left(a_{wi} \cdot v^*_{i-\frac{1}{2}} + b_{ei}\right)}{a_{ei}}, \tag{C.25}$$

with the coefficients defined in Equation (C.34).

(2) The velocity v is calculated by

$$v_{i+\frac{1}{2}} = \tilde{v}_{i+\frac{1}{2}} + d_{ei}(p_i - p_{i+1}) \tag{C.26}$$

with

$$d_{ei} := \frac{1}{a_{ei}}. \tag{C.27}$$

$v_{i-\frac{1}{2}}$ is defined accordingly and both terms inserted into the mass balance of Equation (4.18), obtaining the so-called 'pressure equation', which allows a resolution for the pressure p:

$$a_{mPi} p_i = a_{mWi} p_{i-1} + a_{mEi} p_{i+1} + \tilde{b}_{mi}. \tag{C.28}$$

The detailed coefficients and boundary conditions for this equation are given in Section C.4.2.

(3) The resolved pressure p is then considered as an estimated pressure p^* and inserted into the momentum Equation (4.19), leading to a guessed/estimated velocity field v^*. If this guessed velocity field does not satisfy the mass conservation equation, the estimated pressure field is incorrect.

(4) Therefore, the guessed pressure p^* is corrected by the value $\hat{p}$ (and equivalent for the velocities) according to

$$\begin{aligned} p &= p^* + \hat{p}, \\ v &= v^* + \hat{v}. \end{aligned} \tag{C.29}$$

Based on these equations, we obtain[1] a relation between the corrected pressure and velocity, called 'velocity correction'

$$\hat{v}_{i+\frac{1}{2}} = d_{ei}\left(\hat{p}_i - \hat{p}_{i+1}\right), \tag{C.30}$$

which shows how the velocities react to the pressure corrections [Walter, 2007, p. 569].

(5) By inserting $v = v^* + \hat{v}$ into the mass balance Equation (4.18), the so-called 'pressure correction' is obtained, allowing a resolution by the TDMA for the corrected pressure values

$$a_{mPi}\hat{p}_i = a_{mWi}\hat{p}_{i-1} + a_{mEi}\hat{p}_{i+1} + b_{mi}, \tag{C.31}$$

with the coefficients defined in Section C.4.3.

$$b_{mi} = \frac{\left(\rho_i^0 - \rho_i\right)\Delta x}{\Delta t} + (\rho v^*)_{i-\frac{1}{2}} - (\rho v^*)_{i+\frac{1}{2}} \tag{C.32}$$

is the discretized form of the mass conservation equation. It represents the error of the mass conservation equation caused by the estimated velocity field v^* obtained by the momentum equation. Hence, the b_m-term can be used to measure the correctness of the solution. If v^* fulfills the mass conservation equation, $b_m = 0$ as well as the pressure correction $\hat{p} = 0$.

(6) The corrected pressure $\hat{p}$ is used to calculate the pressure field p, the corrected velocity field $\hat{v}$ and accordingly the velocity field v.

(7) With the new pressure and velocity, the energy conservation equation is solved in order to obtain the specific enthalpy of every node. Thereby, the densities and other properties, which are needed to calculate the pressure drop due to friction and the heat flux into the absorber, can be calculated by means of Equation (4.20). For the specific coefficients and boundary conditions see Section C.4.4

(8) With all new calculated values, convergence is checked. If no convergence is reached, the velocity field is then used as a newly guessed value and proceeded again at step (1).

■ C.4 Complete Discretization Equations Used in SIMPLER

■ C.4.1 Discrete Momentum Conservation Equation

The discretized momentum equation implemented within the SIMPLER approach of the present thesis is represented by

$$a_{ei}v_{i+\frac{1}{2}} = a_{wi}v_{i-\frac{1}{2}} + b_{ei} + \left(p_i - p_{i+1}\right), \tag{C.33}$$

[1] By subtracting the momentum equation with the guessed velocity field from the ordinary momentum equation and omitting the velocity changes of the neighboring cells, the relation between the pressure and velocity correction is obtained. For details see Patankar [1980]. This is the essential step for the SIMPLER being a semi-implicit approach.

with the coefficients for $i \in [2; N]$

$$\begin{aligned}
a_{ei} &= a_{wi} + a_{ei}^0 - S_{v,pi} \Delta x, \\
a_{wi} &= (v\rho)_{i-\frac{1}{2}}, \\
a_{ei}^0 &= \frac{\rho_i^0 \cdot \Delta x}{\Delta t}, \\
b_{ei} &= S_{v,ci} \Delta x + a_{ei}^0 v_{i+\frac{1}{2}}^0.
\end{aligned} \tag{C.34}$$

The balance is drawn over a control volume with staggered grid according to Figure 4.2. The source of the momentum conservation equation equals

$$\begin{aligned}
S_{v,pi} &= -\left| \frac{\Delta p_{f,i+\frac{1}{2}}}{v_{i+\frac{1}{2}}} \right|, \\
S_{v,ci} &= 0,
\end{aligned} \tag{C.35}$$

consisting of the pressure loss due to friction, which acts against the flow and therefore is considered within the proportional source term $S_{v,pi}$. The specific equations are taken from VDI-GVC [2010, Chap. L 1.2 and L 2.2]. Pressure loss due to gravity is neglected ($S_{v,ci} = 0$), since the absorber is considered horizontally not being inclined. The local pressure difference is separately considered in Equation (C.33).

For $i = 1$, the velocity $v_{1-\frac{1}{2}}$ equals $\frac{\dot{m}_{in}}{A \cdot \rho_1^*}$, with ρ_1^* being a guessed value and the boundary condition of the mass flow rate at the entrance of the absorber.

■ C.4.2 Pressure Equation

The pressure equation is obtained by resolving the discrete mass conservation Equation (4.18) with inserted velocity $v = f(\tilde{v}, p)$ depending on the pseudo-velocity $\tilde{v}$:

$$a_{mPi} p_i = a_{mWi} p_{i-1} + a_{mEi} p_{i+1} + \tilde{b}_{mi}. \tag{C.36}$$

with the coefficients $i \in [2; N-1]$

$$\begin{aligned}
a_{mPi} &= a_{mWi} + a_{mEi}, \\
a_{mWi} &= \rho_{i-\frac{1}{2}} d_{wi} = \rho_{i-\frac{1}{2}} \frac{1}{a_{wi}}, \\
a_{mEi} &= \rho_{i+\frac{1}{2}} d_{ei} = \rho_{i-\frac{1}{2}} \frac{1}{a_{ei}}, \\
\tilde{b}_{mi} &= \frac{\left(\rho_i^0 - \rho_i\right) \Delta x}{\Delta t} + (\rho \tilde{v})_{i-\frac{1}{2}} - (\rho \tilde{v})_{i+\frac{1}{2}}.
\end{aligned} \tag{C.37}$$

Values of a_{wi} and a_{ei} are corresponding to Equation (C.34).

For $i = N$, the boundary condition of the outlet pressure of the absorber is given by $p_N = p_{out}$. For $i = 1$, the coefficients are according to Walter [2001, p. 26]:

$$a_{mP1} p_1 = a_{mE1} p_2 + \tilde{b}_{m1}, \tag{C.38}$$

with

$$
\begin{aligned}
a_{mP1} &= a_{mE1}, \\
a_{mE1} &= \rho_{1+\frac{1}{2}} d_{e1}, \\
\tilde{b}_{m1} &= \frac{\left(\rho_i^0 - \rho_i\right)\Delta x}{\Delta t} + \frac{\dot{m}_{in}}{A} - (\rho \tilde{v})_{1+\frac{1}{2}}.
\end{aligned}
\tag{C.39}
$$

■ C.4.3 Pressure Correction Equation

The pressure correction equation is obtained by resolving the discrete mass conservation Equation (4.18) with inserted velocity $v = f(v^*, \hat{p})$ depending on the guessed velocity v^* and the pressure correction $\hat{p}$:

$$
a_{mPi}\hat{p}_i = a_{mWi}\hat{p}_{i-1} + a_{mEi}\hat{p}_{i+1} + b_{mi},
\tag{C.40}
$$

with the coefficients of Equation (C.37) for $i \in [2; N-1]$ and

$$
b_{mi} = \frac{\left(\rho_i^0 - \rho_i\right)\Delta x}{\Delta t} + (\rho v^*)_{i-\frac{1}{2}} - (\rho v^*)_{i+\frac{1}{2}}.
\tag{C.41}
$$

For $i = 1$ and $i = N$, the coefficients are calculated as suggested by Walter [2001, pp. 25–26]

$$
\begin{aligned}
b_{m1} &= \frac{\left(\rho_i^0 - \rho_i\right)\Delta x}{\Delta t} + \frac{\dot{m}_{in}}{A} - (\rho v^*)_{i+\frac{1}{2}}, & b_{mN} &= 0, \\
a_{mE1} &= \rho_{1+\frac{1}{2}} d_{ei}, & a_{mEN} &= 0, \\
a_{mW1} &= 0, & a_{mWN} &= 0, \\
a_{mP1} &= a_{mW1} + a_{mE1}, & a_{mPN} &= 1.
\end{aligned}
\tag{C.42}
$$

■ C.4.4 Discrete Energy Conservation Equation

The discretized energy equation implemented corresponds to

$$
a_{hPi}h_i = a_{hWi}h_{i-1} + b_{hi},
\tag{C.43}
$$

with the coefficients for $i \in [2; N]$:

$$
\begin{aligned}
a_{hPi} &= a_{hWi} + a_{hPi}^0 - S_{h,pi}\Delta x_i, \\
a_{hWi} &= (v\rho)_{i-\frac{1}{2}}, \\
a_{hPi}^0 &= \frac{\rho_i^0 \Delta x_i}{\Delta t}, \\
b_{hi} &= S_{h,ei}\Delta x_i + a_{hPi}^0 h_i^0.
\end{aligned}
\tag{C.44}
$$

The source of the energy conservation equation represents the heat flux into the absorber S_h, corresponding to the solar gains $\dot{Q}_{gains,n} = \dot{Q}_{abs,n} - \dot{Q}_{HL,n}$. A positive heat flux is added to $S_{h,ci}$, a negative heat flux to $S_{h,pi}$ according to

$$
\begin{aligned}
S_{h,ci} &= \max(S_h, 0), \\
S_{h,pi} &= -\frac{\max(-S_h, 0)}{h_i}.
\end{aligned}
\tag{C.45}
$$

Specific enthalpy at the entrance $h_{in} = h_1$ and mass flow rate at the entrance $\dot{m}_{in} = v_{1-\frac{1}{2}} \cdot \rho_1 \cdot A$ are considered as boundary conditions. Thereby, for $i = 1$, the coefficients become

$$a_{hP1} h_1 = b_{h1}, \tag{C.46}$$

with

$$\begin{aligned}
a_{hP1} &= a_{hW1} + a^0_{hP1} - S_{h,p1}\Delta x, \\
a_{hW1} &= \frac{\dot{m}_{in}}{A}, \\
a^0_{hP1} &= \frac{\rho^0_1 \cdot \Delta x}{\Delta t}, \\
b_{h1} &= S_{h,c1} \cdot \Delta x + a^0_{hP1} h^0_{in}.
\end{aligned} \tag{C.47}$$

Appendix D

Further Results of BS Verification

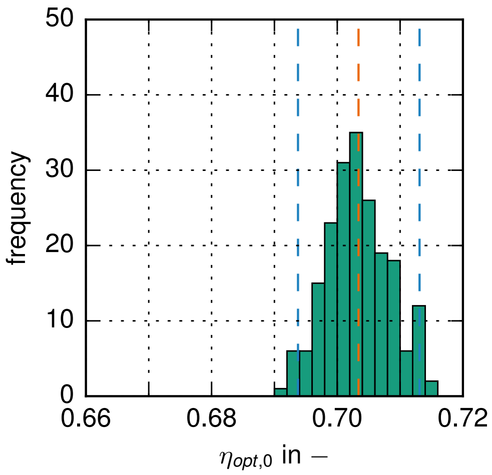

(a) $\eta_{opt,0}$-histogram based on drawing with high initially identified value

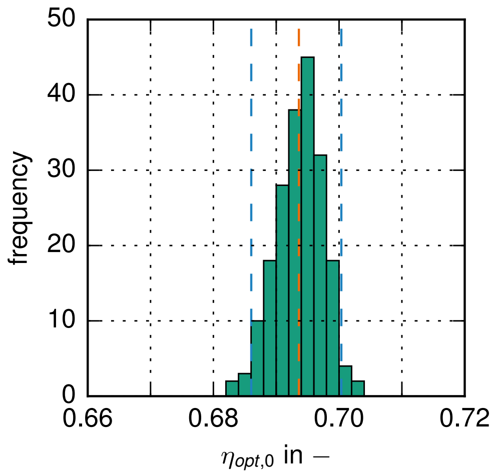

(b) $\eta_{opt,0}$-histogram based on drawing with low initially identified value

Figure D.1: Bootstrapping results of optical efficiency for simple identification model. Histogram of identified $\eta_{opt,0}$ based on non-representative initial drawings with high (a) and low (b) initially identified $\eta_{opt,0}$-value for simple identification model ($\eta_{opt,0}$, u_0/u_1).

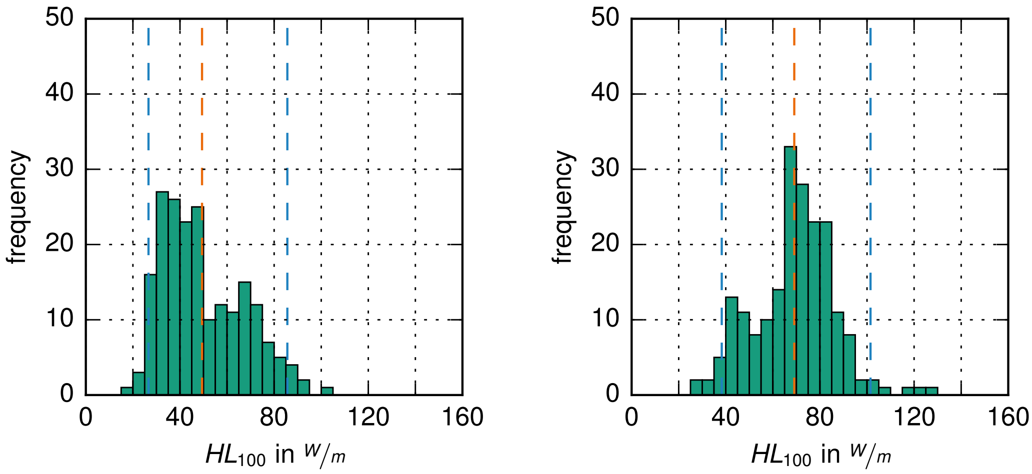

(a) BS histogram of HL_{100} (b) RSS histogram of HL_{100}

Figure D.2: Comparison of heat loss results for complete identification model. Histogram of identified HL_{100} based on bootstrapping (a) versus random sub-sampling (b) for complete identification model ($\eta_{opt,0}$, u_0/u_1, K_T/K_L) with five measurement days at 15 s time step with 5 °-IAM identification.

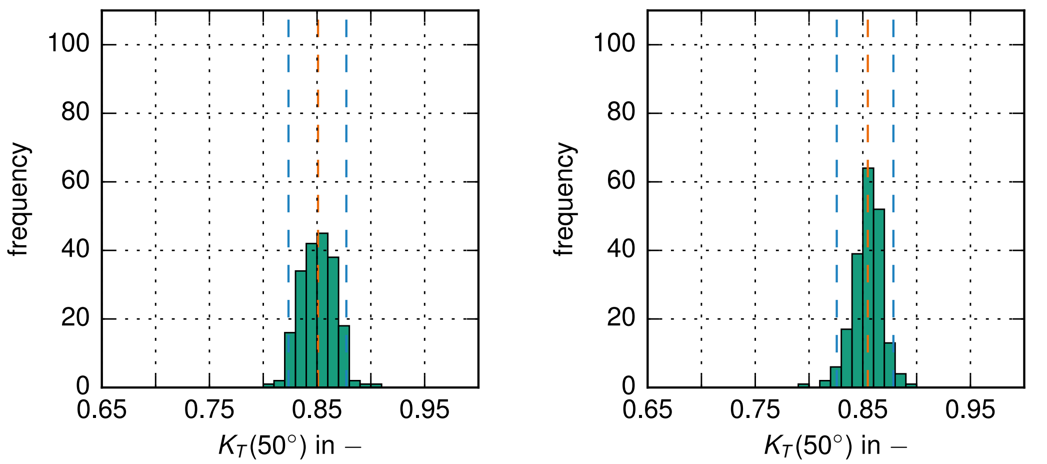

(a) BS histogram of $K_T(50°)$ (b) RSS histogram of $K_T(50°)$

Figure D.3: Comparison of transversal IAM results for complete identification model. Histogram of $K_T(50°)$ based on bootstrapping (a) versus random sub-sampling (b) for complete identification model ($\eta_{opt,0}$, u_0/u_1, K_T/K_L) with five measurement days at 15 s time step with 5 °-IAM identification.

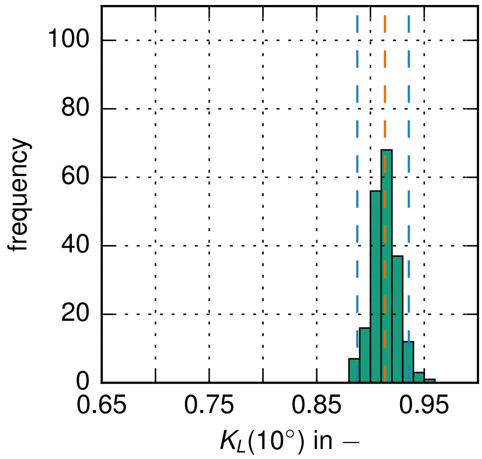

(a) BS histogram of $K_L(10\,°)$

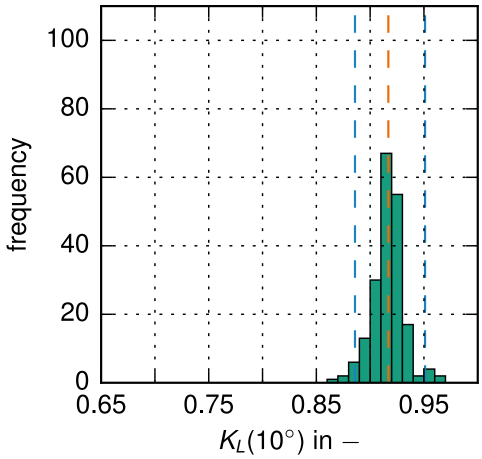

(b) RSS histogram of $K_L(10\,°)$

Figure D.4: Comparison of longitudinal IAM results for complete identification model. Histogram of $K_L(10\,°)$ based on bootstrapping (a) versus random sub-sampling (b) for complete identification model ($\eta_{opt,0}$, u_0/u_1, K_T/K_L) with five measurement days at 15 s time step with 5 °-IAM identification.

Appendix E

Uncertainty Calculation

E.1 Specific Uncertainty Equations

For the collector power output $\dot{Q}$, the specifically applied formula for the combined uncertainty takes the form:

$$u_c^2(\dot{Q}) = \left(c_p \cdot \Delta T\right)^2 \cdot u^2(\dot{m}) + (\dot{m}_{in} \cdot \Delta T)^2 \cdot u^2(c_p) + \left(\dot{m}_{in} \cdot c_p\right)^2 \cdot u^2(\Delta T) \tag{E.1}$$

For DSG collectors, the power output $\dot{Q}_{DSG}$ is calculated by the specific formula for combined uncertainty:

$$\begin{aligned} u_c^2(\dot{Q}_{DSG}) = &\left(h_{evap}\right)^2 \cdot u^2(\dot{m}_{steam}) + (\dot{m}_{steam})^2 \cdot u^2(h_{evap}) + \\ &+ \left(c_p \cdot (T_{sat} - T_{in})\right)^2 \cdot u^2(\dot{m}_{in}) + (\dot{m}_{in} \cdot (T_{sat} - T_{in}))^2 \cdot u^2(c_p) + \\ &+ \left(\dot{m}_{in} \cdot c_p\right)^2 \cdot u^2(T_{sat}) + \left(-\dot{m}_{in} \cdot c_p\right)^2 \cdot u^2(T_{in}). \end{aligned} \tag{E.2}$$

The thermal collector efficiency η is defined by:

$$\eta = \frac{\dot{m}_{in} \cdot c_p \cdot \Delta T}{A_{Ap} \cdot G_{bn}}, \tag{E.3}$$

with the specifically applied formula for the combined uncertainty taking the form:

$$\begin{aligned} u_c^2(\eta) = &\left(\frac{c_p \cdot \Delta T}{A_{Ap} \cdot G_{bn}}\right)^2 \cdot u^2(\dot{m}_{in}) + \left(\frac{\dot{m}_{in} \cdot \Delta T}{A_{Ap} \cdot G_{bn}}\right)^2 \cdot u^2(c_p) + \\ &+ \left(\frac{\dot{m}_{in} \cdot c_p}{A_{Ap} \cdot G_{bn}}\right)^2 \cdot u^2(\Delta T) + \left(\frac{-\dot{m}_{in} \cdot c_p \cdot \Delta T}{A_{Ap} \cdot G_{bn}^2}\right)^2 \cdot u^2(G_{bn}) \end{aligned} \tag{E.4}$$

For DSG collectors, the outlet flow enthalpy $\dot{H}_{out}$ is defined in steady-state by:

$$\dot{H}_{out} = \dot{m}_{steam} \cdot h_{evap} + \dot{m}_{in} \cdot c_p \cdot T_{sat}, \tag{E.5}$$

with the specifically applied formula for the combined uncertainty being:

$$\begin{aligned} u_c^2(\dot{H}_{out}) = &\left(h_{evap}\right)^2 \cdot u^2(\dot{m}_{steam}) + (\dot{m}_{steam})^2 \cdot u^2(h_{evap}) \\ &+ \left(c_p \cdot (T_{sat} - T_{in})\right)^2 \cdot u^2(\dot{m}_{in}) + (\dot{m}_{in} \cdot (T_{sat} - T_{in}))^2 \cdot u^2(c_p) \\ &+ \left(\dot{m}_{in} \cdot c_p\right)^2 \cdot u^2(T_{sat}) \end{aligned} \tag{E.6}$$

Note that h_{evap} and T_{sat} represent a function of the steam drum pressure p_{SD} and can be calculated by a polynomial function

$$\begin{gathered} h_{evap} = A \cdot p_{SD}^2 + B \cdot p_{SD} + C, \\ A = 0.0286; \quad B = -10.209; \quad C = 2078.1. \end{gathered} \tag{E.7}$$

Similarly,

$$\begin{gathered} T_{sat} = A \cdot p_{SD}^3 + B \cdot p_{SD}^2 + C \cdot p_{SD} + D, \\ A = 0.0001; \quad B = -0.0337; \quad C = 3.4914; \quad D = 155.14. \end{gathered} \tag{E.8}$$

For the specific uncertainty calculation, the concept as introduced in Zirkel-Hofer et al. [2016, pp. 302–303] of uncertainty calculation in fluid properties is applied, leading to

$$u^2(h_{evap}) = \frac{\partial h_{evap}}{\partial p_{SD}}^2 \cdot u^2(p_{SD}) + h_{evap} \cdot u^2(h_{evap}), \tag{E.9}$$

and analogously

$$u^2(T_{sat}) = \frac{\partial T_{sat}}{\partial p_{SD}}^2 \cdot u^2(p_{SD}) + T_{sat} \cdot u^2(T_{sat}). \tag{E.10}$$

Uncertainties of the fluid properties are considered according to IAPWS [2003, p. 13] with 0.5 kJ/kg in uniform distribution for $u(h_{evap})$, which equals 0.034 % in the worst case. Linstrom and Mallard [1997] indicate an uncertainty of 0.025 % (1σ) for T_{sat}.

■ E.2 Nominal Operating Conditions for Uncertainty Calculation

Table E.2.1: Overview on measurement uncertainty of evaluated test collectors. Combined, expanded uncertainty of the collector power output with its reference operating conditions for every evaluated test collector.

Variable	Unit	LFC_w1	LFC_w2	LFC_w3	PTC_o1	LFC_s1	PTC_s1
HTF		water	water	water	thermal oil	DSG	DSG
T_{in}	°C	130	170	155	270	220	255
T_{out}	°C	144	183	161	358	–	–
p_{SD}	bar	–	–	–	–	30	70
$\dot{m}_{in}$	kg/s	0.85	0.58	2.72	3.60	1.25	1.31
$\dot{m}_{steam}$	kg/s	–	–	–	–	0.11	0.75
$\dot{Q}$	kW	50	32	66	742	271	1216
$U_c(\dot{Q})$ (2σ)	kW	0.70	0.53	2.98	29.21	11.12	22.37
$U_{c,rel}(\dot{Q})$ (2σ)	–	1.39 %	1.65 %	4.54 %	3.94 %	4.10 %	1.84 %
$U_c(\dot{H}_{out})$ (2σ)	kW	–	–	–	–	27.83	39.43
$U_{c,rel}(\dot{H}_{out})$ (2σ)	–	–	–	–	–	2.04 %	2.22 %
Ref. $u(sensor)$		Table B.2.1	Table B.2.2	Table B.2.3	Table B.2.6	Table B.2.4	Table B.2.5

Appendix F

Complements to the Testing Strategy

F.1 Supplementary Information

Table F.1.1: Settings of the reference collectors within the artificial data study. Artificial data are created for two exemplary small- and large-scale reference collectors with HTFs of water or salt and listed geometric and operating characteristics.

Variable	Unit	Small-scale collector	Large-scale collector
Heat transfer fluid		water	salt
Fluid temperature range	°C	50–240	250–550
Aperture area A_{Ap}	m^2	130	600
Collector length l_{col}	m	25	100
Orientation		17° West	17° West
Location		Germany	Spain

F.2 Justification of Using Ten Forks

The mathematical derivation of the justification was elaborated in Perry [2017]. Analog to the definitions introduced in Chapter 5, we refer to θ as the real—and in the case of artificial measurement data *known*—parameter vector. $\widehat{\theta}$ represents the best-fit estimate from the parameter identification procedure and is considered a random variable normally distributed with expected value $E[\widehat{\theta}] = \mu$ and variance σ^2. The distribution of this variable is approximated by sampling different forks i with their best-fit estimates $\widehat{\theta}_i$. The expected value μ of the random variable is estimated by the mean value $\overline{\theta}$ of the distribution for large N as follows:

$$\mu \approx \overline{\theta} = \overline{\widehat{\theta}} = \frac{1}{N}\sum_{i=1}^{N}\widehat{\theta}_i \tag{F.1}$$

The sample average represents a standard estimator for the expected value and is considered a point estimator for this value, with N being the number of forks.

Furthermore, the value can be described by an interval estimate, which allows to indicate the confidence interval of this mean value as a function of the number of forks N. For this interval estimate, an equation is given in literature (e.g., in Beichelt and

Montgomery [2003, pp. 258–259]). Instead of using S (the standard unbiased variance estimator) in the case of artificial measurement data—as the true value is known—we use the Root Mean Square Error (RMSE) defined by:

$$RMSE := \sqrt{\frac{1}{N}\sum_{i=1}^{N}(\widehat{\theta}_i - \theta)^2} \tag{F.2}$$

The confidence intervals can then be calculated analog to Beichelt and Montgomery [2003][1]:

$$\overline{\theta} - \frac{RMSE}{\sqrt{N}} \cdot t_N^{\alpha/2} \quad \leq \quad \mu \quad \leq \quad \overline{\theta} + \frac{RMSE}{\sqrt{N}} \cdot t_N^{\alpha/2} \tag{F.3}$$

In this case, the factor $t_N^{\alpha/2}$ is defined as the $\alpha/2$-percentile of the t-distribution with the degrees of freedom N.

Applying this concept to the case of artificial measurement data in dependence on the number of forks N, the following exemplary confidence intervals are obtained:

$$\begin{aligned} N = 3: &\quad \mu = \overline{\theta} \pm 1.837 \cdot RMSE \\ N = 10: &\quad \mu = \overline{\theta} \pm 0.7 \cdot RMSE \\ N = 30: &\quad \mu = \overline{\theta} \pm 0.37 \cdot RMSE \\ N = 120: &\quad \mu = \overline{\theta} \pm 0.18 \cdot RMSE \end{aligned} \tag{F.4}$$

The given intervals show a considerable improvement of the error bands from three to ten forks. Increasing the number of forks further improves the results, but the computation expense rises over-proportionally to the improvement. In the case of $N = 120$, the computational effort increases 12 times in comparison to $N = 10$. However, the narrowing of confidence intervals is only improving to $1/4$. With $N = 10$, computational efforts are large but still manageable, coupled with an acceptable accuracy of the corresponding confidence intervals. For this reason, a number of forks equal to ten was chosen.

[1] For a mathematical validity proof of this analogy see Perry [2017].

■ F.3 Calculation of Reference Heat Loss Standard Deviation

The introduced concept of reference heat loss error values (i.e., standard deviations) in Section 7.1.3 leads to the following particular calculations:

Small-scale water collector:
For the artificial data evaluation in the case of the small-scale water collector, the maximum of collector power output amounts approximately 48 kW. Considering a standard deviation of approximately 0.5 % (1σ) according to the values indicated in Figure 6.1(a), this leads to a power output uncertainty $u_c(\dot{Q})$ of 240 W. Dividing by the collector length of 25 m gives a reference heat loss standard deviation of approximately 10 W/m.

Large-scale molten salt collector:
For the artificial data evaluation in the case of the large-scale molten salt collector, the maximum of collector power output amounts approximately 230 kW. Considering a standard deviation of approximately 0.7 % (1σ) according to the values indicated in Figure 6.1(b), this leads to a power output uncertainty $u_c(\dot{Q})$ of 1610 W. Dividing by the collector length of 100 m gives a reference heat loss standard deviation of approximately 16 W/m.

Test collector `LFC_w2`:
For the real data evaluation of collector `LFC_w2`, the standard uncertainty $u_c(\dot{Q})$ amounts 265 W as given in Table 2.2 (with 530 W of $U_c(\dot{Q})$ (2σ)). Dividing by the collector length of 12 m leads to a reference heat loss standard deviation of approximately 22 W/m.

■ F.4 Extended Results

Table F.4.1: Dependency of optical identification quality on noise level for study including IAM identification. Mean error values over all measurement days and forks are split up according to their noise level. Results for the exemplary case of a collector with molten salt and evacuated receiver are shown.

Error	Noise level	Unit	IAM study
$\varepsilon_{rel}(\eta_{opt,0})$	0 %	%	0.00
	0.1 %	%	0.42
	0.5 %	%	1.24
$\varepsilon_{rel}(K_T)$	0 %	%	0.00
	0.1 %	%	0.44
	0.5 %	%	1.30
$\varepsilon_{rel}(K_L)$	0 %	%	0.00
	0.1 %	%	0.48
	0.5 %	%	1.54

Table F.4.2: Dependency of optical identification quality on number of measurement days for study including IAM identification. Mean error values and standard deviations over all forks, noise levels, and operating conditions are differentiated according to the number of included measurement days in the corresponding evaluation.

Study	Number of days	Unit	$\varepsilon_{rel}(\eta_{opt,0})$	$\sigma(\varepsilon_{rel}(\eta_{opt,0}))$	$\varepsilon_{rel}(K_L)$	$\varepsilon_{rel}(K_T)$
IAM with molten salt	1	%	1.07	1.81	1.22	1.00
	2	%	0.57	0.81	0.66	0.62
	3	%	0.52	0.98	0.67	0.52
	4	%	0.42	0.61	0.57	0.45
	>5	%	0.34	0.51	0.45	0.41

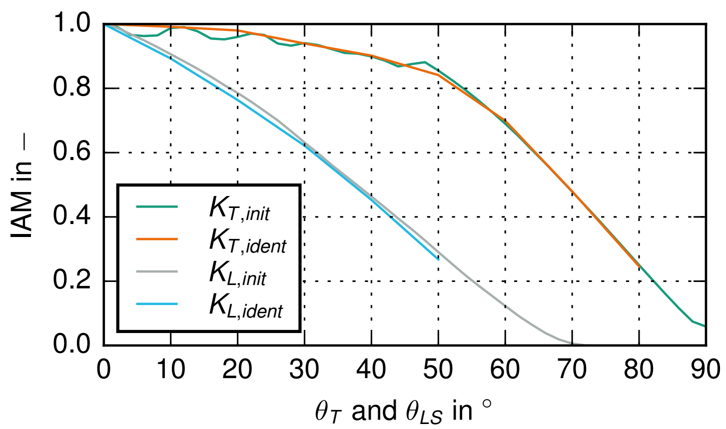

Figure F.1: Exemplary illustration of identified IAM curve with 10° angle step. For small transversal incidence angles the identified curve overestimates the IAM of the reference curve obtained by ray tracing.

Appendix G

Basic Characteristics of Artificial Data

Table G.0.1: Properties of artificially created days for the study with HTF water. Mean values are based on 0 % noise level and evacuated receiver. [adapted from Nettelstroth, 2015]

Name	Date	$\overline{T}_{in}$	$\sigma(T_{in})$	$\overline{T}_{out}$	$\sigma(T_{out})$	$\Delta\overline{T}$	$\overline{G_{bn}}$	$\sigma(G_{bn})$	$\overline{{}^{dG_{bn}}/_{dt}}$	$\sigma({}^{dG_{bn}}/_{dt})$	$\overline{\dot{m}_{in}}$	$\sigma(\dot{m}_{in})$	Start	End
–	yymmdd	°C	°C	°C	°C	°C	$^{W}/_{m^2}$	$^{W}/_{m^2}$	$^{W}/_{s \cdot m^2}$	$^{W}/_{s \cdot m^2}$	$^{kg}/_{s}$	$^{kg}/_{s}$	hhmmss	hhmmss
A1	130501	67.69	10.36	78.03	13.05	10.34	734.5	144.9	0.124	0.622	0.93	0.01	055300	185000
A2	130502	117.69	10.36	127.88	12.99	10.19	734.5	144.9	0.124	0.622	0.93	0.01	055300	185000
A3	130503	167.69	10.36	177.57	12.89	9.88	734.5	144.9	0.124	0.622	0.93	0.01	055300	185000
A4	130504	217.69	10.36	226.97	12.70	9.28	734.5	144.9	0.124	0.622	0.93	0.01	055300	185000
B1	130601	40.11	18.00	49.97	6.52	9.86	405.9	350.0	3.319	7.251	0.89	0.13	055300	181800
B2	130602	80.11	18.00	89.88	6.49	9.77	405.9	350.0	3.319	7.251	0.89	0.13	055300	181800
B3	130603	130.11	18.00	139.67	6.40	9.56	405.9	350.0	3.319	7.251	0.89	0.13	055300	181800
B4	130604	180.11	18.00	189.34	6.23	9.23	405.9	350.0	3.319	7.251	0.89	0.13	055300	181800
B5	130605	220.11	18.00	228.91	5.96	8.80	405.9	350.0	3.319	7.251	0.89	0.13	055300	181800
E1	130615	52.48	1.07	64.02	4.39	11.54	653.8	155.7	0.722	1.099	0.90	0.01	063000	180000
E2	130616	102.48	1.07	113.84	4.34	11.36	653.8	155.7	0.722	1.099	0.90	0.01	063000	180000
E3	130617	152.48	1.07	163.49	4.26	11.01	653.8	155.7	0.722	1.099	0.90	0.01	063000	180000
E4	130618	192.48	1.07	203.05	4.14	10.57	653.8	155.7	0.722	1.099	0.90	0.01	063000	180000
E5	130619	232.48	1.07	242.36	3.95	9.88	653.8	155.7	0.722	1.099	0.90	0.01	063000	180000
C1	130701	49.90	12.64	61.22	12.80	11.31	696.9	170.2	0.225	0.617	0.95	0.01	055600	184300
C2	130702	89.90	12.64	101.09	12.76	11.19	696.9	170.2	0.225	0.617	0.95	0.01	055600	184300
C3	130703	149.90	12.64	160.70	12.70	10.80	696.9	170.2	0.225	0.617	0.95	0.01	055600	184300
C4	130704	209.90	12.64	219.98	12.57	10.07	696.9	170.2	0.225	0.617	0.95	0.01	055600	184300
F1	130715	43.85	28.45	55.49	29.02	11.65	685.4	164.8	1.116	3.590	0.93	0.01	070000	170000
F2	130716	93.85	28.45	105.31	28.90	11.47	685.4	164.8	1.116	3.590	0.93	0.01	070000	170000
F3	130717	143.85	28.45	154.95	28.78	11.10	685.4	164.8	1.116	3.590	0.93	0.01	070000	170000
F4	130718	193.85	28.45	204.35	28.55	10.50	685.4	164.8	1.116	3.590	0.93	0.01	070000	170000
D1	130801	52.57	1.09	64.83	5.20	12.25	768.1	175.0	0.099	0.327	0.90	0.01	060200	182000
D2	130802	102.57	1.09	114.58	5.13	12.00	768.1	175.0	0.099	0.327	0.90	0.01	060200	182000
D3	130803	152.57	1.09	164.15	5.02	11.58	768.1	175.0	0.099	0.327	0.90	0.01	060200	182000
D4	130804	192.57	1.09	203.63	4.87	11.05	768.1	175.0	0.099	0.327	0.90	0.01	060200	182000
D5	130805	232.57	1.09	242.85	4.63	10.27	768.1	175.0	0.099	0.327	0.90	0.01	060200	182000

Table G.0.2: Properties of artificially created days for the study with HTF molten salt. Mean values are based on 0 % noise level and evacuated receiver. [adapted from Nettelstroth, 2015]

Name	Date	$\overline{T}_{in}$	$\sigma(T_{in})$	$\overline{T}_{out}$	$\sigma(T_{out})$	$\Delta\overline{T}$	$\overline{G_{bn}}$	$\sigma(G_{bn})$	$\overline{dG_{bn}/dt}$	$\sigma(dG_{bn}/dt)$	$\overline{\dot{m}_{in}}$	$\sigma(\dot{m}_{in})$	Start	End
—	yymmdd	°C	°C	°C	°C	°C	W/m^2	W/m^2	$W/s{\cdot}m^2$	$W/s{\cdot}m^2$	kg/s	kg/s	hhmmss	hhmmss
Gaa1	110401	410.00	0.00	486.64	5.35	76.64	900.7	58.7	0.042	0.056	1.98	0.41	083000	180000
Gaa2	110402	440.00	0.00	515.98	5.24	75.98	900.7	58.7	0.042	0.056	1.98	0.41	083000	180000
Gaa3	110403	470.00	0.00	545.24	5.13	75.24	900.7	58.7	0.042	0.056	1.98	0.41	083000	180000
Gaa4	110404	500.00	0.00	574.45	5.03	74.45	900.7	58.7	0.042	0.056	1.98	0.41	083000	180000
Haa1	110701	410.00	0.00	496.43	5.58	86.43	626.7	164.2	0.831	0.783	1.52	0.51	083000	180000
Haa2	110702	440.00	0.00	524.69	5.61	84.69	626.7	164.2	0.831	0.783	1.52	0.51	083000	180000
Haa3	110703	470.00	0.00	552.87	5.75	82.87	626.7	164.2	0.831	0.783	1.52	0.51	083000	180000
Haa4	110704	500.00	0.00	580.96	6.03	80.96	626.7	164.2	0.831	0.783	1.52	0.51	083000	180000
Iaa1	110801	410.00	0.00	498.97	6.09	88.97	548.0	229.9	1.707	1.363	1.21	0.60	090000	180000
Iaa2	110802	440.00	0.00	526.62	5.71	86.62	548.0	229.9	1.707	1.363	1.21	0.60	090000	180000
Iaa3	110803	470.00	0.00	554.17	5.48	84.17	548.0	229.9	1.707	1.363	1.21	0.60	090000	180000
Iaa4	110804	500.00	0.00	581.62	5.45	81.62	548.0	229.9	1.707	1.363	1.21	0.60	090000	180000
Gab1	120401	410.00	0.00	473.40	13.32	63.40	900.7	58.7	0.042	0.056	2.40	0.00	083000	180000
Gab2	120402	440.00	0.00	502.87	13.23	62.87	900.7	58.7	0.042	0.056	2.40	0.00	083000	180000
Gab3	120403	470.00	0.00	532.29	13.14	62.29	900.7	58.7	0.042	0.056	2.40	0.00	083000	180000
Gab4	120404	500.00	0.00	561.66	13.05	61.66	900.7	58.7	0.042	0.056	2.40	0.00	083000	180000
Hab1	120701	410.00	0.00	483.07	21.03	73.07	626.7	164.2	0.831	0.783	1.80	0.00	083000	180000
Hab2	120702	440.00	0.00	511.76	20.96	71.76	626.7	164.2	0.831	0.783	1.80	0.00	083000	180000
Hab3	120703	470.00	0.00	540.39	20.89	70.39	626.7	164.2	0.831	0.783	1.80	0.00	083000	180000
Hab4	120704	500.00	0.00	568.97	20.82	68.97	626.7	164.2	0.831	0.783	1.80	0.00	083000	180000
Iab1	120801	410.00	0.00	453.81	18.25	43.81	548.0	229.9	1.707	1.363	2.50	0.00	090000	180000
Iab2	120802	440.00	0.00	482.82	18.14	42.82	548.0	229.9	1.707	1.363	2.50	0.00	090000	180000
Iab3	120803	470.00	0.00	511.78	18.03	41.78	548.0	229.9	1.707	1.363	2.50	0.00	090000	180000
Iab4	120804	500.00	0.00	540.70	17.92	40.70	548.0	229.9	1.707	1.363	2.50	0.00	090000	180000
Gba1	210401	432.11	13.21	487.12	5.09	55.01	900.7	58.7	0.042	0.056	2.80	0.69	083000	180000
Gba2	210402	462.11	13.21	516.62	5.06	54.51	900.7	58.7	0.042	0.056	2.80	0.69	083000	180000
Gba3	210403	492.11	13.21	546.08	5.05	53.97	900.7	58.7	0.042	0.056	2.80	0.69	083000	180000
Gba4	210404	522.11	13.21	575.49	5.05	53.38	900.7	58.7	0.042	0.056	2.80	0.69	083000	180000
Hba1	210701	432.11	13.21	494.07	3.90	61.96	626.7	164.2	0.831	0.783	2.17	0.78	083000	180000
Hba2	210702	462.11	13.21	522.74	4.17	60.63	626.7	164.2	0.831	0.783	2.17	0.78	083000	180000

Table G.0.2: Properties of artificially created days for the study with HTF molten salt. Mean values are based on 0 % noise level and evacuated receiver. (continued)

Name	Date	$\overline{T}_{in}$	$\sigma(T_{in})$	$\overline{T}_{out}$	$\sigma(T_{out})$	$\Delta\overline{T}$	$\overline{G_{bn}}$	$\sigma(G_{bn})$	$\overline{dG_{bn}/dt}$	$\sigma(dG_{bn}/dt)$	$\overline{\dot{m}_{in}}$	$\sigma(\dot{m}_{in})$	Start	End
—	yymmdd	°C	°C	°C	°C	°C	W/m^2	W/m^2	$W/s{\cdot}m^2$	$W/s{\cdot}m^2$	kg/s	kg/s	hhmmss	hhmmss
Hba3	210703	492.11	13.21	551.35	4.60	59.24	626.7	164.2	0.831	0.783	2.17	0.78	083000	180000
Hba4	210704	522.11	13.21	579.90	5.19	57.79	626.7	164.2	0.831	0.783	2.17	0.78	083000	180000
Iba1	210801	433.34	12.47	495.97	4.36	62.63	548.0	229.9	1.707	1.363	1.74	0.92	090000	180000
Iba2	210802	463.34	12.47	524.22	4.24	60.88	548.0	229.9	1.707	1.363	1.74	0.92	090000	180000
Iba3	210803	493.34	12.47	552.39	4.30	59.06	548.0	229.9	1.707	1.363	1.74	0.92	090000	180000
Iba4	210804	523.34	12.47	580.49	4.56	57.15	548.0	229.9	1.707	1.363	1.74	0.92	090000	180000
Gbb1	220401	432.11	13.21	477.73	15.08	45.62	900.7	58.7	0.042	0.056	3.30	0.00	083000	180000
Gbb2	220402	462.11	13.21	507.34	15.02	45.23	900.7	58.7	0.042	0.056	3.30	0.00	083000	180000
Gbb3	220403	492.11	13.21	536.90	14.96	44.79	900.7	58.7	0.042	0.056	3.30	0.00	083000	180000
Gbb4	220404	522.11	13.21	566.43	14.91	44.32	900.7	58.7	0.042	0.056	3.30	0.00	083000	180000
Hbb1	220701	432.11	13.21	471.69	19.24	39.58	626.7	164.2	0.831	0.783	3.30	0.00	083000	180000
Hbb2	220702	462.11	13.21	500.96	19.20	38.85	626.7	164.2	0.831	0.783	3.30	0.00	083000	180000
Hbb3	220703	492.11	13.21	530.21	19.15	38.10	626.7	164.2	0.831	0.783	3.30	0.00	083000	180000
Hbb4	220704	522.11	13.21	559.42	19.10	37.31	626.7	164.2	0.831	0.783	3.30	0.00	083000	180000
Ibb1	220801	433.34	12.47	469.18	19.52	35.84	548.0	229.9	1.707	1.363	3.00	0.00	090000	180000
Ibb2	220802	463.34	12.47	498.33	19.41	34.99	548.0	229.9	1.707	1.363	3.00	0.00	090000	180000
Ibb3	220803	493.34	12.47	527.44	19.30	34.11	548.0	229.9	1.707	1.363	3.00	0.00	090000	180000
Ibb4	220804	523.34	12.47	556.52	19.19	33.18	548.0	229.9	1.707	1.363	3.00	0.00	090000	180000
Gca1	310401	437.03	15.64	487.86	4.30	50.83	900.7	58.7	0.042	0.056	3.39	1.49	083000	180000
Gca2	310402	467.03	15.64	517.39	4.22	50.36	900.7	58.7	0.042	0.056	3.39	1.49	083000	180000
Gca3	310403	497.03	15.64	546.87	4.14	49.85	900.7	58.7	0.042	0.056	3.39	1.49	083000	180000
Gca4	310404	527.03	15.64	576.31	4.08	49.28	900.7	58.7	0.042	0.056	3.39	1.49	083000	180000
Hca1	310701	437.03	15.64	494.94	5.72	57.91	626.7	164.2	0.831	0.783	2.59	1.34	083000	180000
Hca2	310702	467.03	15.64	523.67	5.54	56.65	626.7	164.2	0.831	0.783	2.59	1.34	083000	180000
Hca3	310703	497.03	15.64	552.35	5.49	55.32	626.7	164.2	0.831	0.783	2.59	1.34	083000	180000
Hca4	310704	527.03	15.64	580.96	5.58	53.94	626.7	164.2	0.831	0.783	2.59	1.34	083000	180000
Ica1	310801	437.43	15.95	496.85	6.32	59.42	548.0	229.9	1.707	1.363	2.07	1.27	090000	180000
Ica2	310802	467.43	15.95	525.14	5.62	57.71	548.0	229.9	1.707	1.363	2.07	1.27	090000	180000
Ica3	310803	497.43	15.95	553.35	5.09	55.92	548.0	229.9	1.707	1.363	2.07	1.27	090000	180000
Ica4	310804	527.43	15.95	581.48	4.82	54.06	548.0	229.9	1.707	1.363	2.07	1.27	090000	180000

Table G.0.2: Properties of artificially created days for the study with HTF molten salt. Mean values are based on 0 % noise level and evacuated receiver. (continued)

Name	Date	$\overline{T}_{in}$	$\sigma(T_{in})$	$\overline{T}_{out}$	$\sigma(T_{out})$	$\Delta\overline{T}$	$\overline{G_{bn}}$	$\sigma(G_{bn})$	$\overline{dG_{bn}/dt}$	$\sigma(dG_{bn}/dt)$	$\overline{\dot{m}_{in}}$	$\sigma(\dot{m}_{in})$	Start	End
—	yymmdd	°C	°C	°C	°C	°C	W/m^2	W/m^2	$W/s\cdot m^2$	$W/s\cdot m^2$	kg/s	kg/s	hhmmss	hhmmss
Gcb1	320401	437.03	15.64	462.33	20.31	25.30	900.7	58.7	0.042	0.056	6.00	0.00	083000	180000
Gcb2	320402	467.03	15.64	492.11	20.27	25.08	900.7	58.7	0.042	0.056	6.00	0.00	083000	180000
Gcb3	320403	497.03	15.64	521.87	20.23	24.84	900.7	58.7	0.042	0.056	6.00	0.00	083000	180000
Gcb4	320404	527.03	15.64	551.61	20.18	24.58	900.7	58.7	0.042	0.056	6.00	0.00	083000	180000
Hcb1	320701	437.03	15.64	458.99	19.24	21.96	626.7	164.2	0.831	0.783	6.00	0.00	083000	180000
Hcb2	320702	467.03	15.64	488.59	19.22	21.56	626.7	164.2	0.831	0.783	6.00	0.00	083000	180000
Hcb3	320703	497.03	15.64	518.17	19.19	21.14	626.7	164.2	0.831	0.783	6.00	0.00	083000	180000
Hcb4	320704	527.03	15.64	547.73	19.17	20.71	626.7	164.2	0.831	0.783	6.00	0.00	083000	180000
Icb1	320801	437.43	15.95	459.21	20.31	21.78	548.0	229.9	1.707	1.363	5.00	0.00	090000	180000
Icb2	320802	467.43	15.95	488.70	20.28	21.27	548.0	229.9	1.707	1.363	5.00	0.00	090000	180000
Icb3	320803	497.43	15.95	518.16	20.25	20.73	548.0	229.9	1.707	1.363	5.00	0.00	090000	180000
Icb4	320804	527.43	15.95	547.60	20.22	20.18	548.0	229.9	1.707	1.363	5.00	0.00	090000	180000

Table G.0.3: Properties of artificially created days for the study with IAM identification. Mean values are based on 0 % noise level, evacuated receiver and HTF molten salt. [adapted from Nettelstroth, 2015]

Name	Date	$\overline{T}_{in}$	$\sigma(T_{in})$	$\overline{T}_{out}$	$\sigma(T_{out})$	$\Delta\overline{T}$	$\overline{G_{bn}}$	$\sigma(G_{bn})$	$\overline{dG_{bn}/dt}$	$\sigma(dG_{bn}/dt)$	$\overline{\dot{m}_{in}}$	$\sigma(\dot{m}_{in})$	Start	End
–	yymmdd	°C	°C	°C	°C	°C	W/m^2	W/m^2	$W/s{\cdot}m^2$	$W/s{\cdot}m^2$	kg/s	kg/s	hhmmss	hhmmss
Ap1	910412	470.00	0.00	506.07	13.65	36.07	703.1	156.7	0.854	0.782	3.30	0.00	074000	184000
Ma1	910512	470.00	0.00	512.65	13.96	42.65	742.9	130.9	0.573	0.684	3.30	0.00	073500	190000
Jn1	910609	470.00	0.00	512.52	15.32	42.52	721.8	152.9	0.549	0.683	3.30	0.00	072300	192300
Jl1	910705	470.00	0.00	508.35	16.32	38.35	658.5	176.2	0.854	0.839	3.30	0.00	070700	191800
Jl2	910710	470.00	0.00	509.49	17.40	39.49	677.8	182.7	0.612	0.747	3.30	0.00	072100	194500
Jl3	910718	470.00	0.00	506.96	15.16	36.96	639.4	172.5	0.877	0.822	3.30	0.00	071400	190600
Jl4	910728	470.00	0.00	504.24	15.50	34.24	599.8	199.5	0.901	0.968	3.30	0.00	073900	190300
Ag1	910805	470.00	0.00	502.31	14.51	32.31	579.5	170.0	0.876	0.839	3.30	0.00	073100	190000
Ag2	910813	470.00	0.00	504.37	14.58	34.37	623.6	173.2	0.887	0.801	3.30	0.00	073200	185100
Ag3	910822	470.00	0.00	501.64	11.92	31.64	587.1	150.5	0.854	0.881	3.30	0.00	074900	182500
Ag4	910831	470.00	0.00	507.81	13.47	37.81	703.9	173.6	0.815	0.826	3.30	0.00	080500	182000
Sp1	910906	470.00	0.00	504.50	13.53	34.50	682.7	175.3	0.800	0.780	3.30	0.00	080500	183500
Oc1	911006	470.00	0.00	500.03	11.99	30.03	740.2	165.3	0.766	0.683	3.30	0.00	080800	175000